

Lecture Notes on Multidisciplinary Industrial Engineering
Series Editor: J. Paulo Davim

Babu Subramanian
Shiao-Shing Chen
Krishna R. Reddy *Editors*

Emerging Technologies for Agriculture and Environment

Select Proceedings of ITsFEW 2018

 Springer

Lecture Notes on Multidisciplinary Industrial Engineering

Series Editor

J. Paulo Davim, Department of Mechanical Engineering, University of Aveiro, Aveiro, Portugal

“Lecture Notes on Multidisciplinary Industrial Engineering” publishes special volumes of conferences, workshops and symposia in interdisciplinary topics of interest. Disciplines such as materials science, nanosciences, sustainability science, management sciences, computational sciences, mechanical engineering, industrial engineering, manufacturing, mechatronics, electrical engineering, environmental and civil engineering, chemical engineering, systems engineering and biomedical engineering are covered. Selected and peer-reviewed papers from events in these fields can be considered for publication in this series.

More information about this series at <http://www.springer.com/series/15734>

Babu Subramanian · Shiao-Shing Chen ·
Krishna R. Reddy
Editors

Emerging Technologies for Agriculture and Environment

Select Proceedings of ITsFEW 2018

 Springer

Editors

Babu Subramanian
Vellore Institute of Technology
Vellore, Tamil Nadu, India

Shiao-Shing Chen
National Taipei University of Technology
Taipei City, Taiwan

Krishna R. Reddy
University of Illinois at Chicago
Chicago, IL, USA

ISSN 2522-5022

ISSN 2522-5030 (electronic)

Lecture Notes on Multidisciplinary Industrial Engineering

ISBN 978-981-13-7967-3

ISBN 978-981-13-7968-0 (eBook)

<https://doi.org/10.1007/978-981-13-7968-0>

© Springer Nature Singapore Pte Ltd. 2020

This work is subject to copyright. All rights are reserved by the Publisher, whether the whole or part of the material is concerned, specifically the rights of translation, reprinting, reuse of illustrations, recitation, broadcasting, reproduction on microfilms or in any other physical way, and transmission or information storage and retrieval, electronic adaptation, computer software, or by similar or dissimilar methodology now known or hereafter developed.

The use of general descriptive names, registered names, trademarks, service marks, etc. in this publication does not imply, even in the absence of a specific statement, that such names are exempt from the relevant protective laws and regulations and therefore free for general use.

The publisher, the authors and the editors are safe to assume that the advice and information in this book are believed to be true and accurate at the date of publication. Neither the publisher nor the authors or the editors give a warranty, expressed or implied, with respect to the material contained herein or for any errors or omissions that may have been made. The publisher remains neutral with regard to jurisdictional claims in published maps and institutional affiliations.

This Springer imprint is published by the registered company Springer Nature Singapore Pte Ltd. The registered company address is: 152 Beach Road, #21-01/04 Gateway East, Singapore 189721, Singapore

Contents

1	A Comparative Study of Conventional and Smart Farming	1
	Nipun Katyal and B. Jaganatha Pandian	
2	Evolutionary Relationship of Penicillin-Binding Protein 2 Coding <i>penA</i> Gene and Understanding the Role in Drug-Resistance Mechanism Using Gene Interaction Network Analysis	9
	Sravan Kumar Miryala, Anand Anbarasu and Sudha Ramaiah	
3	The Effect of Alccofine on Blended Concrete Under Compression	27
	A. Narender Reddy and T. Meena	
4	IoT Sensor-Based Smart Agricultural System	39
	J. Mahalakshmi, K. Kuppusamy, C. Kaleeswari and P. Maheswari	
5	Smart Monitoring of Farmland Using Fuzzy-Based Distributed Wireless Sensor Networks	53
	Anagha Rajput, Vinoth Babu Kumaravelu and Arthi Murugadass	
6	Genetic Algorithm to Find Most Optimum Growing Technique for Multiple Cropping Using Big Data	77
	Vinamra Das and Sunny Jain	
7	A Study on Strength Properties and Cost Analysis of Industrial Byproduct-Based Ternary Blended Geopolymer Concrete	95
	Kuunreddy Srinivas Reddy and S. Bala Murugan	
8	Monitoring Quality of Tap Water in Cities Using IoT	107
	Asis Kumar Tripathy, Tapan Kumar Das and Chiranjil Lal Chowdhary	
9	Smart Bin with Automated Metal Segregation and Optimal Distribution of the Bins	115
	K. C. Saranya, Vijayaraj Sujana, Balasubramanian Abivishaq and K. Nithish Kanna	

10	Solar-Assisted Smart Solid Waste Dustbin	127
	R. Jayagopal, T. Devapounraj and V. Mayilvelnathan	
11	Development of Bio-hybrid Tractor for Farming Applications	143
	Intakhab Khan, Vinayak A. Modi, Sohail Akhtar Khan and C. Kannan	
12	Study of Lightweight Mortar by Replacing Cement and Aggregates with Admixtures	157
	Pankaj Sharma, Rajat Gupta, Kshethra Pradeep, Hritik S. Kothari and A. Sofi	
13	Design of a Domestic Defluoridizing Unit	173
	Shaheda Parveen, Venkata Nadh Ratnakaram, Sireesha Malladi and K. Kiram Kumar	
14	Simultaneous Saccharification and Fermentation of Watermelon Waste for Ethanol Production	185
	Venkata Nadh Ratnakaram, C. G. Prakasa Rao and Satya Sree	
15	Autonomous Multifunctional Quadcopter for Real-Time Object Tracking and Seed Bombing in a Dynamic Environment	199
	Pratham Nar, Shashank Sadanand Amin, Sashwata Banerjee, Vaibhav Garg and Arjun Pardasani	
16	Designing of a Bulk Dishwasher for Water Conservation in Mega Kitchens	213
	Adheesh Shah, Vinayak A. Modi and M. Boopathi	
17	Modelling Water Resources in the Ancient Indus Valley City of Dholavira and Lessons Learnt	223
	Satyajit Ghosh, M. Umashankar and Sayan Chowdhury	
18	Smart Printed Paperboard for Green Infrastructure	239
	T. K. S. LakshmiPriya and N. Alagusundari	
19	WSN-Based System for Forest Fire Detection and Mitigation	249
	Kotish Grover, Ditsha Kahali, Shreya Verma and Balaji Subramanian	
20	Analysis of Grid Parameter Variation with Renewable Energy Sources on Variable Frequency Drive DC Capacitor Reliability	261
	P. Ramesh, R. Govarthan, K. Palanisamy and S. Paramasivam	

About the Editors

Dr. Babu Subramanian is currently Professor and Dean of VIT School of Agricultural Innovations and Advanced Learning (VAIAL). He graduated from Tamil Nadu Agricultural University, Tamil Nadu, India with vast post-doctoral research experience from University of Angers, France, University of Alberta, Canada, Pennsylvania State University, USA, North Eastern Ohio Universities College of Medicine, USA, Florida Atlantic University, USA. His research areas include molecular plant-microbe interactions and functional genomics and he is currently working on proteome level investigations on cross-talking genes in rice during abiotic and biotic stress, role of transcription factors and their downstream genes in plant disease resistance, metabolic engineering of tomato for over-expression of stigmasterol biosynthesis, molecular interactions of human enteric bacteria in fruits and vegetables, compatibility of biocontrol and biofertilizer bacteria in crop growth and health and bacterial biofilms: metagenomics and bioinformatics. He has published around 75 papers in notable journals and more than 100 papers in reputed conferences.

Dr. Shiao-Shing Chen is currently working as Distinguished Professor at the Institute of Environmental Engineering and Management, National Taipei University of Technology. He obtained his Ph.D. from the University of Central Florida, Master from the University of Maryland, College Park, and Bachelor from National Cheng Kung University. He also had his sabbatical researches in University of Washington, Seattle and University of Technology, Sydney. He has over 20 years of research, teaching and consulting experience. His areas of interest include physicochemical process on water and wastewater treatment by incorporation of membrane. Currently, his projects have primarily dealt with membrane, oxidation-reduction, and catalysis processes for application in the High-Tech industries in Taiwan and several full scale plants have been built based on his researches. He has published more than 100 papers in reputed journals and more than 100 papers in conference proceedings. He has also authored four book chapters including Sustainable Desalination Process in Environmental Chemistry for a Sustainable World and Nanoscale Materials in Water Purification. He was a guest

editor for Journal of Environmental Engineering, ASCE and was on the editorial board of several renowned journals. He has received several awards for excellence in research including Taipei Tech Distinguished Researcher Award two times and Research Award from Chinese institute of environmental engineering (CIEE).

Dr. Krishna R. Reddy is Professor of Civil and Environmental Engineering, the Director of Sustainable Engineering Research Laboratory (SERL), and also the Director of the Geotechnical and Geoenvironmental Engineering Laboratory (GAGEL) in the Department of Civil and Materials Engineering at the University of Illinois at Chicago (UIC). Dr. Reddy has over 25 years of research, teaching and consulting experience within the broad fields of civil, geotechnical, materials and environmental engineering, addressing the nexus among sustainability, resiliency, infrastructure, water, energy, and the environment in an urban setting. His research expertise includes: environmental remediation of soils, sediments, groundwater, and stormwater; solid and hazardous waste management and landfill engineering; engineering applications of waste/recycled materials; life cycle assessment and sustainable engineering; and geotechnical engineering. His research is funded by the U.S. National Science Foundation, the United States Environmental Protection Agency, several prominent state and local government agencies, and industries. Dr. Reddy is the author of three books: (1) *Geoenvironmental Engineering: Site Remediation, Waste Containment, and Emerging Waste Management Technologies*, (2) *Electrochemical Remediation Technologies for Polluted Soils, Sediments and Groundwater*, and (3) *Sustainable Remediation of Contaminated Sites*. He has also published 193 journal papers, 14 edited books and conference proceedings, 12 book chapters, and 175 full conference papers. He has served or currently serves as an Associate Editor or Editorial Board Member of over 10 different journals, including the ASCE Journal of Geotechnical and Geoenvironmental Engineering, the ASTM Geotechnical Testing Journal, the ASCE Journal of Hazardous, Toxic and Radioactive Waste, the Journal of Hazardous Materials, among others. Dr. Reddy has received several awards for excellence in research and teaching, including the ASTM Hogentogler Award, the UIC Distinguished Researcher Award, the University of Illinois Scholar Award, and the University of Illinois Award for Excellence in Teaching. He is a Fellow of the American Society of Civil Engineers (FASCE), a Diplomat of Geotechnical Engineering (DGE), and a Board Certified Environmental Engineer (BCEE). He is also a registered Professional Civil Engineer (PE) and an Envision™ Sustainability Professional (ENV SP).

Chapter 1

A Comparative Study of Conventional and Smart Farming



Nipun Katyal  and B. Jaganatha Pandian 

Abstract Agriculture is at the heart of all occupations in developing countries, and with developing technologies, the application should be cost-effective and efficient. The proposed setup includes low-cost moisture, temperature sensors for optimizing water usage and yield, and radar sensors for monitoring any invasion in the farm. The setup is aimed to provide a study a miniature setup representing smart agriculture including smart water management with consistent monitoring for weather conditions in the present and future. An intelligent invasion monitoring system which can indicate animals or specifically pests invading the fields. This setup represents a part of a grid which will be utilizing solar power to prevent periodic replacements of batteries, and for this purpose, a solar panel will be used in the miniature farm. The main objective is to provide a comparative study of smart farms to conventional farms; these smart farms employ machine learning algorithms in real time to tackle problems related to water and energy. The Internet of things and machine learning have been advancing industrial purposes in each and every way, and finding its way in agriculture is still difficult due to the expenses which might not be affordable for a farmer. This research is a step toward efficient yet cost-effective farming.

Keywords Smart farming · Arduino · DHT11 · Soil moisture sensor · Neural network · Internet of things

1.1 Introduction

The aim of this research is to provide an approximate comparison between conventional farming methods and smart farming methods. The competition among these methods is defined under water usage as well as energy usage. The first experiment is to test the usage of water for both the methods, where the process of irrigation is

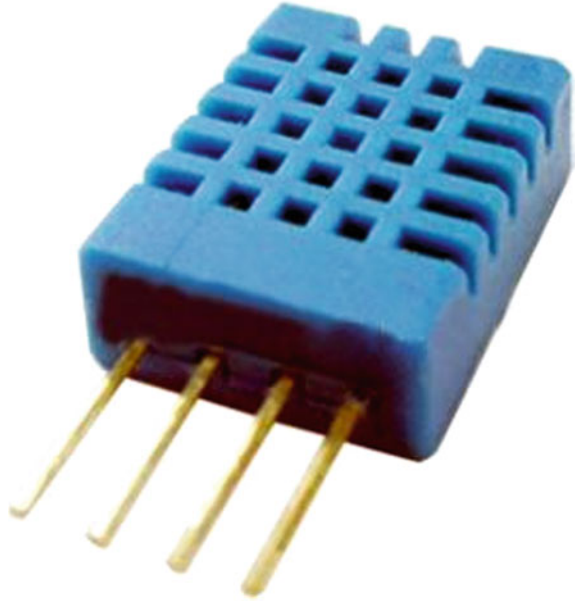
N. Katyal (✉) · B. Jaganatha Pandian
School of Electrical Engineering, Vellore Institute of Technology, Vellore 632014, Tamil Nadu, India
e-mail: nipunkatyal9@gmail.com

© Springer Nature Singapore Pte Ltd. 2020
B. Subramanian et al. (eds.), *Emerging Technologies for Agriculture and Environment*, Lecture Notes on Multidisciplinary Industrial Engineering, https://doi.org/10.1007/978-981-13-7968-0_1

determined by human in the conventional method and a neural network in the proposed method, which is implemented for conventional farming as a certain amount water given to the crops with little or no intervention by the farmer on the possibility of rain while for smart farming a neural network is deployed which takes as input the humidity and temperature, and returns the chances of rainfall. This data is checked with the soil moisture at that point, and the decision to whether the crops should be watered or not is taken depending on the type of crops. The second experiment determines the power consumption for both conventional and smart farming, as it is obvious that the cost of smart farms is an issue, getting the most out of it is essential so that the invested amount is covered as soon as possible. The energy consumptions of smart farms will be comparable to normal farms although we still want a ratio so as to know what we are getting.

The idea behind the setup is having a grid of sensors all connected to the control room through the internet. At each of the grid point, we have a humidity sensor, a temperature sensor, and a soil moisture sensor. These sensors will send real-time data to the control room. The control room also receives information about the weather forecast and will primarily depend on the percentage of precipitation abbreviated as PoP. The functioning of the system is that the input, which is the humidity and temperature reading from the farm, is used to find out the chances of rain in the near future and a threshold can decide when should the crops be watered and how much water should be used. The system employs neural networks to create a lookup table between humidity, temperature, and probability of precipitation. The neural network is trained for a particular season and is updated simultaneously, while it is being used to optimize water consumption. The aim of using neural networks is that if any other parameter is to be added in, along with the existing inputs, the solution will just be another set of weights with minimal changes in the existing weight. The first part of the research is acquisition of the data set, and the second part is testing. The concept of a sensor sticks in [1] uses a soil moisture and a temperature sensor which has been extended to a sensor grid. In [2], the different conditions required for a crop to flourish are documented which can be used for the neural network training. Since we are using a sensor grid, the data can be handled as mentioned in [3]. Wolters et al. [4] include the different parameters that can be included in the computation. Implementing GSM modules as in [5] to create a wireless sensor network is an energy efficient solution, but the speed provided by a GSM module is not required at that level. The concept of a control room to monitor the data as well as taking suitable actions is provided by [6]. In [7], the use of an app to monitor data from the field is implemented using MySQL database which can be formed using the concept of big data. The microcontroller unit is interfaced with the help of arduino forum [8] and sensor data sheets provided by adafruit industries [9].

Fig. 1.1 DHT 11
Temperature and Humidity
Sensor



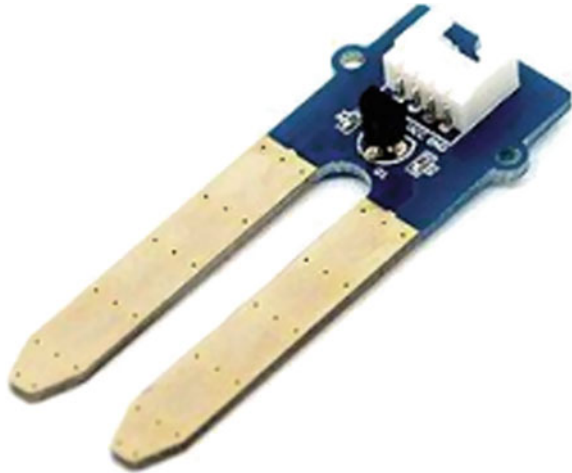
1.2 Preparation of Setup

The acquisition of data to train the neural net as well as to update the weight with the changing weather conditions is taken live from the field and stored, to convert the physical conditions to voltage values we need a transducer, it is done through a simple humidity and temperature sensor-DHT11 by Adafruit and a soil moisture sensor. These sensors are described in detail below.

1.2.1 Humidity and Temperature Sensor-DHT11

The DHT11 sensor has a low power requirement and works on 3 V with a sampling period not less than 1 s. The range of the sensor lies between 0 and 50 °C for temperature and 20–90% of relative humidity. The accuracy for humidity is $\pm 5\%$ RH and for temperature is ± 1 °C. These specifications are well suited for our application and are compatible with 8-bit microcontroller units. The working of the sensor is based on a resistive-type humidity measurement and a negative temperature coefficient measurement portion. The most important feature of this sensor is the high reliability and long-term stability (Fig. 1.1).

Fig. 1.2 Soil moisture sensor



1.2.2 Soil Moisture Sensor

The soil moisture sensor is another low power sensor which utilizes 5 V to operate and typical current of 300–700 mA. The sampling period has been set in sync with the former sensor as 1 s. The working of this sensor is based on the measurement of capacitance between the two plates. The sensor output voltage is directly proportional to the dielectric permittivity and hence the water content (Fig. 1.2).

1.2.3 Arduino MCU

This Arduino works on ATmega 2560 which has 54 digital pins and 16 analog pins, out of which 2 will be used for our sensors. It has a clock speed of 16 MHz and a dc current of 20 mA per pin. This microcontroller has been chosen for its low power consumption and support of serial communication protocols in practical applications where instead of a single sensor we have a grid of sensors, and each sensor will be connected to a bus. The identifier assigned to each of the sensors will then determine the parameter value in the proximity of that sensor (Fig. 1.3).

1.3 Training of the Neural Network

A neural network is analogous to the human brain with the cell body as the summing point of all the signal entering it from other neurons. The cell triggers when the threshold has been reached. The signals then travel down the axon and reach the

synapse where they are multiplied with the weights. Neural network learns when these weights are modified in a way that the error between the true output and the computed output is the least. The data acquired from the sensors in the field and weather forecast is used to train the neural network consisting of two input neurons, five hidden neurons, and one output neuron. The input variables are humidity and temperature in the field, and the output variable is the percentage of precipitation. The values will be compared with the values of the chances of raining from a trusted weather forecast data. The soil moisture data has no part in the neural network training but will give us the amount of water in the soil. The neural network is simulated using MATLAB, choosing the problem as a mapping from input to output feedforward network, although the use of a feedback network which will compare the computed percentage of precipitation with the data acquired from the forecast will increase the accuracy of the net. The reason behind not using the weather forecast data directly is that it is indicative of a generalized percentage, but the one we calculate from the neural network will be very specific and will include the effect of nearby industry emissions. The method used for minimizing the error in the cost function is scaled conjugate gradient method because it uses less memory and stops when the mean squared error stops decreasing.

1.3.1 Sample Data Set

This data set is one of many data sets on which we have trained the neural network. The samples show the variance of temperature, humidity, and soil moisture during the day. The output of the neural network, that is, the percentage of precipitation has been taken from the weather forecast for that particular time instant (Figs. 1.4 and 1.5).

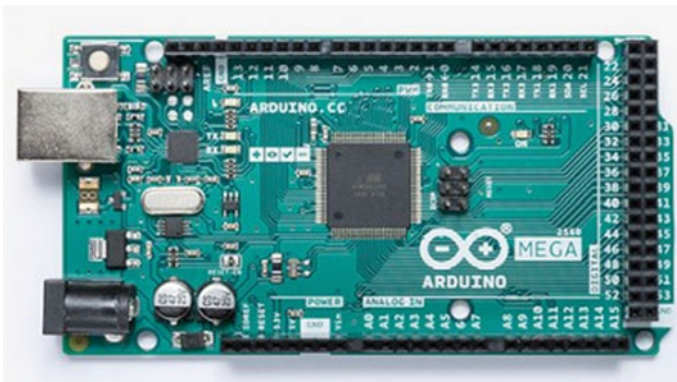


Fig. 1.3 Arduino Mega 2560

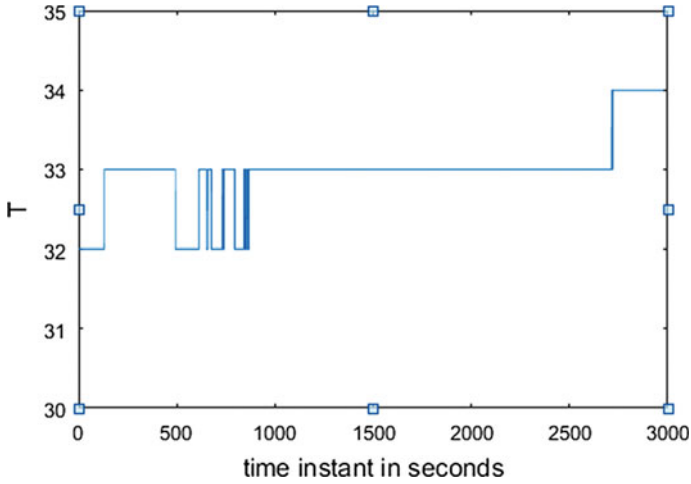


Fig. 1.4 Temperature readings from the field

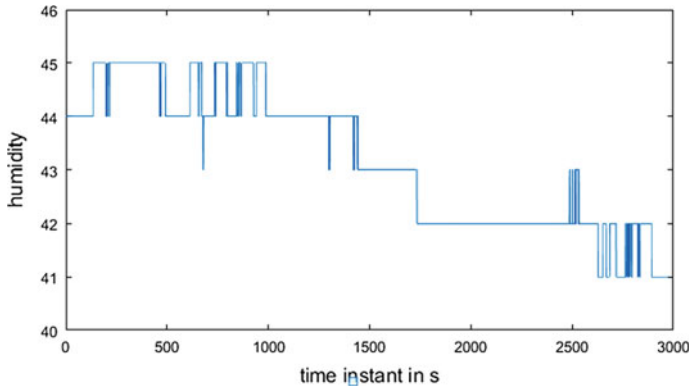


Fig. 1.5 Humidity readings from the field

1.4 Testing of the Neural Network

The neural network was tested on a variety of data set acquired during day and night with the accuracy of 76% and can be improved by adjusting the number of weights or in other words number of hidden neurons in the network. The neural network will have to be trained again and again as the seasons change and as the effect of pollutants increases, keeping in mind that it is just an approximation by a machine, human intellect can still overcome it by giving the person in-charge in the control room to have a provision to control the setup.

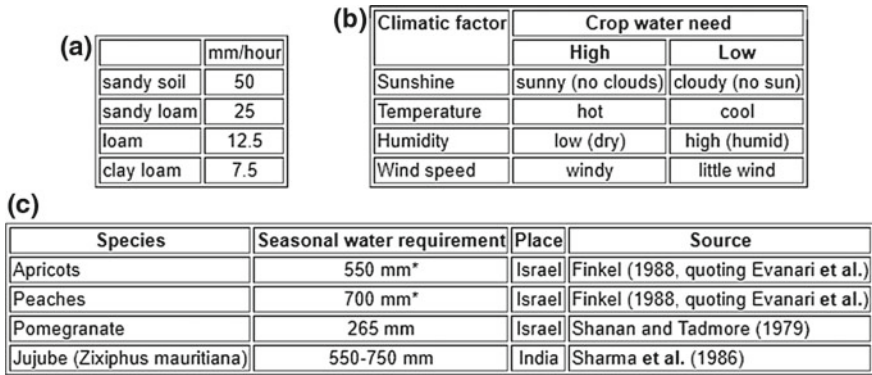


Fig. 1.6 a Infiltration rate for different kinds of soil. b Water requirement for crops under different weather conditions. c Water requirements by different crops

1.5 Optimization of Water Usage

The percentage of precipitation calculated on the basis of humidity and temperature using the neural network is used as a future reference whether the crops should be watered or not. There are different soil moisture levels, and different kinds of soils have different infiltration rate (Fig. 1.6).

The advantage of using a neural network is that another custom factor can be included in the network. Thus, adding a feature will yield better results and use water more optimally. The crop yield will also be higher and of better quality. Furthermore, the characteristics of the soil can be determined on the rate at which the water seeps down the soil or the infiltration rate.

1.6 Conclusion

Although the availability of water is an issue in both the cases, but having a limited amount of water and using it optimally can be achieved only through smart farming. The conventional farming methods are dependent on the capability of the farmer on how well can he determine whether the crops are in need of water, or the soil need to be manured because the top layer has changed in its composition, or is not suitable for the particular crop. On the other hand, smart farming can provide additional information about the soil and the changing weather conditions and save water in the best way. A farmer without the support of these new techniques would be no different from a farmer from the last century with similar machinery and the same farming techniques going down through generations. Everything is on the basis of a wild guess with no involvement of science. Using smart farming does not imply the elimination of human intellect but as an add-on to the benefits of having a system

that depends on the present and future conditions and produces a better yield. As the conventional farming is subjective and will vary from place to place, there is no definite comparison, while smart farming brings out the best possible solutions according to the place and the present conditions.

References

1. Nayar, A., Puri, V.: Smart farming: IoT based smart sensors agriculture stick for live temperature and moisture monitoring using Arduino, cloud computing & solar technology. In: The International Conference on Communication and Computing Systems (ICCCS-2016). <https://doi.org/10.1201/9781315364094-121>
2. Food and agriculture organization of the United Nations, <http://www.fao.org/docrep/u3160e/u3160e04.htm#TopOfPage>
3. Wu, Q., Liang, Y., Li, Y., Liang, Y.: Research on intelligent acquisition of smart agricultural big data. In: 2017 25th International Conference on Geoinformatics, pp. 1–7. IEEE (2017)
4. Wolters, S.L., Balafoutis, T., Fountas, S., van Evert, F.K.: D1.2 Research project results on Smart Farming Technology, Project coordinator: Spyros Fountas
5. Gondchawar, N., Kawitkar, R.S.: IoT based smart agriculture. *Int. J. Adv. Res. Comput. Commun. Eng. (IJARCCE)* **5**(6), 177–181 (2016)
6. Vidya Devi, V., Meena Kumari, G.: Real-time automation and monitoring system for modernized agriculture. *Int. J. Rev. Res. Appl. Sci. Eng. (IJRRASE)* **3**(1), 7–12 (2013)
7. Sen, S., Madhu, B.: Smart agriculture: a bliss to farmers. *Int. J. Eng. Sci. Res. Technol.* (2017)
8. Evans, B.W.: Arduino programming notebook
9. Adafruit Industries, www.adafruit.com

Chapter 2

Evolutionary Relationship of Penicillin-Binding Protein 2 Coding *penA* Gene and Understanding the Role in Drug-Resistance Mechanism Using Gene Interaction Network Analysis



Sravan Kumar Miryala , Anand Anbarasu  and Sudha Ramaiah 

Abstract The class A β -lactamase *penA* gene codes for penicillin-binding protein 2 (PBP2) which plays an important role in assembling the peptidoglycans on the outer side of the plasma membrane. The alteration in the structure of PBP2 protein makes the pathogen to gain resistance against penicillin. Thus, it is important to understand the role of drug-resistant mechanism by *penA* gene to develop potent drugs against penicillin-resistant pathogenic strains. In our study, we have used gene interaction network analysis of *penA* gene in various bacteria to understand its role in drug-resistant mechanisms. We have collected a total of 1039 interactions from 28 organisms available from STRING database. The *penA* gene interaction network was constructed using Cytoscape 3.6.1. The network analysis has shown that, along with *penA* gene, the genes *murG*, *ftsW*, *murC*, *ftsA*, and *ftsQ* are observed to have more number of interactors and they may be considered as the key candidates to understand the *penA* drug-resistant mechanism. Functional enrichment analysis has shown the important GO terms and pathways where *penA* gene plays an important role. We have also elucidated the evolutionary relationship of *penA* gene in various Gram-positive and Gram-negative bacteria. Our study helps in understanding the drug-resistant patterns of *penA* gene in various bacteria and also their evolutionary relationships.

Electronic supplementary material The online version of this chapter (https://doi.org/10.1007/978-981-13-7968-0_2) contains supplementary material, which is available to authorized users.

S. K. Miryala · A. Anbarasu · S. Ramaiah (✉)
Medical and Biological Computing Laboratory, School of Biosciences and Technology, Vellore Institute of Technology (VIT), Vellore 632014, Tamil Nadu, India
e-mail: sudhaanand@vit.ac.in

S. K. Miryala
e-mail: miryalasravankumar@vit.ac.in

A. Anbarasu
e-mail: aanand@vit.ac.in

© Springer Nature Singapore Pte Ltd. 2020
B. Subramanian et al. (eds.), *Emerging Technologies for Agriculture and Environment*, Lecture Notes on Multidisciplinary Industrial Engineering, https://doi.org/10.1007/978-981-13-7968-0_2

Keywords Penicillin-binding protein 2 · *penA* gene · Antimicrobial resistance · Gene interaction network · Functional enrichment analysis

2.1 Introduction

Multidrug resistance (MDR) in pathogenic bacteria is a serious problem and becomes a public health threat worldwide. MDR in bacteria occurs mainly by the accumulation of antimicrobial-resistant (AMR) genes on resistance plasmid or transposons. In general, AMR genes code for resistance to a specific agent, but when the genes accumulate in bacterial plasmid, the bacteria show resistance to multiple drugs and make the treatment more critical [1]. Penicillin-binding proteins (PBPs) are one among such a class of proteins which shows reduced susceptibility to penicillin and other beta lactams. Penicillin-binding proteins (PBPs) are the enzymes that assemble the peptidoglycans, which are the main constituents of the cell wall on the outer side of the plasma membrane and help the bacteria to resist the intercellular pressure caused by any external factors such as antimicrobial drugs. Because of the important role in cell wall maintenance, PBP proteins are considered as the major molecular targets for β -lactam antibiotics. The β -lactams such as penicillin inhibit the transpeptidase activity and thus inhibit the peptidoglycan cross-links in the bacterial cell wall [2, 3]. The pathogens acquires resistance to β -lactam drugs by developing more strategies and makes the treatment difficult and cause life threatening disease. Several studies have reported that the alterations in the structure of PBP proteins are the reason for the resistance to penicillin [4, 5]. The β -lactam resistance in Gram-positive bacteria is via two main mechanisms: One mechanism is by enzymatic degradation through the production of β -lactamases, and other mechanism is by the decreasing the affinity of the antibiotics for its target [2], whereas in the Gram-negative bacteria, the β -lactamase-mediated resistance is due to either acquisition of new genes or the mutations affecting the expression of its chromosomal β -lactamases [6].

In our present study, we have analyzed the gene interaction network of the extended spectrum beta lactamase (ESBL), *penA* gene. *penA* gene belongs to the class A of beta lactamases and codes for the protein, penicillin-binding protein 2 (PBP2). Various studies have confirmed that penicillin resistance due to *penA* alleles has been arisen from either recruitment of sequence blocks from natural resistance species or by point mutations such as codon insertion or substitution [3]. The gene interaction network (GIN) approaches are becoming famous and drawing the scientific community attention and are considered to be the more reliable approach to study the antimicrobial-resistant mechanisms in pathogenic bacteria. The GIN analysis in AMR genes provides new insights to various drug-resistant mechanisms by analyzing the AMR genes along with their functional partners [7–11]. We have also collected the *penA* protein sequences from various bacterial strains and constructed the phylogenetic tree to understand the phylogenetic relationship between the bacterial *penA* gene among the bacteria. We have collected functional interactions

of *penA* gene from both Gram-positive and Gram-negative bacteria and constructed gene interaction network to understand the molecular-level interactions of *penA* gene with the functional partners. We further analyzed the functional enrichment of genes in the network to understand the role of *penA* gene along with its functional partners. We have also constructed a phylogenetic tree of *penA* gene from different bacteria to understand the evolutionary relationship between various bacterial species. Our results will be helpful in better understanding the role of *penA* gene in drug-resistant mechanism in various pathogenic bacteria. The genes which play an important role in various biological pathways were reported, and they can be useful as potent drug targets in new drug discovery.

2.2 Materials and Methods

2.2.1 Gene Interaction Data Curation from STRING Database

We have collected the *penA* gene interactions from STRING database from different Gram-negative and Gram-positive bacteria. STRING databases consist of protein–protein interactions curated from various sources such as high-throughput experimental data, data mining, literature survey, and co-expression analysis studies. All the interactions are broadly classified as direct (physical interactions curated from laboratory techniques) and indirect (functional associations extracted from computational prediction). Each interaction is provided with a confidence score that lies between 0 and 1. Each interaction further classified based on the confidence scores as highest (≥ 0.90 –1.0), high (≥ 0.70 –0.89), medium (≥ 0.40 –0.69), and low (≥ 0.15 –0.39) [12].

2.2.2 Interaction Network Construction

We have used Cytoscape 3.6.1 for the gene interaction network construction and analysis. Cytoscape is an open-source visualization tool used for constructing molecular interaction networks and biological pathways. Cytoscape tool comes with the core distribution with basic features for data integration, visualization, and analysis. The additional features such as network and molecular profiling analysis, new layouts, additional file format support, and cross-reference with databases can be available as Cytoscape plugins or apps [13].

2.2.3 Clustering Analysis

Clustering analysis of interacting network was carried out by using Cytoscape plugin MCODE. MCODE is based on molecular complex detection (MCODE) algorithm. The algorithm operates mainly in three different stages such as vertex weighing, complex prediction, and optionally postprocessing. In an interaction network, every vertex is a molecule and edge is an interaction between the molecules. Based on the type of data used, the graphs are divided into direct (known cell signaling and known pathways) and indirect graph [14].

2.2.4 Shortest Path Length and Closeness Centrality Analysis

The interaction network of *penA* gene was analyzed by using Cytoscape app NetworkAnalyzer. It is used to compute and display topological parameters such as a number of nodes, connecting edges, the network diameter, density, radius, centralization, heterogeneity, clustering coefficient, the characteristic path length, the distribution of node degrees, neighborhood connectivity, average clustering coefficients, and the shortest path lengths. It helps in analyzing both the types of networks (directed and undirected) and also allows to construct the intersection or union of two networks [15].

2.2.5 Phylogenetic Tree Construction

For the phylogenetic tree construction, we have used MEGA7. The phylogenetic tree construction involves in multiple sequence alignment (MSA) using MEGA inbuilt tools ClustalW or MUSCLE and followed by the construction of phylogenetic tree from the aligned sequences. The gaps and the missing data from all the positions were removed from phylogenetic analysis. For phylogenetic tree construction, there are various methods used such as neighbor-joining method, maximum likelihood method, evolutionary distance method, and maximum parsimony method [16].

2.3 Results

2.3.1 *penA* Gene Interaction Network Analysis

Network analysis of *penA* gene along with the functional partners was done using STRING database. A total of 144 *penA* gene interactors with 1039 functional interactions from 28 bacterial strains were curated with medium (>0.4) confidence

scores. Out of 28 bacterial species used in this study, 20 belong to Gram-negative (*Achromobacter piechaudii*, *Ahrensia* sp. R2A130, *Bordetella petrii*, *Burkholderia cenocepacia*, *Burkholderia mallei*, *Burkholderia pseudomallei*, *Campylobacter coli*, *Campylobacter jejuni* 414, *C. jejuni* 81176, *C. jejuni* NCTC11168, *Collimonas fungivorans*, *Kingella kingae*, *Legionella pneumophila* Paris, *Neisseria lactamica*, *Neisseria meningitidis*, *N. C102*, *Neisseria* sp. F0314, *Oligotropha carboxidovorans*, *Oxalobacter formigenes* OXCC13, *Rhodopseudomonas palustris* CGA009) and 8 belong to Gram-positive (*Brevibacillus laterosporus*, *Lactobacillus antri*, *Saccharopolyspora erythraea*, *Streptococcus oralis* ATCC35037, *Streptococcus pneumoniae* D39, *S. pneumoniae* R6, *S. pneumoniae* TIGR4). A list of interactions from each bacterial species is provided in Table 2.1. There are no significant interactions with medium and above confidence scores available in STRING for the bacterial species *A. piechaudii*. To obtain the maximum number of *penA* gene interactors from all the possible bacteria, we have curated the low confidence score interactions in the case of *A. piechaudii* (Fig. 2.1). Out of 1039 functional interactions, there are 522, 269, 229, and 19 belong to highest, high, medium, and lowest confidence scores, respectively. Out of 144 functional interactors, 130 directly interact with *penA* gene and are highlighted in red color in the network (Fig. 2.2).

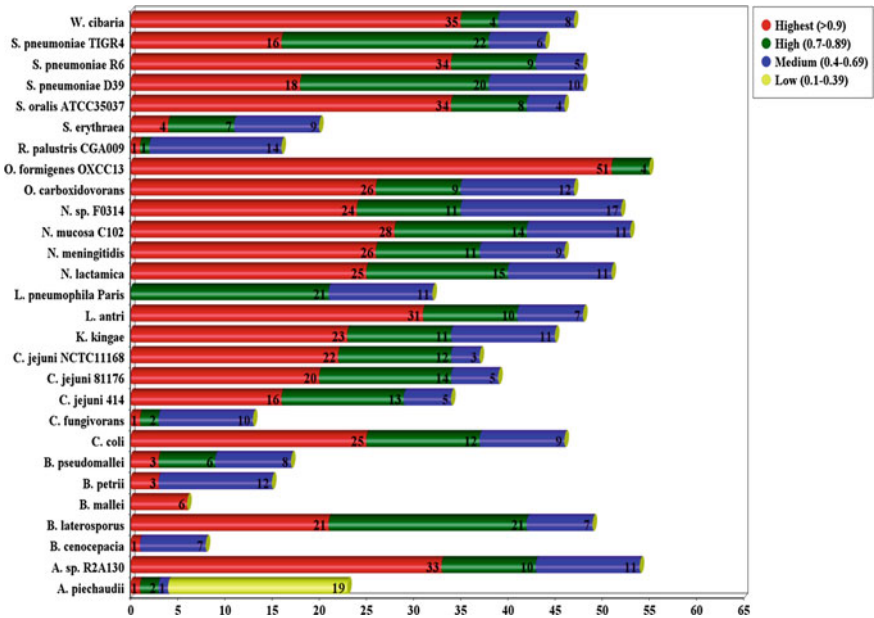


Fig. 2.1 List of *penA* gene interactions collected from STRING database for different organisms. The interactions are given scores as highest ($\geq 0.90-1.0$), high ($\geq 0.70-0.89$), medium ($\geq 0.40-0.69$), and low ($\geq 0.15-0.39$) confidence scores. Out of 28 bacterial species, 27 have interactions with medium and above medium confidence scores. In *A. piechaudii*, we have collected interactions with low confidence scores as there are not many interactions above the medium confidence scores

Table 2.1 List of bacteria along with the number of interactions extracted from STRING database

Organism	Combined score			Total number of interactions
	Highest (0.9–1)	High (0.7–0.89)	Medium (0.4–0.69)	
<i>Oxalobacter formigenes</i> OXCC13	51	4	0	55
<i>Ahrensia</i> sp. R2A130	33	10	11	54
<i>Neisseria mucosa</i> C102	28	14	11	53
<i>Neisseria</i> sp. F0314	24	11	17	52
<i>Neisseria lactamica</i>	25	15	11	51
<i>Brevibacillus laterosporus</i>	21	21	7	49
<i>Lactobacillus antri</i>	31	10	7	48
<i>Streptococcus pneumoniae</i> D39	18	20	10	48
<i>Streptococcus pneumoniae</i> R6	34	9	5	48
<i>Oligotropha carboxidovorans</i>	26	9	12	47
<i>Weissella cibaria</i>	35	4	8	47
<i>Campylobacter coli</i>	25	12	9	46
<i>Neisseria meningitidis</i>	26	11	9	46
<i>Streptococcus oralis</i> ATCC35037	34	8	4	46
<i>Kingella kingae</i>	23	11	11	45
<i>Streptococcus pneumoniae</i> TIGR4	16	22	6	44
<i>Campylobacter jejuni</i> 81176	20	14	5	39
<i>Campylobacter jejuni</i> NCTC11168	22	12	3	37
<i>Campylobacter jejuni</i> 414	16	13	5	34

(continued)

Table 2.1 (continued)

Organism	Combined score			Total number of interactions
	Highest (0.9–1)	High (0.7–0.89)	Medium (0.4–0.69)	
<i>Legionella pneumophila</i> Paris	0	21	11	32
<i>Achromobacter piechaudii</i>	1	2	1	4
<i>Saccharopolyspora erythraea</i>	4	7	9	20
<i>Burkholderia pseudomallei</i>	3	6	8	17
<i>Rhodopseudomonas palustris</i> CGA009	1	1	14	16
<i>Bordetella petrii</i>	3	0	12	15
<i>Collimonas fungivorans</i>	1	2	10	13
<i>Burkholderia cenocepacia</i>	1	0	7	8
<i>Burkholderia mallei</i>	6	0	0	6

The interactions are classified as highest, high, and medium based on the confidence scores. Out of 29 bacterial species, 28 have interactions with medium and above medium confidence scores. But there are no interactions with desired confidence scores available in the bacterial species *A. piechaudii*

2.3.2 Network Analysis Using NetworkAnalyzer

NetworkAnalyzer is used for network analysis of *penA* gene. For each node, individual centrality scores, along with the average shortest path length and degree, were given (Supplementary File S1). Among the 145 genes used in the study the top 20 genes with direct interactions (degree), average shortest path length score, closeness centrality, and between centrality scores have been provided in Table 2.2. All the 145 nodes are arranged in 3 layers based on the number of individual direct interactions. There are 37 nodes with more than 10 interactions, 53 nodes with interactions in between 05–10, and 45 nodes with less than 05 direct interactions (Fig. 2.3).

2.3.3 Clustering Analysis Using MCODE

MCODE has been resulted in 12 highly interconnected clusters. Out of 145 genes used in the interaction network, 90 genes were included in 12 clusters and the clusters are named as C1–C12. We have used default MCODE parameters for filtration of

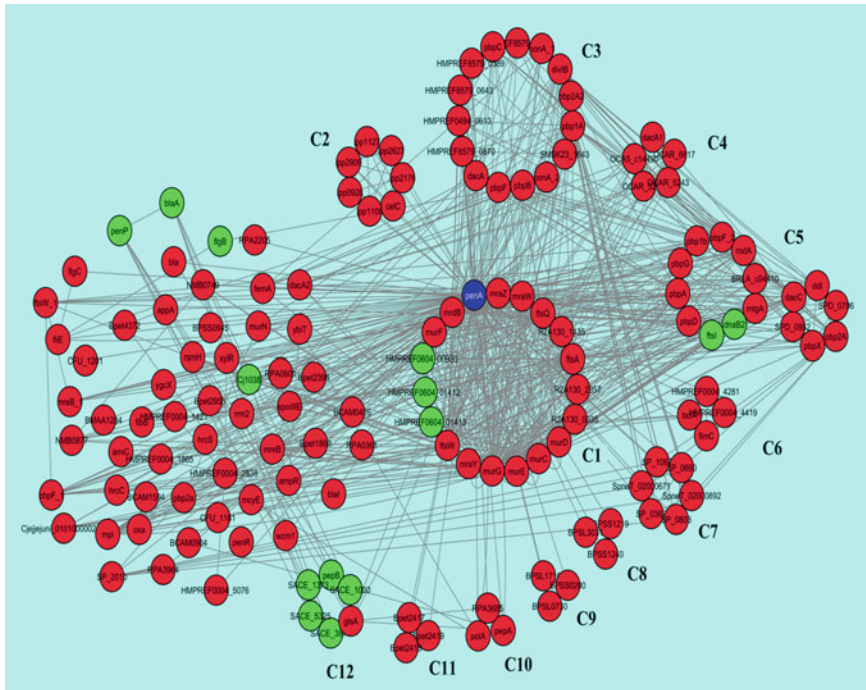


Fig. 2.2 *penA* gene interaction network along with the functional interactors. Genes are clustered into 12 densely interconnected clusters (C1–C12) using Cytoscape MCODE. For easy identification, *penA* gene is given in blue color, red-colored nodes are the direct interactors of the *penA* gene, and those nodes which are not direct interactors have given green color

nodes and edges. Among the clusters, there are only C1, C3, and C5 clusters having more than 15 nodes. The *penA* gene was included in cluster C1, and it consists of 19 nodes and 171 edges with 13.44 MCODE score (Table 2.3).

2.3.4 Functional Enrichment Analysis Using STRING Database

All the genes from 12 clusters are analyzed for the functional enrichment of genes using STRING database. Various GO terms such as biological processes (BP), molecular functions (MF), and cellular components are enriched along with the KEGG pathway-related genes, PFAM, and InterPro domain-related genes. Out of 145 genes, 49 genes are enriched in BP, MF, CC, KEGG, PFAM, and InterPro domains (Fig. 2.4). The clusters C2, C6, and C12 have been observed with no significant enrichment results (Supplementary File S2). Cluster C1 consists of genes related to mur ligase family-related genes and peptidoglycan synthase-related genes. The enriched GO

Table 2.2 Network analysis using NetworkAnalyzer tool

Genes	Degree	Avg. shortest path length	Closeness centrality	Betweenness centrality
<i>penA</i>	142	1.125926	0.888158	0.767209
<i>murG</i>	75	1.62963	0.613636	0.056708
<i>ftsW</i>	68	1.681481	0.594714	0.036728
<i>murC</i>	52	1.792593	0.557851	0.018124
<i>ftsA</i>	48	1.807407	0.553279	0.01702
<i>ftsQ</i>	36	1.881481	0.531496	0.006286
<i>mrdB</i>	35	1.859259	0.537849	0.00867
<i>murE</i>	34	1.874074	0.533597	0.007444
<i>pbp1A</i>	29	1.874074	0.533597	0.00944
<i>rodA</i>	29	1.881481	0.531496	0.006594
<i>dacA</i>	27	1.888889	0.529412	0.008643
<i>divIB</i>	27	1.888889	0.529412	0.007284
<i>mtgA</i>	24	1.940741	0.515267	0.005793
<i>murF</i>	24	1.962963	0.509434	0.002863
<i>mraW</i>	23	1.962963	0.509434	0.001896
<i>murD</i>	23	1.925926	0.519231	0.002166
<i>mraY</i>	22	1.948148	0.513308	0.000697
<i>pbp2A</i>	19	1.933333	0.517241	0.003368
<i>pbpB</i>	19	1.925926	0.519231	0.013447
<i>mpl</i>	18	1.985185	0.503731	0.002688

The top 20 genes with the degree, average shortest path length, closeness centrality, and betweenness centrality scores are given. The average shortest path length gives the expected distance between the two connected nodes, and genes with shortest path length and high closeness centrality are considered as the controlling points of molecular communication. Smaller edge betweenness values indicate the stronger interactions

terms include the BP such as regulation of cell shape (GO.0008360), peptidoglycan biosynthetic process (GO.0009252), cell wall organization (GO.0071555), cellular component biogenesis (GO.0044085), nitrogen compound metabolic process (GO.0006807), MF acid-amino acid ligase activity (GO.0016881) and various CC's related to cell (GO.0005623), cell part GO.0044464), intracellular (GO.0005622), cytoplasm (GO.0005737). PFAM and InterPro domains such as mur ligase family, glutamate ligase domain cell cycle protein related are enriched in cluster C1. The genes *mraY*, *mraZ*, *murC*, *murD*, *murG*, and *rsmH* are found in multiple GO terms and protein domain-related enriched entities.

In cluster C3, there are no significant GO terms enriched, but the genes related to PFAM, InterPro domains related to transglycosylase (PF00912), penicillin-binding protein transpeptidase domain (PF00905), D-alanyl-D-alanine carboxypeptidase, penicillin-binding protein 5-C terminal domain (PF07943),

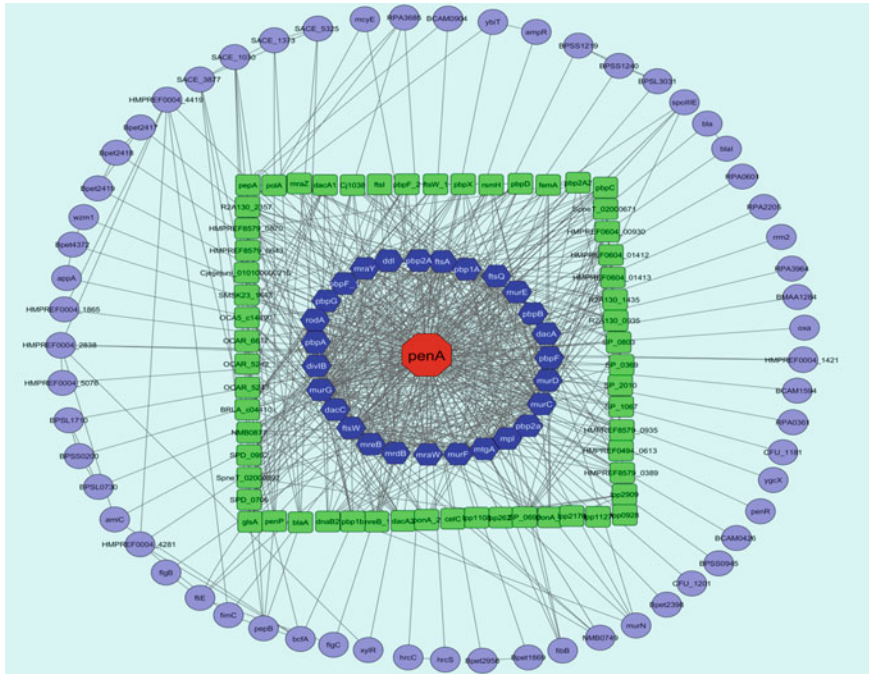


Fig. 2.3 *penA* gene interactions: All the 145 nodes are arranged in three layers based on the number of individual direct interactions. *penA* gene is denoted with octagonal red color node followed by 37 nodes with more than 10 interactions in hexagonal blue color node followed by 53 nodes with interaction in between 05 and 10 in rounded edge rectangular green color nodes and 45 nodes with less than 5 direct interactions

beta lactamase/transpeptidase-like (IPR012338), glycosyl transferase family 51 (IPR001264), and penicillin-binding protein transpeptidase (IPR001460) were enriched. The cluster C4 genes are enriched with the KEGG pathway peptidoglycan biosynthesis (KEGG ID: 550) along with PFAM and InterPro domains related to penicillin-binding protein transpeptidase domain and transglycosylase related domains. In cluster C5, the BPs related to regulation of cell shape (GO.008360) and peptidoglycan biosynthetic process (GO.009252) and KEGG pathways such as peptidoglycan biosynthesis (KEGG ID: 550) and beta lactam resistance (KEGG ID: 312) were enriched. Along with protein domains related to penicillin-binding protein dimerization, penicillin-binding protein transpeptidase was also enriched. Whereas in cluster C7, cell cycle protein-related PFAM and InterPro domains are enriched.

In cluster C8, KEGG pathways beta lactam resistance (KEGG ID: 312), peptidoglycan biosynthesis (KEGG ID: 550), and protein domains related to penicillin-binding protein dimerization and penicillin-binding protein transpeptidase domains were enriched. In cluster C9, the KEGG pathways penicillin and cephalosporin biosynthesis (KEGG ID: 311) and biosynthesis of secondary metabolites were enriched. The protein domains penicillin amidase, penicillin acylase, and nucleophile

Table 2.3 Clustering analysis of *penA* gene interactions

Cluster	Score	Nodes	Edges	Node IDs
C1	13.444	19	171	<i>ftsA, ftsQ, mraW, mraZ, R2A130_2357, murE, murF, penA, fisW, mraY, mrdB, murG, murC, murD, HMPREF0604_01413, HMPREF0604_01412, R2A130_1435, R2A130_0935, HMPREF0604_00930</i>
C2	7	7	21	<i>lpp0928, lpp2176, lpp2627, lpp1127, lpp2909, lpp1108, celC</i>
C3	5.143	15	37	<i>divIB, HMPREF8579_0389, HMPREF8579_0643, ponA_1, pbp1A, pbp2A2, pbpB, HMPREF8579_0870, ponA_2, dacA, pbpF, HMPREF8579_0935, SMSK23_1643, pbpC, HMPREF0494_0613</i>
C4	4.5	5	9	<i>OCAR_5242, OCAR_6617, OCA5_c14490, OCAR_5243, dacA1</i>
C5	4	16	30	<i>mtgA, ddl, dnaB2, fisI, pbpG, pbpF_2, BRLA_c04410, rodA, dacC, pbp1b, SPD_0952, pbpX, pbpD, pbpA, pbp2A, SPD_0706</i>
C6	4	4	6	<i>HMPREF0004_4281, bcfA, fimC, HMPREF0004_4419</i>
C7	3.6	6	9	<i>SP_0369, SP_0690, SpneT_02000671, SP_0803, SP_1067, SpneT_02000892</i>
C8	3	3	3	<i>BPSL3031, BPSS1240, BPSS1219</i>
C9	3	3	3	<i>BPSS0200, BPSL1710, BPSL0730</i>
C10	3	3	4	<i>pepA, RPA3685, polA</i>
C11	3	3	3	<i>Bpet2419, Bpet2417, Bpet2418</i>
C12	2.8	6	7	<i>glsA, SACE_3877, SACE_5325, pepB, SACE_1373, SACE_1030</i>

MCODE has resulted in 12 densely interconnected clusters. Each cluster along with the MCODE scores, nodes, and edges is provided. Clusters are named as C1–C12 for convenience

aminohydrolases related PFAM and InterPro domains were enriched. In cluster C10 there is only one KEGG pathway glutathione metabolism (KEGG ID: 480) was enriched. In cluster C12, the KEGG pathways penicillin and cephalosporin biosynthesis (KEGG ID: 311), beta lactam resistance (KEGG ID: 312), and glutathione metabolism (KEGG ID: 480) were enriched along with cytosol aminopeptidase family domains and beta lactam transpeptidase-like domains.

2.3.5 Phylogenetic Tree Construction and Analysis

We have collected the protein sequences for *penA* gene for 28 bacterial strains. Out of 28 bacterial strains, we have collected available 23 protein sequences from NCBI GenBank database. By using MEGA-muscle MSA tool, we have aligned the 23 amino acid sequences. We have used the aligned sequences for constructing phylogenetic

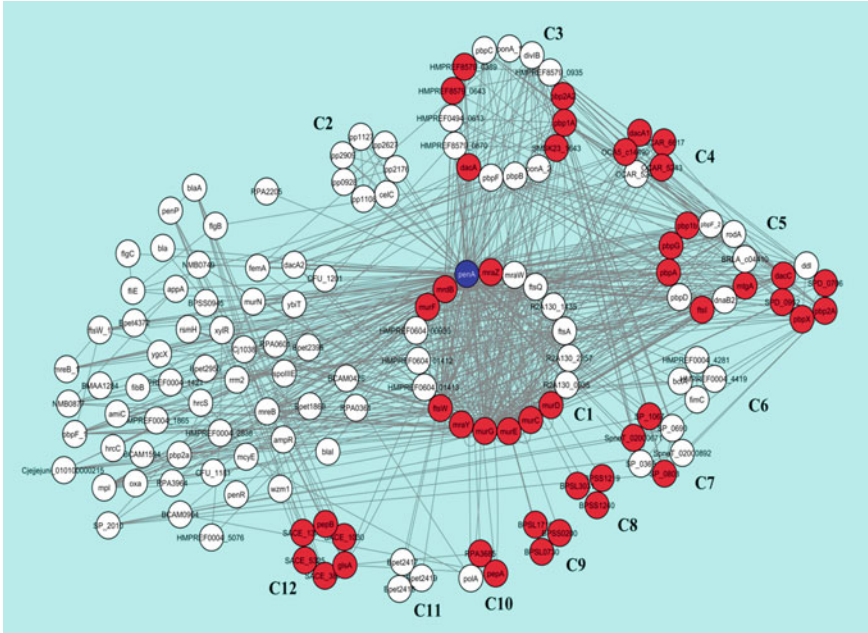


Fig. 2.4 *penA* gene interaction network functional enrichment analysis: Out of 145 genes in the network, 49 genes are functionally enriched with biological processes, molecular functions, cellular compartments, KEGG, PFAM, and InterPro domain-related genes. All the 49 enriched genes are highlighted in red color

tree (Fig. 2.5). We have used neighbor-joining method with the bootstrap consensus tree inferred from 1000 replicates. The evolutionary distances were computed using the poisson correction method and are in the units of the number of amino acid substitutions per site. All positions containing gaps and missing data were eliminated. There were a total of 207 positions in the final dataset.

2.4 Discussion

Multidrug resistance exerted by the pathogenic bacteria has become a global threat for treatment. PBP proteins assemble at the cell wall of the bacteria and help bacteria to resistant the intracellular pressure caused by external agents such as antimicrobials. In our present study, we have used PBP protein-coding gene *penA* to understand the molecular-level interactions of PBP in various bacteria. The mutation in *penA* gene is associated with the resistance to tetracycline/azithromycin, spectinomycin, and ceftriaxone. In *N. gonorrhoeae*, the mutation (insertion of aspartate at 345 position) in *penA* gene along with the *ponA*, *gyrA*, and *parC* genes determines the susceptibility

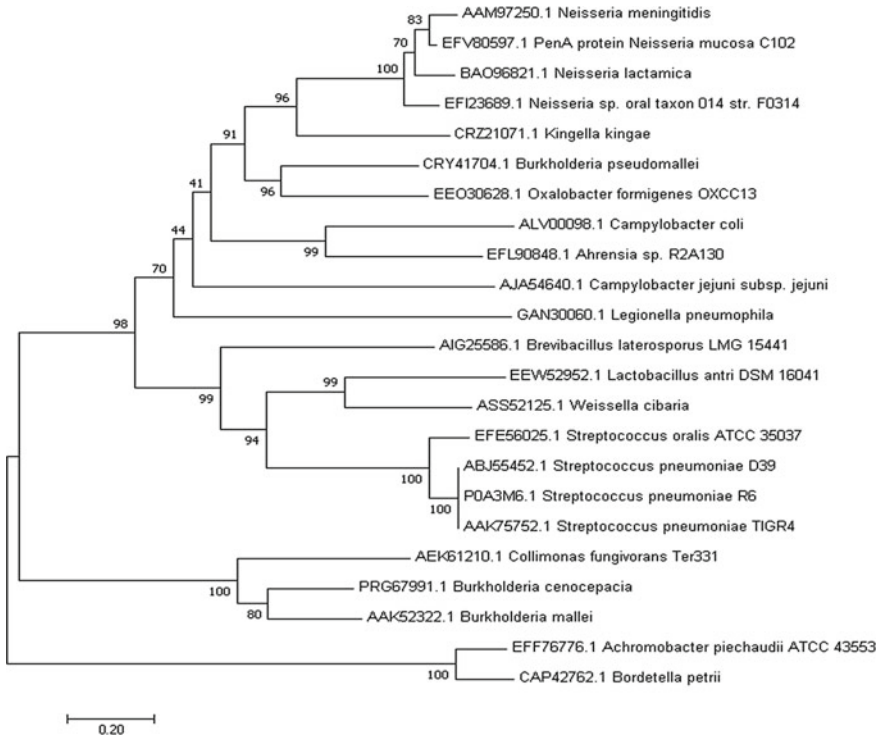


Fig. 2.5 Phylogenetic analysis of *penA* related proteins: Out of 28 bacteria, we have curated 23 available protein sequences and multiple sequence alignment is carried out by using MEGA7-muscle MSA program. The evolutionary history was inferred using the neighbor-joining method. The optimal tree with the sum of branch length = 9.64624886. The percentage of replicate trees in which the associated taxa clustered together in the bootstrap test (1000 replicates) is shown next to the branches

to penicillins, tetracyclines, and fluoroquinolones [17, 18]. In our results, we have observed that the *penA* gene with 142 total interactions constitutes 13.66% of total interactions in the whole interaction network followed by *murG* (75 interactions; 7.22%), *ftsW* (68 interactions; 6.54%), *murC* (52 interactions; 5%), *ftsA* (48 interactions; 4.62%), and *ftsQ* (36 interactions (3.46%). Along with the *penA* gene, these five genes constitute 40% of total interactions from the whole interaction network. With the maximum number of direct interactions, these nodes may be considered to have a high impact on the network; thus, these can be considered as functional hub nodes and further used as potent drug targets.

The functional enrichment analysis of genes in the interaction network has been shown that the *penA* gene along with the functional interactors is mainly responsible for peptidoglycan biosynthesis, mur ligase synthesis, β -lactam resistance, and glutathione metabolism. It is well known that Gram-positive and Gram-positive bacterial peptidoglycan composition is similar, while Gram-positive bacteria consist of

more thick and cross-linked peptidoglycan layer. Peptidoglycan is the main component of the bacterial cell wall, and it plays a key role in cell shape maintenance, facilitates the attachment for surface-exposed virulence factors, and avoids the modification in internal osmotic pressure. Thus, peptidoglycan biosynthesis mechanism-related genes are the preferred targets in the discovery of new antibiotics for many decades. The antibiotic-resistant mechanisms developed by the pathogenic bacteria against the antibiotics that targets the precursors of bacterial cell wall and biosynthesis machinery-related genes draw the attention of research community in overcoming the resistance strategies exhibited by the pathogens. There is an immediate necessity to study the resistance strategies and identify the new potent drug targets [19]. In our present study, we have observed the genes *OCAR_5243*, *dacC*, *BPSL3031*, *OCAR_6617*, *ddlB*, *BPSS1219*, *ftsI*, *BPSS1240*, *mtgA*, and *pbpA* are related to peptidoglycan biosynthesis, and these genes are found to have more dense interactions within the network. There are many clinically used antibiotics, especially various β -lactams, glycopeptides, fosfomycin, and cycloserine, which targets the genes involved in peptidoglycan biosynthesis pathway. Although the amide ligases (*murC*, *murD*, *murE*, and *murF*) play an important role in peptidoglycan biosynthesis by catalyzing the non-ribosomal peptide bond formations for the addition of peptide moiety on the peptidoglycan blocks, there are no antibacterial agent targets these amide ligases [20, 21]. In our results, the amide ligase-coded genes *murC*, *murD*, *murE*, and *murF* are enriched with Pfam and InterPro domains. It is also noticed that the MUR family genes *murG*, *murC*, and *murE* genes were in the top 10 genes with more number of direct interactions, which show the importance of amide genes in resistance caused by the *penA* gene along with its interactors. The other notable result is the enrichment of KEGG pathway glutathione metabolism (KEGG ID: 480). The genes *pepA*, *pepB*, *RPA3685*, and *SACE_1030* were involved in glutathione metabolism. Various studies have shown that the antibiotics used against the pathogenic Gram-positive and Gram-negative bacteria results in the formation of reactive oxygen species (ROS). When the cell is exposed to an antibiotic, glutathione plays a key role in maintaining the cellular redox poise by the detoxification the xenobiotics [22]. Another interesting observation in our results is the enrichment of KEGG pathway, β -lactam resistance (KEGG ID: 312), which includes the genes *pbp1B*, *BPSL3031*, *SACE_1373*, *pbp2A*, *BPSS1219*, *SACE_3877*, *pbpX*, and *BPSS1240*. The gene *pbp1B* is a peptidoglycan glycosyltransferase or murein synthase, and it plays an essential role in synthesizing peptidoglycan in the absence of a pre-existing template [23]. Whereas the gene *pbp2A* is found in *staphylococcal* cell wall biosynthesis along with the known PBP family proteins *PBP2* and *PBP4*, *PBP2A* which is an acquired transpeptidase plays a crucial role in susceptibility to antimicrobial agents [24]. *pbpX* gene is a homologous to the pneumococcal *PBP2x* gene, and it is isolated from penicillin-sensitive *S. oralis* strain [25]. The genes *SACE_1373* and *SACE_3877* belong to *S. erythraea* strain and coded for beta lactamase. The genes *BPSL3031*, *BPSS1219*, and *BPSS1240* belong to *B. pseudomallei* strain. *BPSL3031* gene codes for peptidoglycan synthase, and *BPSS1219* and *BPSS1240* code for penicillin-binding protein.

Out of 28 bacterial *penA*-related proteins, there are only 23 sequences available in NCBI GenBank database. We have collected the 23 *penA*-related protein sequences and used for the construction of phylogenetic tree. Among the bacterial species used for the study, few are non-pathogenic, and most of them are pathogenic. The phylogenetic analysis of *penA* genes from various bacterial species has confirmed the lineage of different bacteria with respect to *penA* gene. We have used neighbor-joining method for the phylogenetic tree construction with 1000 bootstraps. In the phylogenetic tree, the bootstrap values more than 70% show more confidence and less than that show poor confidence of the phylogeny with respect to the entry. In our results, there are only two bootstrap values less than 70%. The constructed phylogenetic tree shows that the bacteria *C. jejuni* showed boot strap values 44% with the other Gram-negative bacteria such as *Neisseria* genus and *K. kingae*. The bacteria belonging to *Neisseria* genus are closely related (bootstrap values 96%) to *K. kingae*. The bacteria *B. pseudomallei* and *O. formigenes* OXCC13 have bootstrap value 96%. The Gram-positive bacteria used in the study have shown the bootstrap values more than 90%, which shows the confidence of the *penA* gene lineage among the Gram-positive bacteria. All the *streptococcus*-related *penA* proteins have shown bootstrap values 100%, and they are highly similar to other Gram-positive bacterial *penA* protein sequences. We have also observed that the bacteria belonging to the same genus showed less than 100% bootstrap values. The bacteria *B. mallei* and *B. cenocepacia* show the bootstrap values 80%; *N. meningitidis* and *Neisseria mucosa* C102 show 83%; and with respect to *N. lactamica* shows, the bootstrap value is 70%. Our phylogenetic studies have provided a detailed lineage of *penA* gene in various pathogenic and non-pathogenic bacteria.

2.5 Conclusion

The gene interaction analysis of PBP2 coding *penA* gene provides a comprehensive evidence on *penA* gene and their functional partners in antibiotic resistance in various bacteria. In our present study, we have identified functional interactors of the *penA* gene from different bacterial species, and by using functional enrichment analysis, we have analyzed the role of these genes in peptidoglycan biosynthesis, mur ligase synthesis, β -lactam resistance, and glutathione metabolism. The constructed *penA* gene network helps in understanding the functional relationship of these interactors in biological pathways. Our results give critical information on various biological processes such as gene functions and complex cellular mechanisms. The phylogenetic tree of *penA* related amino acids from various bacteria gives a glance of lineage of *penA* gene in various Gram-positive and Gram-negative bacteria. To conclude, from our study, we have observed the *penA* gene along with the interactors plays a major role in peptidoglycan biosynthesis, amide ligase biosynthesis, β -lactam resistance, and glutathione metabolism. Our results will help in better understanding the functional role of β -lactamase *penA* gene in β -lactam induction. The molecular interactions of *penA* along with the functional partners will be useful for researchers

exploring the β -lactam-mediated antibiotic resistance in pathogenic bacteria, and the identified resistance genes play major roles in various biological processes, and these can be considered as potent drug targets for developing new drugs.

Acknowledgements The authors gratefully acknowledge the Indian Council of Medical Research (ICMR), Government of India agency for the research grant (IRIS ID: 2014-0099). MSK thanks ICMR for the research fellowship. The authors would like to thank the management of VIT for providing the necessary facilities to carry out this research work.

Conflict of Interest Statement None declared.

References

1. Nikaido, H.: Multidrug resistance in bacteria. *Annu. Rev. Biochem.* 119–146 (2009). <https://doi.org/10.1146/annurev.biochem.78.082907.145923.multidrug>
2. Munita, J.M., Bayer, A.S., Arias, C.A.: Evolving resistance among gram-positive pathogens. *Clin. Infect. Dis.* **61**, S48–S57 (2015). <https://doi.org/10.1093/cid/civ523>
3. Zapun, A., Morlot, C., Taha, M.-K.: Resistance to β -Lactams in *Neisseria ssp* due to chromosomally encoded penicillin-binding proteins. *Antibiotics* **5**, 35 (2016). <https://doi.org/10.3390/antibiotics5040035>
4. Thulin, S., Olcén, P., Fredlund, H., Unemo, M.: Total variation in the penA gene of *Neisseria meningitidis*: correlation between susceptibility to β -lactam antibiotics and penA gene heterogeneity. *Antimicrob. Agents Chemother.* **50**, 3317–3324 (2006). <https://doi.org/10.1128/AAC.00353-06>
5. Powell, A.J., Tomberg, J., Deacon, A.M., et al.: Crystal structures of penicillin-binding protein 2 from penicillin-susceptible and -resistant strains of *Neisseria gonorrhoeae* reveal an unexpectedly subtle mechanism for antibiotic resistance. *J. Biol. Chem.* **284**, 1202–1212 (2009). <https://doi.org/10.1074/jbc.M805761200>
6. Sanders, C.C., Sanders, W.E.: β -Lactam resistance in gram-negative bacteria: global trends and clinical impact. *Clin. Infect. Dis.* **15**, 824–839 (1992). <https://doi.org/10.1093/clind/15.5.824>
7. Anitha, P., Anbarasu, A., Ramaiah, S.: Computational gene network study on antibiotic resistance genes of *Acinetobacter baumannii*. *Comput. Biol. Med.* **48**, 17–27 (2014). <https://doi.org/10.1016/j.compbiomed.2014.02.009>
8. Anitha, P., Anbarasu, A., Ramaiah, S.: Gene network analysis reveals the association of important functional partners involved in antibiotic resistance: a report on an important pathogenic bacterium *Staphylococcus aureus*. *Gene* **575**, 253–263 (2016). <https://doi.org/10.1016/j.gene.2015.08.068>
9. Parimelzaghan, A., Anbarasu, A., Ramaiah, S.: Gene network analysis of metallo beta lactamase family proteins indicates the role of gene partners in antibiotic resistance and reveals important drug targets. *J. Cell. Biochem.* **117**, 1330–1339 (2016). <https://doi.org/10.1002/jcb.25422>
10. Miryala, S.K., Ramaiah, S.: Exploring the multi-drug resistance in *Escherichia coli* O157 : H7 by gene interaction network : a systems biology approach. *Genomics* (2018) <https://doi.org/10.1016/j.ygeno.2018.06.002>
11. Miryala, S.K., Anbarasu, A., Ramaiah, S.: Discerning molecular interactions: a comprehensive review on biomolecular interaction databases and network analysis tools. *Gene* **642** (2018). <https://doi.org/10.1016/j.gene.2017.11.028>
12. Szklarczyk, D., Morris, J.H., Cook, H., et al.: The STRING database in 2017: quality-controlled protein-protein association networks, made broadly accessible. *Nucleic Acids Res.* **45**, D362–D368 (2017). <https://doi.org/10.1093/nar/gkw937>

13. Shannon, P., Markiel, A., Ozier, O., et al.: Cytoscape: a software environment for integrated models of biomolecular interaction networks. *Genome Res.* 2498–2504 (2003). <https://doi.org/10.1101/gr.1239303.metabolite>
14. Bader, G.D., Hogue, C.W.V.: An automated method for finding molecular complexes in large protein interaction networks. *BMC Bioinformatics* **4**, 1–27 (2003). <https://doi.org/10.1186/1471-2105-4-2>
15. Assenov, Y., Ramírez, F., Schelhorn, S.E.S.E., et al.: Computing topological parameters of biological networks. *Bioinformatics* **24**, 282–284 (2008). <https://doi.org/10.1093/bioinformatics/btm554>
16. Kumar, S., Stecher, G., Tamura, K.: MEGA7: molecular evolutionary genetics analysis version 7.0 for bigger datasets. *Mol. Biol. Evol.* **33**, 1870–1874 (2016). <https://doi.org/10.1093/molbev/msw054>
17. Török, M.E., Chantratita, N., Peacock, S.J.: Bacterial gene loss as a mechanism for gain of antimicrobial resistance. *Curr. Opin. Microbiol.* **15**, 583–587 (2012). <https://doi.org/10.1016/j.mib.2012.07.008>
18. Ohnishi, M., Watanabe, Y., Ono, E., et al.: Spread of a chromosomal cefixime-resistant *penA* gene among different *Neisseria gonorrhoeae* lineages. *Antimicrob. Agents Chemother.* **54**, 1060–1067 (2010). <https://doi.org/10.1128/AAC.01010-09>
19. Nikolaidis, I., Favini-Stabile, S., Dessen, A.: Resistance to antibiotics targeted to the bacterial cell wall. *Protein Sci.* **23**, 243–259 (2014). <https://doi.org/10.1002/pro.2414>
20. Kouidmi, I., Levesque, R.C., Paradis-Bleau, C.: The biology of Mur ligases as an antibacterial target. *Mol. Microbiol.* **94**, 242–253 (2014). <https://doi.org/10.1111/mmi.12758>
21. Vollmer, W., Blanot, D., De Pedro, M.A.: Peptidoglycan structure and architecture. *FEMS Microbiol. Rev.* **32**, 149–167 (2008). <https://doi.org/10.1111/j.1574-6976.2007.00094.x>
22. Cameron, J.C., Pakrasi, H.B.: Glutathione facilitates antibiotic resistance and photosystem I stability during exposure to gentamicin in cyanobacteria. *Appl. Environ. Microbiol.* **77**, 3547–3550 (2011). <https://doi.org/10.1128/AEM.02542-10>
23. Ranjit, D.K., Jorgenson, M.A., Young, K.D.: PBP1B glycosyltransferase and transpeptidase activities play different essential roles during the de novo regeneration of rod morphology in *Escherichia coli*. *J. Bacteriol.* **199** (2017). <https://doi.org/10.1128/jb.00612-16>
24. Leski, T.A., Tomasz, A.: Role of penicillin-binding protein 2 (PBP2) in the antibiotic susceptibility and cell wall cross-linking of *Staphylococcus aureus*. *J. Bacteriol.* **2**, 1815–1824 (2005). <https://doi.org/10.1128/jb.187.5.1815>
25. Sibold, C., Henrichsen, J., König, A., et al.: Mosaic pbpX genes of major clones of penicillin-resistant *Streptococcus pneumoniae* have evolved from pbpX genes of a penicillin-sensitive *Streptococcus oralis*. *Mol. Microbiol.* **12**, 1013–1023 (1994). <https://doi.org/10.1111/j.1365-2958.1994.tb01089.x>

Chapter 3

The Effect of Alccofine on Blended Concrete Under Compression



A. Narender Reddy  and T. Meena 

Abstract Nowadays cement had become the most extensively used construction material worldwide. The global demand of cement had reached about 5.2 billion metric tons. These lead to huge consumption of raw material and in production of cement huge amount of greenhouse gases like CO₂ was released, about 5% of total man-made CO₂ emission is through cement manufacture industry. To safeguard the environment, efforts are being made to recycle different industrial by-products and utilize them in value-added applications. The use of industrial wastes, which are pozzolanic in nature, can minimize the use of cement. Fly ash (FA) and slag (GGBS) are the most common pozzolan and are being used worldwide in concrete works. Recently, some researchers notified that a new by-product from iron ore industry, namely Alccofine, also processes pozzolanic nature. The objective of the present investigation is to evaluate the effect of Alccofine with fly ash and Alccofine with ground-granulated blast furnace as the supplementary cementitious material with reference to the compressive strength property of hardened concrete and to probe the optimal replacement level of cement with combination of fly ash with Alccofine and ground-granulated blast furnace with Alccofine.

Keywords Alccofine · Fly ash · Ground-granulated blast furnace · Blended concrete

3.1 Introduction

The advancement in concrete technology has been widely improved in line with the rise of options of material combination to replace ordinary Portland cement (OPC) [1]. The ultimate purpose of the replacement is likely to increase the strength and to provide sufficient serviceability of a structural element. Besides the economic con-

A. N. Reddy (✉) · T. Meena

Department of Structural and Geo-Technical Engineering, School of Civil Engineering (SCE),
Vellore Institute of Technology, Vellore, Tamil Nadu 632014, India
e-mail: avuthunarender05@gmail.com

© Springer Nature Singapore Pte Ltd. 2020

B. Subramanian et al. (eds.), *Emerging Technologies for Agriculture and Environment*, Lecture Notes on Multidisciplinary Industrial Engineering,
https://doi.org/10.1007/978-981-13-7968-0_3

siderations toward the material cost of conventional concrete, it is also necessary to utilize industrial wastes such as Fly Ash (FA), Slag (GGBS), Silica Fume, and Alccofine (AL), [2–5]. The mineral admixture considerably increases the workability of concrete. A number of investigations show that the minimum capacity of modified concrete could be increased by multiple replacement mechanisms, thereby improving the performance of concrete [6–9]. This practical idea tends to be a promising alternative in terms of concrete strength and green construction [10, 11]. As the material AL is a newly introduced pozzolanic material and from literature review, it proves better results in binary mixes as cement replacement [12, 13]. We tried using AL along with our pozzolanic materials to form blended concrete [14, 15]. Two pozzolanic materials which are most commonly in construction nowadays such as FA and GGBS are selected and compressive strength were found to check the compatibility nature of AL with other pozzolanic materials.

The characteristics of combination of mineral admixtures such as FA with AL and GGBS with AL to replace partially cement in concrete have been tested. The aim of this study is to determine the optimum percentage of combination of AL with other pozzolanic materials like FA and GGBS forming a blended concrete (BC).

3.2 Materials

3.2.1 Cement

OPC 53 grade cement confirming the requirements according to IS 12269 was used in our investigation having specific gravity of 3.12, normal consistency of 32%, fineness modulus of 6.5%, initial setting time of 50 min, final setting time of 420 min, and soundness of 1.2 mm.

3.2.2 Fly Ash (FA)

Class F type of FA was used in the entire investigation; it was acquired from Dr. NTR-VTPS, Vijayawada, AP having a specific gravity 2.3 and fineness modulus of 1.1% (Table 3.1, Figs 3.1 and 3.2).

3.2.3 Slag (GGBS)

GGBS is the by-product from blast furnace in steel industry. It is a by-product which consists of high silicates and aluminosilicates of calcium and other bases, which are

Table 3.1 Properties of FA by EDAX analysis

Characteristics of element	Results for EDAX	
	Weight %	Atomic %
C K	59.19	68.02
O K	31.99	27.60
Al K	2.75	1.41
Si K	6.07	2.98

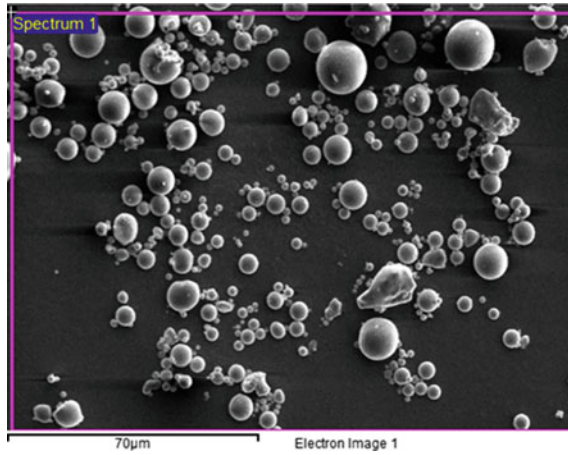


Fig. 3.1 SEM image of FA

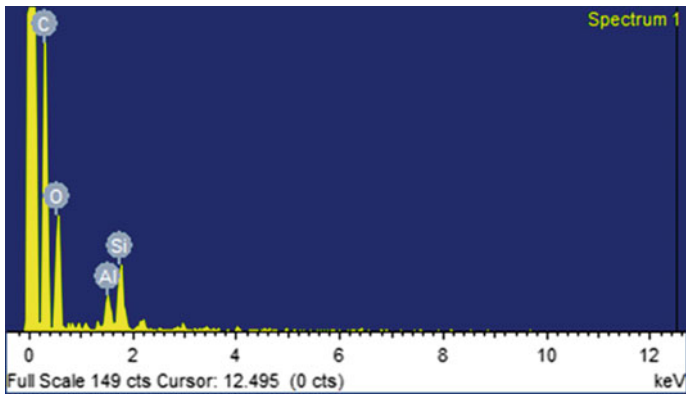
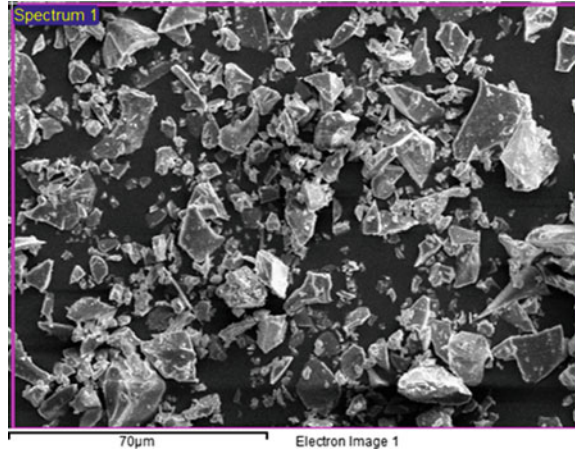


Fig. 3.2 EDAX image of FA

Table 3.2 Properties of GGBS by EDAX analysis

Characteristics of element	Results for EDAX	
	Weight %	Atomic %
C K	38.52	51.43
O K	36.19	36.27
Al K	3.84	2.28
Si K	8.36	4.77
Ca K	13.09	5.24

Fig. 3.3 SEM image of GGBS



developed in molten condition in blast furnace. GGBS was acquired from Salem Steel Plant Salem, TN having a specific gravity of 2.8, particle size of 97 µm and fineness (m/kg) of 390 (Table 3.2, Figs. 3.3 and 3.4).

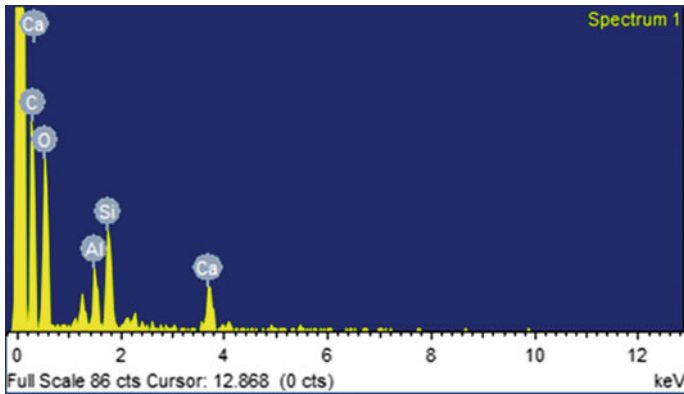
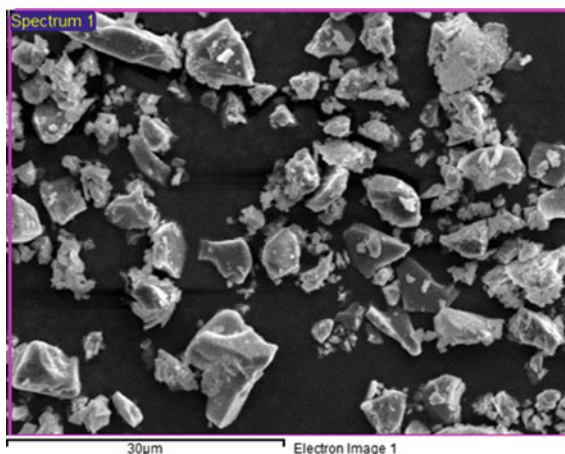


Fig. 3.4 EDAX image of GGBS

Table 3.3 Chemical properties of AL by EDAX analysis

Characteristics of element	Results for EDAX	
	Weight %	Atomic %
C K	45.69	57.64
O K	35.26	33.39
Al K	4.01	2.25
Si K	6.38	3.44
Ca K	8.66	3.27

Fig. 3.5 SEM image of AL

3.2.4 Alccofine (AL)

AL is a slag-based product produced by control granulation of iron waste with high glass content. AL-1203 type is used in our investigation having specific gravity of 2.9; particle size varies from 1.5 to 9 μm (Table 3.3, Figs. 3.5 and 3.6).

3.2.5 Fine Aggregate

Regionally accessible river sand conforming to IS 383 specifications were used in our investigation having fineness modulus of 2.7%, water absorption of 1.02%, specific gravity of 2.68 and belongs to the grading zone of II.

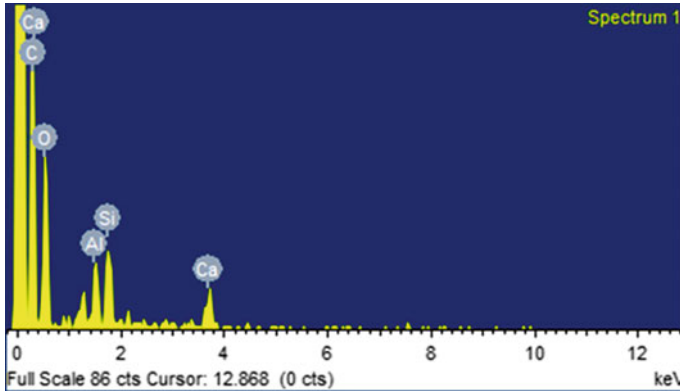


Fig. 3.6 EDAX image of AL

3.2.6 Coarse Aggregate

Locally available crushed stone passing through 20-mm sieve confirming to IS 383 was used as coarse aggregate in our investigation having fineness modulus of 7.2%, specific gravity of 2.78, water absorption of 0.8%.

3.2.7 Water

Water with pH of 7.0–8.0 available in our campus was used in our investigation.

3.2.8 Superplastizer

High-performance superplasticizer based on poly-carboxylic ether was used in the investigation.

3.3 Mix Proportions

In the present investigation, M30 grade concrete standard mix design is carried out according to Indian standard code 10262. The proportions of concrete mix are given below in Table 8 and the compression strength test was conducted as per Indian standard code 516. The $100 \times 100 \times 100$ mm cube specimens are tested at 7 and 28 days (Tables 3.4 and 3.5).

Table 3.4 Mix design

Material	Cement	Fine aggregate	Coarse aggregate	w/c ratio
Quantity (kg/m ³)	350.2	721.5	1273.8	150.6

Control Mix Proportion = 1:2.06:3.63:0.43

Table 3.5 Mix proportions (kg/m³)

Mix ID	Cement	FA	GGBS	AL	Fine Agg.	Coarse Agg.	Water
CM	350.2	–	–	–	721.5	1273.8	150.6
F1	332.69	17.51	–	–	721.5	1273.8	150.6
F2	315.18	35.02	–	–	721.5	1273.8	150.6
F3	297.67	52.53	–	–	721.5	1273.8	150.6
F4	280.16	70.04	–	–	721.5	1273.8	150.6
F5	262.65	87.55	–	–	721.5	1273.8	150.6
F6	245.14	105.06	–	–	721.5	1273.8	150.6
F7	227.63	122.57	–	–	721.5	1273.8	150.6
F8	210.12	140.08	–	–	721.5	1273.8	150.6
G1	332.69	–	17.51	–	721.5	1273.8	150.6
G2	315.18	–	35.02	–	721.5	1273.8	150.6
G3	297.67	–	52.53	–	721.5	1273.8	150.6
G4	280.16	–	70.04	–	721.5	1273.8	150.6
G5	262.65	–	87.55	–	721.5	1273.8	150.6
G6	245.14	–	105.06	–	721.5	1273.8	150.6
G7	227.63	–	122.57	–	721.5	1273.8	150.6
G8	210.12	–	140.08	–	721.5	1273.8	150.6
FA1	246.9	87.55	–	15.75	721.5	1273.8	150.6
FA2	241.63	87.55	–	21.01	721.5	1273.8	150.6
FA3	236.38	87.55	–	26.26	721.5	1273.8	150.6
FA4	231.13	87.55	–	31.51	721.5	1273.8	150.6
FA5	225.87	87.55	–	36.77	721.5	1273.8	150.6
FA6	220.62	87.55	–	42.02	721.5	1273.8	150.6
GA1	263.35	–	70.04	16.80	721.5	1273.8	150.6
GA2	257.74	–	70.04	22.41	721.5	1273.8	150.6
GA3	252.16	–	70.04	28.01	721.5	1273.8	150.6
GA4	247	–	70.04	33.16	721.5	1273.8	150.6
GA5	240.94	–	70.04	39.22	720.8	1273.7	150.6
GA6	235.34	–	70.04	44.82	720.8	1273.7	150.6

3.4 Results and Discussions

3.4.1 Evaluation of Optimum Percentage of FA and GGBS

The cement is replaced with FA and GGBS separately at 5, 10, 15, 20, 25, 30, 35, and 40% to evaluate the optimum percentage of cement replacement by FA and GGBS separately. The results are graphically represented as in Figs. 3.7 and 3.8.

Figure 3.7 represents the evaluation of optimum percentage of FA content and Fig. 3.8 represents the evaluation of optimum percentage of GGBS content. From Fig. 3.7, the higher compressive strength is achieved for F5 mix (concrete mix with 25% Flash), and from Fig. 3.8, the higher compressive strength was achieved for G4 mix (concrete mix with 20% GGBS). So, it is concluded that the optimum replacement percentage of cement by FA is 25% and for GGBS is 20%. Therefore the mixes F5 and G4 are selected for further studies.

3.4.2 Evaluation of Optimum Percentage of FA with AL and GGBS with AL

By maintaining the constant FA content at 25% and GGBS at 20%, the remaining cement content was replaced with AL at 6, 8, 10, 12, 14 and 16% with FA and GGBS separately to find the compatibility nature of the AL the results are graphically represented in Figs. 3.9 and 3.10.

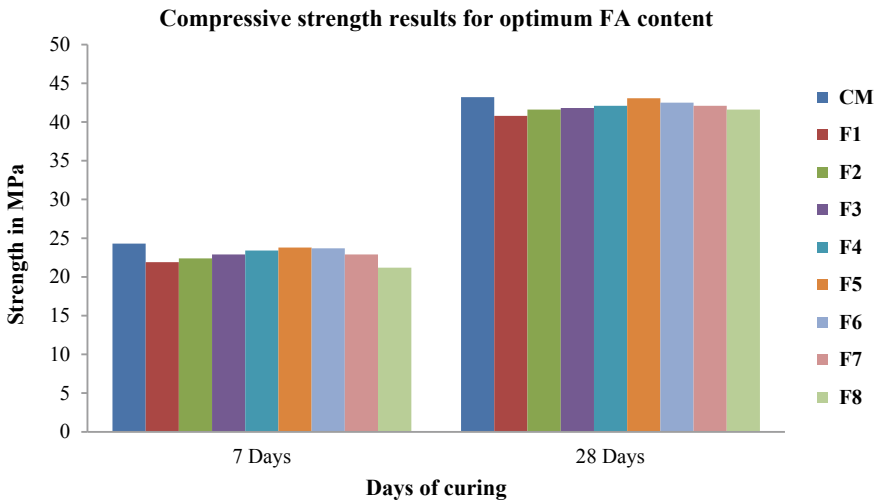


Fig. 3.7 Graphical representation for optimum percentage of FA content

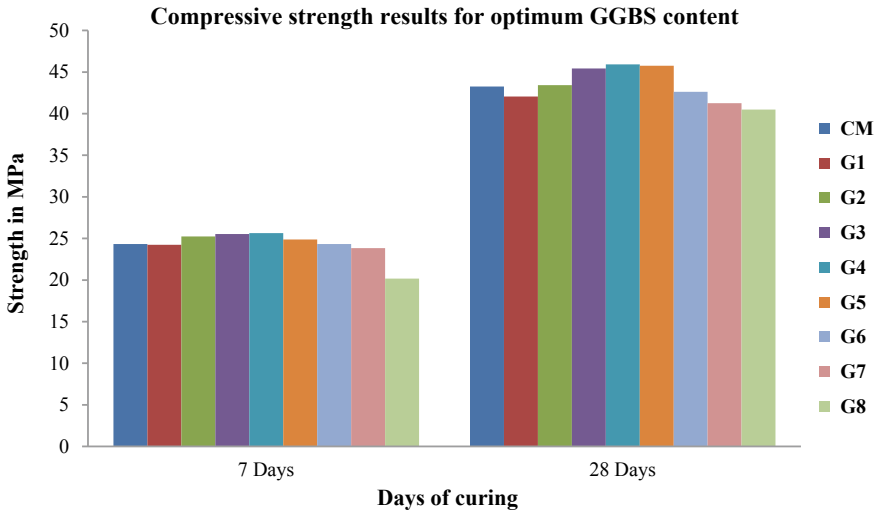


Fig. 3.8 Graphical representation for optimum percentage of GGBS content

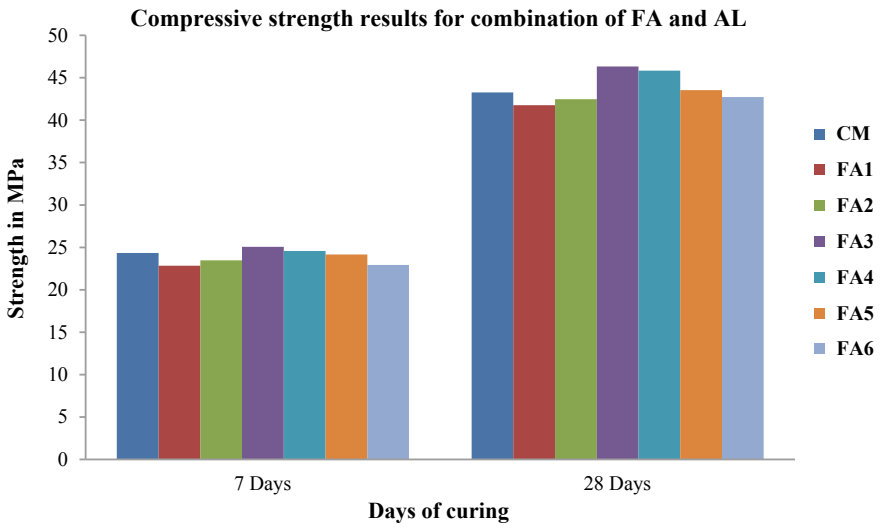


Fig. 3.9 Graphical representation for combination of FA and AL

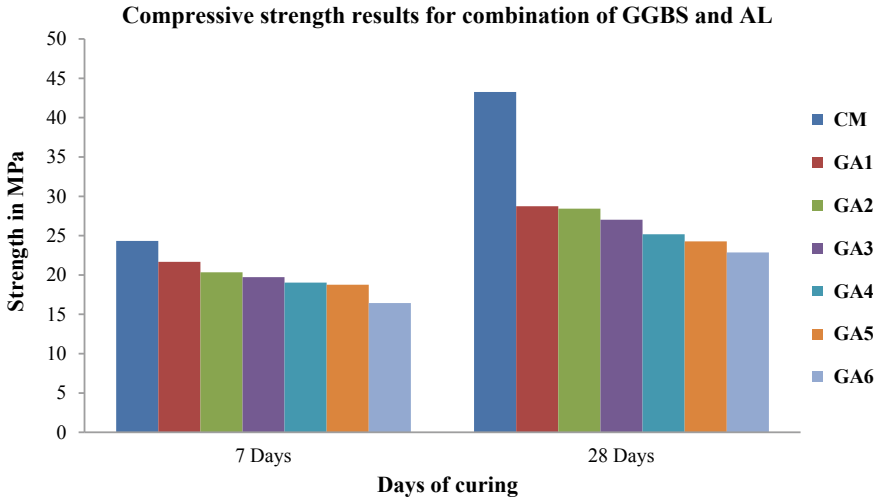


Fig. 3.10 Graphical representation for combination of GGBS and AL

Figure 3.9 represents the optimum percentage of FA and AL content, and Fig. 3.10 represents the optimum percentage of GGBS and AL content. From Fig. 3.9, the maximum compressive strength is achieved for FA3 mix (concrete mix with combination of 25% FA with 10% AL totally 35% as replacement of cement), and from Fig. 3.10 result, it is clearly seen that the combination of GGBS and AL had failed to achieve the design strength. Also it is clearly observed that as the AL percentage in the concrete mix increases the compressive strength decreases. This may be due to the incompatibility nature of these two pozzolanic materials.

3.5 Conclusion

From the investigation, it is clearly observed that the mix containing AL sets very quickly than all mixes. The results of compressive strength on BC with combination of 25% FA and 10% AL had shown highest strength than that of all other mixes. But the mixes with combination of GGBS and AL compressive strength were not superior when compared to normal concrete. It is clearly seen from Fig. 3.10 as the AL percentage in the concrete mix increases the compressive strength decreases. This is may be due to the incompatibility nature between AL and GGBS. From Fig. 3.9, it is clearly seen that the compatibility nature of FA and AL is good, and the strength had increased 7.08% at 28 days with total cement replacement of 35%. The highest compressive strength for BC mix was achieved for FA3 mix (Mix with combination of Cement–FA–AL at 65–25–10%), respectively. The cement replacement with combination of FA and AL materials leads to eco-friendly and sustainable concrete

and at the same time results in the reduction of overall cost of manufacture of blended concrete.

References

1. Flower, D.J.M., Sanjayan, J.G.: Green house gas emissions due to concrete manufacture. *Int. J. Life Cycle Asst.* **12**, 282–288 (2007). <https://doi.org/10.1065/lca2007.05.327>
2. Narender Reddy, A., Meena, T.: The behaviour of ternary blended concrete under compression. *Int. J. Civ. Eng. Tech.* **8**, 2089–2097 (2017)
3. Part, W.K., Ramli, M., Cheah, C.B.: An overview of the influence of various factors on the properties of geopolymer concrete derived from industrial byproducts. In: *Handbook of Low Carbon Concrete*, pp. 263–334 (2016). <https://doi.org/10.1016/b978-0-12-804524-4.00011-7>
4. Patil, J., Pendharkar, U.: Study of effect of nanomaterials as cement replacement on physical properties of concrete. *Int. Res. J. Eng. Tech.* **3**, 300–308 (2016)
5. Roy, D.K.S., Rajesh Kumar, S., Samanta, Amiya K.: Characterization and development of eco-friendly concrete using GGBS and Alccofine. *Res. J. App. Sci.* **11**, 183–187 (2016)
6. Kockal, N.U.: Study on the strength characteristics of high strength concrete with micro steel fibers. In: *IOP Conference Series: Earth and Environmental Science*, vol. 80, pp. 1–6 (2017). <https://doi.org/10.1088/1755-1315/80/1/012010>
7. Pavan Kumar, M., Prasada Rao, D.V.: A study on influence of fly ash and nano—silica on strength properties of concrete. *Int. J. Adv. Res. Eng. Tech.* **5**, 94–102 (2014)
8. Narender Reddy, A., Meena, T.: An experimental investigation on mechanical behaviour of eco—friendly concrete. In: *IOP Conference Series: Materials Science and Engineering* vol. 263, p. 032010 (2017). <https://doi.org/10.1088/1757-899X/263/3/032010>
9. Narender Reddy, A., Meena, T.: Study on effect of colloidal Nano silica blended concrete under compression. *Int. J. Eng. Tech.* **7**, 210–213 (2018). <https://doi.org/10.14419/ijet.v7i1.9538>
10. Reddy, M.V.S., Ashalatha, K., Surendra, K.: Studies on eco-friendly concrete by partial replacement of cement with Alccofine and fine fly ash. *ARPN J. Eng. App. Sci.* **11**, 3445–3448 (2016)
11. Narender Reddy, A., Meena, T.: A study on compressive behavior of ternary blended concrete incorporating Alccofine. *Matr. Today Proc.* **5**, 11356–11363 (2018). <https://doi.org/10.1016/j.matpr.2018.02.102>
12. Narender Reddy, A., Meena, T.: A comprehensive overview on performance of nano-silica concrete. *Int. J. Phar. Tech.* **9**, 5518–5529 (2017)
13. Supit, S.W.M., Shaikh, F.U.A.: Durability properties of high volume fly ash concrete containing nano-silica. *Matr. Stru.* **48**, 2431–2445 (2015). <https://doi.org/10.1617/s11527-014-0329-0>
14. Sivakumar, D., Hemalatha, T., Sri, N.S., Shobana, T., Soundarya, C.: Durability and mechanical characterization of concrete using Alccofines durability and mechanical characterization of concrete using Alccofines. *Int. J. App. Eng. Res.* **10**, 178–182 (2016)
15. Jindal, B.B., Singhal, D., Sharma, D.K.: Improving compressive strength of low calcium fly ash geopolymer concrete with Alccofine. *Adv. Con. Const.* **5**, 17–29 (2017). <https://doi.org/10.12989/acc.2017.5.1.17>

Chapter 4

IoT Sensor-Based Smart Agricultural System



J. Mahalakshmi, K. Kuppusamy, C. Kaleeswari and P. Maheswari

Abstract IoT is a reflective system of connecting the real-world objects that are accessed via the network. Sensors are involved for the data collection, in which the objects are having their own IP address and having the ability to access and transmit the resources through the Internet without manual performance. It is an architectural framework that offers integration and transfers the information between the computational devices. Its application areas are wide spread across smart homes, wearables, automation of vehicles, industrial Internet, smart cities, smart agriculture, smart retail, energy engagement, poultry and farming. In intelligent agriculture circumstances, to control the progress and to attain better yield in harvests are the primary focuses of this research work. The objective is to present new methodologies for the smart agricultural system, for monitoring and tracking, manufacturing of crops, import and export process, sales details, etc. By implementing the IoT-based smart sensors for the crop management, one can efficiently conquer the impulse of difficult and changing climate, the geographical disability, natural calamity, plagues and ailments about the crop. This research work proposes a cloud platform for smart agriculture data with wireless sensor network based on IOT. In cloud, intelligent production information is stored securely and made open for the authorized users.

Keywords Cultivation management · Cloud computing · Smart agriculture · Wireless sensor network · Internet of things

J. Mahalakshmi (✉) · K. Kuppusamy · P. Maheswari
Department of Computer Science, Alagappa University, Karaikudi, India
e-mail: lakshmimsc19@gmail.com

C. Kaleeswari
Department of Computational Logistics, Alagappa University, Karaikudi, India

© Springer Nature Singapore Pte Ltd. 2020
B. Subramanian et al. (eds.), *Emerging Technologies for Agriculture and Environment*, Lecture Notes on Multidisciplinary Industrial Engineering, https://doi.org/10.1007/978-981-13-7968-0_4

4.1 Introduction

Cloud computing, the interpersonal computing paradigm, gains its popularity by offering various services to the users on demand. This computing paradigm is scalable and has the capacity to work in heterogeneous application despite their computing structure. It provides varied services, among which the software, infrastructure, database are notable services. The innovative application model proposed in this paper is designed as an encryption service based on symmetric key to store the information received from the built-in sensors located in the field.

Cloud Computing, a rapidly developing computing paradigm in the technology era, offers computing resources as a service whenever and wherever on demand. The notable feature of Cloud Computing is its scalability and alleviating access, additionally offers a shared pool of resources makes it as a victorious computing paradigm. Based on the security policies guaranteed by the cloud service providers, the integrity of the data remains safe. Receptive data such as patient's medical history in the form of scans and reports, insurance policies and records while outsourced should maintain high protection. In connection with this, an encryption-as-a-service is one of the most interesting application services offered via the Cloud Computing archetype that recommends the users to encrypt the data received from the built-in sensors via application models.

One way to receive the data from the sensors is via the software tools such as Arduino, eclipse IoT, Kinoma, Node-RED, IoT System and Open IoT. It is the vast area of research domain and has a lot of security issues for researchers, while implementation. Researchers around the world proposed a lot of techniques to secure the data from unauthenticated access when it is outsourced via open paradigm. A conventional technique pave way to resist threats and vulnerabilities toward the data, were such as cryptographic processes, authentication mechanisms and access control policies. Cryptographic algorithm alters the consigner provided raw data into inarticulate form, via encryption process, and gets back the original form from the decryption process, upon authenticated consignee identified. In cloud computing, there exist numerous services such as secret storage-as-a-service [1], data encryption-as-a-service [2], data protection-as-a-service [3] and privacy-as-a-service [4] that all offer security to the data using different algorithms.

This research paper mainly concentrated on IoT sensor for smart agriculture, the data analytics that is needed for assisting the farmers to use the modern technologies to improve the production and make it as a smart cultivation. The data stored and shared via the sensors might take any format such as maybe an image related to crop data or maybe the farmers' details, such as in documents, or maybe the spreadsheet files. The security-as-a-service offers an application model that encrypts files converted to unintelligible format. The proposed encryption-as-a-service application model will encrypt the file and decrypt only upon the authenticated access [5].

Rest of the paper is structured as follows. Section 4.1 shows the basic information on encryption, cloud services and optimization techniques found in the literature. It is followed by the related research work in this field at Sect. 4.2. The fundamental

notations are briefly explained as mathematical preliminaries in Sect. 4.3. The meta-heuristic simulated annealing algorithm, which is the basic theory of the proposed encryption algorithm, is clearly stated under Sect. 4.4. The procedure and algorithm for the proposed application service fall under Sect. 4.5, where Sect. 4.6 is comprised of the experimental outcomes. Section 4.7 comes out with the conclusion made on this research work.

4.2 Related Research Work

Ray [6] proposed the technique for IoT to solve real-time or practical life problems by constructing and exploration of power fact IoT notions. The author discussed the recent trends of architectural frameworks available for the academics and industries. Srinivasan et al. [7] discussed the alternate way of research in cultivation management using the WSN. The author reviewed the WSN applications, issues and challenges for improving the smart farming. The author also reported on various cloud computing techniques used for the agriculture modernization and its help in smart solution for agriculturalists.

Tongke [8], Work, concentrated on Cloud Computing and Smart Farming that builds in the combination of IoT and Radio Frequency Identification (RFID). The technique reported by the author helps to build the plant factory and analyze self-moving control production of farming management. Channe et al. [9] provided information on multidisciplinary model for smart agricultural management. The research work given by the author is based on the IoT sensors, cloud computing, mobile computing as well as the big data analysis.

Li et al. [10] stated the use of private cloud file encryption methodology with the aid of tripartite secret key protocol. A certificate-less encryption algorithm is recommended by the authors and yields better results for large-scale environment. Computational cost for the key exchange between the consigner and the consignee is the limitation found in this method. Despite this, the results made by the authors reveal high security of the files communicated.

Vu et al. [11] reported a data protection-as-a-service, to the clients in multi-cloud environment. The authors apply access policy mechanisms that include automatic encryption. It reveals encrypted format to the intruders. By offering specific plugin, the application model developed by the authors is flexible to fit into any cloud infrastructure irrespective of the model. Thamizhselvan et al. [12] reported on the V-GRT methodology to improvise the data security model in cloud computing. The authors developed a new key generation methodology and named it as Chaive Unica, an advanced substitution method. The results depict the security analysis and the way it defends against various cryptanalytic attacks than the existing algorithm in various metrics. Liu et al. [13] have been credited for the concern provided over the reliability and confidentiality of the data transferred via cloud networks. The authors discussed the functionality that the converted plain data can be forwarded without

being retrieved back. A variant of ElGamal-based proxy re-encryption algorithm was employed by the authors to provide original inaccessibility to the data.

Nafi et al. [14] discussed the working procedure of file encryption in distributed server-based cloud architecture. The algorithm designed by the authors for file encryption makes it ease of access to various data formats in cloud computing paradigm. Information security occupies a major role in the author's contribution. AES and RSA standard algorithms are used for encryption that shows less execution time. Distributed servers are involved in file uploading and downloading which increases the time complexity. Moreover, the storage space for this also remains high.

Siddagangaiah [15] discussed the proposed work of a plant health monitoring system. The work explained by the author is to examine the plants' effects as platform parameters like humidity, light intensity along with the temperature. The data passed via the Arduino Uno boards to the cloud environment for storage and analysis. Sujatha and Nithya [16] reported on the overview of the surveys about the IoT sensors with cloud platforms to validate and monitor the soil. The authors explained about the bulk density test, respiration test, moisture test and quality of the water required for the crop maintenance. Aliev et al. [17] introduced a practical approach to acquire temperature of plants, soil moisture and humidity. The authors also credit for the invention of prototype device with an Android application used for transferring the data into cloud. Uchiyama [18] proposed a status labeling for IoT systems in agro-products, to make the agriculturalist to use a large volume of data at ease.

4.3 Cloud Computing Encryption Service for Secure IoT Data Storage

Cloud computing archetype offers abundant services to its clients from pool of resources with utmost reliability and scalability. Security services occupy a vital position between various services offered by the cloud. Authentication of the data transferred through open medium requires protection from various vulnerabilities and threats. Concentrating on this juncture, encryption services are offered as security services in cloud computing paradigm. This security service consists of various conventional encryption methodologies which convert the data into the inarticulate form. Multimedia files can be encrypted by using the proposed technique which is the hybridization of conventional encryption technique with optimization technique. This process is converted as an application service that allows a large scale of users to encrypt their files in secured manner simultaneously by sharing the service. The key management takes concern on the exchange of keys between the consigner and the consignee to maintain authenticity.

Main inspiration toward the construction of this application service model is to offer encryption-as-a-service to the end users despite the form of data being engaged for encryption. A new symmetric key encryption algorithm is developed by hybridization of two independent techniques, namely the improved cipher block

chaining encryption operation and the metaheuristic simulated annealing algorithm. Two key elements are marked as the objective for this application service: One is to minimize the execution time, and other is to increase the complexity of the generated key. The size of the key comes in three diverse sizes such as 64, 128 and 256 bits. Regardless, this interesting application allows the user to encrypt assorted file types. The sub-optimal key generation takes place in two phases and makes this application service a better solution for encryption.

4.3.1 Notations

This section briefly explains the basic mathematical notations used in the construction of the proposed symmetric key application model. Variety of files can be encrypted by using this innovative application model in a rapid manner. The basic design notation to implement the algorithm is in matrix forms that are used for ease of access. Every element in the matrix should possess the binary strings 0, 1. If Z is a matrix, then Z_{mn} is an 8×8 matrix where m, n indicate the row and column of the matrix. The following depicted format in Eq. (4.1) shows the basic design notation of the input. In the case of images, individual color channels are separated and transformed into corresponding pixel values. The pixel values possess the binary positions in the mathematical model.

$$Z_{xy} = \begin{bmatrix} 10101101 \\ 10010101 \\ 01011101 \\ 10010010 \\ 10101011 \\ 01010101 \\ 11001011 \\ 10011010 \end{bmatrix} \quad (4.1)$$

4.3.2 Design Goals

The state of the art paves the way to convert the varied form of elements to its corresponding binary bits to alleviate access. The depicted matrix notation is the sample matrix with an element filled that shows the conversion of user-defined plain text conversion to bit blocks. In the case of the image either compressed or uncompressed, individual color bands are separated, respectively, into the red band, blue band and green band. Each pixel element exists between 0 and 255 and is again transformed into its binary values, and then implementation follows. The improved

cipher block chain encryption operation is performed on the bit blocks. Block ciphers encrypt the data simultaneously irrespective of the length. Each block size is predominantly defined, and the key value passed for every block is identified. For the inimitable decryption, every single element in the block is encrypted with the fixed key generated.

The cipher block chaining encryption operation is improvised in this encryption algorithm, while encryption with multiple keys takes place, the first key whose elements are from improvised cipher block chaining encryption operation. The ICBC in return when cascaded is resistant against known—IV, Chosen-Plain text Attacks. The feedback of the input is hidden from the output revealed. The output of the first block remains as the input of the successor block. This basic building block makes the algorithm stronger; since if the single element gets changed, the whole pattern is collapsed. The cipher block chaining is the self-synchronizing mode where the error propagation is less since every block output remains different. This property is the basis for the improved cipher block chaining algorithm.

4.4 Optimization Technique and Objective Function Formulation

The main objective of this proposed algorithm is to generate the sub-optimal key to encrypt the user-defined data with potential authentication. The optimization algorithms help to find out the sub-optimal solution to the problem formulation that it defined. In the literature, there exist numerous optimization algorithms such as the bio-inspired genetic algorithm, bull optimization algorithm, cuttlefish algorithm, bees algorithm, memetic algorithm and ant colony optimization, among which, in this proposed research work, the simulated annealing algorithm is applied to encrypt the data.

4.4.1 Simulated Annealing—A Metaheuristic Optimization Technique

Sub-optimal key generation for high-profiled encryption is the main motivation behind this novel application designing. The end users will be able to encrypt their data with potential authentication and the decryption or vice versa. Optimization algorithms were evolved to find either the maximum or the minimum for the given problem. The feasible solution should be attained by incorporating the optimization techniques based on the need. A lot of optimization algorithms are in the literature, such as bull optimization algorithm, cuttlefish algorithm, bees algorithm and memetic algorithm. Genetic algorithm is one of the most frequently used, yet prevailing algorithm is nature-inspired search algorithm and natural selection mechanics based on

Darwin’s theory of evolution. Apart from that in this proposed research work, the simulated annealing algorithm is employed so as to generate the sub-optimal key generation, to encrypt the data.

Simulated annealing (SA) algorithm is one of the metaheuristic and probabilistic algorithms that finds the approximate global solution for the specific function. Especially, it finds the global maximization in a large search space. When the problem defined is in the discrete form, then the simulated annealing will be found as the better solution for finding an approximate global optimum solution. It is also considered as an alternative method used instead of the gradient descent algorithm.

The method is inspired from the thermodynamic process of annealing of molten metals to attain the lowest free energy as stated by Kirkpatrick et al. [19]. Simulated annealing algorithm works in the following procedure.

In every phase of iteration, the heuristic simulated annealing algorithm decides some state “s” as the current phase. Then, the algorithm probably chooses between whether to retain at the same state and whether to move to the neighbor, until the near optimum level is reached. The fundamental optimization is the searching of neighbors, by continuous iteration, and moves across every state till finding the better neighbor.

To achieve optimum results, constraints should be clearly defined as an objective function. This objective function falls as two divisions: single-criterion objective function and multi-objective function. The linear constraint is applied in this proposed encryption algorithm with multi-objective function. The following are the basic terminologies used in the mathematical implementation of simulated annealing algorithm.

Objective Function

The optimization problem is expressed as a mathematical function. An example is shown below (Table 4.1):

$$F(x) = \text{Objective Function}$$

Table 4.1 Notations and definitions

Notations	Definitions
Solver	Simulated annealing algorithm
Objective function	Global optimum
Bounds	Specifies the limit of the upper and lower bounds
Annealing function	Takes random steps to generate new points that are directly with size proportional to the temperature and move to the next iteration
Temperature update function	Update when temperature decreases
Acceptance probability function	Use the default acceptance function

The above stated are the basic simulated annealing parameters that were employed in this working procedure.

4.5 Hybrid Encryption and Decryption Process

In this proposed research work, an interesting yet new application service model is designed and their efficiency is verified under various metrics. Since security of crop data is taken into account, an innovative symmetric key encryption algorithm is designed as a service offered via cloud archetype. For every encryption process, the key generation decides the quality of encryption. It is the most important that should avoid various vulnerabilities and threats that are found in the communication medium. This research work uses the convention encryption operation block ciphers and modifies its working procedure to generate a key for encryption. Moreover, the optimization technique yields another key and together makes the process complex. The main advantage of including the block ciphers in the proposed model is it performs against the parallelization and also allows the data to be encrypted at chunks at a same time. Throughout the implementation process in this research work, a consistent design rationale is followed so as to maintain uniformity as well as to perform in a rapid manner.

4.5.1 Encryption and Decryption Scheme for Text Data

In this section, the algorithm for the encryption of text data is briefly stated. Core components of the algorithm are encryption process, key generation using multiple techniques as well as the decryption scheme. After preprocessing of the user plain data, as explained above, it is converted to its corresponding binary bits and separated into 8×8 blocks for further implementation. Let us assume the input data as 8×8 matrix blocks. If Z is a matrix, then Z_{mn} is an 8×8 matrix, whose elements were represented using 8-bit binary structure, where m, n indicate the elements in the matrix as X_i, Y_i .

After the conversion, the improved cipher block chaining operation mode follows.

$$X_i^n = \{X_0^1, X_1^2 X_2^3, \dots X_7^8\} = \{0, 1, 1, 0, 0, 1, 1, 0\} - \text{Input Data Bit}$$

$$Y_i^n = \{Y_0^1, Y_1^2, Y_2^3, \dots Y_7^8\} = \{1, 1, 0, 0, 1, 0, 1, 0\} - \text{Key Elements}$$

The plain text character is converted into corresponding binary bits and filled in the matrix Z with the elements as X_i . The Y_i is the matrix element for single row acquired from the improved cipher block chaining process. It is obtained as the result of the following procedure. Complete the matrix Z_{mn} with the binary value formulated in horizontal manner. Till end of the file is reached, the conversion follows. These blocks

are fed as input for improved cipher block chaining operation. Key generation is most important for any cryptographic process. In this proposed encryption algorithm, key generation takes place from the block that is fed as input. The resultant matrix from the encryption process is taken as input to generate a key matrix. It is now passed through the improved block chaining operation mode, with initialization vector. Set the initialization vector (IV) with 8-bit binary input as in Eq. 8.

$$IV = \{0, 1, 0, 1, 0, 1, 0, 0\} \quad (4.2)$$

The input matrix X_i element is exclusive disjunct (XOR) with the initialization vector IV. The result vector is then passed as the input for the predecessor X_i matrix elements. Hence, a single-bit error in a block will cause failure of decryption in the subsequent block as well. The cipher block chaining is the self-synchronizing mode where the error propagation is less since every block output remains different. This property is the basis for the improved cipher block chaining algorithm. The substitution operation ends after the key block of 8×8 matrix acquires from the improved cipher block chaining algorithm.

The second key is generated from the pseudorandom number generators. Final is the most important key generation, the construction of sub-optimal key. This key is generated from the simulated annealing, with the procedure as represented in Sect. 4.4. The input for the initial population is the matrix blocks which consist of partially encrypted data. These partially ciphered bits are taken as the initial population based on the objective function recited, and a key matrix consists of sub-optimal binary bits which are generated. This key is passed, and encryption is done to completely cipher the plain text. The typical architecture for the text encryption with the algorithm and illustration is presented in Fig. 4.1.

The example explained below shows the working method of the proposed encryption algorithm. Let us assume the text file of the user is allowed with finite characters that hold numerals, characters, special characters, etc. (for sample: on-2015-105009.pdf Title: A New Cryptosystem MKE). Each individual character is articulated into matrix elements. In the key generation phase, the size of the key varies either as 64, 128 or 256 bits. The steps for the encryption, decryption and key generation are as follows.

4.5.1.1 Algorithm for Encryption Process

- *Step 1:* Read the input file that consists of the text data.
- *Step 2:* As depicted in the design rationale, independently split the data.
- *Step 3:* Convert Step 2 data to its corresponding binary bits.
- *Step 4:* Let us take the input as X_i , and fill the block elements X_i in 8×8 matrices, till end of the file is reached.

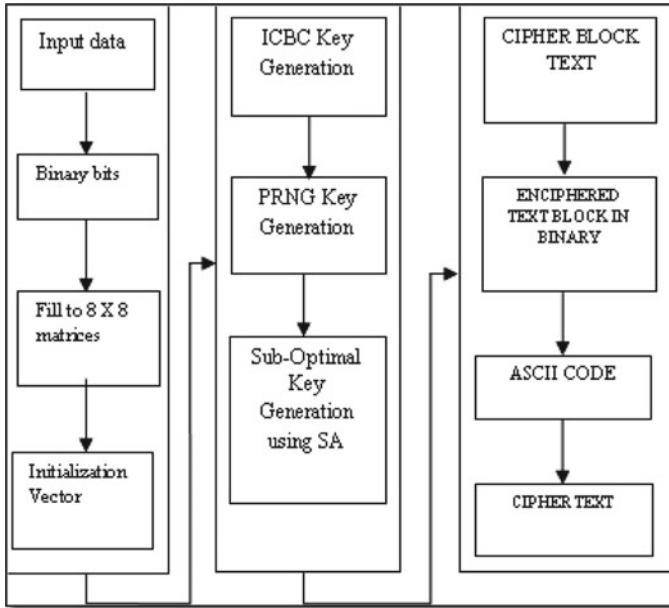


Fig. 4.1 Block diagram of data encryption

4.5.1.2 Algorithm for Key Generation Process

- *Step 5:* Generate the initialization vector IV with eight binary bits for the first key generation process.
- *Step 6:* Apply the improved cipher block chaining procedure, such that $Y_i = X_i \oplus IV$. The Symbol may be placed here to denote the XoR operation \oplus .
- *Step 7:* The obtained result matrix is the key of the successor block matrices.
- *Step 8:* One more key matrix is generated via the pseudorandom number generators.
- *Step 9:* The next key generation is the most important key that is constructed as a sub-optimal key to obtain the optimized key for the encryption from the simulated annealing as explained in Sect. 4.4.
- *Step 10:* The size of the key values is in three various sizes either as 64, 128 or 256 bits. If the size of the key is 64, the block size is designed as 8×8 , and if it is 256 then the block size is 16×16 , where the key size is of 128 bit then the block size is 8×16 .
- *Step 11:* This key value is again disjunct with the partially encrypted elements in the matrices.
- *Step 12:* As a result from Step 11, completely ciphered data is available at the matrices.
- *Step 13:* The blocks with the binary elements are again converted to 'corresponding ASCII code.
- *Step 14:* Detaching the blocks will yield the encrypted text data.

4.5.1.3 Algorithm for Decryption

- *Step 15*: File that contains the encrypted text data is taken as input.
- *Step 16*: Convert the encrypted data into equivalent binary bits.
- *Step 17*: Fill the matrices of 8×8 with the converted ciphered binary bits, yet the end is reached.
- *Step 18*: Reverse is the process of encryption, along with the key generation.
- *Step 19*: The key is similar since the symmetric key scheme is followed.
- *Step 20*: The deciphered, original text data is obtained as the result of the key generation.

4.6 Experimental Results

The experimental results obtained from the proposed hybrid encryption algorithm are presented below. The implementation is done with the simulation environment of simulated annealing [simulannealbnd] solver found in MATLAB R2013a. The encryption and the decryption processes are implemented with the Visual Studio 2010, C# language under the configuration of Windows 7 operating system with Core i3 and 3 GB RAM. The experimental outcomes stated below include the consequences that are obtained by applying varied key size such as 64, 128 and 256-bit key. Diverse metrics are analyzed based on the results attained. Time complexity is the main factor elaborated in the case of text encryption process.

4.6.1 Simulation Environmental Setup

The selective objective function is as expressed in Sect. 4.4 and is tested using the simulated annealing [simulannealbnd] solver in the Global Optimization Toolbox. The simulation setup for the formulation of objective function along with its constraints that includes the input parameters, acceptance criteria, acceptance probability function, temperature update functions, the bounds that specify the key sizes is listed in Table 4.2.

4.7 Conclusion

Multimedia data can be encrypted and transferred over the open transmission medium with the help of this application service in cloud computing. The performance results reveal that for the crop encryption this security service works better with less encryption time of about 2.986 ms, and it is resistance against statistical attacks. In cloud computing, space complexity is a prominent issue; it is almost minimized with the

Table 4.2 The text data encryption and decryption process

Key size (in bits)	File size (in bytes)	Input text data	Encrypted data	Decrypted data
256 bits	442 bytes	<pre>< rdf: Description rdf: about = "h t tp://sensordb.c s i r o Temp <rdf: type rdf: resource = "h t tp://sensordb.c s i r o.au/ontology/phenonet 20140611 - 1962 - 0012"> #ArduCrop"/> .u/phenonet/sensor/arducrop</pre>	<pre>wJyTwNyXwZyfwVyHwIy3wRyXwdybwFy38.+78. + 7wRyzwd+n85+n85yXwZ2vwZyb8.+78.+7k52Tk.mX _____ kxmXkhmXk9ifkxmnk l+n85+n85+ n85ubkxiHgJmXkpmXsRyPwZyTwVyL</pre>	<pre>< rdf: Description rdf: about = "h t tp://sensordb.c s i r o Temp <rdf: type rdf: resource = "h t tp://sensordb.c s i r o.au/ontology/phenonet 20140611 - 1962 - 0012"> #ArduCrop"/> u/phenonet/sensor/arducrop</pre>

second objective storage space reduction by converting the contents to binary bits. The data thus stored securely in this private cloud can be accessed upon proper authentication and used for the smart agricultural management.

References

1. Vu, Q.H., Colombo, M., Asal, R., Sajjad, A., El-Moussa, F.A., Dimitrakos, T.: Secure cloud storage: a framework for data protection as a service in the multi-cloud environment. In: IEEE Conference on Communications and Network Security (CNS), Florence, Italy, 28–30 September, pp. 1–6 (2015). <https://kar.kent.ac.uk/id/eprint/50845>
2. <http://www.amazonencryptionsservice.com/>; <http://docs.aws.amazon.com/AmazonS3/latest/dev/serv-side-encryption.html>
3. Escudo-Cloud, <http://www.escudocloud.eu/index.php>
4. Itani, W., Kayssi, A., Chehab, A.: Privacy as a service: privacy-aware data storage and processing in cloud computing architectures. In: Proceedings of the 8th IEEE International Conference on Dependable, Autonomic and Secure Computing (DASC), pp. 711–716 (2009). <https://doi.org/10.1109/dasc.2009.139>
5. Kakkar, A., Singh, M.L., Bansal, P.K.: Mathematical analysis and simulation of multiple keys and S-boxes in a multinode network for secure transmission. *Int. J. Comput. Math.* **89**(16), 2123–2142 (2012). <https://doi.org/10.1080/00207160.2012.704022>
6. Ray, P.P.: A survey on internet of things architectures. *J. King Saud Uni.-Comput. Info. Sci.* **30**(3), 291–319 (2018)
7. Srinivasan, G., Vishnu Kumar, N., Shafeer Ahamed, Y., Jagadeesan S.: Providing smart agricultural solution to farmers for better yielding using IoT. *Int. J. Adv. Sci. Eng. Res.* **2**(1) (2017)
8. TongKe, F.: Smart agriculture based on cloud computing and IOT. *J. Convergence Info. Technol.* **8**(2) (2013). <https://doi.org/10.4156/jcit.vol8.issue2.26>
9. Channe, H., Kothari, S., Kadam, D.: Multidisciplinary model for smart agriculture using internet-of-things (IoT), sensors, cloud-computing, mobile-computing & big-data analysis. *Int. J. Comput. Technol. Appl.* **6**(3), 374–382 (2015)
10. Li, X., Li, W., Shi, D.: Enterprise private cloud file encryption system based on tripartite secret key protocol. In: International Industrial Informatics and Computer Engineering Conference, Published by Atlantis Press, pp. 166–169 (2015)
11. Vu, Q.H., Colombo, M., Asal, R., Sajjad, A., El-Moussa, F.A., Dimitrakos, T.: Secure cloud storage: a framework for data protection as a service in the multi-cloud environment. In: 2015 IEEE Conference on Communications and Network Security (CNS), pp. 1–6 (2015). <https://doi.org/10.1109/cns.2015.7346879>
12. Thamizhselvan, M., Raghuraman, R., Manoj, S.G., Paul, P.V.: Data security model for Cloud Computing using V-GRT methodology. In: Intelligent System and Control ISCO 8th IEEE Conference, pp. 224–228 (2014)
13. Liu, J., Wang, H., Xian, M., Rong, H., Huang, K.: Reliable and confidential cloud storage with efficient data forwarding functionality. *IET Commun.* **10**(6), 661–668 (2016). <https://doi.org/10.1049/iet-com.2015.0608>
14. Nafi, K.W., Kar, T.S., Hoque, S.A., Hashem, M. M.A.: A newer user authentication, file encryption and distributed server based cloud computing security architecture. *Int. J. Adv. Comput. Sci. Appl.* **3**(10), 181–186 (2012)
15. Siddagangaiah, S.: A novel approach to IoT based plant health monitoring system. *Int. Res. J. Eng. Technol.* **3**(11), 880–886 (2016)
16. Sujatha, R., Nithya, R.A.: A survey on soil monitoring and testing in smart farming using IoT and cloud platform. *Int. J. Eng. Res. Appl.* **7**(11), 55–59 (2017)
17. Aliev, K., Pasero, E., Jawaid, M.M., Narejo, S., Pulatov, A.: Internet of plants application for smart agriculture. *Int. J. Adv. Comput. Sci. Appl.* **9**(4), 421–429 (2018)

18. Uchiyama, H.: AgriBase: status labeling for IoT systems. In: CIDR '17 Chaminade, California ACM (2017). ISBN 123-4567-24-567/08/06
19. Kirkpatrick, S., Gelatt Jr., C.D., Vecchi, M.P.: Optimization by simulated annealing. *Science* **220**, 671 (1983)

Chapter 5

Smart Monitoring of Farmland Using Fuzzy-Based Distributed Wireless Sensor Networks



Anagha Rajput , Vinoth Babu Kumaravelu  and Arthi Murugadass 

Abstract Agricultural research is practiced globally as farming contributes to national revenue of many countries. The embryonic technologies can be intelligently used to help farmers in automating farming operations for better productivity and reduced human efforts. Recent agricultural researches emphasize majorly on agro-meteorology, wireless sensor network-based Internet of things systems for land surveillance, and geospatial technology for drought assessments. Large farmlands need to be monitored continuously to evaluate soil fertility, crop moisture and protect from crop raiders. This research work proposes an idea of smart monitoring of farmland using wireless sensor networks. The timely collected data by the network will assist the farmers to take precise agronomic decisions. The main constraint of wireless sensor networks is its limited lifetime because sensor nodes are battery-driven devices. The major energy consumption is due to long-distance radio communications. To prolong the lifetime of nodes and reduce the transmission distances, a fuzzy-based distributed clustering protocol is proposed. The network is clustered using fuzzy-c-means algorithm. The cluster head selection in each cluster is then carried out based on perception probability model. The protocol is simulated using MATLAB. The simulation results are obtained for different coverage areas. The proposed protocol outperforms the recent conventional protocols in terms of energy savings and network sustainability. The results indicate that the proposed protocol is scalable and sustainable. Hence, it can be efficiently used in farmland monitoring systems.

Keywords Fuzzy-c-means (FCM) clustering · Farmland monitoring · Perception probability · Wireless sensor networks (WSNs)

A. Rajput · V. B. Kumaravelu (✉)
School of Electronics Engineering, Vellore Institute of Technology, Vellore, Tamil Nadu, India
e-mail: vinothbab@gmail.com

A. Rajput
e-mail: anagharajput@gmail.com

A. Murugadass
Sreenivasa Institute of Technology and Management Studies, Chittoor, Andhra Pradesh, India
e-mail: arthimdas@gmail.com

5.1 Introduction

Agriculture serves nations food products, and many of the developing countries rely on agriculture for their annual revenues. Agriculture is one of the most prompted applications of wireless sensor network (WSN)-based Internet of Things (IoT) systems. The embryonic of IoT and WSN for precision agriculture has the potential to provide automated systems and quick services to farmers and experts. WSN is considered as an important and sustainable technology to realize the monitoring infrastructure of IoT systems because the future Internet is visualized to be a large omnipresent network where people, objects, or anything will be connected at any time [1]. This has encouraged the agricultural research in a new direction, where traditional agrarian methods are being replaced by automated techniques. Farmlands need to be monitored incessantly to protect the field from crop raiders, monitor soil quality and irrigation requirements for better harvest productivity and crop development.

Agricultural activities can be categorized like seed sowing, irrigation system, crop growing, soil fertilizing, and so forth. At each phase of farming, the field climate, soil, and crop growth are to be monitored in order to get a good yield. For instance, plant growth is affected by different facets like climatic conditions, soil mineral contents, a quantity of composts used, water supply. For better productivity, attaining accurate estimations of these facets is a basic need of the agriculturist [2]. Another aspect of observing the farmlands is to protect the harvests from crop raiders like mammals and birds. The wildlife is hazardous to farmers as they damage the plants, destroy the grains, and at times harm the human beings. There are several traditional methods used by farmers to safeguard their farms like wire fencing, helikites, dog guarding. In any case, these are not safe and economical provisions. Subsequently, farmland monitoring is a vital and critical issue challenged by farmers [3].

In precision agriculture, systems like smart irrigation, cattle monitoring, controlled fertilization are been developed [4–6]. The real-time field information is gathered by sensors, which are embedded on microprocessor circuits. Such large number of sensor nodes deployed in the farm can quickly capture the farm conditions and transmit information to the required recipient. These information gathered from deployed sensors are utilized by farmers, experts or computerized control systems to take decision on agricultural policies like scheduling water supply to crops, soil composting. Here, agrarian fields can spread over large acres of land. Thus, WSN is well suited to automate the farming process, where wireless sensor nodes can be placed over large open space. WSNs are ad hoc and infrastructure less networks intended for specific applications. Thus, the deployment of WSN differs from one application to another.

The sensor nodes deployed for farmland monitoring to realize precision agricultural operations are portrayed in Fig. 5.1. The sensor nodes are deployed in the farming region where parameters like ambient temperature, humidity, soil moisture, carbon content are to be measured. The sensors are smart devices with radio circuit embedded on the device. These sensors can communicate with the gateway node

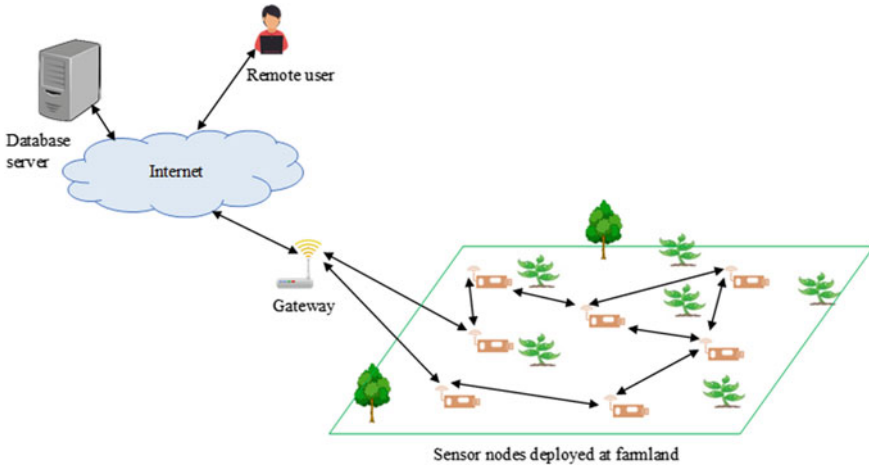


Fig. 5.1 WSN-based IoT system for precision agriculture

(also called as sink) to transmit the sensed data either periodically or on demand. The gateway node is the intermediate device that forwards sensor data into the Internet database system. Once the data is available at Internet database system, it can be retrieved by any users for knowledge acquisition or data analysis. A remote user can monitor the field and control the sensors and actuators [7, 8]. For instance, the valve of water pump can be controlled remotely by the user, when an alarm is given by on-field deployed water level indicating sensors. As the data is instantly available on Internet, the end user can use any of the devices like computer, laptop, or mobile phone to get access to the data. The remote user is connected to Internet via base stations of the cellular network. The recent research concentrates on the sustainability of WSN because the network can be large in size but restricted to the short battery lifetime. WSNs are designed for specific applications, and therefore, the network deployment has to satisfy application-based requirements [9].

Rest of the paper is organized in the following order: Sect. 5.2 discusses the potential of WSN for agricultural applications. Section 5.3 represents the literature studied. Section 5.4 illustrates the proposed clustering protocol based on fuzzy-c-means (FCM) algorithm and perception probability. Simulation results and discussions are presented in Sect. 5.5. The paper is concluded in Sect. 5.6.

5.2 Potential of WSN for Agricultural Applications

In precision agriculture, sensor nodes are deployed to capture the climate conditions of the field. These sensor nodes communicate with each other and form a network that works collaboratively to collect the environmental data. WSNs are ad hoc and

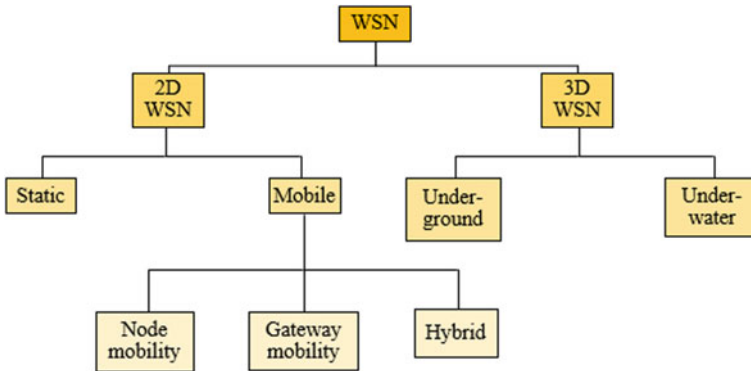


Fig. 5.2 Classification of WSN in context to the sensor node deployment

infrastructure less in nature. This gives them the flexibility to organize themselves into a network that will effectively send information from field to the remote user. The classification of WSN in context to the sensor node deployment is shown in Fig. 5.2. Broadly, WSN is classified as two-dimensional (2D) and three-dimensional (3D) network.

5.2.1 2D WSN

In 2D WSN, sensor nodes are deployed on or above the ground surface as shown in Fig. 5.1. The location tracking of such nodes is done using two geographical axes. Thus, the network formed by these nodes is called as 2D WSN. It is also called as terrestrial WSN in [2]. It is further classified into static and mobile networks.

5.2.2 Static 2D WSN

In this type, all the sensor nodes are assumed to be static after their deployment on the field. The gateway node that collects network data is also static at a particular location. Many WSN protocols are implemented considering its static nature [10–12]. This type of network is suitable for monitoring system, which can be used to observe climatic conditions, controlling pump valves, cattle monitoring, etc. The network performance in static scenarios is improved by constructing hierarchical layers of the network. Every WSN protocol design considers energy-efficient utilization of the nodes to enhance the lifetime of the network.

The more number of layers, the better is the energy savings. This is illustrated by implementing modified version of low-energy adaptive clustering hierarchy protocol

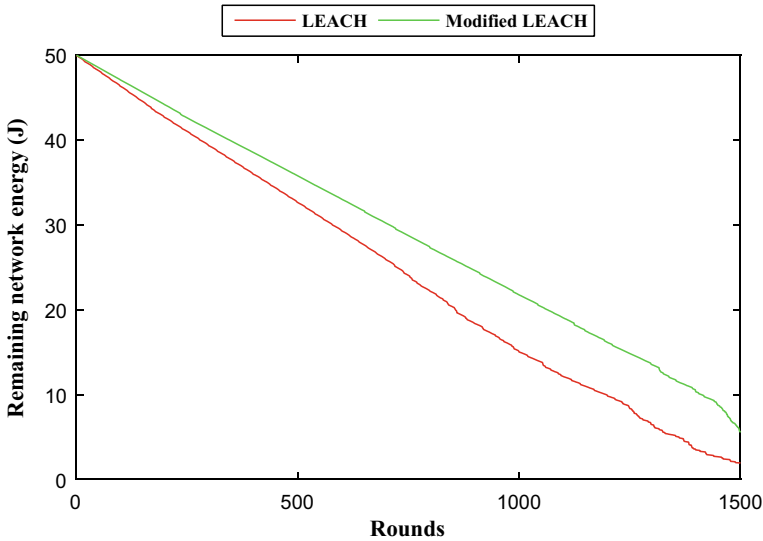


Fig. 5.3 Remaining network energy of LEACH and Modified LEACH protocols

(LEACH) [11]. In modified LEACH protocol, an additional hierarchical level of super cluster head (SCH) is introduced. All the cluster members send their data to their respective cluster head (CH). One SCH is elected among all the CHs for every round. The CHs transmit their cluster data to SCH. SCH further forwards the whole network data to the gateway. A comparison plot of total remaining network energy of modified LEACH and conventional LEACH is shown in Fig. 5.3. Due to the consideration of one more hierarchical level for data forwarding, the network load distribution is balanced and hence resulted in less number of death nodes compared to its conventional protocol. This is proved by measuring number of alive nodes for every round as shown in Fig. 5.4. The energy model for transceiver and simulation parameters is similar as in [11] and listed in Table 5.1.

5.2.3 Mobile 2D WSN

In this type of WSN, network devices have mobility. The network may not be 100% mobile but can have partial mobility among the devices. As illustrated in Fig. 5.2, mobility can be observed in three different forms:

Node Mobility: The sensor nodes themselves can be mobile, and the mobility completely depends on the application for which the network is established. In case of agriculture, the WSN with node mobility can be used in cattle monitoring system [12]. Here, the network should often re-organize itself to operate effectively.

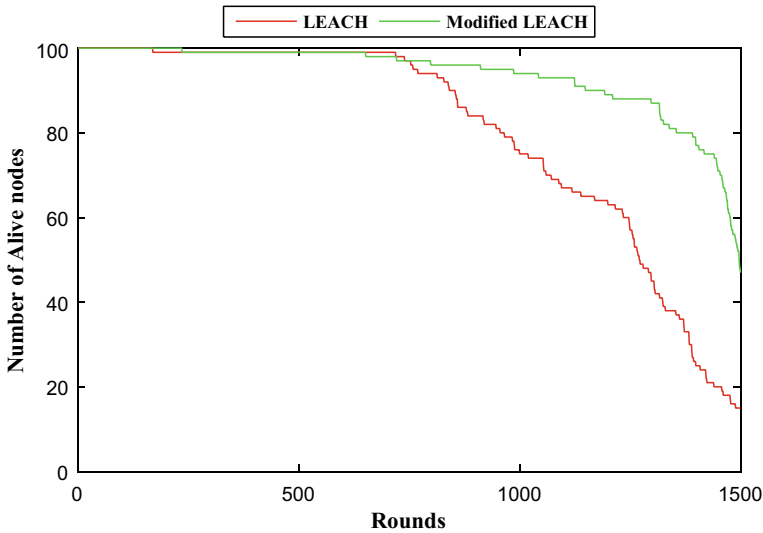


Fig. 5.4 Number of alive nodes of LEACH and modified LEACH protocols

Table 5.1 Parameters used for simulation

Parameters	Values
Monitoring area	100 m × 100 m
Number of sensor nodes	100
Gateway's location	(50,150)
Initial energy of sensor node	0.5 J
Electronic circuit's energy	50 nJ
Data aggregation energy	5 nJ/bit/message
Free space communication energy	10 pJ/bit/m ²
Multipath communication energy	0.0013 pJ/bit/m ⁴
Control packet size	200 bits
Data packet size	2400 bits

The trade-off occurs between the cattle speed and the energy required to attain the functionality of the network.

Gateway Mobility: The gateway is the node that collects data from the deployed sensor nodes. The mobility of gateway is rarely implemented, but in precision agriculture, mobility of gateway node can make a user-flexible system. The farmers can use personal digital assistants (PDA), while moving through field, which can be connected wirelessly to the nearby nodes for data collection. The option of communicating to all the nodes or few nodes at the farm relies on the design of an appropriate protocol.

Hybrid: This is a category with both sensor nodes, and gateway has mobility or one of the either becomes mobile as per requirement. Such type of network must be completely autonomous and independent to dynamically self-organize frequently. The monitoring drones are the example of such networks [13]. The issue faced in such mobility scenarios is the communication range required to deliver data toward gateway. Also, the hostile climatic conditions may erupt the communication. Another hybrid mobility is the mobility of the event occurring. The animal tracking at forests and crop raiders at farms are the examples of WSN, where event (crop raiders) is moving. In this case, to track the movement of event, sufficient number of sensor nodes are required to cover the event at all the time. An attempt by [14] is done to detect the crop-raider entering into farm by using ultrasonic sensors.

The communication protocols designed for such mobile cases should be rendered by appropriate support of the existing technology. The hybrid mobility is very uncommon compared to other mobile WSNs, but in real-time scenario, mobility of events and sensor nodes cannot be restricted.

5.2.4 3D WSN

The necessity for monitoring the environment has been increased substantially in the past few decades. The factors like climatic changes, decrease in water resources, and increase in livelihood habitats are motivating the need to monitor the environment and apply better policies to protect the scar resources. 3D WSN is the network that is been researched to monitor the changes occurring deep into the soil or the water [2, 9, 15]. Based on this research, 3D WSN is categorized as underground and underwater sensor networks. The 3D WSN applications are ocean monitoring, soil monitoring, disaster prevention, estimating burials and excavations, pipeline monitoring, etc. These types of networks are inherently three dimensional. The depth at which the sensor node is immersed into water [16] or soil [17] will become the third direction to track the location of the sensor node. The location tracking of these nodes is one of the challenging tasks due to two main reasons: The underwater sensor nodes are subjected to mobility often. Thus, tracking such nodes is tedious. The second reason is the communication interference caused by soil or objects under water. The issues faced by underwater WSN due to mobility are more than the underground WSN. The wireless communication used for underground WSN and underwater WSN is electromagnetic waves and acoustic waves, respectively. The challenges faced in using these communication systems are listed as follows:

- Lower propagation speed;
- Noise;
- Path loss due to various physical obstacles.

The above issues degrade the signal. Thus, reliable communication protocols need to be developed for these WSNs. For agricultural application, the WSNs are deployed

Table 5.2 Difference between 2D and 3D WSN

S. No.	2D WSN	3D WSN
1	Sensor is placed on the surface	Sensors are immersed into soil/water
2	Communication range is up to 100 m [2]	0.1–10 m [2]
3	High-frequency communication is efficient	High-frequency communication is attenuated by the soil. Thus, lower frequency communication is preferred
4	Frequency used is 868/915 MHz and 2.4 GHz [17]	Frequency range used is 433 MHz and 8–300 kHz [17]
5	Energy consumption is less	Energy consumption is more compared to 2D
6	Installation cost is lower	Installation cost is higher

underground, where sensors are mainly used to measure moistness, minerals, and compost proportion present in the soil. The sensor nodes are buried in two layers—topsoil and subsoil. The communication links of the nodes are affected by the soil. High-frequency signals suffer severe attenuation compared to lower frequency signals [18]. Due to this, communication range of the sensor nodes gets limited. Thus, more number of nodes is required to cover the large farmland.

The advantage of 3D over 2D is that the soil mineral and moisture in depth can also be monitored so that the fertilizers and compost will be adequately used as per the requirement. The water supply can also be made precise for drought-affected agricultural lands. The major differences between 2D and 3D WSN are listed in Table 5.2.

5.3 Study of Literature

The literature on clustering protocols is studied and summarized in this section. The nearby sensor nodes form clusters using various techniques like query-driven model, probability-based model [19–25]. The appropriate formation of clusters will reduce intra-cluster transmission distances required to forward the sensed data to CH. In [19], a distributed cluster computing energy-efficient routing scheme (DCCEERS) is implemented. A node is eligible to form cluster if its random counter becomes zero. The node form clusters using queries exchanged between the sensor nodes within its transmission range. The center of gravity of the clusters is then calculated and used to determine the centrality of the sensor nodes. The CHs are elected in each round based on remaining energy of the node and its centrality. The protocol does not limit the number of clusters formed in the network because any node in the network can start cluster formation on the condition of random counter.

The WSN is used for potato crop monitoring in Egypt as explained in [20]. Potato fields are mostly affected by fungal disease called as phytophthora. The preferable

land for good quality potato cultivation is loamy and well-aerated soil. The soil must not contain high level of calcium carbonate. This affects the starch quality of potatoes. The project used adaptive threshold sensitive energy-efficient sensor network (APTEEN) protocol for routing the sensed data [21]. APTEEN is the hierarchical cluster-based routing protocol. The field is assumed to be divided into small tubs of one carat area. Every carat will have two nodes deployed at the central region with a separation distance of approximately six meters. Also one node is deployed at the edges of the carat so as to communicate with another carat node.

In [22], the monitoring of cotton plant vigor to enhance its productivity and protect from damage is illustrated. Here, low-power sensor nodes are used to monitor potency in terms of chlorophyll concentration of the leaf. The sensor nodes sense the leaf information. This data is transmitted to sink node. The sink node forwards the data to remote host computer through universal serial bus (USB). The plants are separated evenly into small bunches. Every bunch has a sensor node deployed. The images of the leaves captured are judged for its strength. In minor abnormal situation also, an alarm is given. This makes the system fully flexible and avoids human efforts of manually observing the plants. The data collected can be used by experts to analyze the cultivation crop. The WSN is thus used in agriculture to enhance the crop protection as well as improve the farming techniques to achieve better productivity and quality.

Another initiative taken by the institute of agriculture and natural resources under University of Nebraska, Lincoln, used crop canopy sensors to measure liquid rate of nitrogen as per plant need [23]. The objective of the project is to manage nitrogen spray rate depending on the need of the crop using crop canopy sensors mounted on the node. This node can be fitted to the existing liquid nitrogen applicator, which uses electronic spray. The node also consists of electronic flow meter, pump speed hydraulic valve, and global positioning system (GPS). The monitoring central system receives sensor data along with GPS location. The data is processed using sufficiency index algorithm, and the desired nitrogen rate is provided to the rate controller. Thus, the pump valves control the flow of nitrogen spray.

A dynamic CH selection method (DCHSM) [24] forms clusters using Voronoi cells. The mean point of each Voronoi cell is used to determine centrality of the sensor node, while selecting a CH for every cluster. Two sets of eligible nodes are selected in a cluster. CH is then selected from first set initially. The second set is utilized only after the death of all the nodes in the first set. This results in unbalanced energy distribution among the network because every Voronoi cell does not have uniform number of nodes. In saving energy clustering algorithm (SECA) [25], mean points of the clusters are calculated using pre-defined single central point of the monitoring region and the average distances between the central point and the sensor nodes. The mean points are then determined iteratively by shifting away from the central point. The mean points depend on the number of sensor nodes in the cluster and their positions in the monitoring region. The change in number of cluster members will change the mean point location of that cluster. Thus, determining mean point of the region within a group of sensor nodes is likely to be ambiguous in nature.

Fuzzy-based clustering protocols also find tremendous scope in improving network performance. FCM is one of the optimization algorithms to categorize given objects [26, 27]. The nodes in the network are clustered using FCM. A fuzzy logic-based clustering protocol is proposed in [28]. To balance the network load and minimize hot spots in the network, unequal clustering is implemented. The fuzzy logic-based efficient clustering hierarchy (FLECH) is proposed in [29]. The CHs selected in the network are based on fuzzy logic system. The inputs to this system are remaining energy of the node, its centrality and distance toward gateway. It uses network dimension and number of one-hop neighbors to calculate the centrality of the sensor node to its associated cluster.

Based on the above literature, it is inferred that the cluster formation has major effects on the network performance. The nodes in a cluster must be near located nodes so that the intra-cluster distances are reduced. If the distances are considerably large, then energy consumption is also more. This ultimately reduces the overall network lifetime.

5.4 Proposed Clustering Protocol

An energy-efficient distributed cluster computing protocol is proposed in this work for farmland monitoring. The crops are grown on large surface region, and they are to be monitored using sensor nodes. Thus, the WSN deployed must be scalable. The sensor nodes are battery driven, and therefore, their energy must be utilized in proper manner so that the network can monitor the farmland for long period of time. Thus, the WSN must be sustainable and maintain alive nodes in the network for long duration. In the proposed protocol, an attempt is made to fulfill both—scalability and sustainability of the network.

In this work, FCM algorithm is used to determine mean points among the randomly deployed sensor nodes in the farmland. The clusters are formed within t iterations of the FCM algorithm. Once clusters are formed, every sensor node calculates its perception probability, which depends on the distance between node and mean point of the associated cluster. A set of eligible nodes is formed based on the perception probability of these nodes. All the CH-eligible nodes then calculate their perception value (V) and energy ratio (E) and broadcast to other nodes in the cluster. A node with highest V or highest E value will declare itself as CH.

The communication model decides the energy utilization of the sensor node because the major energy consumption is due to radio transmissions. The communication model used in the proposed protocol is similar to the model used in [11]. The energy required to transmit Q bits of data is given as,

$$E_{Tx} = \begin{cases} Q(E_{elec} + E_{fs}D^2); & D < D_{ref} \\ Q(E_{elec} + E_{mp}D^4); & D \geq D_{ref} \end{cases} \quad (5.1)$$

where E_{Tx} is the energy utilized for transmission. Q is the number of bits. E_{elec} is the energy required by hardware for processing and data aggregation. E_{fs} is the energy utilization due to free space channel propagation. E_{mp} is the energy required due to multipath fading channel propagation. D is the distance between transmitter and receiver nodes. D_{ref} is the reference distance used to choose the propagation model for data transmission. The energy required at the receiver end to receive Q bits is calculated as,

$$E_{Rx} = QE_{elec} \quad (5.2)$$

where E_{Rx} is the energy utilized for data reception. The proposed cluster formation and the CH selection are explained in the following subsections. It is assumed that the nodes are familiar with their node locations. It is also assumed that all the distances calculated are based on the received signal strength (RSS).

5.4.1 FCM-Based Clustering

The locations of sensor nodes and number of mean points are the inputs to FCM algorithm. Let us consider X number of sensor nodes in the network. These are grouped into Y clusters. The node location is denoted by two coordinates. FCM computes membership values between 0 and 1 as illustrated in this subsection. A value of 0 indicates no membership and 1 indicates complete membership. In between values indicate proportionate membership. The sum of the membership values for each sensor node to all clusters will be equal to 1. Also, different membership values show the probability of each sensor node to different clusters. A node is associated with that cluster mean point, whose corresponding membership value is highest. The first input data, i.e., node locations, is given as

$$\mathbf{A} = \{a_1, a_2, \dots, a_i, \dots, a_X\} \quad (5.3)$$

where X is total number of sensor nodes in the network. \mathbf{A} is a matrix of dimension $X \times 2$. a_i is the node location of the i th node. Similarly, the matrix of mean points, \mathbf{M} , is given as,

$$\mathbf{M} = \{m_1, m_2, \dots, m_j, \dots, m_Y\} \quad (5.4)$$

where Y is total number of clusters to be formed in the network. m_j is the mean point of the j th cluster. Initially, random mean points are considered for the first iteration. These mean points are shifted in the next iteration as per the objective function. The objective function with respect to membership value Z_{ij} and the distance D is formulated as

$$F = \sum_{i=1}^X \sum_{j=1}^Y (Z_{ij})^\alpha D(a_i, m_j)^2 \quad (5.5)$$

where F is the objective function. Z_{ij} is the degree of membership that the i th sensor node pertains to the j th cluster mean point. $\alpha \in [1, \infty]$ is the fuzzy factor. Practically, many studies show that α value is considered to be $[2, 2.5]$ [26]. In our work, α is considered to be equal to 2. $D(a_i, m_j)$ is the distance between i th sensor node and j th mean point. For every iteration, Z_{ij} and m_j are calculated as,

$$Z_{ij} = \frac{1}{\sum_{k=1}^Y \left(\frac{\|a_i - m_j\|}{\|a_i - m_k\|} \right)^{\frac{2}{\alpha-1}}} \quad (5.6)$$

$$m_j = \frac{\sum_{i=1}^X Z_{ij}^\alpha a_i}{\sum_{i=1}^X Z_{ij}^\alpha} \quad (5.7)$$

In order to minimize the objective function F , partial derivative of F with respect to Z_{ij} and m_j is performed iteratively using Eqs. (5.6) and (5.7). m_k is the mean point calculated in the past iteration, for the j th cluster. The iterations are performed subject to the following conditions,

$$\sum_{j=1}^Y Z_{ij} = 1, i = 1, 2, \dots, X \quad (5.8)$$

$$0 \leq Z_{ij} \leq 1, i = 1, 2, \dots, X \text{ and } j = 1, 2, \dots, Y \quad (5.9)$$

The condition in Eq. (5.8) is used to remove node isolation issue in the network. Every node has some membership toward each cluster within value one. After optimum iterations, each node is associated with one cluster, whose corresponding membership value is the highest. The condition in Eq. (5.9) restricts membership value within the given range so as to satisfy Eq. (5.8). The algorithm is halted in two cases—algorithm has reached either minimum threshold or maximum iterations. The proposed FCM algorithm for cluster formation is given as follows:

FCM algorithm for cluster formation

Initialization:

1. Initialize minimum_threshold;
2. Initialize maximum iterations (t_{max});
3. Initialize cluster mean points;

Input:

4. Node locations;

Main function:

5. For each iteration (t)
6. If $t < t_{max}$
7. Calculate objective function (F);
8. Improvement = absolute F^t - absolute F^{t-1} ;
9. If improvement > minimum_threshold
10. Update Z_{ij} and m_j ;
11. Else
12. Break;
13. End
14. Else
15. Break;
16. End
17. End

5.4.2 CH Selection Using Perception Probability

After clusters are formed in the network, each sensor node is associated with a mean point of its cluster. All the nodes then calculate perception probability using,

$$P(a_i, m_j) = \begin{cases} 1, & D(a_i, m_j) < S - \tau \\ e^{-\vartheta D_i}, & S - \tau \leq D(a_i, m_j) < S + \tau \\ 0 & D(a_i, m_j) \geq S + \tau \end{cases} \quad (5.10)$$

where $P(a_i, m_j)$ is the perception probability of i th node with respect to its mean point m_j . a_i is the i th node location associated with j th cluster. $D(a_i, m_j)$ is the distance of the i th sensor node from its mean point m_j . S is the sensing range of the sensor node. τ is the uncertainty factor of the sensor hardware circuit, and ϑ is the exponent factor. D_i is the term used as an exponential variable and calculated as,

$$D_i = D(a_i, m_j) - (S - \tau) \quad (5.11)$$

where D_i affects the probable value of node proportionately to the sensing range of the sensor hardware circuit. The use of sensing range assures node's coverage over other nodes within the cluster. This assures that none of the node is isolated. Then, a set of redundant nodes are found, whose perception probability is greater than 0.3 and less than 1. This range is selected because the perception probability model is distance based. The nodes having probability less than or equal to 0.3 are

reasonably away from center point compared to other cluster members. Such nodes have comparatively less reach ability or cluster coverage, which affects the average transmission distance of the nodes in the cluster.

The redundant nodes are the eligible nodes that can become CH for the given round. For each redundant node, V is calculated. At initial round, all nodes have equal energy level. Thus, for the initial few rounds, CH is selected based on V value. It is calculated as,

$$V_q = \frac{P(a_q, m_j)}{\sum_{l=1}^q P(a_q, m_j)} \quad (5.12)$$

V_q is the perception value of q th node in the j th cluster. The node with highest V_q value is selected as CH. After few rounds, the energy of the nodes apparently becomes heterogeneous in nature. Hence, for further rounds, CH is selected based on perception probability and remaining energy of the node. The E value is calculated as,

$$E_q = P(a_q, m_j) \frac{E_{\text{residual}}^q}{E_{\text{average}}^j} \quad (5.13)$$

where E_q is the energy ratio of the q th node of j th cluster. E_{residual}^q is the remaining energy of q th node. E_{average}^j is the total average energy of all the q nodes of j th cluster. The node having maximum E_q value is selected as CH. The total average energy of all the nodes in the cluster is considered to calculate energy ratio, because it will estimate the accurate perception of the node with respect to all its cluster members.

Once the CH is selected for every cluster, a time division multiple access (TDMA) scheduling is done at every CH node. Cluster members transmit their sensed data to CH in their allocated time slots. When all the cluster data is received, CH performs data aggregation to form a single data packet. This aggregated data packet is then transmitted to gateway. For every round, new CH is elected by comparing the V and E values among the cluster members.

5.5 Simulation Results and Discussions

In this section, the simulation results of the proposed clustering protocol are presented. The MATLAB R2017b is used to implement the proposed protocol. A WSN for given monitoring region consists of 200 sensor nodes and one gateway. All the network devices are static after deployment. The sensor nodes are randomly deployed, while gateway is located at (0, 0). The clustering protocol is executed for increasing monitoring area, and the corresponding network performance metrics are observed. The simulation parameters used are listed in Table 5.3.

Table 5.3 Simulation parameters

Parameters	Values
Monitoring region	100 m × 100 m, 200 m × 200 m
Number of sensor nodes	200
Gateway's location	(0,0)
Initial energy of sensor node	0.5 J
Energy consumed by electronic circuits	50 nJ
Energy for data aggregation	5 nJ/bit/message
Energy of free space propagation	10 pJ/bit/m ²
Energy of multipath fading channel	0.0013 pJ/bit/m ⁴
Packet of control bits	200 bits
Packet of data bits	2400 bits
Fuzzy factor (α)	2
Uncertainty factor of sensor node (τ)	0.2
Exponent factor (ϑ)	0.1
Improvement threshold of objective function	1×10^{-5}
Termination threshold for FCM (t_{\max})	100

The performance of proposed protocol is compared with LEACH [11], DCCEERS [19], DCHSM [24], and FLECH [29] in terms of remaining network energy and number of alive nodes. It is evaluated for two scenarios.

5.5.1 Scenario 1: Monitoring Region of 100 m × 100 m

The comparative plot of total remaining network energy and number of alive nodes with respect to number of rounds is shown in Figs. 5.5 and 5.6, respectively. The proposed protocol outperforms the conventional protocols because of efficient cluster formation using FCM algorithm, which reduces the intra-cluster transmission distances of the sensor nodes significantly. The centrality of the sensor node in the cluster is decided by the perception probability, which is based on factors like S , ϑ , and distance between sensor nodes and cluster mean point. Due to consideration of all above-mentioned factors, proper CH is been elected and the network load distribution among the sensor nodes is done in efficient manner. Therefore, the network sustains for long duration with more number of nodes alive as shown in Fig. 5.6.

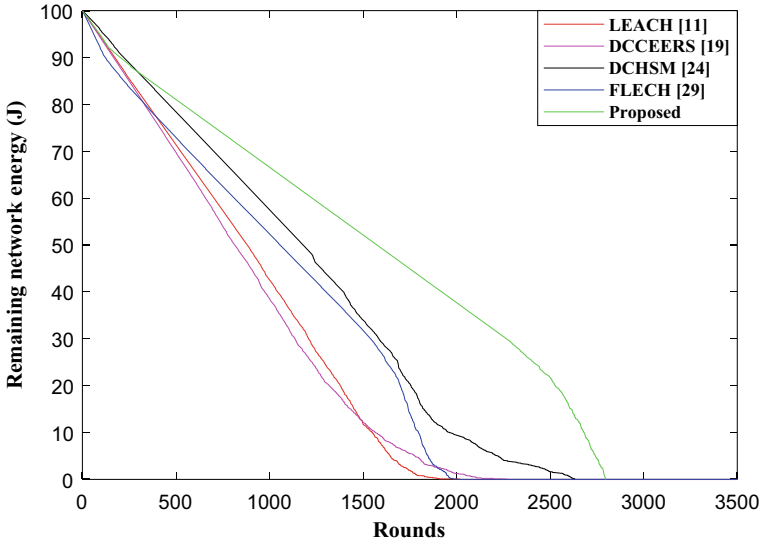


Fig. 5.5 Remaining network energy for monitoring region of size 100 m × 100 m

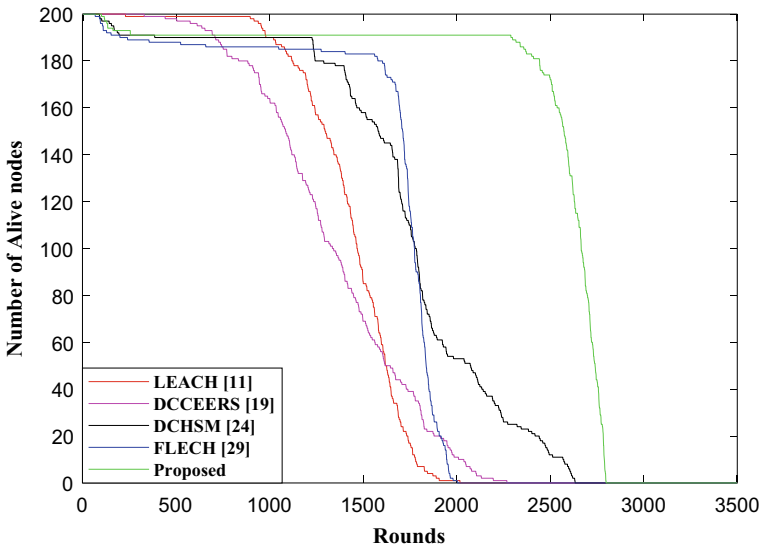


Fig. 5.6 Number of alive sensor nodes for monitoring region of size 100 m × 100 m

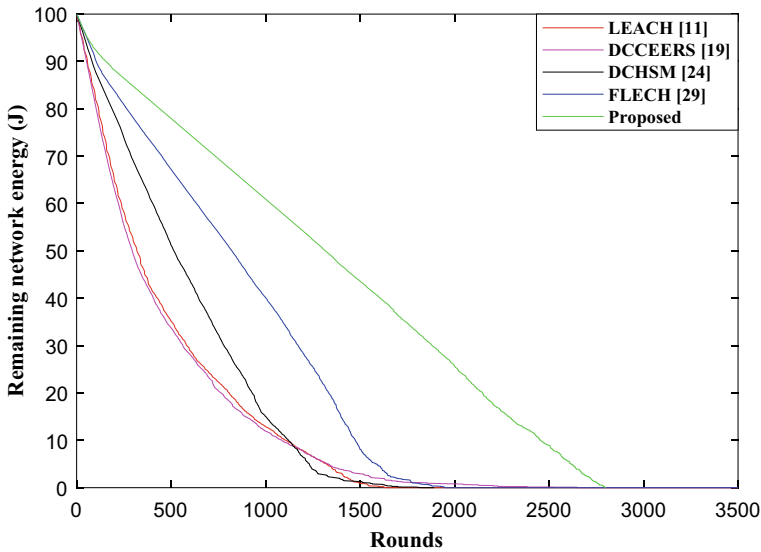


Fig. 5.7 Remaining network energy for monitoring region of size $200\text{ m} \times 200\text{ m}$

5.5.2 Scenario 2: Monitoring Region of $200\text{ m} \times 200\text{ m}$

As the proposed protocol is simulated for farmland monitoring system, it is also tested for increase in coverage area. In this scenario, 200 sensor nodes are deployed in the area of $200\text{ m} \times 200\text{ m}$. The protocols are executed, and the results are plotted as shown in Figs. 5.7 and 5.8. The results obtained proved that the proposed protocol performs better than other conventional protocols even for scalable scenario.

The proposed protocol is further analyzed for the sustainability in terms of first node dead (FND), half of the nodes dead (HND), and last node dead (LND). The round at which FND, HND, and LND occurred for all the simulated protocols is observed for five different WSN deployments. The readings for these set of WSN deployments are observed for both scenarios. The readings are listed in Tables 5.4 and 5.5 for $100\text{ m} \times 100\text{ m}$ and $200\text{ m} \times 200\text{ m}$, respectively.

The average values of HND and LND readings are calculated and plotted as shown in Figs. 5.9 and 5.10, respectively. The HND value indicates 50% of the WSN to be alive. From Fig. 5.9, it is seen that the proposed protocol sustains with 50% alive nodes for more number of rounds compared to other protocols in both the scenarios. This is because, as nodes start exhausting their energy, CHs are elected based on centrality as well as energy ratio values determined by Eqs. (5.10) and (5.11). The result for LND also holds better as seen from Fig. 5.10. Thus, the proposed protocol is energy efficient as well as sustainable and thus can be implemented for agricultural applications. The FND values of the proposed protocol occur at very early rounds because at the initial few rounds, the CHs are elected based on only distance parameter. Thus, the node that

Table 5.4 Network lifetime in terms of FND, HND, and LND (monitoring region = 100 m × 100 m)

WSN	LEACH [11]			DCCEERS [19]			DCHSM [24]			FLECH [29]			Proposed		
	FND	HND	LND	FND	HND	LND	FND	HND	LND	FND	HND	LND	FND	HND	LND
1	308	1437	1832	363	1380	2510	63	1742	2219	93	1669	1978	124	2671	2799
2	209	1489	1865	361	1367	2982	60	1699	2329	79	1732	1989	105	2685	2799
3	204	1421	1762	414	1380	2520	78	1733	2659	90	1693	1977	98	2697	2796
4	211	1514	1992	338	1411	2422	68	1770	2282	80	1773	1992	112	2664	2798
5	230	1467	2018	330	1336	2269	91	1778	2633	68	1774	2004	102	2666	2799
Average	232.4	1465.6	1893.8	361.2	1374.8	2540.6	72	1744.4	2424.4	82	1728.2	1988	108.2	2676.6	2798.2

Table 5.5 Network lifetime in terms of FND, HND, and LND (monitoring region = 200 m × 200 m)

WSN	LEACH [11]			DCCEERS [19]			DCHSM [24]			FLECH [29]			Proposed		
	FND	HND	LND	FND	HND	LND	FND	HND	LND	FND	HND	LND	FND	HND	LND
1	119	675	1632	92	635	2650	25	866	1892	94	1402	1950	26	2309	2795
2	117	650	1584	91	616	2473	26	905	2056	92	1418	1959	29	2391	2792
3	120	679	1674	70	668	2030	27	885	1600	93	1463	1955	38	2469	2796
4	124	589	1747	91	560	2345	27	893	1756	86	1391	1968	36	2371	2786
5	100	524	2049	66	556	2536	26	857	2249	95	1365	1939	31	2400	2793
Average	116	623.4	1737.2	82	607	2406.8	26.2	881.2	1910.6	92	1407.8	1954.2	32	2388	2792.4

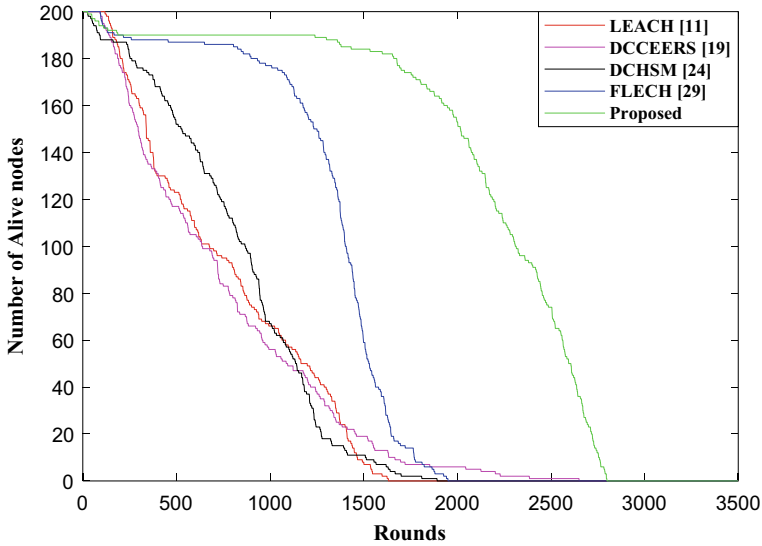


Fig. 5.8 Number of alive sensor nodes for monitoring region of size 200 m × 200 m

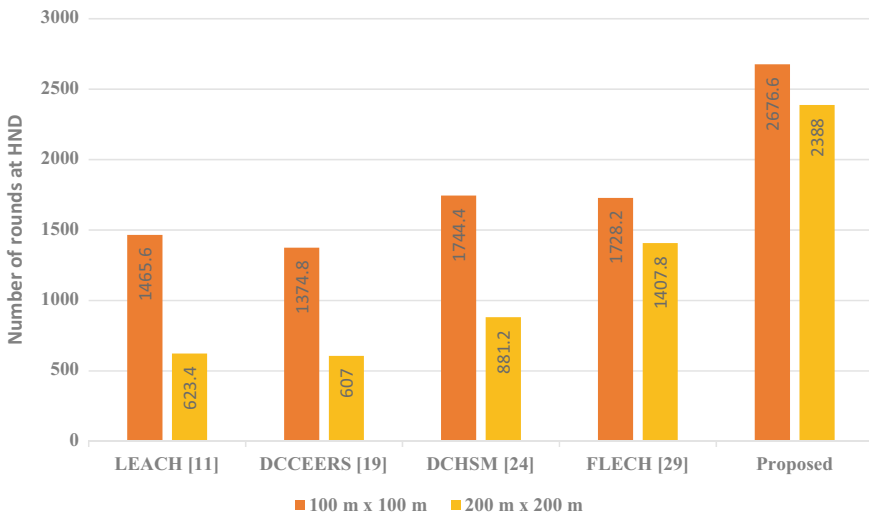


Fig. 5.9 Effect of monitoring region on HND of simulated protocols

is more central to the cluster gets repeated chance to become CHs in the initial few rounds. These nodes deplete their energy very soon ultimately decreasing the FND metric. In later rounds, the network load is distributed evenly based on distance as well as energy parameters. Hence, the HND and LND are attained at higher rounds, prolonging the network lifetime.

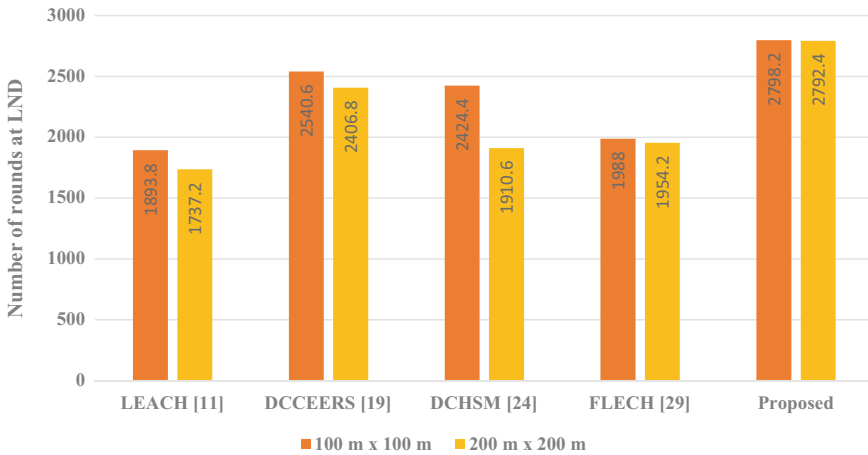


Fig. 5.10 Effect of monitoring region on LND of simulated protocols

5.6 Conclusions

A sustainable WSN clustering protocol is proposed using FCM algorithm and the perception probability. The protocol aims at increasing network lifetime, while increasing coverage area. This paper discussed the basic requirements of the WSN-based IoT system for smart monitoring of the farmlands. In the literature framework, 2D and 3D WSNs are illustrated in detail, focusing the implementation aspects. A modified LEACH is implemented to demonstrate the effect of hierarchical levels in clustering techniques.

The proposed clustering protocol outperforms the existing conventional protocols in terms of energy saving and network lifetime. Due to FCM algorithm, proper clusters are formed with significantly reduced intra-cluster distances. The appropriate selection of CH based on perception probability distributed the network load evenly among the nodes. For monitoring applications in agriculture, a maximum number of nodes are required to be functional till the crop development period. The proposed protocol sustains more than 50% of nodes for long period of time making it suitable for agrarian monitoring systems. The results observed in terms of alive nodes indicate that the proposed protocol is energy efficient and sustainable.

References

1. Stankovic, J.: Research directions for the internet of things. *IEEE Internet Things J.* **1**(1), 3–9 (2014)
2. Tamoghna, O., Sudip, M., Narendra, S.G.: Wireless sensor networks for agriculture: the state of the art in practice and future challenges. *Comput. Electron. Agric.* **118**, 66–84 (2015). <https://doi.org/10.1016/j.compag.2015.08.011>

3. Mohanraj, I., Kirthika, A., Naren, J.: Field monitoring and automation using IoT in agriculture domain. *Procedia Comput. Sci.* **93**, 931–939 (2016). <https://doi.org/10.1016/j.procs.2016.07.275>
4. Stefanos, A.N., Dionisis, K., Dimitrios, D.V., Christos, D.: Energy efficient automated control of irrigation in agriculture by using wireless sensor networks. *Comput. Electron. Agric.* **113**, 154–163 (2015)
5. Awasthi, B., Singh, N.B.: Status of human-wildlife conflict and assessment of crop damage by wild animals in Gaurishankar conservation area, Nepal. *J. Inst. Sci. Technol.* **20**(1), 107–111 (2015)
6. Subramania, A.K., Paramasivam, I.: The impact of wireless sensor network in the field of precision agriculture: a review. *Wireless Personal Communications* (2017)
7. Gubbi, J., Buyya, R., Marusic, S., Palaniswami, M.: Internet of Things (IoT): a vision, architectural elements, and future directions. *Future Gener. Comput. Syst.* **29**(7), 1645–1660 (2013)
8. Kumar, A., Shwe, H., Wong, K., Chong, P.: Location-based routing protocols for wireless sensor networks: a survey. *Wireless Sens. Netw.* **9**, 25–72 (2017). <https://doi.org/10.4236/wsn.2017.91003>
9. Tifenn, R., Abdelmadjid, B., Yacine, C.: Energy efficiency in wireless sensor networks: a top down survey. *Comput. Netw.* **67**, 104–122 (2014)
10. Owojaiye, G., Sun, Y.: Focal design issues affecting the deployment of wireless sensor networks for pipeline monitoring. *Ad Hoc Netw.* **11**(3), 1237–1253 (2013)
11. Heinzelman, W.R., Chandrakasan, A., Balakrishnan, H.: Energy-efficient communication protocol for wireless microsensor networks. In: *Proceedings of the 33rd Hawaii International Conference on System Sciences*, pp. 1–10 (2000)
12. Juan, I., Von, D.: Zigbee based wireless sensor network localization for cattle monitoring in grazing fields. *Comput. Electron. Agric.* **74**(2), 258–264 (2010)
13. Samuel, D., Timothy, S., Jan, D.P., Ellen, V., Philippe, D.S., Marc, V.M.: Evaluating corrections for a horizontal offset between sensor and position data for surveys on land. *Precision Agric.* **17**, 349–364 (2015)
14. Varsha, B., Prasad, K., Vijaykumar, S., Neha, D., Arvind, S.: WSN application for crop protection to divert animal intrusions in the agricultural land. *Comput. Electron. Agric.* **133**, 88–96 (2017)
15. Serrano, J.M., Shahidian, S., Marques, J., Carvalho, M.: Monitoring of soil organic carbon over 10 years in a Mediterranean silvo-pastoral system: potential evaluation for differential management. *Precision Agric.* **17**, 274–295 (2016)
16. Akylidiz, L.F., Pompoli, D., Melodia, T.: Underwater acoustic sensor networks: research challenges. *Ad Hoc Netw.* **3**(3), 257–279 (2005)
17. Akylidiz, L.F., Stuntebeck, E.P.: Underground sensor networks: research challenges. *Ad Hoc Netw.* **4**(6), 669–686 (2006)
18. Parameswaran, V., Zhou, H.: Irrigation control using wireless underground sensor networks. In: *Proceedings of 6th International Conference on Sensing Technology*, pp. 653–659 (2012)
19. Chang, J.Y.: A distributed cluster computing energy-efficient routing scheme for internet of things systems. *Wireless Pers. Commun.* **82**(2), 757–776 (2014)
20. Sherine, M., Abd, E., Basma, M.: Precision farming solution in Egypt using the wireless sensor network technology. *Egyptian Info. J.* **14**, 221–233 (2013)
21. Manjeshwar, A., Agrawal, D.: APTEEN- a hybrid protocol for efficient routing and comprehensive information retrieval in wireless sensor networks. In: *proceeding of 16th International Parallel and Distributed Processing IEEE Symposium* (2002)
22. Rongbiao, Z., Zuowei, R., Jian, S., Wenjing, T., Dongmin, N., Yang, Q.: Method for monitoring the cotton plant vigor based on the WSN technology. *Comput. Electron. Agric.* **133**, 68–79 (2017)
23. Hardware components for crop canopy sensor based Nitrogen management. <http://www.agleader.com>
24. Jia, D., Zhu, H., Zou, S., Hu, P.: Dynamic cluster head selection method for wireless sensor network. *IEEE Sens. J.* **16**(8), 2746–2754 (2016). <https://doi.org/10.1109/JSEN.2015.2512322>

25. Chang, J.Y., Pei, H.J.: An efficient cluster-based power saving scheme for wireless sensor networks. *EURASIP J. Wireless Commun. Netw.* 1–10 (2012)
26. Anjana, G., Sonika, D.: Performance analysis of various fuzzy clustering algorithms: a review. *Seventh Int. Conf. Commun. Comput. Virtualization.* **79**, 100–111 (2016)
27. Hoang, D.C., Kumar, R., Panda, S.K.: Realization of a cluster-based protocol using fuzzy-c-means algorithm for wireless sensor networks. *IET Wireless Sensor Syst.* **3**(3), 163–171 (2013)
28. Logambigai, R., Kannan, A.: Fuzzy logic based unequal clustering for wireless sensor networks. *Wireless Netw.* **22**(3), 945–957 (2016)
29. Baranidharan, B., Santhi, B.: FLECH: fuzzy logic based energy efficient clustering hierarchy for non-uniform wireless sensor networks. *Hindawi Wireless Commun. Mobile Comput.* (2017)

Chapter 6

Genetic Algorithm to Find Most Optimum Growing Technique for Multiple Cropping Using Big Data



Vinamra Das and Sunny Jain

Abstract In the present scenario, it is extremely important for any farmer to increase his farm productivity and using multi-farming techniques; it is one of the most suitable ways to achieve that (Paudel in J Nepal Agricu Res Council 2:37–45, 2016 [1]). Many new farming techniques are being introduced to which a general farmer has no access to and hence his growth rate is monotonous. Even after having the cutting-edge technology and farming techniques, a general farmer has no access to any of it, i.e. the outreach of information technology in farming is still very low. As the number of parameters to optimize farm productivity increases, so thus the permutations of number of techniques and hence expertise is needed to analyse the best farming technique for the given scenario. Given so many existing techniques which vary over even a slight change in parameters, only the experts in farming are adaptable to them and hence it is extremely important to automate the technique generation process so as to put the capability of generating the best farming output to a non-farming expert. From the farmer's point of view, smart farming should provide him with the best crop output in the most sustainable manner. Moreover, multiple cropping over single piece of land has become a necessity to meet the financial requirements and the demand-supply chain in the market. Due to multiple crops being planted on the same piece of land, it makes the technique generation process more ambiguous and time-consuming. To tackle this problem, a big data analysis of farming parameters might prove to be helpful (Wolfert et al. in Agricu Syst 153:69–80, 2014 [2]). Big data analysis helps in exploiting large datasets computationally to observe hidden patterns, trends and outcome of each technique. The combination of using smart farming with the big data for multiple cropping can provide the most well-analysed results and the complex patterns which are not perceivable to humans in providing the most optimum use of farming resources under the given constraints. Using an analysis algorithm over the big-dataset might be able to provide faster and precise

V. Das (✉) · S. Jain
VIT Vellore, Vellore, India
e-mail: vinamra.das2017@vitstudent.ac.in

S. Jain
e-mail: sunny.jain2017@vitstudent.ac.in

techniques over the complex set of quantifiable parameters and widely changing constraints.

Keywords Smart farming · Multiple cropping · Big data

6.1 Introduction

In order to increase the farming output of the land under various constraints and parameters, aim is to utilize the big-dataset provided. Today, there are multiple number of agricultural challenges a farmer has to face including inadequate technology, improper irrigation systems, climatic factors [3]. Various parameters affect the crop productivity like soil type, types of fertilisers used, amount and frequency of water given, dependability of multiple crops over each other when planted on a single land, ambient temperature, amount of moisture, number and type of pesticides which affects all the crops in the most optimum way, duration of sunlight exposure. Another subjective parameter is the effect of past technique used in the present scenario and the effect of present technique for the latter generation must be analysed and a way to quantify is devised. In addition to this, it must be kept in mind that a well-balanced farming structure has to be maintained which means the interdependence of various parameters must be well dealt with. Since, almost all the parameters are interrelated and all of them might affect the growth output in different weights, hence an algorithm is needed which maintains an optimum balance according to the importance of each parameter. For example, the change in amount of water given might result in bigger changes in the crop output than the change in sunlight; hence, in this case, more priority should be given towards optimization of water content in comparison with amount of sunlight.

To implement this structure, genetic algorithm might prove to be helpful as it is an evolutionary algorithm which foresees the effectivity of the proposed technique by extracting data from big-dataset. Since the dataset is going to be very large hence, the time complexity will also be huge to calculate the best offspring. Use of genetic algorithm here ensures minimizing time complexity, since it works on probabilistic approach to find better offsprings faster than usual iterative method as, herein, the selection of gene with better fitness value is higher.

There is an estimate that more than 55% of Indians depend on farming alone [4], out of which majority are residing in rural areas with negligible or no knowledge of scientific approach of farming. For better farming techniques to be provided to every farmer with proper analysis and expertise a huge amount of manpower is needed. For example, various farmer helplines are introduced by the government, but the number of experts is exponentially less than the number of farmers, resulting in delayed response. In addition to that the expert's advice is going to be less informed and less precise as it is humanly impossible to retrieve and analyse big data.

Hence, the use of a big-dataset with the list of action of quantifiable parameters on the crop cultivation and their outputs in a tabulated way can help in analysing the crop

outputs in every possible permutation quite effectively. A method of representing the whole farming technique is applied in a binary string fashion, upon which the genetic algorithm acts based on the constraints specified by the farmer in order to produce the most optimum farming technique for the given multiple crops. As a result, the most optimum technique for cultivation is generated which is completely personalized and caters to the individual constraints of each farmer in form of a binary string of the required parameters, which is delivered to the farmer in normalized language.

Smart farming has become the present need so as to produce the maximum crop outputs, and genetic algorithm has been used in order to predict weather [5], which ensure that the crops are safe from any climatic harsh and also determine the most favourable time to grow them by predicting the weather conditions. Big data has a huge effect on farming techniques. By providing information that can lead to analysis of data revealing such trends which are not possible manually. IoT has made information gathering much more effective and less time-consuming and drones are being used to collect agricultural data efficiently [6]. Another important factor is the land allocation technique while dealing with multiple crops. The division should be done in the most optimal way such that the output of the land as a whole is highest. [7]. Usage of different pesticides and their cross-cutting effects on each other also has to be optimized while dealing with crops. Further, these problems become more complex as the number of crops increases, as each crop has its own pesticide demands and hence might lead to heavy cross-cutting needs. The multiple-cropping problem is important as it has led to better yields and more cost-effective methods in the past, but a thorough study on the past patterns was needed and hence high expertise is needed. The above methods deal with every single aspect of farming individually and have given reasonable results but the final crop output is a cumulative of a number of factors such as soil fertility, exposure to sunlight, amount of water given, types of pesticides used, soil type, fertilizers used so on and so forth. All of these play their weighted roles in the final crop output. A method for tackling this problem of multiple parameters and quantifying them is introducing the use of genetic algorithms [8]. In the literature mentioned here, all the parameters are taken as a single equation with each parameter having its own coefficients resembling the weight of each in the final output. Then, the output function is maximized using genetic algorithm. This method works well for problems with only one crop type, as the data for the function has to be fetched from a database, hence an assumption is made that ample amount of data is present for each of the crops. Thinking further, if the number of crops to be cultivated increases, it is not possible to have the output data of each combination (say there are 30 crops, then the number of crop combinations itself rises to $2^{30}-1$) which is not a feasible number to have a database for. Note that these are just the number of combinations the crops can be chosen, the database further requires data points for each parameter to gain the knowledge as to how each parameter affects the growth which will in turn increase the size of database further. Furthermore, if any of the parameters is constrained in a way (say only a single soil type is present or the amount of water is restricted), then the complexity increases even further to find

the most optimum growing technique. Hence, the solution we propose is to look at the whole growing technique as a bit string and using genetic algorithm to find the technique with the highest fitness value. Advantages are that the output data for all the crops' data is no longer needed as 'mirroring approach' is used to determine the approximate value for fitness of offspring taking in account the fitness value of the parent generations.

6.2 Materials and Methodology

In order to implement the proposed algorithm, a big-dataset consisting of the list of crops, soils used in past, fertilizers used, pesticides sprayed, amount and frequency of water sprayed, time for which sunlight [9] is received throughout the day, amount of moisture, temperature, humidity, previous crop output for that particular crop is maintained. These data values are termed as input values and change over time as more techniques are introduced by the farmer, hence the database evolves over time, becoming vaster and covering a greater number of possibilities. Another set of values is maintained for each technique for that particular crop known as output values, these values determine the validity of the technique and used in fitness function calculation (a quantum for how good the technique is). The 'output values' consist of the number of crops produced, number of crops planted, number of crop units sold in market, time of yield and cost required for the whole technique.

Further, the following computations are done in the given order:

- Take the number of crops to be planted as N from the user.
- Check for any constraints entered by the user, for example, limited water supply, limited sunlight or only a fixed type of soil present.
- Represent the whole farming technique by using a binary string and set the initial standardized set of technique as parent generation.
- The whole binary string is divided into various subparts where each subpart representing a particular parameter and mutation [10] is only allowed between specific bit of string.
- A fitness function is generated for each offspring (represented by a binary string) and the fittest of them is selected and mutated for second generation.
- Note that the part of the binary string which represents the parameter constrained by the user remains the same in every offspring and hence, its status is termed as locked.
- The process of generating new offspring and calculating fitness function for mutation leading to the production of the next generation is repeated until the required fitness value is obtained.
- The binary, hence generated, represents the most suited farming techniques and is converted into normal language for the user.

6.2.1 Input

For input, take the number and name of crops the farmer intends to plant. The main aim here is multi-cropping, so the farmer can grow more than one crop in the land. The division of the land will solely be the choice of the user (Farmer) as the process output will have no concerns with the land distribution decided before the initiation of the process. The constraints also have to be given as input. For example, there might be some rigid resources which cannot be changed by him such as only one type of soil might be present. In such a scenario, parameter remains constant throughout the process.

6.2.2 Representation of Input

Once the valid input is received from the user, retrieval of data takes place from the big-dataset for the corresponding crop. Herein, the whole farming technique is represented as a binary string where “1” represents the presence of any factor and “0” represents the absence of those factors. The whole string is divided into various substrings, each substring quantifying that parameter in terms of 0’s and 1’s in their own way.

For example, (Fig. 6.1).

6.2.3 Representation of Each Factor

Soil type: The list of soils is taken in a particular order for each crop and 0 represents the absence of that soil for the cropping technique and 1 represents the presence of that soil for that technique. It can have multiple 1’s in its string representing that more than one type of soil can be used.

Fertilizers user: In this case, we list the standardized fertilizers used for the production of the listed crops, and here also, 1 represents the presence of that fertilizer and 0 the absence. Same goes with the types and number of pesticides used [11]. Here also, multiple 1’s can be used as different fertilizers can be used for different crops.

Fig. 6.1 Sample representation of farming technique as a bit string

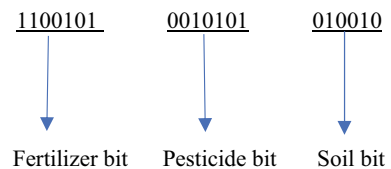


Table 6.1 Table representing bit position and the temperature range it shows

Position bit	Temperature bit
1st	5–10
2nd	10–15
3rd	15–20
4th	20–25
5th	25–30
6th	30–35

Note

1. In the temperature and the water string and the Seasonal Growth bit only one bit can be 1 as the presence of one condition surely means the absence of others
2. Each factor represents the substring involved for the given input. The Boolean value in these substrings may represent the range of the factor or just their presence

Temperature and water used: These kinds of factors deal with ranges and the position of each bit also holds significance apart from its value (0 or 1), here also 1 represents the presence of that temperature range and 0 the absence. We quantify the temperature required for the given crops in temperature range as follows (Table 6.1).

6.3 Genetic Algorithm General Overview

General Overview of algorithm: Genetic algorithm is a brute force hit and trial algorithm but with a probability roulette spinning method which increases the chances of acceptance of the cases which might lead towards the result. This reduces time complexity to a much larger extent [12].

Parent Generation selection: Initially, the parent generation is selected as the binary bit string which represents the already existing or previously tried farming technique of each crop which the farmer intends to plant. If he wants to plant a total of 4 crops on his land ($N = 4$) and let our big-dataset contains a total of five already tried techniques for each of the crops, then a total of 20 parent generations (represented in the form of binary strings) are taken. Note that each single bit is termed as chromosome in genetic algorithm terminology [13].

Fitness function calculation: Fitness function is basically the quantum of how to fit our offspring or already existing parent generation is. In this case, fitness function represents how good or effective the farming technique has been for that crop or the combination of crops. We use a probability-based approach for the selection of parents for mutation. Which means the more fit generation has more chances of being selected for mutation to produce future offsprings.

Next-generation production: The production of next generation of binary strings is generally done by dividing the string into two parts and follows a criss-cross

exchange operation between the chromosomes (bits). For example: 110011 and 011110, when mutated in the criss-cross manner will produce the offspring as follows:

Mutation 1: 110 011

The first three bits are taken from the first substring, and the last three bits are taken from the second substrings

Mutation 2: 011 110

The first three bits are taken from the second substring, and the last three bits are taken from the first substrings.

Evolution: On mutation, the offsprings having most high fitness function have the maximum probability of getting selected, the future generation produced generally have the higher fitness value, and if not, they are rejected by the algorithm as their probability of getting selected gets lower. This means that as we proceed further (as the algorithm increases number of iterations) so thus increases the fitness values of the offsprings; hence, selection of the fitter generations takes place.

Repetition: The process of mutation, fitness function calculation and next-generation production takes place until the desired fitness value of any one of the offsprings obtained, and that gene in the generation is our desired output. Then, we find the curve of best fit to find the additional number of iterations in order to find loop termination limit (Fig. 6.2).

Algorithm

```

Initialize n fitness factors as F[1], F[2].....F[n]
/*fitness values of n genes*/

for (i=1; i<n;i++)
{
sum=sum+f[i]
}
for (j=1; j<n;j++)
{
P[j]=f[j]/sum; /*P[j] stores the probability of selection
of F[j] gene*/
}
Initialize range [k]
/*defining the range of random() number generator for which
F[k] will be selected */
for (i=2;i<n;i++)
{
range [i] =P[i-1] to P[i]
}
for (k=1; k<number; k++)
/*k stores the number of genes to be selected for mutation */
{
r=random()
if (r=range[k])
select k
}

```

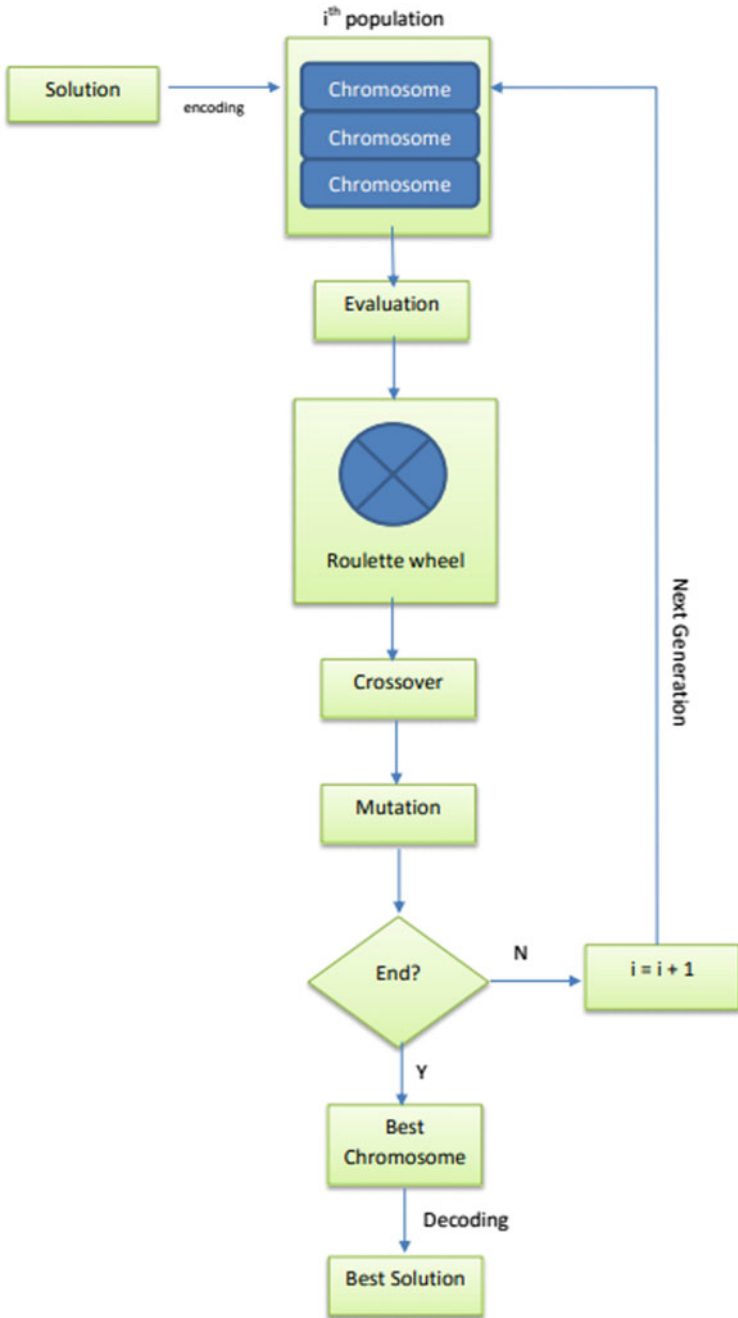


Fig. 6.2 Flowchart of genetic algorithm

6.4 Calculation of Fitness Function

Calculation of fitness function in genetic algorithm varies from case to case. In general, it represents how close the fitness value of produced generation is close to the desired fitness values. In certain cases, the final value of the fitness function is absolute and known to the user in advance (generally its value being 1), this case arises when we are dealing with more mathematically quantifiable problems like finding solution to a multi-variable equation, determining the coefficients of curve of best fit and so on. But in many other cases, majorly where a research output has to be generated, the programmer lacks the knowledge of final of apex fitness value. Same goes with this case as a definite value of fitness function is not known prior to the system; hence, it lacks the knowledge as to when to stop the mutation-fitness function generation loop. In order to limit the number of iterations, the following steps are taken:

Consider three parent generations already existing, the initial fitness value of the three parent generations are:

$$F_1 = 0.60 \text{ (first gene)}$$

$$F_2 = 0.75 \text{ (second gene)}$$

$$F_3 = 0.45 \text{ (third gene)}$$

The highest among the three is taken as the highest fitness value (HFV).

Here, HFV = 0.75

Here, the loop is continued until the point that the maximum value of fitness function of each generation (max) exceeds the HFV (that is 0.75 in this case). For predicting the additional numbers of iterations from that point on, a number of increasing curve fitting models are applied for the number of generation (x value) versus maximum fitness values for that generation (y value).

Note: Only ever-increasing curve fitting models are applied as the maximum fitness value is expected to increase and hence over-fitting of curve is avoided. Quadratic or any higher order polynomial might give a better fit, but there is a chance that while equating it to 1 (to find the number of iterations), the roots might be negative, since quadratic functions are not always increasing.

Regression models [14] applied are:

- Linear Function $(y = ax + b)$
- Exponential Function $(y = ab^x)$
- Logarithmic Function $(y = a + b \ln(x))$
- Power Function $(y = ax^b)$

Whichever of the above four models shows the highest correlation value, that model will be the most suitable for deciding the number of iterations, which is computed by substituting the y value as 1. Here, Y value is taken as 1 because it is the highest theoretical value any fitness function can obtain (Table 6.2; Figs. 6.3, 6.4, 6.5 and 6.6).

Table 6.2 Table showing sample fitness function values versus generation number

x_1	y_1
1	0.62
2	0.63
3	0.65
4	0.69
5	0.68
6	0.68
7	0.70
8	0.72
9	0.73
10	0.75

A dummy dataset for number of iteration (x -axis) versus maximum fitness value for that generation (y -axis) is plotted, showing a loose trend of increasing values

Various regression models are plotted to provide an approximate value for number of generation when fitness value reaches its theoretical maximum value of '1'

Fig. 6.3 Exponential model curve for the data in Table 6.2

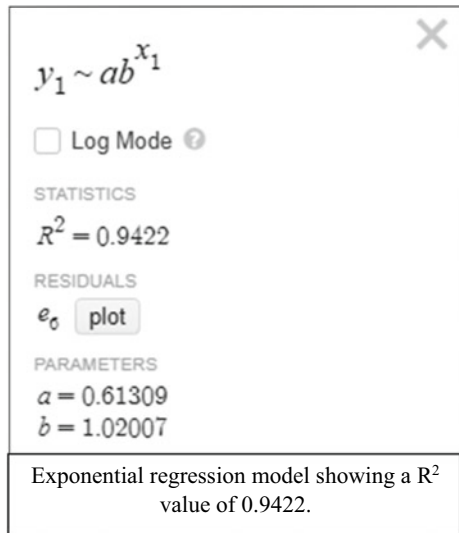


Fig. 6.4 Logarithmic model curve for data in Table 6.2

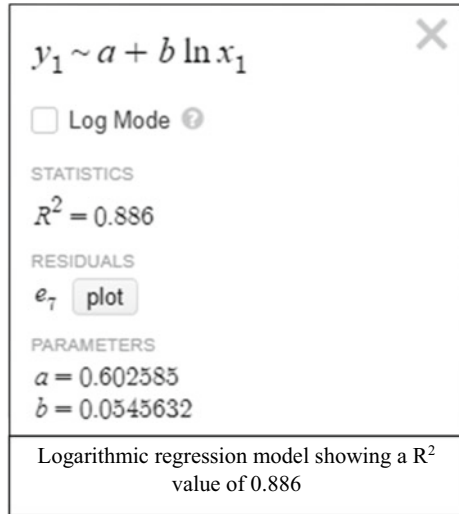
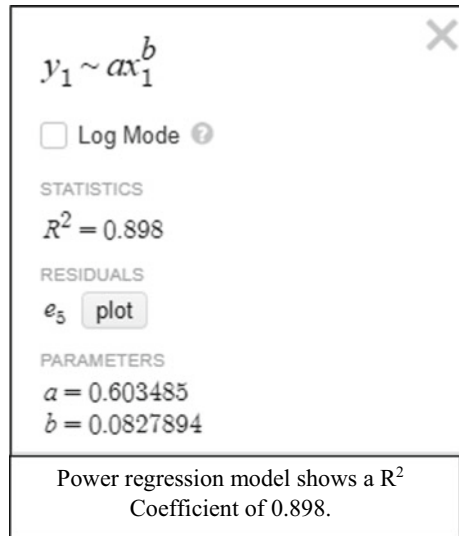


Fig. 6.5 Power model curve for data in Table 6.2



Since the maximum coefficient of correlation is shown by the linear model here, in this case (0.9422), hence its graph is plotted for number of iterations versus maximum fitness value gene generated (Fig. 6.7).

It is seen that the x value becomes 1 for $y = 28.6$; hence, a total of 29 iterations more will be done once the fitness value reaches HFV (0.75 in this case).

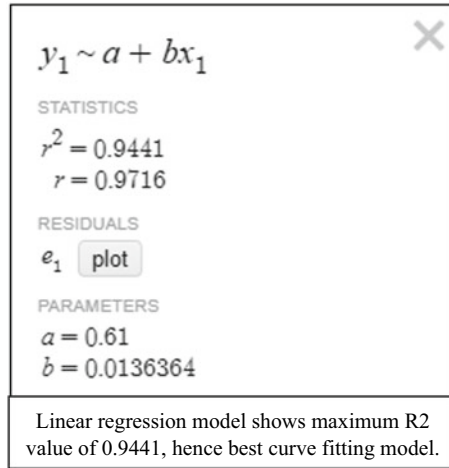


Fig. 6.6 Linear model curve for data in Table 6.2

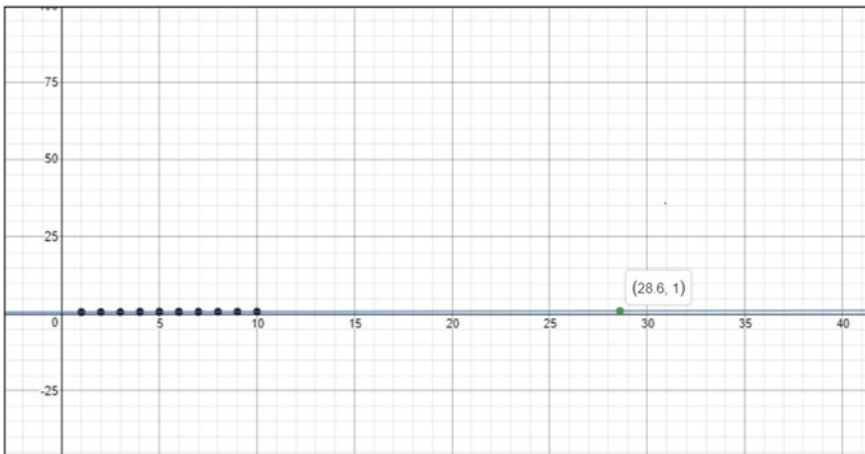


Fig. 6.7 Representation of Linear curve fitted on the graph, with x value = 1 for y value = 29

6.5 Quantifying the Value of Fitness Function

The binary string here represents the whole farming technique, and hence the fitness function value depends upon various parameters like amount of sunlight, water content provided, fertilizers used, pesticides used and so on, but these are input factors and not available in database. Hence, output parameters are used to quantify the fitness value (data retrieved from big-dataset).

Overcoming interdependence of internal factors is a major problem faced. Since agricultural growth and farming outputs are dependent on a number of external

factors and these factors do not affect the output independently but can also affect each other in various combinations (interdependence of factors on each other). In order to overcome such intermingling effects of factors over each other, only the final output of growth is taken into account while fitness value calculation. This helps as whatever interdependence the factors might have on each other it is directly reflected in the output parameters like crop output and growth.

For example: One fertilizer might have a positive effect on that crop independently, and another type of pesticide can also have a positive effect when used independently, but when the fertilizer and pesticide combinations are used it might lead to a degrading effect over the crop production as a whole due to chemical action of the two over each other. Hence while calculating the fitness function to tackle this problem, instead of analysing the effect of both over each other, only the crop output versus crop input ratio is taken into consideration, which in itself reflects the overall effect of the two factors over the process. If 1000 seedlings are planted and only 200 grow fully due to the two clashing factors, the fitness value corresponding to the above parameter itself becomes 0.2 (200/1000).

6.5.1 Components for Calculation of Fitness Value (FV)

Crop output versus Crop Input (F_1): In order to quantify the affectivity of farming process as a whole, this factor ensures a consistent and overall healthy crop quality. If “a” seedling is planted and “b” is able to fully grow for harvesting process, then a/b is the F_1 value.

Sold in market versus sent to market (F_2): This factor provides a feasibly computable way of determining the score which directly maps to the crop quality without getting into the details of crop farming. Only the crop output is not the quantum to declare a farming process as overall effective as it might be a possibility that a high number of seedlings do get harvested but only a few of them are able to match the threshold quality. Hence, taking the crops sold in market versus sent to market gives us a number signifying the health of the harvested crops produced.

Standard time for yield versus time taken for actual yield (F_3): Of all the crops taken into account for calculation, one crop must be taking the minimum amount of time to grow fully and its value is taken as ‘ T_1 ’. The current generation take a time of harvesting say T_2 ($T_2 > T_1$), hence T_1/T_2 ratio assures that the farming technique gives effective results in a plausible amount of time. As the value of T_2 (time taken for crop generation) increases, the T_1/T_2 factor decreases, signifying that more the amount of time taken, lesser is the F_3 value.

Minimum cost for one crop/cost required (F_4): From the farmer’s point of view, not only getting the best crop output in the most practical amount of time is important, but so is the overall capital he has to invest for that process. More the capital required, lesser will be the F_4 value.

Self-learning factor (F_5): From the point of view of the whole farming process, it also matters that how is that technique going to affect the land or other farm-

ing resources which might be used in future for some other crops. [15] Hence, the self-learning factor is added which is the fitness value (FV) of the past generation mentioned in that database, hence as time passes and number of times the algorithm is implemented, this factor changes as it is in a recursive relation with the fitness value of the past generation.

Note that self-learning factor is customized for each farmer as each farmer has his own set of land and other farming resources, and self-learning factor remains constant throughout the one whole technique production, and changes for every farmer as he uses the algorithm, moreover, the span of time. It basically takes in consideration of to what has been done to the land earlier and what will be its aftermath.

Hence, F_5 gets better with each phase.

$$\text{Average} = (F_1 + F_2 + F_3 + F_4 + F_5)/5 \tag{6.1}$$

$$\text{Consistency factor} = 1 - \left(\sum_{i=1}^n (\text{Average} - F_i) \right) / n, \text{ For every } F_i, \text{ less than average,} \tag{6.2}$$

n is the number of factors having value less than the arithmetic mean

$$\text{Fitness value} = \text{Consistency factor} * \text{Average} \tag{6.3}$$

The consistency factor ensures that the fitness value (FV) is not a sheer average of all the values as it is a possibility that a considerably high value of one factor might compensate the lower value of another, hence giving a decent average but the overall farming technique might not be up to mark.

For example: For two factors, consider $F_1 = 0.4$ and $F_2 = 0.9$. Its average is $0.65 [(0.4 + 0.9)/2]$, but the two values are not consistent hence compromising with the overall fitness quality of the technique. For this case:

$$\text{Consistency factor} = 1 - (0.65 - 0.4)/1 = 0.75.$$

$$\text{Fitness value} = 0.75 * 0.65 = 0.4875.$$

For a second case take $F_1 = 0.6$ and $F_2 = 0.7$, here also average = $0.65 [(0.4 + 0.9)/2]$.

$$\text{But, consistency factor} = 1 - (0.65 - 0.6)/1 = 0.95.$$

$$\text{Fitness value} = 0.95 * 0.65 = 0.6175.$$

It is seen that as the data becomes more and more consistent the value of consistency factor increases and it, when multiplied with average, ensures a higher average value in addition with the consistency of values.

Note: In order to maintain a minimum level of fitness of each of the factors (F_1, F_2, F_3, F_4, F_5), if any generation with any of the values less than a threshold value (0.2) is encountered, that whole generation is rejected no matter, however, high the overall average might be, as such a low value of any factor renders the whole farming technique ineffective.

Algorithm:

```

Initialize F1, F2, F3, F4, F5
/* 5 factors cumulating to fitness value */

Initialize count=0
average= (F1+F2+F3+F4+F5)/5;
X=Average
for (i=1; i<5; i++)
{
if (fi<average)
{
x=x-fi
count=count+1;
}
}
consistency_factor=1-X/count;
fitness_value=consistency_factor*average;

```

6.5.2 Mirroring Approach

To find the fitness value of the upcoming generations, since there are no resources in database to calculate the F_1, F_2, F_3, F_4, F_5 values for every possible combination, hence a mirroring approach is applied for finding the FV of that gene. Let the gene G come from mutation of G_1 and G_2 with fitness values FV_1 and FV_2 . In order to calculate the fitness factor of G (let FV), a mirror approach is applied by analysing the amount of resemblance it shows to its parent. More the amount of resemblance towards a fitter parent gene, more will be the FV value. For example: if the parent generation have bit strings as 100101 (fitness value FV_1) and 100111 (fitness value FV_2), and let the child offspring's string be 111011, then compare each bit which resembles the parent one, which gives a resemblance factor of $2/6$ (2 bits at the same position as the parent gene) for the first one and $3/6$ (3 bits at the same position as the parent gene) for the second one, hence its fitness index becomes $((FV_1 \times 2/6) + (FV_2 \times 3/6))$. The remaining bits which represent none of the parent genes (loss due to criss-cross mutation), the average of FV_1 and FV_2 is taken. In this case, the remaining $(1/6)$ th portion is taken as $((FV_1 + FV_2)/2) \times (1/6)$.

6.5.3 Mutation

Once the fitness value is calculated for every gene in the given generation, mutation of the fitter genes has to be done with higher probability. In order to ensure that the following method is undertaken:

Let the present generation genes have fitness values as $FV_1 = 0.4, FV_2 = 0.6, FV_3 = 0.75, FV_4 = 0.65$.

From the above case, the probability of selection of FV_3 should be the highest as it is the gene with highest fitness value (0.75), and probability of picking FV_1 should be the lowest (fitness value = 0.4). Hence, a fitness function summation (FFS) is computed and probability of selection of each gene:

$$\begin{aligned} & \text{Probability of selection of a gene for mutation} \\ & = (\text{fitness value})/(\text{fitness function summation}) \end{aligned} \quad (6.4)$$

Let it be termed as the P function.

Then,

$$P(FV_1) = 0.40/(0.4 + 0.6 + 0.75 + 0.65) = 0.17.$$

$$P(FV_2) = 0.60/(0.4 + 0.6 + 0.75 + 0.65) = 0.25.$$

$$P(FV_3) = 0.75/(0.4 + 0.6 + 0.75 + 0.65) = 0.31.$$

$$P(FV_4) = 0.65/(0.4 + 0.6 + 0.75 + 0.65) = 0.27.$$

In order to facilitate such a selection which is directly proportional to the above-given probabilities, a random number generator is used which produces a totally random value ranging from 0 to 1.

If the value lies in 0–0.17: FV_1 gene is selected for mutation.

If value lies in 0.17–0.42 (0.17 + 0.25): FV_2 is selected for mutation.

If value lies in 0.42–0.73 (0.42 + 0.31): FV_3 is selected for mutation.

If value lies in 0.73–1.00 (0.73 + 0.27): FV_4 is selected for mutation.

The random number generator is executed for a limited number of times (equal to the number of parent genes needed for mutation) and the parent gene hence selected is mutated pairwise.

6.5.4 Evolution

In order to facilitate the generation of better offsprings, the above processes of parent generation, fitness value calculation and mutation is repeated until the desired output is reached. The final string hence produced represents the best possible technique for the crop production under the given requirements.

6.6 Conclusion

With the increase in parameters governing crop outputs and the simultaneous increase in the number of crops has made the selection procedure ambiguous even for the trained professionals in the farming sector without computational aid. Having a big database proves to be helpful over having manual expertise. The genetic algorithm

solution proposed provides a way to analyse the big data to produce the most optimum farming technique under the given constraints, with less time complexity. The automation of ‘farming technique generation process’ has the potential to give a large number of farmers (currently lacking technical support) the ability to get the best of agricultural practices with much less hassle, like approaching for manual help. Representing the presence or absence of factors as bits and mirroring approach for calculation of fitness factor covers a wide range of crop permutations. Hence, using this technology in future and aiming to make it available in hands of as much farmers as possible will give them the ability to get the most optimized production techniques under the given set of constraints most optimally. Another direction for future research includes introduction of smarter and faster IoT-based devices which if used in unison with our proposed method [16], will be capable to remove human intervention to a much larger extent.

The drawbacks include the cross-cutting negative effects that might arise from fusion of multiple parameters such as a pesticide and a fertilizer might work well individually for crop production, but when used together give rise to negative effects on the crop. Keeping this in mind, future scope of this work indicates towards addition of computational chemistry tools to better identify their outcomes on the crop output.

References

1. Paudel, M.: Multiple cropping for raising productivity and farm income of small farmers. *J. Nepal Agric. Res. Council* **2**, 37–45 (2016). <https://doi.org/10.3126/jnarc.v2i0.16120>
2. Wolfert, S., Ge, L., Verdouw, C., Bogaardt, M.J.: Big data in smart farming—a review. *Agric. Syst.* **153**, 69–80 (2017)
3. Dwivedy, N.: Challenges faced by the agriculture sector in developing countries with special reference to India. *Int. J. Rural Stud.* **18**(2) (2011)
4. More than 55% of Indians make a living from farming. Here’s how we can double their income. (2018). Retrieved from <https://www.weforum.org/agenda/2017/10/more-than-55-of-indians-make-a-living-from-farming-heres-how-we-can-double-their-income/>
5. Gumaste, S.S., Kadam, A.J.: Future weather prediction using genetic algorithm and FFT for smart farming. In: *Computing Communication Control and automation (ICCUBEA), 2016 International Conference on IEEE* pp. 1–6 (2016). <https://doi.org/10.1109/iccubea.2016.7860028>
6. Prathibha, S.R., Hongal, A., Jyothi, M.P.: IOT based monitoring system in smart agriculture. In: *Recent Advances in Electronics and Communication Technology (ICRAECT), 2017 International Conference on IEEE*, pp. 81–84 (2017). <https://doi.org/10.1109/icraect.2017.52>
7. Ruoff, E.: Optimizing Crop Land Allocation for Smallholder Farmers in Central Uganda (2017)
8. Olakulehin, O.J., Omidiora, E.O.: A genetic algorithm approach to maximize crop yields and sustain soil fertility. *Net J. Agric. Sci.* **2**(3), 94–103 (2014)
9. Palmer, A.H.: The agricultural significance of sunshine as illustrated in California. *Mon. Weather Rev.* **48**(3), 151–154 (1920). [https://doi.org/10.1175/1520-0493\(1920\)48%3c151:tasosa%3e2.0.co;2](https://doi.org/10.1175/1520-0493(1920)48%3c151:tasosa%3e2.0.co;2)
10. Soni, N., Kumar, T.: Study of various mutation operators in genetic algorithms. *Int. J. Comput. Sci. Inf. Technol.* **5**(3), 4519–4521 (2014)
11. Aktar, W., Sengupta, D., Chowdhury, A.: Impact of pesticides use in agriculture: their benefits and hazards. *Interdisc. Toxicol.* **2**(1), 1–12 (2009)

12. Hermawanto, D.: Genetic algorithm for solving simple mathematical equality problem (2013). arXiv preprint [arXiv:1308.4675](https://arxiv.org/abs/1308.4675)
13. Carr, J.: An introduction to genetic algorithms. Senior Project **1**(40), 7 (2014)
14. Walpole, R.E.: Probability & Statistics for Engineers & Scientists, 9th edn, Prentice Hall (2012)
15. Moula, M.S., Hossain, M.S., Farazi, M.M., Ali, M.H., Mamun, M.A.A.: Effects of consecutive two years tobacco cultivation on soil fertility status at Bheramara Upazilla in Kushtia District. J. Rice Res **6**(1), 190 (2018). <https://doi.org/10.4172/2375-4338.1000190>
16. Jayaraman, P.P., Yavari, A., Georgakopoulos, D., Morshed, A., Zaslavsky, A.: Internet of things platform for smart farming: experiences and lessons learnt. Sensors **16**(11), 1884 (2016)

Chapter 7

A Study on Strength Properties and Cost Analysis of Industrial Byproduct-Based Ternary Blended Geopolymer Concrete



Kuunreddy Srinivas Reddy  and S. Bala Murugan 

Abstract Flyash, ground granulated blast-furnace slag (GGBFS) and Alccofine are industrial byproduct materials and require large area of land for the safe disposal. These byproducts which are rich in alumina and silica can be value added, by using as binder in geopolymer concrete. The industrial byproducts are activated by NaOH- or KOH-based alkaline solution. Effective utilization of industrial byproducts in the construction industry will reduce the impact on the environment, which is caused due to ordinary portland cement (OPC). Previous studies on geopolymer concrete are at high molarity of NaOH and curing adopted is hot air oven curing for the effective polymerization of binder material and the alkaline activator solution (AAS). The present study is aimed to understand the effect of Alccofine as a ternary binder in geopolymer concrete at low molarities of NaOH-based alkaline solution under ambient temperature curing. Flyash, GGBFS, and Alccofine are the binder materials considered in geopolymer concrete by complete replacement of OPC. The ratio of Na_2SiO_3 to NaOH is fixed at 2.5 for all the geopolymer concrete mixes. Msand is used as fine aggregate by replacing with river sand in geopolymer concrete. The study also focused on comparing the compressive strength, split tensile strength, flexural strength, and cost analysis of ternary blended geopolymer concrete with conventional concrete of M30 grade. It is observed from the results that the geopolymer concrete has attained better strength properties than OPC concrete at the lesser cost and the impact on environment is reduced.

Keywords Flyash · GGBFS · Alccofine · Msand · Alkaline solution · Geopolymer concrete

K. Srinivas Reddy (✉) · S. Bala Murugan
Department of Structural and Geotechnical Engineering, School of Civil Engineering, Vellore Institute of Technology, Vellore, Tamilnadu 632014, India
e-mail: kuunreddy.srinivas@vit.ac.in

S. Bala Murugan
e-mail: balamurugan.s@vit.ac.in

© Springer Nature Singapore Pte Ltd. 2020
B. Subramanian et al. (eds.), *Emerging Technologies for Agriculture and Environment*, Lecture Notes on Multidisciplinary Industrial Engineering, https://doi.org/10.1007/978-981-13-7968-0_7

7.1 Introduction

Production of ordinary portland cement (OPC) is energy intensive, and large amount of CO₂ gases are released into the atmosphere, which is the primary source of global warming [1–3]. The available natural resources (limestone) are consumed at faster rate due to increase in production of OPC. By replacing the conventional concrete with geopolymer concrete, the CO₂ emissions are reduced and the impact on the environment is reduced and the available natural resources are protected for the future generation without compromising the present need (sustainability) [4]. The geopolymer concrete is manufactured by utilizing the byproduct materials generated from the thermal power plant, iron and steel industries. The industrial byproduct materials which are rich in silica and alumina are used as primary source of binder in geopolymer concrete [5]. Industrial solid byproduct materials such as flyash, GGBFS, bottom ash, copper slag, palm oil fuel ash, and Alccofine are activated by sodium/potassium-based alkaline solution to form the geopolymer concrete which is a “green concrete” [6–8]. It is identified the following factors are affecting the compressive strength of geopolymer concrete: source type and percentage of binder materials, molarity of the NaOH, and ratio of the Na₂SiO₃/NaOH and method of curing adopted [9]. Geopolymer concrete has better mechanical and durability properties than OPC concrete [10]. Different trial mixes are done to identify the M30 grade of geopolymer concrete by varying the proportions of constituent’s materials of geopolymer concrete. The compressive strength, split tensile strength, and flexural strength of ternary blended geopolymer concrete with different percentages of Alccofine, and the effect of compressive strength on low molarities of NaOH was studied. The study also compared the cost analysis of geopolymer concrete for M30 grade with OPC concrete of similar grade. In the present study due to the shortage of good quality Natural River sand, msand is used as fine aggregates.

7.2 Materials

7.2.1 Flyash

Low-calcium class F flyash is produced by burning bituminous coal (IS: 3812-2003) [11]. Flyash is obtained from Kakatiya Thermal Power Plant, Telangana. Elemental compositions of the flyash obtained from the EDAX are shown in Table 7.1, and Fig. 7.1 shows the SEM and EDAX analysis of flyash. From the SEM analysis, the particle shape of the flyash particles is spherical, which helps in improving the workability of the geopolymer concrete.

Table 7.1 Weight percentage of elements present in the binder materials

Element	C	O	Al	Si	Ca	Mg	Br
Flyash	59.19	31.99	2.75	6.07	–	–	–
GGBFS	38.52	36.19	3.84	8.36	13.09	–	–
Alccofine	45.69	35.26	4.01	6.38	8.66	–	–

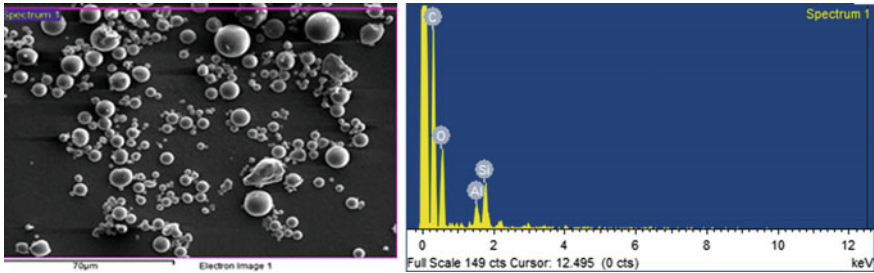


Fig. 7.1 Images of SEM and EDAX of flyash

7.2.2 Ground Granulated Blast-Furnace Slag (GGBFS)

Ground granulated blast furnace was purchased from the local distributor in Chennai. Ground granulated blast-furnace slag is the byproduct obtained from steel manufacturing industry. The elemental composition of GGBFS obtained from EDAX is presented in Table 7.1. From the SEM analysis, the shape of the GGBFS particle is angular. Figure 7.2 shows the SEM and EDAX of GGBFS.

7.2.3 Alccofine 1203 (ASTM C 989-1989)

Alccofine the industrial byproduct is obtained from Counto Microfine products Pvt. Ltd. Elemental composition of the Alccofine is provided in Table 7.1. From the SEM

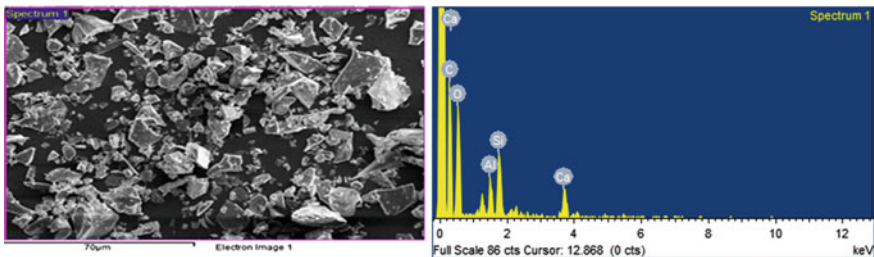


Fig. 7.2 Images of SEM and EDAX of GGBFS

particle, the shape of the Alccofine is angular. Figure 7.3 shows the SEM and EDAX of the Alccofine. The ultra-fine material helps in filling the pores in the concrete. This Alccofine 1203 helps increase in particle packing and reduces the pores in the concrete. Alccofine 1203 improves the workability of the concrete.

7.2.4 Aggregates

Due to the shortage of good quality of natural river sand, it is replaced 100% by msand as fine aggregates. Mining of river sand in India is banned due to the deepening of the water table, erosion of river banks, diversion of natural river flow, and widening of the stream mouths [12]. Msand is collected from the granite quarry site in Vellore, Tamilnadu. Sieve analysis for the msand was conducted, and msand falls under the zone II [13]. Figure 7.4 shows the sieve analysis graph of msand. The fineness modulus of msand is 3.2. The size of the coarse aggregates used is retained on 12.5 mm and passing through 20 mm.

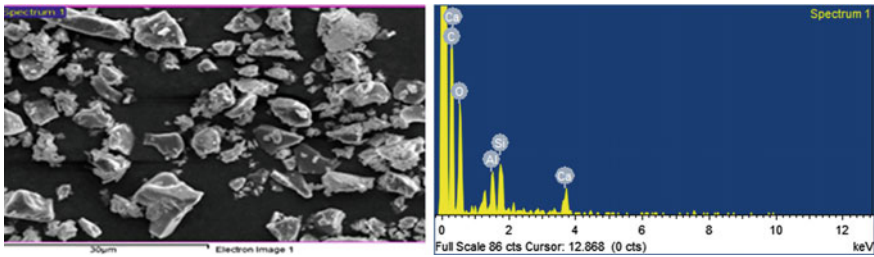


Fig. 7.3 Images of SEM and EDAX of Alccofine

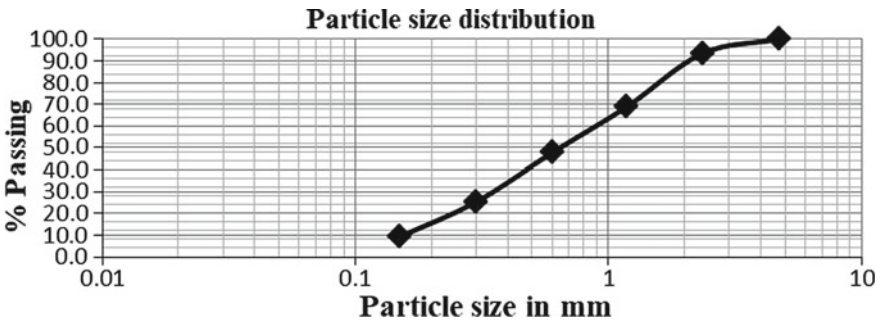


Fig. 7.4 Sieve analysis of msand

7.2.5 Alkaline Solution

Alkaline solution acts as a hardening agent in the geopolymer concrete. The combination of sodium hydroxide and sodium silicate is alkaline solution. Sodium silicate and sodium hydroxide are purchased at Vellore. In the present study, the ratio of sodium silicate to sodium hydroxide is fixed to 2.5 and sodium hydroxide molarities is varied from 0.5, 1, 2, and 3 for all the replacement percentages of flyash with Alccofine, i.e., 5, 10, and 15%. Sodium hydroxide is 99% pure without impurities. The mass ratio of sodium to silicate in sodium silicate is 1:2.23.

7.2.6 Superplasticizer (ASTM C494-2017)

Naphthalene-based superplasticizer is used in the study to improve the workability of the geopolymer concrete. In the present study, 1.5% of binder is used as the superplasticizer content in all the mixes.

7.3 Experimental Work

7.3.1 Manufacturing and Casting of Ternary Blended Geopolymer Concrete

Mix design of geopolymer is trial and error method, mix design is continued until we attain the required strength and workability parameters, and the mix design should be economical when compared to similar grade of OPC concrete. Previous studies on the geopolymer concrete mix design depend on the fineness of binder material [14, 15], molarity of NaOH, ratio of $\text{Na}_2\text{SiO}_3/\text{NaOH}$ ratio [16], water to binder ratio [17], alkaline to binder ratio, and the method adopted for curing [18]. In the present study, mix design of ternary blended geopolymer concrete was done according to the Lloyd and Rangan [19]. The following factors are considered in the mix design of geopolymer concrete, alkaline to binder 0.4, water to binder 0.15, and Na_2SiO_3 to NaOH 2.5, and the alkaline solution should be prepared at least 24 h before mixing in the concrete. Different molarities of NaOH are 0.5, 1, 2, and 3 in all the replacement levels of flyash with Alccofine, i.e., 5, 10, and 15%.

Manufacturing of geopolymer concrete is similar to that of OPC concrete. Collect all the dry material in required quantities. Control mix of M30 grade and 12 geopolymer concrete mixes are casted, and details of the mix proportions are given in Table 7.2. Mix all the dry materials for 4 min until it attains uniform distribution of aggregates and add the liquid components to the mixture, and mix is continued for another 4 min until the mix has become homogeneous. Place the concrete in the cube mold of $100 \times 100 \times 100$ mm in three different layers, and place the cube

molds on vibration table for 20–40 seconds to expel air from the concrete. After 24 h of casting demold, the cubes and place the cubes in room temperature till the age of testing, i.e., 7 and 28 days [20]. The rate of loading applied is 2.5 MPa.

7.4 Results and Discussion

7.4.1 Compressive Strength

The quality of concrete is based on the compressive strength. Compressive strength is determined according to the IS codes 516 [20]. Compressive strength results are shown in Fig. 7.5. The compressive strength is the average strength of three cubes. The mixes with 3 molarity NaOH have obtained higher compressive strength at all the 5, 10, and 15% replacement of flyash with Alccofine due to effective leaching of Si and Al to form a hardened geopolymer concrete. The mix 12 with 35% flyash, 50% GGBFS, and 15% Alccofine at 3 molarity NaOH has effective dissolution of Si and Al in the alkaline solution, high calcium content, and high particle packing on comparing with other geopolymer concrete mixes, resulted in highest compressive strength of 62 MPa at 28 days. The similar findings were observed by Jariwala et al. [21–23]. The mix 1 with 45% flyash, 50% GGBFS, and 5% Alccofine at 0.5 molarity NaOH has obtained the lowest compressive strength of 26.1 MPa at 28 days due to the leaching of Si, and Al is less in the alkaline solution and low calcium content in the mix. Calcium content improves the strength of geopolymer concrete. Geopolymer concrete mixes have attained its 95% of compressive strength in 7 days compared with OPC concrete. The mix 7 with 40% flyash, 50% GGBFS, and 10% Alccofine at 2 molar NaOH has attained a compressive strength of 40.2 MPa which is similar to the target strength of M30 OPC concrete.

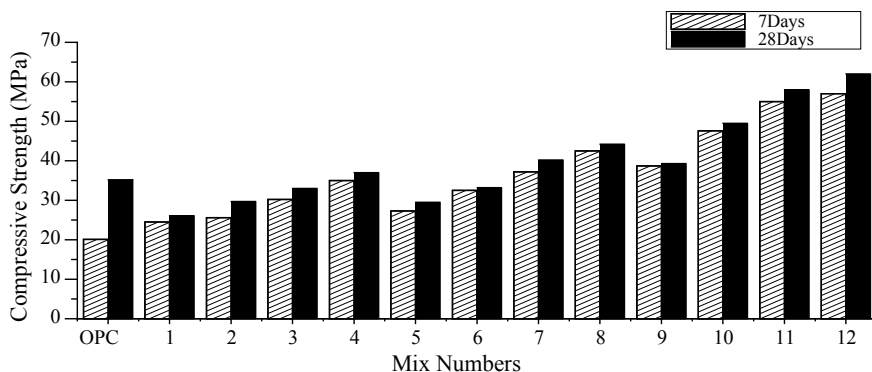


Fig. 7.5 Details of compressive strength

Table 7.2 Details of mix proportions in kg/m³

Mix Id	Flyash/cement	GG BFS	Alcofine	C.A	F.A	Molarity of NaOH	NaOH solution	Na ₂ SiO ₃ solution	Alkaline solution	Water	SP
OPC	350.22	-	-	1213.5	698.16	-	-	-	-	157.6	5.25
1	177.3 (45)	197 (50)	19.7 (5)	1108	739	0.5	45.07	112.12	157.19	59	5.9
2	177.3 (45)	197 (50)	19.7 (5)	1108	739	1	45.07	112.12	157.19	59	5.9
3	177.3 (45)	197 (50)	19.7 (5)	1108	739	2	45.07	112.12	157.19	59	5.9
4	177.3 (45)	197 (50)	19.7 (5)	1108	739	3	45.07	112.12	157.19	59	5.9
5	157.6 (40)	197 (50)	39.4 (10)	1108	739	0.5	45.07	112.12	157.19	59	5.9
6	157.6 (40)	197 (50)	39.4 (10)	1108	739	1	45.07	112.12	157.19	59	5.9
7	157.6 (40)	197 (50)	39.4 (10)	1108	739	2	45.07	112.12	157.19	59	5.9
8	157.6 (40)	197 (50)	39.4 (10)	1108	739	3	45.07	112.12	157.19	59	5.9
9	137.9 (10)	197 (50)	59.1 (15)	1108	739	0.5	45.07	112.12	157.19	59	5.9
10	137.9 (10)	197 (50)	59.1 (15)	1108	739	1	45.07	112.12	157.19	59	5.9
11	137.9 (10)	197 (50)	59.1 (15)	1108	739	2	45.07	112.12	157.19	59	5.9
12	137.9 (10)	197 (50)	59.1 (15)	1108	739	3	45.07	112.12	157.19	59	5.9

Note % of binder materials are shown in brackets ()

F.A fine aggregates, C.A coarse aggregates

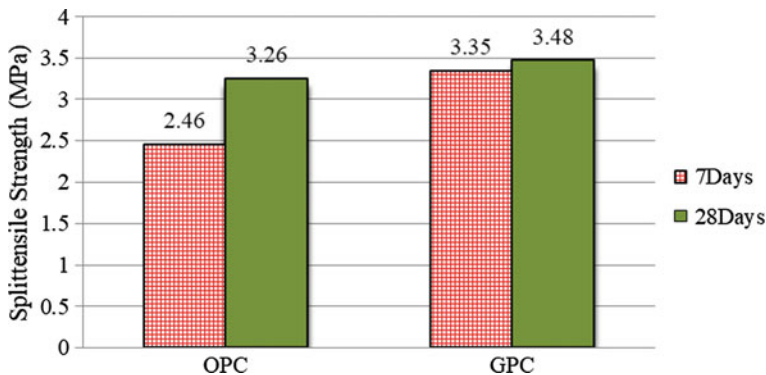


Fig. 7.6 Split tensile strength of OPC and GPC

7.4.2 Split Tensile Strength

Split tensile strength is used to determine the indirect tensile strength of concrete as per (IS 5816). Concrete is weak in tension, and it is necessary to determine the tensile strength of concrete. Cylindrical mold of dimension 100 mm diameter and 200 mm height is used to cast the specimens. The average of three-cylinder specimens is taken as the split tensile strength. From the compressive strength results, the mix 7 has obtained the optimum compressive strength of M30 grade. The mix 7 is 100% geopolymer concrete (GPC). From Fig.7.6, geopolymer concrete specimens have obtained the split tensile strength of 3.35 and 3.48 MPa at 7 and 28 days. The split tensile strength of GPC is comparatively higher than OPC in all the 7 and 28 days.

7.4.3 Flexural Strength of the Ternary Blended Geopolymer Concrete

Flexural strength of concrete is determined by casting the beam specimen of $100 \times 100 \times 400$ mm. Flexural strength helps in finding the bending strength of concrete without reinforcement. From Fig. 7.7, GPC specimens have high flexural strength of 4.26 and 4.4 MPa at 7 and 28 days than OPC specimens.

7.4.4 Cost Analysis of Ternary Blended Geopolymer Concrete

The cost analysis of geopolymer concrete is done based on the standard schedule rates. The price of all the materials is mentioned in Table 7.3. Cost analysis of ternary blended geopolymer concrete is done for 1 m^3 .

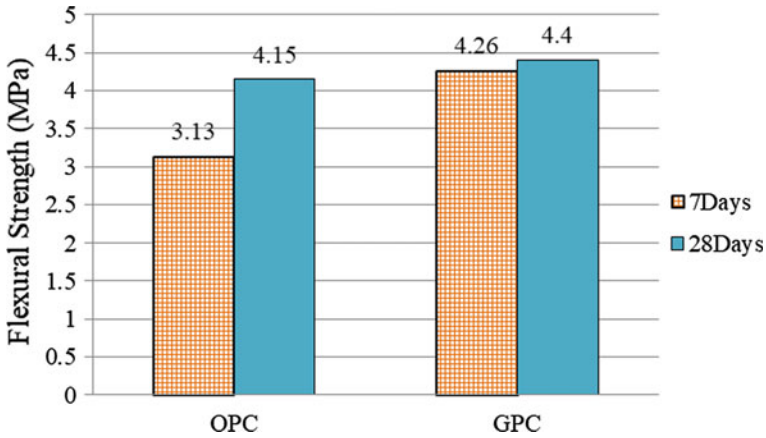


Fig. 7.7 Flexural strength of OPC and GPC

Table 7.3 Details of material cost

Material	Rupees	Unit
Cement	8	Kg
Coarse aggregate	1065	Cum
Fine aggregate (msand)	600	Cum
Flyash	72	Cum
GGBFS	2	Kg
Alccofine	5	Kg
Sodium silicate	9	Kg
Sodium hydroxide	25	Kg
Superplasticizer	200	Kg

From the cost analysis shown in Table 7.4, manufacturing cost of 1 m³ of geopolymer concrete is 3986.03 rupees and OPC concrete is 5004.17 rupees. The manufacturing of geopolymer concrete is economical in the construction industry than OPC concrete. Similarly, cost analysis is done for all the mixes of ternary blended geopolymer concrete. From Fig. 7.8, cost of all the geopolymer concrete mixes is less than that of OPC concrete and the compressive strength attained is 62 MPa for the mix 12 which is equal to the M60 grade.

Table 7.4 Cost analysis of geopolymer concrete and ordinary portland cement (OPC) concrete for 1 m³ of M30

S.No.	Material	Rate	Unit	Geopolymer concrete		OPC concrete	
				Quantity	Amount	Quantity	Amount
1	Cement	8	Kg	0	0	350.22	2801
2	Flyash	72	Cum	157.6	9.456	0	0
3	GGBFS	2	Kg	197	394	0	0
4	Alccofine	5	Kg	39.4	197	0	0
5	Coarse aggregate	1065	Cum	1108	808.84	1213.5	890.7
6	Fine aggregate	600	Cum	739	295.6	698.16	261.81
7	Sodium silicate	9	Kg	112.12	1009	0	0
8	Sodium hydroxide	25	Kg	3.588	90.14	0	0
9	Superplasticizer	200	Kg	5.91	1182	5.25	1050.66
				Total	3986.03		5004.17

All the quantities are in kg/m³ and amount in rupees

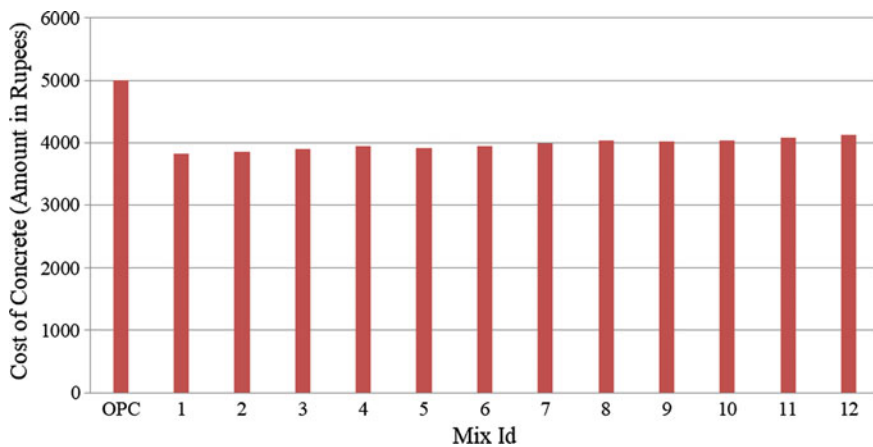


Fig. 7.8 Cost of all the mixes (amount in rupees)

7.5 Conclusions

- Incorporating the industrial byproducts as a binder in geopolymer concrete reduces the impact on the environment, and the problem due to the disposal of byproducts is minimized.
- The production cost of geopolymer concrete is less compared to the production cost of OPC concrete, and the percentage decrease in production cost is 20.35%. At higher grades of geopolymer concrete, higher amount of production cost is saved

on comparing with the OPC concrete of similar grade without compromising the compressive strength.

- With increase in the percentage of Alccofine, the compressive strength is increased due to high particle packing, and with increase in the NaOH concentration in the alkaline solution, the compressive strength is increased due to effective dissolution of Si and Al.
- The energy required for manufacturing of geopolymer concrete is less than the OPC concrete.
- The split tensile strength of GPC specimen is higher than the OPC specimens. The percentage increase in the split tensile strength of GPC is 36.18 and 6.75 at 7 and 28 days.
- The flexural strength of GPC specimens is higher than OPC specimens. The percentage increase in the flexural strength is 36.1 and 6.02 at 7 and 28 days.
- By incorporating the Alccofine in geopolymer concrete improves the compressive strength in ambient temperature curing at low molarities of NaOH and the energy consumption is minimized.

References

1. Pangdaeng, S., Phoo-ngernkham, T., Sata, V., Chindapasirt, P.: Influence of curing conditions on properties of high calcium fly ash geopolymer containing Portland cement as additive. *Mater Design* **53**, 269–274 (2014). <https://doi.org/10.1016/j.matdes.2013.07.018>
2. Pavithra, P., Srinivasula Reddy, M., Pasla Dinakar, B., HanumanthaRao, B.K., Satpathy, A.N.M.: A mix design procedure for geopolymer concrete with fly ash. *J. Clean. Prod.* **133**, 117–125 (2016). <https://doi.org/10.1016/j.jclepro.2016.05.041>
3. Kong, D.L.Y., Sanjayan, J.G.: Damage behavior of geopolymer composites exposed to elevated temperature. *Cement Concr. Compos.* **30**, 986–991 (2008). <https://doi.org/10.1016/j.cemconcomp.2008.08.001>
4. Thaarrini, J., Dhivya, S.: Comparative study on the production cost of geopolymer and conventional concretes. *Int. J. Civil Eng. Res.* **7**(2), 117–124 (2016)
5. Embong, R., Kusbiantoro, A., Shafiq, N., Nuruddin, M.F.: Strength and microstructural properties of fly ash based geopolymer concrete containing high-calcium and water-absorptive aggregate. *J. Cleaner Prod.* **112**, 1–7 (2015). <https://doi.org/10.1016/j.jclepro.2015.06.058>
6. Davidovits, J.: Chemistry of geopolymeric systems terminology. In: *Proceedings of Geopolymer 99 Conference*, Saint-Quentin, France, pp. 9–40 (1999)
7. Palomo, A., Grutzeck, M.W., Blanco, M.T.: Alkali-activated flyash: a cement for the future. *Cem. Concr. Res.* **29**, 1323–1329 (1999). [https://doi.org/10.1016/S0008-8846\(98\)00243-9](https://doi.org/10.1016/S0008-8846(98)00243-9)
8. Fernandez-Jimenez, A., Palomo, J., Puertasalkali, F.: Activated slag mortars: mechanical strength behavior. *Cem. Concr. Res.* **29**, 1313–1321 (1999). [https://doi.org/10.1016/S0008-8846\(99\)00154-4](https://doi.org/10.1016/S0008-8846(99)00154-4)
9. Somna, K., Jaturapitakkul, C., Kajitvichyanukul, P., Chindapasirt, P.: NaOH activated ground flyash geopolymer cured at ambient temperature. *Fuel.* **90**(6), 2118–2124 (2011). <https://doi.org/10.1016/j.fuel.2011.01.018>
10. SrinivasReddy, K., Srinivasan, K.: *IOP Conference Series: Materials Science and Engineering*, 263 (2017). <https://doi.org/10.1088/1757-899x/263/3/032023>
11. Indian Standard Pulverized Fuel Ash—Specification. BIS, IS 3812 (Part 1) 2003 Bureau of Indian Standards: New Delhi, India

12. Padmalal, D., Maya, K.: River sand mining and mining methods. In: *Sand Mining. Environmental Science and Engineering*. Springer, Dordrecht (2014)
13. Specifications for coarse and fine aggregates from natural sources for concrete, IS 383 (1970) reaffirmed 2002, Bureau of Indian Standards: New Delhi, India
14. Patankar, S.V., Jamkar, S.S., Ghugal, Y.M.: Effect of sodium hydroxide on flow and strength of fly ash based geopolymer mortar. *J. Struct. Eng.* **39**(1), 7–12 (2012). <https://doi.org/10.1155/2014/938789>
15. Anuradha, R., Sreevidya, V., Venkatasubramani, R., Rangan, B.V.: Modified guidelines for geopolymer concrete mix design using Indian standard. *Asian J. Civil Eng. (Building and Housing)*, **13**(3), 353–364 (2012)
16. Patankar, S.V., Jamkar, S.S., Ghugal, Y.M.: Effect of solution-to-fly ash ratio on flow and compressive strength of geopolymer concrete. In: *Proceedings of 8th Biennial Conference on Structural Engineering Convention (SEC-2012) at S.V.N.I.T., Surat*, pp. 161–166 (2012)
17. Jamkar, S.S., Ghugal, Y.M., Patankar, S.V.: Effect of fineness of fly ash on flow and compressive strength of geopolymer concrete. *Indian Concrete J.* **87**(4), 57–61 (2013)
18. Patankar, S.V., Ghugal, Y.M., Jamkar, S.S.: Mix design of fly ash based geopolymer concrete. In: *Advances in Structural Engineering*, pp. 1619–1633 (2015). https://doi.org/10.1007/978-81-322-2187-6_123
19. Lloyd, N.A., Rangan, B.V.: Geopolymer concrete with fly ash. In: *Second International Conference on Sustainable Construction Materials and Technologies, Ancona, Italy* (2010)
20. Methods of tests for compressive strength of concrete, IS 516: 1959 (reaffirmed 2004), Bureau of Indian Standards: New Delhi, India
21. Ahmed, A.J., Dhaduk, D., Abhishek, R., Sunil, J., Pritesh, R.: Experimental study on the enhancement in concrete due to the ultra-fine particles. *Global Res. Develop. J. Eng.* 138–141 (2016)
22. Chindaprasit, P.: Influence of fly ash fineness on strength, drying shrinkage and sulfate resistance of blended cement mortar. *Cement Concrte Res.* **34**, 1087–1092 (2004)
23. Singhal, D., Junaid, M.T., Jindal, B.B., Mehta, A.: Mechanical and microstructural properties of fly ash based geopolymer concrete incorporating Alccofine at ambient curing. *Constr. Building Mater.* **180**, 298–307 (2018). <https://doi.org/10.1016/j.conbuildmat.2018.05.286>

Chapter 8

Monitoring Quality of Tap Water in Cities Using IoT



Asis Kumar Tripathy , Tapan Kumar Das 
and Chiranji Lal Chowdhary 

Abstract During the past decade, water requirement has increased many folds in India. However, it has turned out to be a major challenge for the world in matching the increasing demand for water supply. In other hands, water resource has been continuously polluting due to apathetic usage of water, natural and man-made calamity, global warming, sewages, and garbage. Optimal utility of this resource and above all its preservation is the only way to safeguard future life as it is well known that water is life. In this paper, we present a framework based on Internet of Things (IoT) for water monitoring and control activity, which supports Internet-based data collection on a real-time basis. The system addresses the issue of flow rate measuring and in the same time, this study proposes a method to check wastage of water. It has the provision to measure the quality of water dispensed to every household by deploying PH and conductivity sensors.

Keywords IoT · PH sensor · Wi-Fi · Conductivity sensor · Water quality

8.1 Introduction

The World Health Organization (WHO) has reported that 77 million individuals in India struggle to get clean water. In addition to this, the root cause of one-fifth of sicknesses is hazardous water. In other statistics, it has been stated that 1600 deaths are caused because of loose bowels every day, which is also the consequence of consumption of contaminated water. The crumbling of water assets turns into a typical issue for a human being. The conventional strategies for screening water quality

A. K. Tripathy · T. K. Das (✉) · C. L. Chowdhary
School of Information Technology and Engineering, Vellore Institute of Technology, Vellore, India
e-mail: tapan.das@vit.ac.in

A. K. Tripathy
e-mail: asistripathy@vit.ac.in

C. L. Chowdhary
e-mail: cl.chowdhary@gmail.com

© Springer Nature Singapore Pte Ltd. 2020
B. Subramanian et al. (eds.), *Emerging Technologies for Agriculture and Environment*, Lecture Notes on Multidisciplinary Industrial Engineering, https://doi.org/10.1007/978-981-13-7968-0_8

Table 8.1 Specified parameters of water and their quality range

Parameters	Range	Resolution	Accuracy	Quality range
Turbidity	0–100 NTU	0.1	± 0.5	0–5
ORP	–2000 to 2000 mV	2	± 10	600–800
pH	0–14	0.05	± 0.1	6.5–8.5
Conductivity	100–20,000 $\mu\text{S}/\text{cm}$	10	5%	500–1000
Temperature	–5–100 °C	0.1	± 0.1	–
Flow	1–115 L/min	0.0015	15%	–

include the manual accumulation of water test from various areas. These water tests are tried in the laboratory utilizing the diagnostic innovations. Such methodologies are tedious and did not really to be viewed as proficient. In addition, the flow procedures incorporate an examination of different sorts of parameters of water quality, for example, physical and synthetic. Customary strategies for the water quality recognition have the detriments like entangled system, long sitting tight time for results, low estimation exactness, and high cost. Along these lines, there is a need for non-stop checking of quality parameters progressively. Different parameters of water and their range to ensure the quality of water are depicted in Table 8.1.

The IoT turns into an establishment for interfacing objects, sensors, and other shrewd advances. IoT is an augmentation of the Web. It gives prompt access to data about physical protests and prompts imaginative administration with high effectiveness and productivity [1]. There are a few vital advancements identified with the IoT. They are pervasive processing, RFIP, remote sensing, and distributed computing. Distributed computing is an extensive scale, ease preparing unit, which depends on IP, an association for estimation and capacity. The qualities of distributed computing have been examined in various papers [2–6]. The IoT application zones incorporate home robotization, water condition observing, water quality checking, and so on; the water quality checking application includes expansive dispersed exhibit of observing sensor and an extensive circulation organize [7, 8]. It likewise requires isolate checking calculations as inspected in [9, 10]. Above all, various forms of automation were made simpler by using IoT [11].

8.2 Preliminaries

The capacity to screen water level and to shield water from wastage is a critical issue through the fields of the earth and additionally building. The IoT framework is controlling the flow of water through solenoid valves which are controlled by the ultrasonic sensors, water quality sensors, and stream rate sensors. The block diagram for the IoT framework is depicted in Fig. 8.1. There are different subsystems working for this model: (a) focal estimation: it gathers the water quality from the sensors, stores

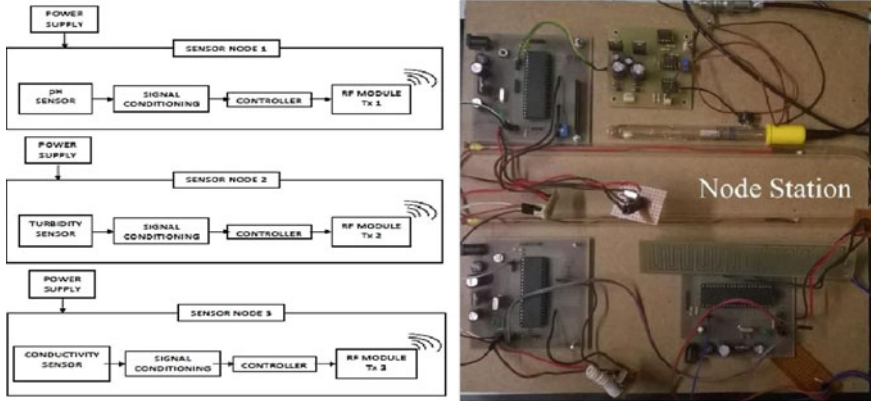


Fig. 8.1 Block diagram of the model

in a database, and then transmits information to different hubs; (b) sending message: after the focal estimation, hub gathers all the information; it will analyze the data and finally, sends email or messages to the responsible persons. Solenoid valve is used to close the principle water valve from capacity tank in the event of any pollution found. The focal estimation hub fills in as the sensor hub. The thought is to introduce these sensor hubs in numerous buyer destinations in a spatially distributed way to shape a WSN that will screen the drinking water quality in the water conveyance framework from the source to the tap.

8.3 Proposed Methodology

The proposed IoT system can be utilized in any of the water tanks, where there is a need to have safe water and minimization of water loss. Whenever the water will be supplied to the water tanks, at that point of time, the pH level of the water will be checked. If the PH level of the supplied water is within the predefined range then we can check the conductivity of water. In this case, when both the pH and conductivity of the supplied water are not in the safe range, then the water supply can be blocked to all the household tanks by blocking the respective valves. We can continue the same process until the water comes in a safe range. Once the water tanks get full based on the availability of safe waters, then the valves will be opened for household use. This model also looks after equal distribution to all the consumers. All the data we are using here for the quality purpose will be sent to the cloud for future use. Once the data are available in the cloud, it can be accessed from anywhere in the world by using authentication mechanism. The quality check and flow of water can be monitored through the Web once the data are available on cloud. In Fig. 8.2, the methodology of the proposed scheme is described.

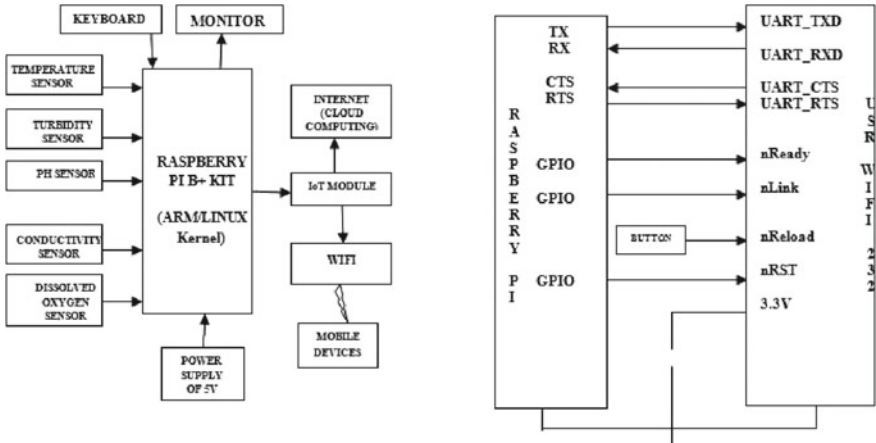


Fig. 8.2 Working model of the proposed scheme

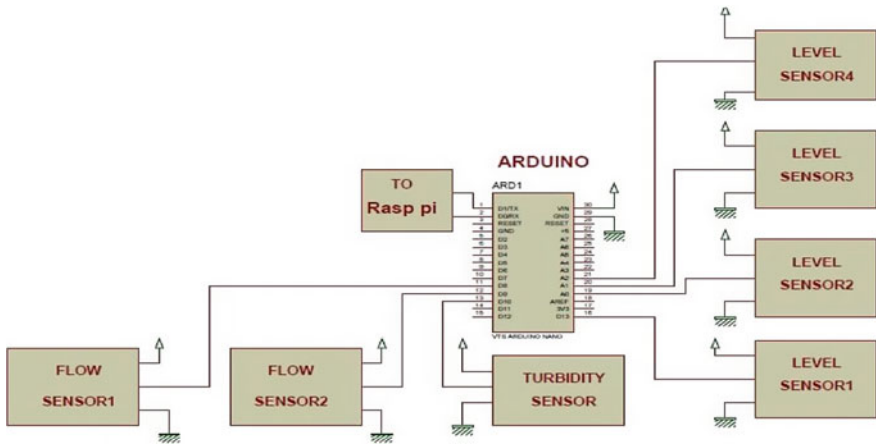


Fig. 8.3 Detailed description of the Arduino system

8.3.1 Detailed Diagram of the System

In this model, the Raspberry Pi and one Arduino board are used for communication purpose. Different sensors are used for data collection, and the examples of those sensors are flow sensor, level sensor, GSM module, and a turbidity sensor. The hardware used in this model is showcased in Fig. 8.3.

The Raspberry Pi, we used in this model, is a tiny size computer board capable of processing the data received from different sensors. Most of the IoT applications prefer to use Raspberry Pi devices for the implementation; as a result, it gives better performance in terms of lifetime. The Raspberry Pi device collects all the data from

the Arduino board and sends it to the cloud continuously. We are using here the microcontroller of 8 bits which is attached to the Arduino nano-board. It has fourteen input/output pins to be connected to the sensors. The level sensors and the flow sensors used in this model are always connected to the analog input pins and to digital input pins, respectively. Whereas, the water flow sensors measure the amount of liquid flown through that valve. The flow rate of the water is calculated in milliliter/sec. In addition, the quantity of suspended particles in the water is measured by the turbidity sensors.

8.4 Results and Discussion

It is highly recommended by some applications to observe the quality of the water before using it. For example, if you want to use any lake water for drinking purpose then your first job is to test the quality of the water. Pollution detection in drinking water is another important application, which requires a different strategy for checking the quality of the water. In this framework, the water quality parameters can be show cased on the Web by utilizing cloud computing paradigm. All the parameters collected from the water samples are kept in some independent servers on the cloud. The water quality parameters can be seen by the authorized devices on the cloud.

Figure 8.4 demonstrates the quality of the water by using different scenarios based on IoT platform.

8.4.1 Configuring the Wi-Fi Module

The ESP8266 device Wi-Fi is configured in such a way that it can send/receive data toward the server. The Wi-Fi device is first connected to the Arduino and then programmed to send data to the server. Table 8.2 represents connections of ESP8266 to Arduino.

After flashing the module, the RX and TX pins are reversed and the Arduino device can be programmed to send or receive data. Figure 8.5 shows the setup for configuring the Wi-Fi module.

Fig. 8.4 Performance analysis of the model

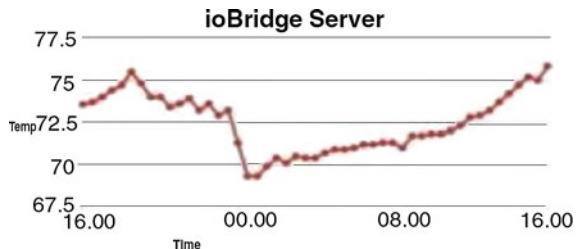
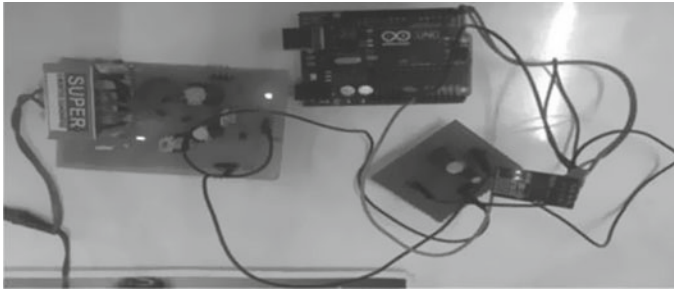


Table 8.2 Connection of ESP 8266 to Arduino for flashing

ESP8266	Arduino Uno
RX	Receive
TX	Transmit
GND	Ground
RESET	Ground
CH_PD	3.3 V (external supply)
VCC	3.3 V (external supply)

**Fig. 8.5** Setup for configuring the ESP 8266

8.4.2 Calibration of pH Sensor

The steps to calibrate a pH sensor are:

- Take two buffer solutions with pH 4.00 and pH 9.20.
- First, dip the probe in the 4.00 pH buffer solution and set the sensor to get pH as 4.00.
- Wash the probe with distilled water.
- Dip the probe in the 9.20 pH buffer solution and check the sensor reading. The reading could be less or more than 9.20. The difference in the reading is the error.
- Then, take the solution for which the pH is to be obtained.
- Dip the probe into the solution and get the reading.
- Actual pH = pH reading \pm error.

First, the average value of six sample values is taken by storing in a buffer. Then, the analog average value is converted to millivolt (mV) using the formula: Value = average value * 5.0/1024/6. Then, the value of the PH can be calculated by using the formula as, pH Value = 3.5* Value + Offset; offset is a parameter to change for the calibration.

8.5 Conclusion

The system explains continuous monitoring of the quality of water supplied to the household automatically. The automation of this process would simplify and would enable to impose the strict quality check standards by the authority. In addition to this, the prevailing practice of the manual field tour for auditing would be resolved. However, the recorded water quality time-series data can be further analyzed to have more insights as to how the quality of water is affected by monsoon or in summer or by wind speed and by different geographical parameters.

References

1. Patawala, A.H., Bansode, N.P., Bhong, Y.P., Zadbuke, A.S.: IOT based water management system for smart city. *Int. J. Adv. Res. Ideas Innovations Technol.* **3**(2) (2017)
2. Kulkarni, P.V., Joshi, M.S.: An IOT based water supply monitoring and controlling system with theft identification. *Int. J. Innovative Res. Sci. Eng. Technol.* **5**(9) (2016)
3. Bhatt, J., Patoliya, J.: IOT Based water quality monitoring system. In: IRF International Conference (2016)
4. PradeepKumar, M., Monisha, J., Pravenisha, R., Praiselin, V., Suganya, K.D.: The real time monitoring of water quality in IoT environment. *Int. J. Innovative Res. Sci. Eng. Technol.* **5**(3) (2016)
5. Khurana, M.K., Singh, R., Prakash, A., Chhabra, R.: An IoT based water health monitoring system. *IJCTA* **9**(21), 07–13 (2016)
6. Vijayakumar, N., Ramya, R.: The real time monitoring of water quality in IoT environment. In: 2015 International Conference on Circuits, Power and Computing Technologies [ICCPCT-2015]. <https://doi.org/10.1109/iccpct.2015.7159459> (2015)
7. Ramprabu, J., Paramesh, C.: Automated sensor network for monitoring and detection of impurity in drinking water. *Int. J. Res. Appl. Sci. Eng. Technol.* **3**(1) (2015)
8. Chavan, P.J., Mechkul, M.A.: IoT based water quality monitoring. *Int. J. Mod. Trends Eng. Res.* **3**(4), 746–750 (2016)
9. Robles, T., Alcarria, R., Martin, D., Navarro, M., Calero, R., Iglesias, S., & Lopez, M. (n.d.). An IoT based reference architecture for smart water management processes. *J. Wireless Mobile Netw. Ubiquit. Comput. Dependable Appl.* **6**(1), 4–23
10. Barabde, M., Danve, S.: Real time water quality monitoring system. *Int. J. Innovative Res. Comput. Commun. Eng.* **3**(6) (2015)
11. Tripathy, A.K., Mishra, A.K., Das, T.K.: Smart lighting: intelligent and weather adaptive lighting in street lights using IOT. In: 2017 International Conference on Intelligent Computing, Instrumentation and Control Technologies (ICICT), pp. 1236–1239 (2017)

Chapter 9

Smart Bin with Automated Metal Segregation and Optimal Distribution of the Bins



K. C. Saranya, Vijayaraj Sujan, Balasubramanian Abivishaq and K. Nithish Kanna

Abstract Waste management has become a serious issue, especially in developing countries with very high population. Lack of bins or proper disposal facilities remains a problem to date. Various governments are also trying hard to push for a cleaner nation by helping curb pollution and improving public sanitation. The smart bin is an important and significant application to deliver cleanliness. A smart bin with automated metal and non-metal segregator is modeled. Using NodeMCU, the level of the bin is monitored in real time and sent to the cloud for further analysis. A novel mathematical model to calculate the most optimal way of distributing the bins in one dimension has also been discussed. Tourist areas, parks, educational institutions, etc., can use the bins in a network to improve sanitation.

Keywords Smart waste management · IoT · ThingSpeak · IFTTT · Smart bin

9.1 Introduction

Conventional waste collection techniques can be dirty and tedious with overflowing bins being emptied too late, and garbage trucks wasting fuel due to poorly planned collection routes and timings. However, smart waste management technologies offer promising solutions to reduce the operational costs and environmental problems associated with the inefficient waste collection. Smart bins are one of the most important

K. C. Saranya (✉) · V. Sujan · B. Abivishaq · K. Nithish Kanna
Department of Communication Engineering, SENSE, Vellore Institute of Technology, Vellore,
India

e-mail: saranya.kc@vit.ac.in

V. Sujan

e-mail: sujankvr@gmail.com

B. Abivishaq

e-mail: b.abivishaq@gmail.com

K. Nithish Kanna

e-mail: nithishkanna10@gmail.com

© Springer Nature Singapore Pte Ltd. 2020

B. Subramanian et al. (eds.), *Emerging Technologies for Agriculture and Environment*, Lecture Notes on Multidisciplinary Industrial Engineering, https://doi.org/10.1007/978-981-13-7968-0_9

applications among smart waste management technologies. It helps to reduce human effort and improve the quality of disposal. Generally, communication chips are used to transfer the data recorded from suitable sensors in the bin. Recycling of waste is an important aspect, but since waste is generally heterogeneous, it becomes difficult to extract the required material. This problem can be overcome by segregating wastes at the source. Information such as fill level can help higher authorities to ensure smooth working of the waste management system.

Much of the literature related to smart bins have fill-level monitoring systems. Ramson et al. [1] have made such a system that sends data to a centralized system. Their work includes waste level sensing, communication to a central system, and an application to display the gathered information. Ultrasonic sensors have widely been used for fill-level identification. In some papers, image processing has been used to determine the fill level. Hannan et al. [2] have used a content-based image retrieval system to estimate the bin level more accurately than the usual ultrasonic setup. Aziz et al. [3] have also used image processing to detect the position and orientation of the bin to check if the bin is empty, partially filled, or full. Optimization of the collection route is also an important result to be determined from fill-level data [4]. The GIS and remote sensing techniques have also been able to reduce the distance travelled by garbage trucks [5]. A wide range of communication devices has been incorporated with smart bins for IoT applications. Frugal Labs have incorporated LoRa technology which uses low power for data communication. MQTT protocol is used for uploading the data to the cloud [6]. ZigBee-PRO and GPRS have also been used for the communication of data from ultrasonic sensors [7]. Wireless monitoring unit (WMU) and wireless access point unit (WAPU) have also been utilized. Power consumption can be minimized by powering the sensors via an RFID tag [8, 9]. A smart recycle bin has also been proposed for selective materials using RFID technology. It can assist the user in classifying materials and calculate the weight of waste thrown inside [10]. Waste segregation at the source helps in efficient recycling. Razari Tomari et al. [11] have developed a reverse vending machine which is said to be an efficient system for recycling. Rajkamal et al. [12] have proposed a GREENBIN which can segregate waste automatically and is also used to generate energy from waste.

Much of the existing literature focuses on using fill-level data for calculating optimal collection routes. A novel method of using fill-level data to compute the optimal placement of bins is shown here. The algorithm is stated and the results when tested with MATLAB have been included. The level of the proposed bin is monitored using an ultrasonic sensor. The bin can also segregate metal and non-metals using a basic RLC circuit which is activated only in the presence of a user. This can help to segregate wastes and maintain cleanliness, besides saving fuel costs of garbage trucks and reducing manpower. Internet of Things (IoT) has been employed to monitor the level of the bin and transmit data. ThingSpeak, an IOT platform is used to store and visualize data from the ultrasonic sensor that is sent via NodeMCU. If This Then That (IFTTT), a free Web-based service, is linked to Thingspeak and is used to trigger an alert email.

The details of the hardware of the bin with appropriate pictures and a flowchart explaining the logic of operation have been discussed in Sect. 9.2. The role of IoT to monitor the level of the bin and the transfer of data is described in Sect. 9.3. Analysis of real-time data is also done with the help of an algorithm for finding the optimal distribution of bins. The results have been presented in Sect. 9.4. Conclusion and the future scope of the project are highlighted in Sect. 9.5.

9.2 System Description

A bin is divided into two halves by means of a partition. A plate is fixed to the bin such that its diameter is attached to the top end of the partition (Fig. 9.1). An Arduino Uno and an ESP8266 Wi-Fi SoC powered by a 9 V battery are used. The bin has three basic features.

9.2.1 Metal/Non-metal Segregator

A basic RLC metal detector circuit is used as shown in Fig. 9.2. It is excited with a square wave pulse and the output voltage is taken across the capacitor. When a metal is placed in the vicinity of the coil, the inductance of the coil will increase. This will change the output voltage across the capacitor. If the change is beyond a threshold, the object is classified as a metal and the plate tilts to one side. If a metal is not detected, the plate tilts to the other side. The plate tilts with the help of a servo motor attached in diametrically opposite ends of the bin. Through this method, metal/non-metal segregation is achieved within the bin itself. The collected metal

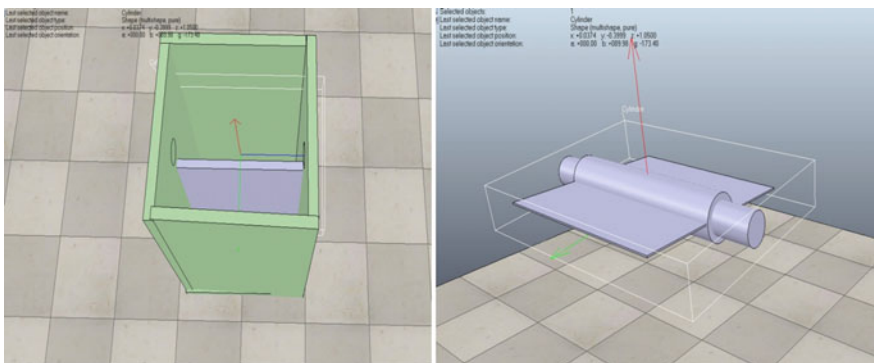


Fig. 9.1 Partition and view of the tilting plate



Fig. 9.2 RLC circuit with the bin used

can later be sent to industries as scrap. This is one of the key features in the bin and can help link scrap collection and waste collection.

9.2.2 *User Detector*

An ultrasonic sensor is placed on the front of the bin. When a person comes close enough to throw the waste, the sensor sends a signal to the Arduino, thereby enabling the rest of the circuits in the bin. This distance is set to forty-five centimeters and will help to minimize power consumption.

9.2.3 *Level Monitor*

Ultrasonic sensor is used for sensing the fill level. A sensor is placed at the center of each partition which is the optimum position for the sensor. An alert will be sent when the waste level reaches a specified threshold. The alert mechanism modeled has two stages in which two different authority levels are notified. The first would be the people directly in charge of the waste collection. The next level is their supervisors. This event-driven process will help garbage trucks to be more efficient by operating when needed.

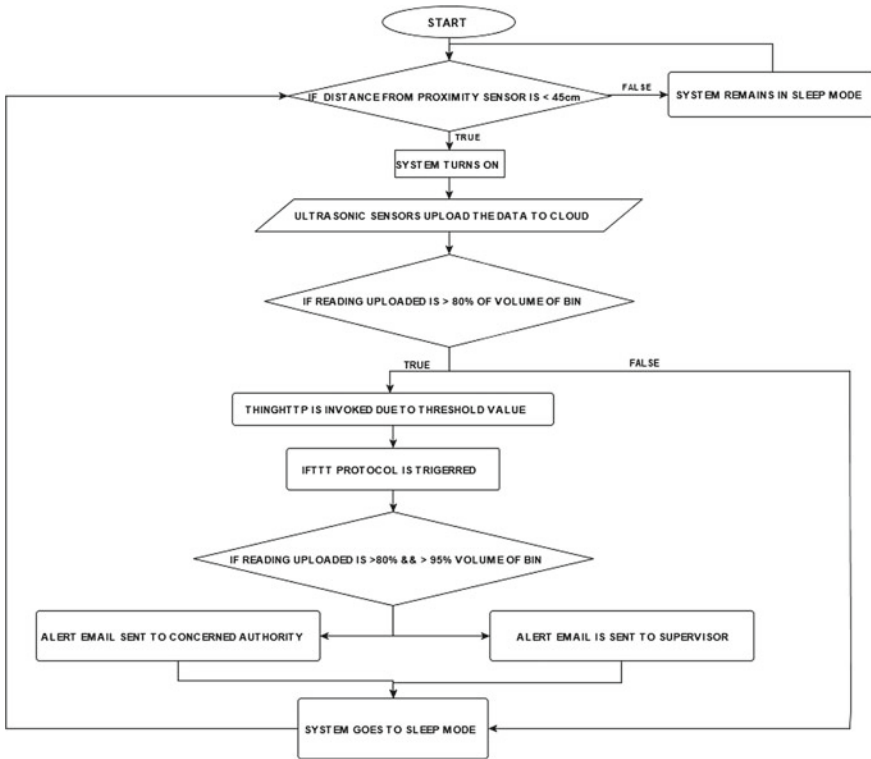


Fig. 9.3 Flowchart for the process

9.3 Network of Bins

NodeMCU, which runs on the ESP8266 Wi-Fi SoC is used to communicate the values read by the ultrasonic sensor to a server. The chip is placed in all bins, and a channel for storing the data recorded by the ultrasonic sensors is established in ThingSpeak. Using IFTTT, we send an email to the concerned when the bin is eighty percent and ninety-five percent full. The former is sent to the garbage trucks whereas the latter can be sent to a supervisor to ensure strict sanitary measures (Fig. 9.3).

Currently, bins in public areas are uniformly spaced or placed by intuition. But practically, some bins can fill faster than others due to higher population density or higher garbage generation closer to the bins. This will reduce the efficiency of garbage trucks and be inconvenient to users if some bins fill up faster. The surrounding bins may fill up sporadically. Hence, it is important to find the most optimal way of positioning the bins in a particular area. This is done by using the data from the ultrasonic sensors. Initially, the bins have to be placed conventionally over an area. Garbage trucks will be notified if any one bin in the area reaches eighty percent. All

the bins are emptied when it happens and the level in each bin before emptying is used for mathematical modelling.

Bins placed in a one-dimensional path are considered. The placement of bins is optimal if the waste in the bins at a given time is nearly uniform. For this purpose, a waste generation density curve is modeled. A waste generation curve $f(x)$ implies a plot between the wastes generated (y -axis) and the position of bins (x -axis). It has been assumed that the waste generated at a point would be dropped in the nearest bin and that all bins have the same dimensions. For the waste generation density curve, a plot between $f(x)$ and x is considered, where $f(x)$ refers to the waste generated per unit distance and x is the position of the bin. The vicinity of a bin refers to the surrounding area of the bin, where the waste generated is assumed to be placed in that bin. The points that are closest to a bin will fall in the vicinity of the bin. In this way, the one-dimensional line can be divided into n regions where “ n ” is the number of bins.

The aim is to find $f(x)$ versus x curve.

$$f(x) = a_n x^{n-1} + a_{n-1} x^{n-2} + a_{n-2} x^{n-3} + \dots + a_3 x^2 + a_2 x + a_1 \quad (9.1)$$

The area under the curve between two points in the x -axis would give the waste generated between the points. The waste generated in the vicinity of Bin1 is assumed to be dropped in Bin1 itself. Therefore, the definite integral from the starting point of the vicinity of Bin1 to the end point of the vicinity of Bin1 should be equal to the waste in Bin1.

$$W \text{ for Bin1} = \int_{s(0)}^{s(1)} f(x) dx \quad (9.2)$$

where W is the height till which the bin has been filled (which is directly proportional to the waste in the bin), $s(0)$ is the starting point of vicinity of Bin1 and $s(1)$ is the ending point of vicinity of Bin1.

$$F(x) = \int f(x) dx \quad (9.3)$$

$$F(x) = (a_n x^n)/n + (a_{n-1} x^{n-1})/(n-1) + (a_{n-2} x^{n-2})/(n-2) + \dots + (a_3 x^3)/3 + (a_2 x^2)/2 + a_1 x + C \quad (9.4)$$

$$W \text{ of Bin1} = F(s(1)) - F(s(0)) \quad W(1) = W \text{ of Bin1} = F(s(1)) - F(s(0)) \quad (9.5)$$

$$W(1) = \left[\left(a_n (s(1))^n + a_{n-1} (s(1))^{n-1} + a_{n-2} (s(1))^{n-2} + \dots + a_3 (s(1))^3 + a_2 (s(1))^2 + a_1 s(1) + C \right) - \left(a_n (s(0))^n + a_{n-1} (s(0))^{n-1} + a_{n-2} (s(0))^{n-2} + \dots + a_3 (s(0))^3 + a_2 (s(0))^2 + a_1 s(0) + C \right) \right] \quad (9.6)$$

$$W(1) = a_n((s(1))^n - (s(0))^n) + a_{n-1}(s(1)^{n-1} - s(0)^{n-1}) + \dots + a_2(s(1)^2 - s(0)^2) + a_1(s(1) - s(0)) \quad (9.7)$$

Similarly, n equations can be generated to find the $(n - 1)$ th degree polynomial to fit the $f(x)$ to x curve. The same can be extended for n equations and the coefficients are found by solving these equations. The data were collected from bins in VIT Vellore.

After generating the curve, the area under the entire curve divided by the number of bins gives the waste each bin should collect for uniform waste collection. Thus, the $f(x)$ curve is divided into n equal areas and the midpoint of the boundary of these areas is the optimal position of the bin. Since the load has been equally divided, each bin would fill at nearly the same time. This process can be repeated until the variance of the fill level of the bins becomes low. The process could be repeated if the variance becomes considerably high over a period. Thus, garbage trucks can handle wastes more efficiently.

9.4 Results and Discussion

To get a clear insight on the efficiency of the system with respect to the measurement of the level of the bin, the following test was performed. Wastes with varied geometry were put inside the bin, and the corresponding reading of the ultrasonic sensor was measured. This value was then compared with the actual waste level in the bin. The objective was to calculate the accuracy of readings obtained for various geometry of wastes put in the bin. In the test, it was noticed that the reading was almost coincident with true value when the accumulated waste made an approximate flat surface. However, when the top surface of the waste made an angle ranging from 15° to 20° with respect to the horizontal, an error of ± 4 cm was recorded. Similarly, when the top surface made an angle of 40° or more, an error of ± 8 cm was recorded. As the area under the partition becomes bigger, more number of ultrasonic sensors could be used as the level of garbage could be uneven.

A setup for bin level monitoring was made as shown in Fig. 9.2. A channel was created to visualize the fill level on ThingSpeak. The fill level obtained is shown in Fig. 9.4. It shows a gradual increase in the fill level followed by a small error due to the difficulties described in the preceding paragraph. An alert email was triggered by IFTTT successfully as shown in Fig. 9.5 after the fill level exceeds the eighty percent threshold value. This email is received by garbage trucks in real time. The bin is emptied and hence the reading resets to the initial value.

Real-time data were gathered from bins in VIT, Vellore along a 450 m linear path. These data along with their relative positions are shown graphically in Fig. 9.6. This graph also elucidates the non-uniform fill level or high variance that prevails in conventional waste collection methods. The vicinity of each bin as discussed in

Channel Stats

Created: [11 days ago](#)
Updated: [less than a minute ago](#)
Last entry: [less than a minute ago](#)
Entries: 773



Fig. 9.4 Channel data in ThingSpeak

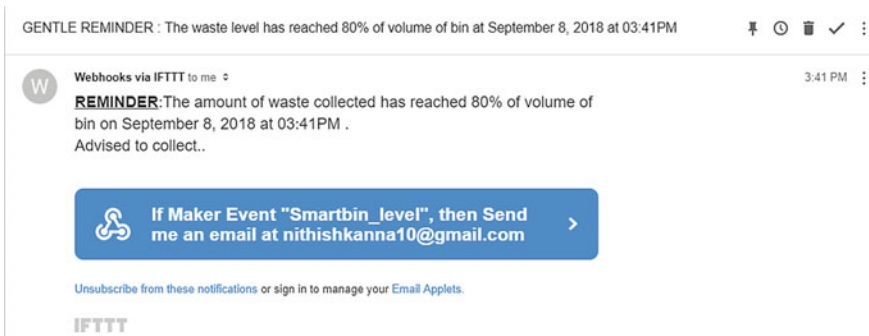


Fig. 9.5 Email reminding the level of the bin through IFTTT

the algorithm is shown in Fig. 9.7. At around three fifty meters, two bins are placed closely owing to higher waste generation from a hostel nearby. Although two bins are still insufficient as the bins collect a considerably higher amount of waste than the rest. At around one twenty meters, there is another small peak observed due to the presence of a shop nearby. The fill-level data clearly reflects the amount of waste generated in the vicinity of the bin. The algorithm for generating the $f(x)$ curve shown in Fig. 9.8 was implemented in MATLAB based on the data obtained from the bins.

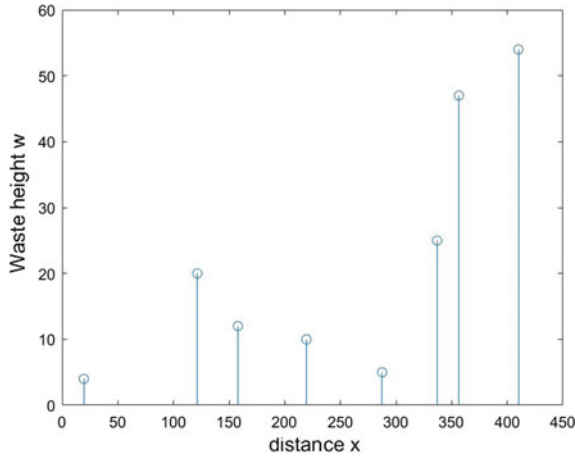


Fig. 9.6 Waste height versus position of bin

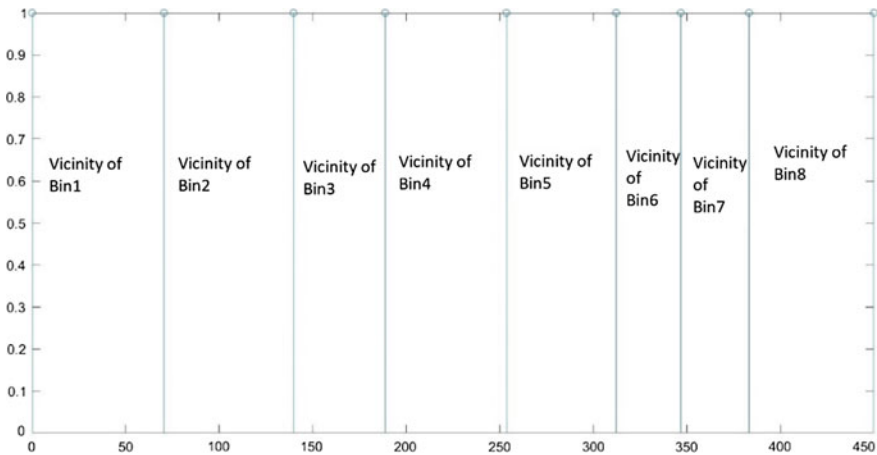


Fig. 9.7 Vicinity of bins

9.5 Conclusion

Efficient waste management solutions are the need of the hour. This smart bin captures an important application pertaining to smart cities worldwide. Making the data available to the public through the cloud can also help improve transparency. The wastes thrown in the bin is generally assumed to be separate and without the involvement of disposable bags. Such wastes cannot be segregated. In addition, weak metals cannot be detected and might slip into the non-metal side. These bins offer tremendous scope for smart cities and are easier to implement on a large scale. They can be improvised by image processing and machine learning to classify different types

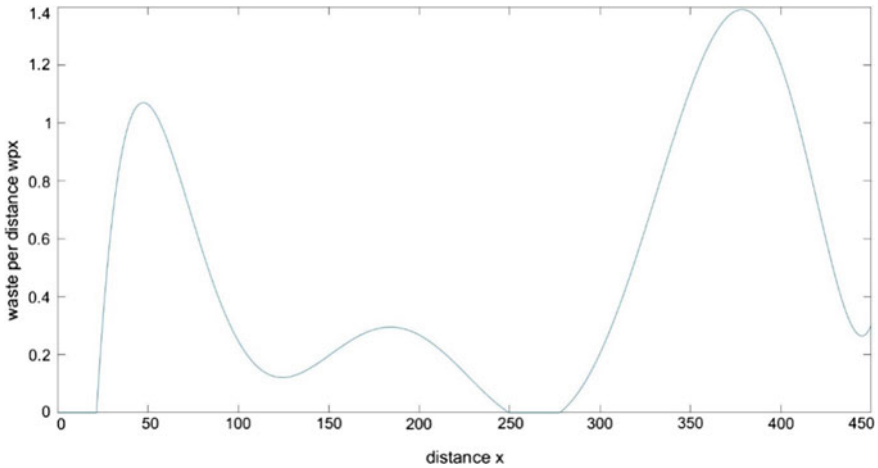


Fig. 9.8 $f(x)$ versus x for data collected from VIT

of wastes with greater accuracy. The mathematical model could be improved when more number of datasets are included. The mathematical model in this paper assumes that the waste per distance is an $(n - 1)$ th degree polynomial but this may not be the case. Modeling with other types of functions depending on the scenario could provide more accurate results. The discussion regarding the optimal placement of bins can also be extended to the two and three-dimensional case.

References

1. Ramson, S.J., Moni, D.J.: Wireless sensor networks based smart bin. *Comput. Electr. Eng.* **64**, 337–353 (2017)
2. Hannan, M.A., et al.: Content-based image retrieval system for solid waste bin level detection and performance evaluation. *Waste Manag.* **50**, 10–19 (2016)
3. Aziz, F. et al.: Rotation invariant bin detection and solid waste level classification. *Measurement* **65**, 19–28 (2015)
4. Al Mamun, M.A., Hannan, M.A., Hussain, A., Basri, H.: Theoretical model and implementation of a real time intelligent bin status monitoring system using rule based decision algorithms. *Expert Syst. Appl.* **48**, 76–88 (2016)
5. Lella, J., Mandla, V.R., Zhu, X.: Solid waste collection/transport optimization and vegetation land cover estimation using Geographic Information System (GIS): a case study of a proposed smart-city. *Sustain. Cities and Soc.* **35**, 336–349 (2017)
6. Bharadwaj, A. S., Rego, R., Chowdhury, A.: IoT based solid waste management system: a conceptual approach with an architectural solution as a smart city application. In: *India Conference (INDICON), 2016 IEEE Annual*, pp. 1–6. IEEE (2016, December)
7. Al Mamun, M. A., Hannan, M. A., Hussain, A.: Real time solid waste bin monitoring system framework using wireless sensor network. In: *2014 International Conference on Electronics, Information and Communications (ICEIC)*, pp. 1–2. IEEE (2014, January)

8. Papalambrou, A., Karadimas, D., Gialelis, J., Voyiatzis, A. G.: A versatile scalable smart waste-bin system based on resource-limited embedded devices. In: 2015 IEEE 20th Conference on Emerging Technologies and Factory Automation (ETFA), pp. 1–8. IEEE (2015, September)
9. Karadimas, D., Papalambrou, A., Gialelis, J., Koubias, S.: An integrated node for smart-city applications based on active RFID tags; Use case on waste-bins. In: 2016 IEEE 21st International Conference on Emerging Technologies and Factory Automation (ETFA), pp. 1–7. IEEE (2016, September)
10. Wahab, M. H. A., Kadir, A. A., Tomari, M. R., Jabbar, M. H.: Smart recycle bin: a conceptual approach of smart waste management with integrated web based system. In: 2014 International Conference on IT Convergence and Security (ICITCS), pp. 1–4. IEEE (2014, October)
11. Tomari, R. et al.: Development of reverse vending machine (RVM) framework for implementation to a standard recycle bin. *Procedia Comput. Sci.* **105**: 75–80 (2017)
12. Rajkamal, R. et al.: A novel approach for waste segregation at source level for effective generation of electricity—GREENBIN. In: 2014 International Conference on Science Engineering and Management Research (ICSEMR). IEEE (2014)

Chapter 10

Solar-Assisted Smart Solid Waste Dustbin



R. Jayagopal, T. Devapounraj and V. Mayilvelnathan

Abstract In the past few decades, the rapid growth of the urbanization rate has taken place, and therefore, plans for sustainable urban planning are required. Using new technologies and a strategic approach, the concept of smart cities is approaching the whole world. A smart city is not built without a smart waste management system. In this article, our model describes the application of “solar-assisted smart solid waste dustbin” for the management of the solid waste system of the city. In our model, the volume of solid wastes has been drastically reduced compared to the conventional process. It reduces the cost of transportation and reduces the odor of waste. First of all, organic waste is ground by grinders and, at the same time, the humidity content is heated to reduce the weight of the waste. Compressors will then compress, and finally, compressed waste materials are stored in the storage unit. The control system is run by solar energy, and the systems are semi-automated. In addition, rented materials are collected by bin to be used for agricultural purposes. Today’s traditional bins will be able to efficiently manage these wastes as they waste their waste on the road, and it may cause insects and mosquito breeding. Dismantling in dirty environments also causes serious illness. It controls through solar energy and is a semi-automatic system; by doing this, we can change the contaminated environment.

Keywords Smart city · Urbanization · Solid waste · Grain size · Waste heating · Odor removing · Waste compressing · Solar power

R. Jayagopal (✉) · T. Devapounraj · V. Mayilvelnathan
Department of Mechanical Engineering, Mohamed Sathak Engineering College, Kilakarai,
Ramanathapuram 623806, India
e-mail: rajjayavip@gmail.com

T. Devapounraj
e-mail: devapounraj@gmail.com

V. Mayilvelnathan
e-mail: nathan_512@yahoo.com

10.1 Introduction

As the world is in the stage of upgradation, there is one stinking problem we have to deal with solid waste management. In our daily life, we see the garbage bins being overfull and all the garbage spills out. This leads to increase the number of diseases because of the large number of insects and mosquitoes breed on it [1]. In current scenario, the solid waste management in urban cities is the big challenge not only in India but for most of the countries in the world. We should eradicate this problem or at least reduce it to the minimum level. The effective solid waste management system is one of the efficient way that to stay our surroundings clean and green. The purpose of establishment of 100 smart cities in India is to create clean and green environment. Now, with the upcoming large number of smart cities, large numbers of responsibilities are also required to be fulfilled. The prime need of a smart lifestyle begins with cleanliness and cleanliness begins with a dustbin. When the dustbins are placed well and collected well, then the society will get clean environment. The main problem in the current waste management system in most of the Indian cities is the unhealthy status of dustbins [2]. In this paper, we have tried to upgrade the trivial but vital component of the urban waste management system, i.e., dustbin.

Here we implemented the bin which consists of solar cells, grinder, drier, compressor, and sensors. Three key implementation challenges are: (1) reduce the transportation cost, (2) reduce the size of waste, and (3) reduce the odor of waste [3]. Our main goal is reducing the waste transportation expenditure by increasing storage capacity of dustbin for same size [4]. Traditional dustbins are not designed to take these advantages. Such methods do not cut and compress the solid waste. Another aspect of that method is to not dry the waste to remove from odor-releasing gases. Our model is semi-automatic so not necessary to operate. It has some other features like solar energy used with sensors. And here it is possible to store waste more than traditional bins. It has three chambers: (1) temporary storage chamber, (2) grinding and heating chamber, and (3) compressing chamber.

10.2 Present Scenario

Normal municipal waste junk is often overwhelmed. The waste management team collects eight times more and is ready to get rid of it. The municipalities can choose the suitable rental program that offers an alternative to the purchase. Leases allow customers to realize immediate savings, instead of spending significant resources. It also works on the management of solar energy waste management, in areas not directly covered by sunlight. With new trainers, the city wants to reduce weekly collections from 17 to 5 intervals [5]. In ten years, these restrictions would have to save more than 12 million dollars and much more. Recently, the capital of Philadelphia has replaced 700 common clays with 500 solid composts and 210 single-stream recycling units. Now that one week of 17 passengers out of 700 containers (annual

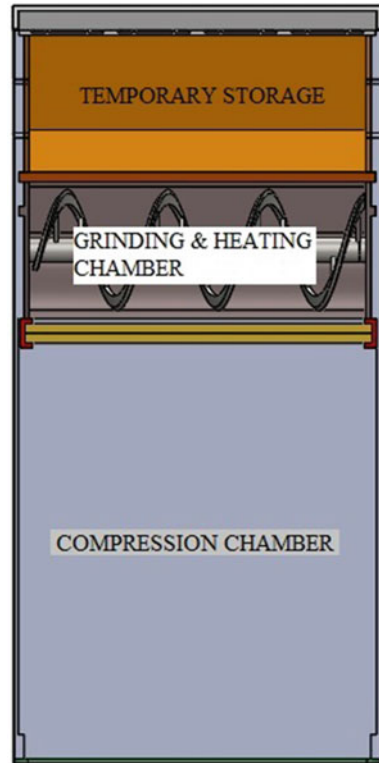
costs of 2.3 million), the city only charges once a week for an operating cost of around 720,000 \$ annually, saving 70%. It requires seven sets per week to run under the new 33-h program instead of a single collection once a week; only nine employees are required in one single change. Other workers have sent other production works together. This increase in the production of solid wastes is becoming a disaster due to poor Indian management practices. These are the basic services and management of the Indian government. In general, municipalities and other local entities regulate the management and disposal of solid wastes in 2000. But municipalities and local organizations generally do not assume this responsibility. The incorrect reasoning is, above all, that it does not have the proper collection, transportation and accessibility system, lack of technical skills, and lack of financial resources. For bad practices, MSWs are distributed in small areas or landfills in cities, without taking the necessary measures. Practical scientific solid waste does not endanger environment due to air, soil, and water pollution. The rapid urbanization and population growth improve the production of solid urban waste [6]. The creation and characteristics of DSM can be modified in different areas of the same country, state, and cities. According to a report from the Indian energy portal, solid waste in India remains uninterrupted from 1971 to 2015. Per capita, waste and urban waste in the city totaled 375 g/day and 14 Mt/year in 1971, 490 g/day and 48.5 MT/year in 1997 respectively. The per capita waste generation is supposed to increase and the city's waste reaches 700 g/day and 97 Mt/year in 2025. The amount of solid waste in 1997, it will be increases twice in 2025.

10.3 The Configuration of Our Model

We constructed our bin by the following content like solar cells, grinder, heater, compressor, AC motors, self-actuating doors (for each chamber), and sensors. The total confirmation of our model is shown in Fig. 10.1. First we discussed temporary solid waste storage chamber. The ultrasonic sensor is fixed at the head of this chamber. And the automated actuating door is located at the bottom surface of the chamber which is actuated by AC motor by accepting the command from control unit by means of sensor. This door will open when the solid wastes are reached to the fixed level. And the solar panels are located at the top surface of this chamber that is immovable. The waste is imported at the top. Here the importing door is operated by human or users. The grinding chamber is located next to the temporary storage chamber. Here cutter and heater are placed. We have designed the cutting blades that are fixed around the rotating arm. This is run by the AC motor that rotates in very slow speed. On the other hand, the heating system is attached to the cutting blades. The top and bottom surfaces of this chamber are the doors for other section. This one is also connected with the AC motor (Figs. 10.2 and 10.3).

The next section is the compression section. In this section, dried waste is compressed into a compact size. Here the reciprocating-type compressor is used which is run by AC motor.

Fig. 10.1 Various chambers of solar-assisted smart solid waste dustbin



10.3.1 Various Chambers

10.3.1.1 Temporary Storage Chamber

Here the solid waste is dumped into the bin. Then the automatic door will open when the waste reaches the predetermined level (max. level) by means of an ultrasonic sensor.

10.3.1.2 Grinding and Heating Chamber

Here the grinding and heating operations were done by means of grinder and heater. The grinder is operated by the DC motor. And where explaining about drier is nothing but a simple heater consists of heating coils. So that the moisture content of waste is to be eliminated.

Fig. 10.2 Various chambers of solar-assisted smart solid waste dustbin

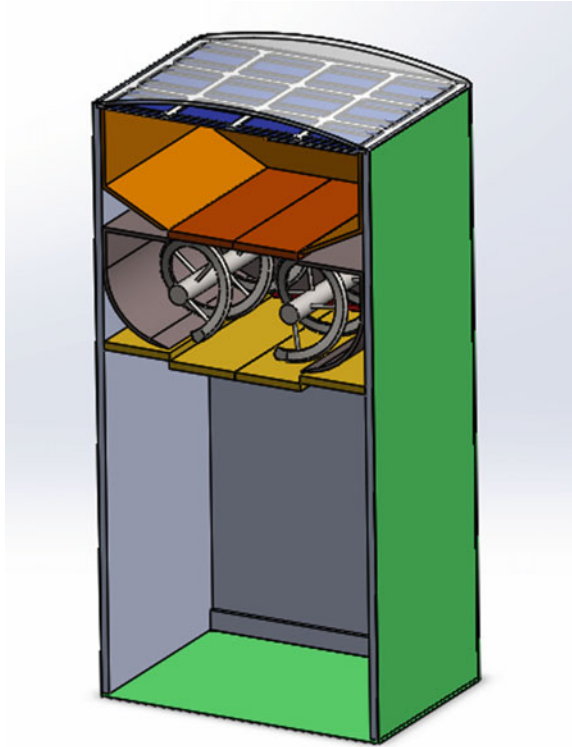
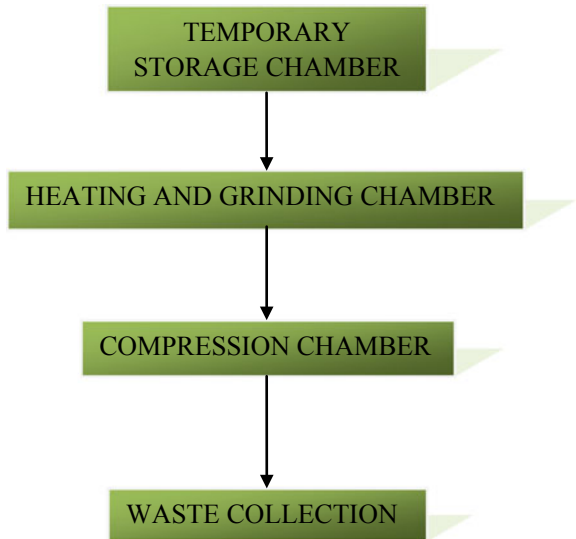


Fig. 10.3 Flowchart



10.3.1.3 Compressing Chamber

After grinding operation is done, the dried waste is introduced to this chamber. Here the total volume of the solid waste is to be reduced by means of compression of waste.

10.3.2 Stepper Motor

DC polished wheels rotate continuously when the DC voltage is applied to its terminals. The stepper engine is known for its properties in the input pulse (usually the square wave poles) for the increase in the position of the shaft to be converted to the train. Each pulse moves the axes through a fixed angle. Stepper engines have many “multiple” electro-windings that are arranged around an iron element. The electrodes are fed through an external controller or a microcontroller. To activate the motor shaft, first of all, an electromagnetism is given strength, which magnetically attracts the gear teeth. When the gear is aligned with the first electromagnetic teeth, they break a bit from the next electromagnet. This means that when the next electromagnetism is switched on and when the first one is deactivated, it turns the gear slightly to align it with the next one. From there the process is repeated. Each of these rotations is called a “step,” with complete steps making a complete step. In this way, the engine can become an exact angle. Here it is used to control this engine, which controls the automatic doors that open and close the doors, separating the chambers. This engine runs in AC power source under the control of microprocessors, clockwise and counterclockwise.

10.3.3 Solar Cell

The solar cell or photovoltaic cell is an electrical device that turns electric energy into a direct photovoltaic effect because it is a physical and chemical phenomenon. The photocell is defined as a device, whose electrical properties, such as electric current, voltage, or resistance, change light. Individual solar cells can be combined into modules, otherwise solar panels. A basic condition is that the maximum voltage of the solar cell in the electric circuit of the solar cell is approximately 0.5–0.6. Here is a photovoltaic installation that uses 12 factors. The control systems and sensors used in our system are solar systems. The live stream generated is stored in the battery for effective use. The curved solar panel is used after a driver and battery connection.

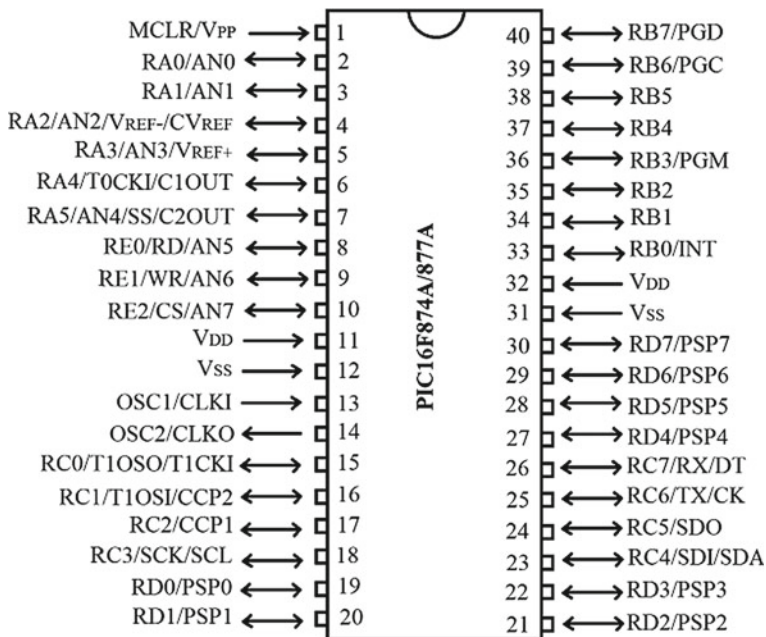


Fig. 10.4 Pin diagram of PIC16F877A

10.3.4 Control System (PIC16F877A Microcontroller)

The control system, PIC16F877A Microcontroller having 200 ns of powerful instruction executions and simple programs (only 35 single word instructions). CMOS Flash based on an 8-bit microcontroller is a powerful Microchip PIC[®] architecture compatible with 40 packages and the PIC16C5X, PIC12CXXX, and PIC16C7X versions (Figs. 10.4 and 10.5).

The PIC16F877A contains 256 bytes of EEPROM data memory with self programming, ICD, two comparators, 8 channels of 10-bit Analog-to-Digital convertor, two capture/comparison/PWM interface functions, or two-wire integrated circuit I²C™ bus and universal asynchronous transceiver (USART). Here, this microcontroller offers a complete control system. It controls the door, compressor, and sensor and heating stages. This system is not included in the figure. The regulator is provided for this power supply in order to make the DC 5 V a suitable power supply.

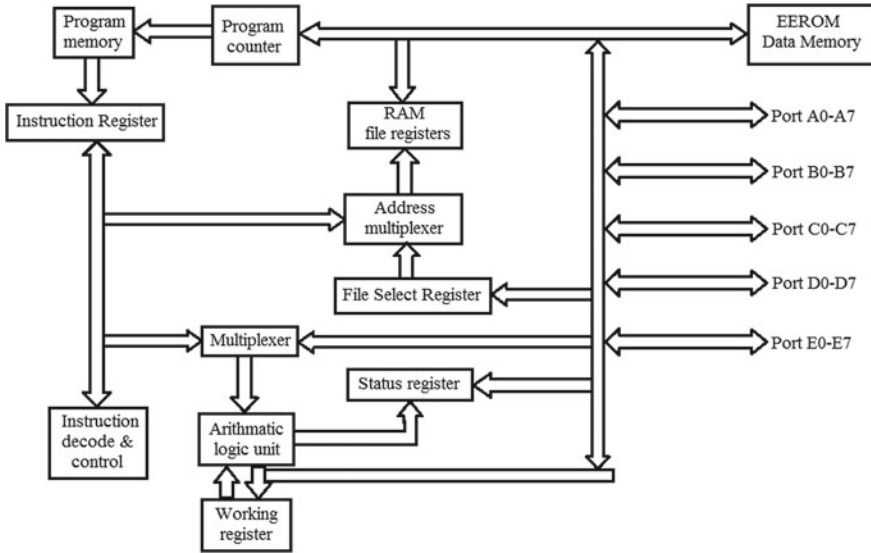


Fig. 10.5 Architecture of PIC16F877A

10.3.5 Sensor

The sensor is a device which is used to detect events or changes in its environment and send the information to the processor. The sensor is still used in other electronic devices, with the exception of the simplest computer or computer.

The sensors used in our model are (1) IR sensor, (2) ultrasonic sensor, and (3) limit sensor.

10.3.5.1 Infrared Sensor

Infrared sensor is an electronic device that sensitively detects some of the environments. An infrared sensor can measure the heat of an object and detect motion. These types of sensors measure only infrared radiation, rather than those called passive infrared. In our model, the sensor type is automatically stabilized next to the import gate and for closing purposes for the use of import waste.

10.3.5.2 Ultrasonic Sensor

As the name implies, ultrasonic sensors measure distance using ultrasound. The sensor head transmits an ultrasonic wave, and the lens reflect the reception of the wave. Ultrasonic sensors measure the target distance to measure the transmit and

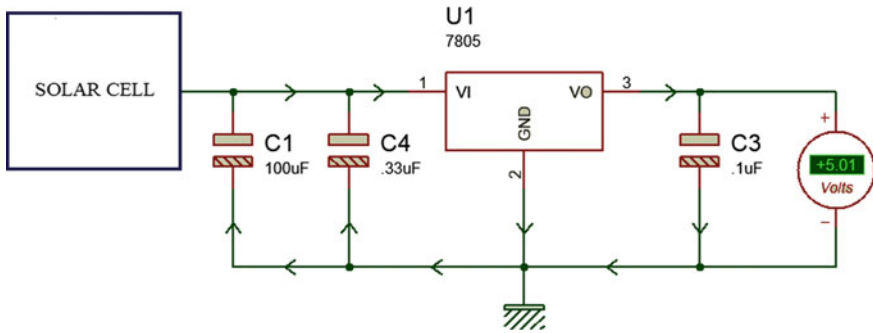


Fig. 10.6 Voltage regulator

receive time. Here it is used to determine the amount of waste import. It is attached to the sides of the first chamber.

10.3.5.3 Temperature Sensor

These temperature sensors can be switched between simple and thermostatic devices that control the heating system. For this reason, it is used in the heating section of our model to maintain the temperature of the particles.

10.3.5.4 Limit the Sensor (Proximity Sensor)

A proximity sensor often emits an electromagnetic field or a beam of electromagnetic radiation (infrared for instance) and looks for changes in the field or return signal. The object being sensed is often referred to as the proximity sensor's target. Different proximity sensor targets demand different sensors. In our model, it is fixed in the compression chamber to indicate the current status of stored waste.

10.3.6 Voltage Regulator

The voltage regulator is a device that reduces the voltage with any device. Here is a microcontroller of power 5 V. The 7805 voltage regulator of 5 V can be easily designed. The 7805 voltage regulator is used to obtain a regulated output of 5 V. A 5-V socket for the PIC16f877A power source microcontroller can be used (Fig. 10.6).

10.3.7 Battery

The solar panels collect energy from the sun and turn it into electricity, which is supplied to run the microcontroller. But it requires only 5 V, so the excess of power can be stored in the battery to use when off-peak period (i.e., when the solar energy not avail).

10.3.8 Control System

The total operation of the bin is semi-automatic (i.e., without human interference), so it is necessary to control the total action of all parts with in feasible time.

10.4 Methodology

Due to population growth in our country, the energy consumption should be necessary. In our model, the control system and sensors are run by solar energy and other systems are run by normal ordinary electric current.

As shown in Fig. 10.3, when the IR sensor senses the person in front of the dustbin the feeding door will be open at the time solid waste is imported from outside. Then the ultrasonic-level sensor senses the garbage level continuously, and when the waste is reached to the predetermined level, then the door will automatically activated by control unit as per program (Figs. 10.7 and 10.8).

At the time of opening the door, the cutter blade and heater have been activated. The grinding blade grinds the solid waste into small grain size. At this time, the moisture content in the waste is eliminated by providing heat using heaters and also eliminates the gases and odor formed by the wet solid waste. In this chamber, the temperature is maintained for certain level by the control system with help of temperature sensor. When the above operation is done, the bottom of heating and grinding chamber door will be open. And the compression chamber will be activated. The all above doors are activated by means of AC stepper motors. Then the compressor compressed the dry solid waste to reduce the volume of waste. And finally, the compressed solid wastes are stored in this chamber or normal dustbin insert to chamber. Here the limit sensor is fixed to indicate the current level of this stored waste. The total volume of waste stored in our proposed bin is to store more quantity of waste than conventional dustbins storage capacity (Fig. 10.9).

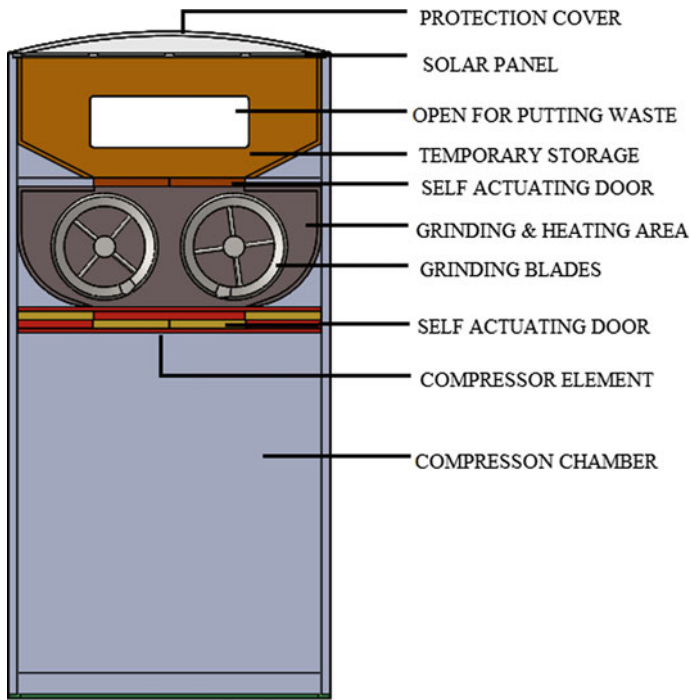


Fig. 10.7 Parts of solar-assisted smart solid waste dustbin

10.5 Benefits

The solar-assisted dustbin supports to reduce cost [7]. It is suitable for all urban cities. It runs with help of solar energy and is renewable one. By using this smart bin, we can store large amount of solid waste and can be eliminate the odor of the solid waste. By using heater, we can also eliminate the water content of the solid waste. This system will occupy the small space (i.e., compact in size). By using this system to Eliminate overflowing of rubbish bins and also Eliminate birds/vermin scattering rubbish across streets, parks, beaches etc. it is also used for advertisement purpose. There is no windblown litter (or) access for critters. Reduce fuel consumption during collection of waste. Reduce the spread of diseases. Cost reduction and resource optimization.

10.6 Limitations

It is difficult to use this system at night, and the compressible waste only can be employed in this system. It is not well suitable for cold areas.

10.7 Application

10.7.1 For Urban Area

In urban areas, there are many more shops and population compared to rural areas, so high amount of solid waste is formed. In traditional method, it is difficult to store, transport, and handle that waste [8] (Fig. 10.10).

So that our model is best suitable for handling that area. In urban area, the traffic is also high but in our model, we can reduce the transportation cost [9]. And in some cases, odor is produced from the traditional dustbins because there is possible leakage. In order to prevent that, the improved dustbin is best suited because here no leakage and no odor (because heater will eliminate the moisture content of the waste), and it reduces the volume of waste, so that we can store more volume of solid waste [10].

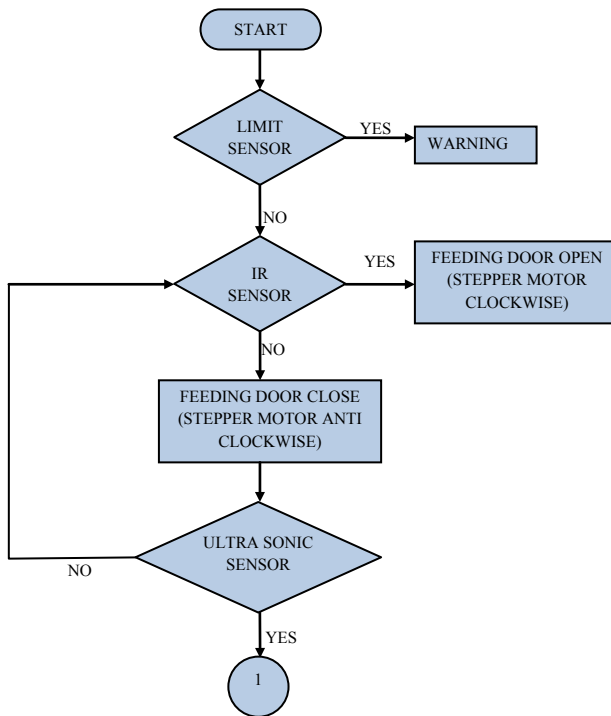


Fig. 10.8 Process flow diagram

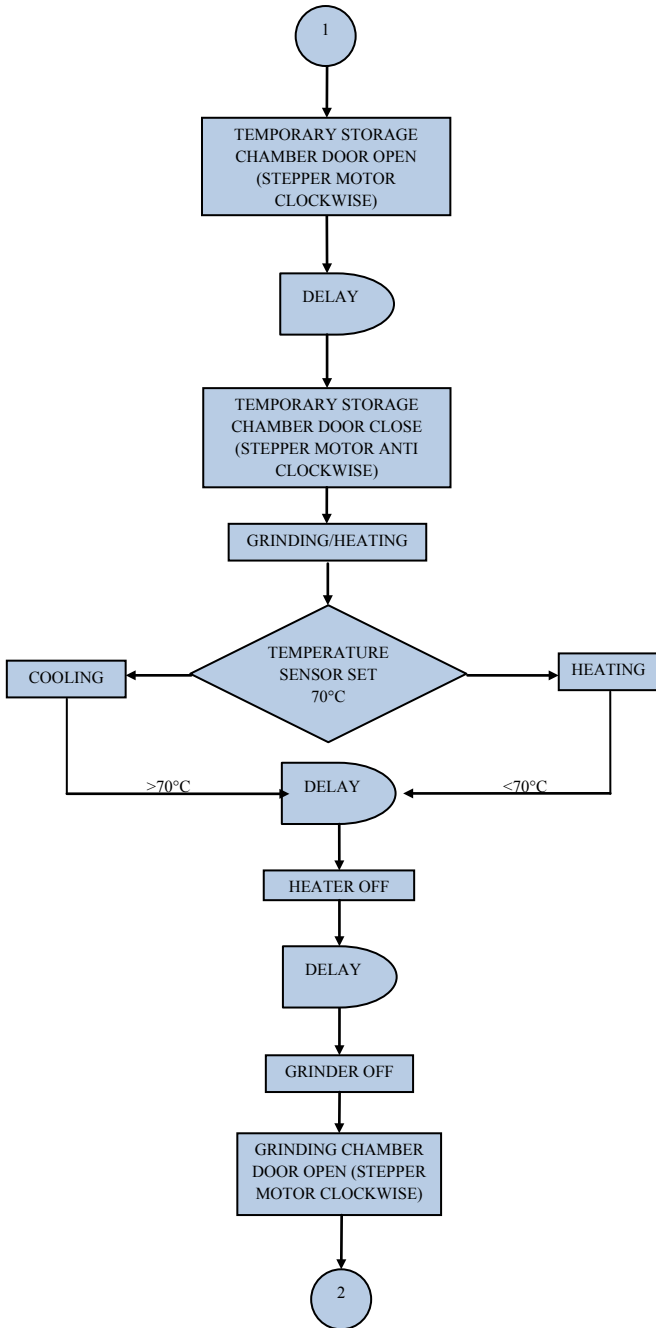


Fig. 10.8 (continued)

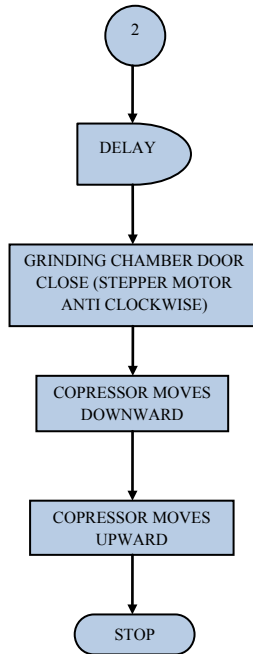


Fig. 10.8 (continued)

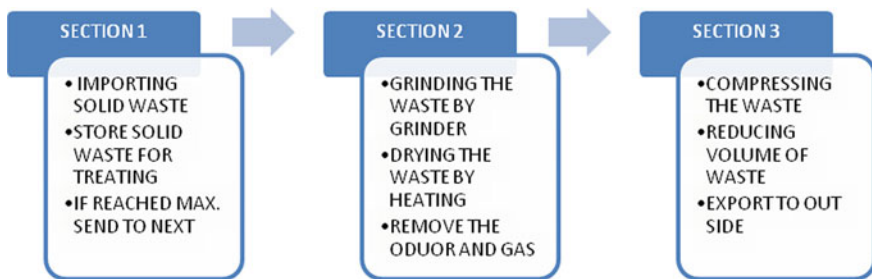
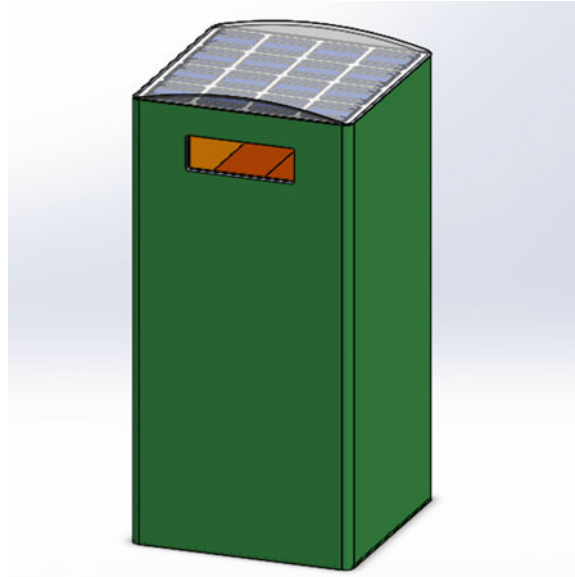


Fig. 10.9 Various sections

10.8 Conclusion

Due to growth in urbanization, the waste is ever-increasing very fast. Therefore, waste management is the essential need to save the environment from harm. The technological augmentation and innovation can contribute to this essential feature to achieve environmental steadiness. To manage waste and scrutinize at the bottom level are the convincing factors for choosing these approaches. The system is a proficient step toward hygiene. As it is being said that the technology which goes equivalent with environment is the need of the hour. Our project is a stride toward

Fig. 10.10 Solar-assisted smart solid waste dustbin



such green technology. This project monitors the fullness of bins from beginning to end by use of sensors; it is feasible to achieve a more well-organized system than the recent existing. Our idea of “solar-assisted smart solid waste management system” primarily concentrates on reducing the volume of solid waste, providing a smart technology for waste system, avoiding human intercession, minimizing human time and effort, which results in healthy and waste-ridden environment. The anticipated idea can be implemented for smart cities where the populace would be busy enough with their frantic schedule and would not have enough time for supervision waste. The bins can be implemented in a city if preferred where there would be a large bin that can have the capacity to collect the waste of solid type for a single public housing.

References

1. Gawade, P.P., Ingale, S.S., Jadhar, G.P., Patil, A.B., Patil, R.R., Ingale, S.S.: Review paper on solar trash powered compactor bin. *J. IARJSET* **4**, 45–48 (2017)
2. Francis, J., Melbin, T.L., Praveen, C.N.: Solar power smart waste bin. *Int. J. Comput. Eng. Res. Trends* **2**(12), 1083–1086 (2015)
3. Ugwuishiwu, B.O., Owoh, I.P., Udom, I.J.: Solar energy application in waste treatment—a review. *Niger. J. Technol.* **35**(2), 432–440 (2016)
4. Sharma, N., Singha, N., Dutta, T.: Smart bin implementation for smart cities. *Int. J. Sci. Eng. Res.* **6**(9), 787–791 (2015)
5. Chugh, H., Singh, D., Shaik, S., Single, A.: IOT based smart bin. *Int. Res. J. Eng. Technol.* **4**(9), 1483–1486 (2017)

6. Singh, M.S., Singh, K.M., Ranjeet, R.K., Shukla, K.K.: Smart bin implementation for smart city. *Int. J. Adv. Res. Comput. Eng. Commun. Eng.* **6**(4), 765–769 (2017)
7. Lazaro, J.P., Rubio, A.J.M.: Solar powered electronic trash can. *Asia Pac. J. Multi. Res.* **2**, 33–37 (2014)
8. Bhor, V., Morajkar, P., Guroav, M., Panlya, D.: Smart garbage management system. *Int. Res. J. Eng. Technol.* **4**(4), 1117–1120 (2015)
9. Samman, E.F.: The design and implementation of smart trash. *Acad. J. Nawroz University* **2**(3), 141–148 (2015)
10. Jenilasree, G., Shenbagavadiv, U.N., Bhuvaneshwari, M.: A study on automatic solid waste management system for smart city. *Int. Res. J. Eng. Technol* **3**(6), 1393–1487 (2016)

Chapter 11

Development of Bio-hybrid Tractor for Farming Applications



Intakhab Khan , Vinayak A. Modi , Sohail Akhtar Khan 
and C. Kannan 

Abstract Present times, the conventional fossil fuel-driven tractors are a major threat to the environment and normally associated with huge running cost which cannot be afforded by the farmers. This project aims at the development of a bio-hybrid tractor that runs on rider's pedalling power coupled with electric motor power. In this tractor, the batteries used for the electric propulsion can be charged either using PV panels or the grid. In addition, a power-split device is mandatory feature of this tractor to provide necessary high torque for off-road applications. As the tractor is using greener energy sources, it has less carbon footprint. This type of tractors will provide a path for alternative way of farming and partial/complete replacement of conventional fossil fuel-driven vehicles in near future.

Keywords Tractor · Hybrid · Solar · Farming · Sowing · Harvesting · Ploughing

11.1 Introduction

Conventional farming techniques are being suppressed with advanced technology which includes the application of tractors, threshers and similar machines. This helps in attaining increased productivity which necessitated by the increasing population

I. Khan · V. A. Modi (✉) · C. Kannan
School of Mechanical Engineering, Vellore Institute of Technology, Vellore 632014,
Tamil Nadu, India
e-mail: vinayaka.modi2015@vit.ac.in

I. Khan
e-mail: intakhab.khan2015@vit.ac.in

C. Kannan
e-mail: kannan.chidambaram@vit.ac.in

S. A. Khan
School of Electrical Engineering, Vellore Institute of Technology, Vellore 632014,
Tamil Nadu, India
e-mail: sohailakhtar.khan2015@vit.ac.in

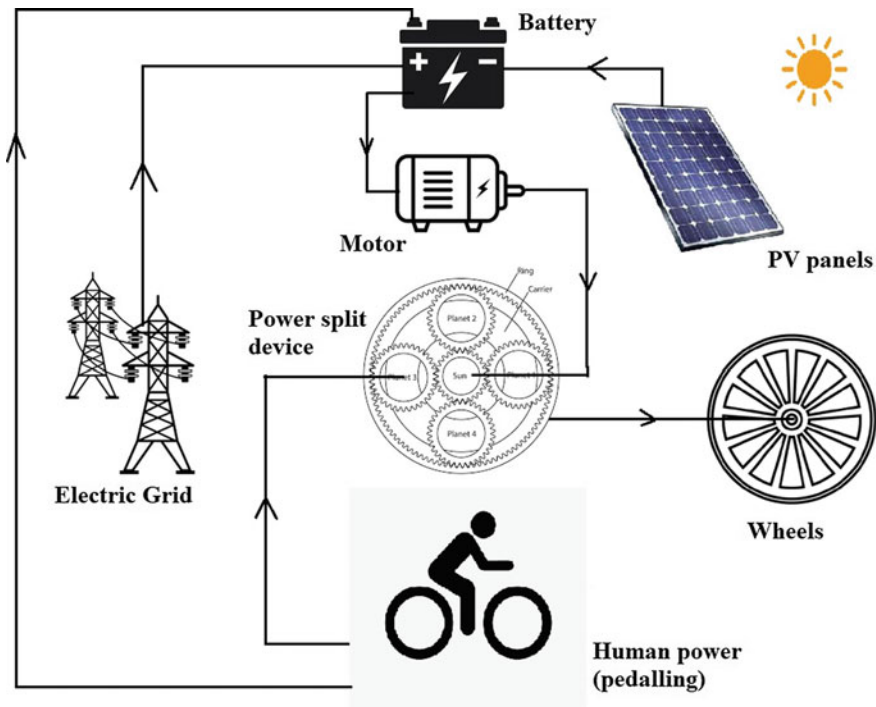


Fig. 11.1 Layout of bio-hybrid tractor

and food demand. However, this advanced technology is associated with augmented energy demands which are currently met by the usage of fossil fuels. This poses a huge challenge for sustainable farming. The depletion times of oil and gas are predicted as 35–37 years [1] which makes it mandatory for developing alternative farming methodologies without compromising the productivity.

Even small tractors of 20–30 HP PTO (power take-off) consume around 3–4 L of diesel per hour of operation [2]. This is a huge consumption considering the scale of agriculture industry. The energy derived from nuclear fuel [3], solar radiation, biogas, alcohol could be alternatively used. Bio-hybrid tractors (BHTs) incorporate the application of renewable sources of energy, i.e. human power coupled with electric power to provide necessary tractive power for farming applications.

The cost of standard tractors varies from 5 to 15 lakhs (INR) which is not affordable to many farmers and is not profitable for small land holdings which is major type of cultivation in India. The rising fuel prices also add additional burden on the farmers. BHTs have almost no cost associated with fuel and will be cheaper to its counterparts. As a result, the running cost of BHTs will be comparatively lower. BHTs can provide an alternative way for farming in many remote locations that do not have fuel sources.

The novelty of BHT is that it has a unique construction which combines the energy from various sources to propel the vehicle. The layout of such BHT is shown

in Fig. 11.1. This vehicle contains an on-board lithium-ion battery pack which can be charged either by grid or by photovoltaic (PV) panels. These panels also help in charging the battery during the running conditions. The vehicle also derives its power through pedalling. The electric motor, pedalling and final transmission are coupled via power-split device, which does not have PTO (power take-off). This is done to avoid an increase in weight. Instead, this vehicle incorporates mechanical links and relies on the vehicle and rider weight for ploughing activities.

11.2 Concept Development

11.2.1 Major Bio-hybrid Tractor Components

Electric Motor

The selection of an electric motor was done considering that the vehicle can deliver all the intended functions purely under electric drive mode. This is considering the fact that there may be some circumstances where the driver is not able to provide his pedalling force. During that time, the vehicle can be operated using the power provided by an electric motor [4].

The tractive force (F_t) required to propel the BHT and attached implements in both forward and backward directions [5] can be calculated using Eq. (11.1)

$$F_t = F_{\text{roll}} + F_{\text{air}} + F_{\text{acc}} + F_{\text{hill}} + F_{\text{drawbar}} \quad (11.1)$$

where F_{roll} is rolling resistance force, F_{air} is aerodynamic drag, F_{acc} is the force required for acceleration, F_{hill} is the hill climbing force, F_{drawbar} is the force required parallel to the vehicle to move the implement and all forces considered here are in Newton.

Draft requirements can be calculated using the Eq. (11.2)

$$F_{\text{drawbar}} = F_i [A + B(V) + C(V^2)] WT \quad (11.2)$$

where F_i is soil adjustment parameter, A , B , C is a machine specific parameter (dimensionless), V is field speed (m/s), W is machine width (m or no. of tools) and T is the tillage depth.

For BHT, $F_i = 1$ is considered for fine surfaces (conservative), machine parameters A , B are taken for sweep plough, and the vehicle speed, V is considered as 2.77 m/s, the plough length, W is 1.2 m and the tillage depth, T is 0.10 m [6].

$$F_{\text{drawbar}} = 1 * [390 + 19 * 2.77] * 1.2 * 0.10$$

$$F_{\text{drawbar}} (\text{BHT}) = 53.11 \text{ N}$$

F_{roll} is the rolling resistance which is caused by the resistance between the soil and the wheels of the vehicle and can be calculated using Eq. (11.3)

$$F_{\text{roll}} = C_{\text{roll}} \cdot m \cdot g \quad (11.3)$$

where C_{roll} is rolling friction coefficient, m is the combined mass of BHT and the rider in kg and g is the acceleration due to gravity in m/s^2 .

For BHT, the mass of the vehicle after material analysis (3D modelling) and combined rider weight was found to be 250 kg, C_{roll} is the rolling resistance coefficient which was taken 0.3 for soil terrain, acceleration due to gravity is 9.81 m/s^2 .

$$F_{\text{roll}}(\text{BHT}) = 0.3 * 250 * 9.81 = 735.75 \text{ N}$$

Aerodynamic drag (F_{air}) which is the air resistance acting on the vehicle, while running under significant velocities can be calculated using the Eq. (11.4)

$$F_{\text{air}} = \frac{1}{2} \rho A C_d (V + V_w)^2 \quad (11.4)$$

where ρ is the density of air in kg/m^3 , A is the frontal area in m^2 , C_d is the coefficient of drag and V is vehicle speed in m/s and V_w is the wind velocity in m/s .

For BHT, air drag is normally ignored as they are going to operate low speeds; hence, F_{air} can be approximated to zero.

F_{acc} is the acceleration force mainly comprises the linear acceleration (F_{lacc}) of the vehicle. For accurate modelling, the acceleration should comprise of both linear and rotational acceleration (F_{racc}). This can be inferred from Eq. (11.5) [7]:

$$F_{\text{acc}} = F_{\text{racc}} + F_{\text{lacc}} \quad (11.5)$$

where F_{lacc} is the linear acceleration of the vehicle, F_{racc} is the rotational acceleration of the vehicle.

According to Newton's second law:

$$F_{\text{lacc}} = m \cdot a_{\text{lacc}}$$

The linear acceleration of the BHT is considered relatively low of 0.2 m/s , and hence, linear acceleration force is 50 N.

$$F_{\text{lacc}}(\text{BHT}) = 250 * 0.2 = 50 \text{ N}$$

The rotational acceleration is calculated using Eq. (11.6) by combining Newton's law and rotational parameters

$$F_{\text{racc}} = I \cdot \frac{G^2}{r^2} a_{\text{lacc}} \quad (11.6)$$

Fig. 11.2 AC induction motor (two-pole three-phase)



where I is the moment of inertia in Kg m^2 of the motor rotor, G is the gear ratio from electric motor to output shaft, r is the tyre radius in m.

Rotational acceleration force is very less compared to linear acceleration force for BHT, and hence, F_{racc} is considered to be zero.

When vehicle is going uphill, the force due to inclination is calculated by Eq. (11.7)

$$F_{\text{hill}} = m \cdot g \cdot \sin \alpha \quad (11.7)$$

where α is the angle of inclination.

As BHT generally will not operate in uphill conditions, hence this factor is ignored.

BHT uses one motor/generator, so the required torque should be provided by the motor provided by the Eq. (11.8)

$$T_m = \frac{r}{G \cdot \eta_m \cdot \eta_g} \left[C_{\text{roll}} \cdot m \cdot g + \frac{1}{2} \rho A C_d (V + V_w)^2 + a_{\text{lacc}} + I \cdot \frac{G^2}{r^2} a_{\text{lacc}} + m \cdot g \cdot \sin \alpha + F_{\text{drawbar}} \right] \quad (11.8)$$

The torque requirement of the electric motor for BHT is calculated considering the radius of wheels to be 0.295 m, the gear ratio as 1:16 (according to suitable motor) and the combined efficiency $\eta_m \cdot \eta_g$ as 0.85 based on standard induction motor.

$$T_m = \frac{0.295}{16 * 0.85} [735.75 + 0 + 50 + 0 + 0 + 53.11]$$

$$T_m = 18 \text{ Nm (Starting torque)}$$

The torque to be delivered by the electric motor is calculated and was found to be around 18 Nm for a gear ratio of 16. The above calculation was done for various iterations until a suitable torque and gear ratio combination was achieved (Fig. 11.2, Table 11.1).

Table 11.1 Electric motor specifications

Motor parameters	Specifications (expected)
Type	AC induction motor (2-pole 3-phase)
Power	2.2 KW/3 HP
Rated speed	2200 rpm
Rated torque	7.35 Nm
Starting torque	18 Nm

Fig. 11.3 Li-ion battery pack 60 V 50 Ah

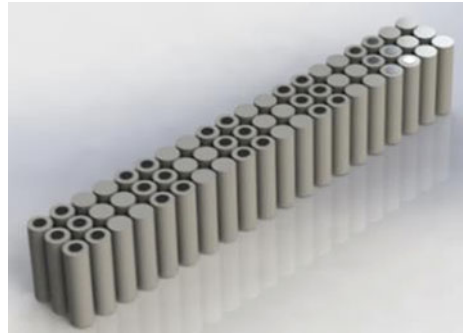


Table 11.2 Battery specifications

Battery parameters	Specifications (expected)
Type	Li-ion battery pack
Rated voltage	60 V
Rated capacity	50 Ah
Discharge current	60 A
Max charge voltage	71.4 V
Discharge cut-off voltage	47.6 V

Battery

Battery is the powerhouse of the BHT [8] and provides power to the induction motor which in turns drives the vehicle. Battery requirement of the BHT is calculated as [4, 9]

$$\text{Required current per hour by the battery} = I_{\text{continuous}} * t \tag{11.9}$$

$$I_{\text{continuous}} (\text{Motor}) = 4.60 \text{ A}$$

$$\text{Time} = 1.5 \text{ h}$$

$$\text{Required Current per hour by the battery} = 4.6 * 1.5 = 6.9 \text{ Ah}$$

DC from the Li-ion Battery 60 V 50 A will be inverted to alternating current 60 V 50 A and then stepped up to 415 V 7 A (as per the induction motor requirements) (Fig. 11.3, Table 11.2).

Fig. 11.4 PV panel (48 cells)

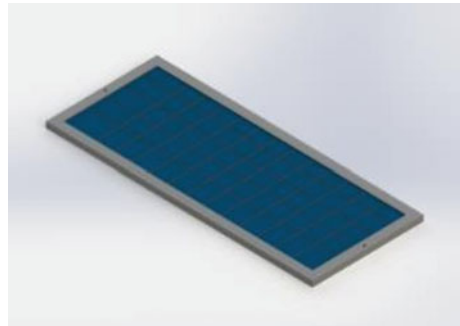


Table 11.3 Solar cell specifications

Solar cells parameters	Specifications (expected)
Rated power of solar cell	4.67 W
Open-circuit voltage	0.5–0.6 V
Short-circuit voltage	5.91–6.12 A
Operating voltage	0.519–0.528 V
Operating current	7–8 A
Dimensions	6 in. * 6 in.
PV panels parameters	Specifications (expected)
No. of cells	48
Power from solar panels	$4.224 * 48 = 202.752$ W
Voltage by solar panel	$48 * 0.528 = 25.344$ V
Current by solar panel	8 A
Time to charge the battery	$50 \text{ Ah} / 3.38 \text{ A} = 15$ h

Solar Photovoltaic Panels

Solar panels provide an auxiliary method of charging the batteries. The output voltage of the panel is around 25 V which has to be boosted to 60 V with the help of boost converter and will be fed to Li-ion battery. Current output by boost converter is 3.38 A (Fig. 11.4, Table 11.3).

Power-Split Device

Power-split device [10, 11] is the heart of BHT as it combines the human (bio) power and electric power from the batteries in various combinations which cater to the needs of the vehicle in different running conditions. Power-split device comprises of an epicyclic gear train [12] with a sun gear, planet gear and ring gear. In BHT, the sun gear is connected to the electric motor/generator, the ring gear is connected to transmission and the planetary carrier (which is connected to the planet gears) is connected to crank which is powered via pedalling. There can be four operating regions of the gear assembly depending on a particular gear being stationary, which is shown in Fig. 11.5.

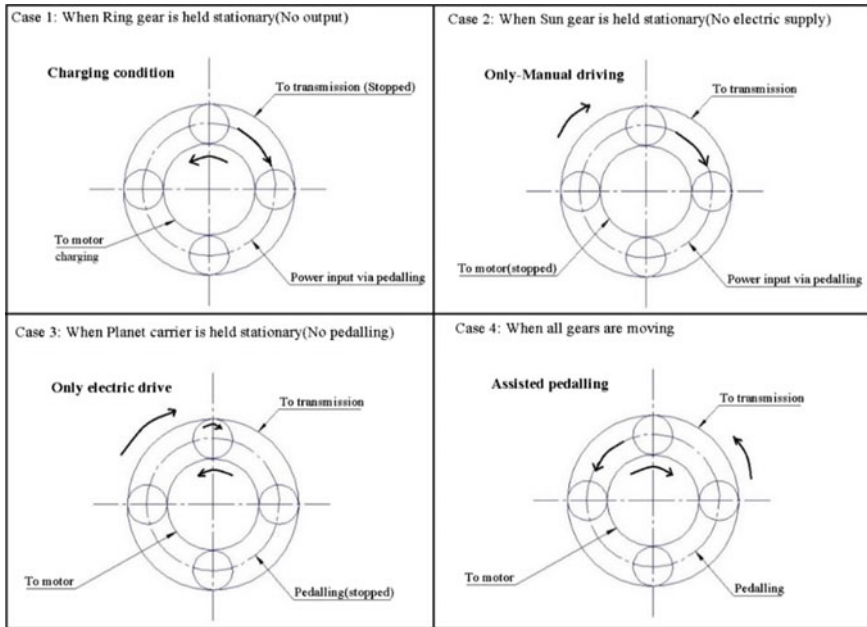


Fig. 11.5 Different operating regions of the power-split device

Case 1: When Ring gear is stationary (Charging condition)

As the ring gear is connected to the transmission, there will be no output in this mode. There can be further two sub-cases one in which pedal drives the motor rotor and vice versa. Rotation of pedals via motor is undesirable, but driving the motor via pedalling can result in motor working as a generator which can be used for charging the vehicle in case of unavailability of power from solar sources as well as from the grid.

Case 2: When Sun gear is stationary (Only Manual drive)

Sun gear being stationary results in input from motor/electric sources. Hence, the planet carrier driven via pedalling rotates the ring gear. In this case, the vehicle acts as a human-powered vehicle with no support from batteries. This mode can be used for normal locomotion under less load. This mode will be particularly useful in case of completely discharged batteries.

Case 3: When Planet carrier is stationary (Only Electric drive)

If there is no pedalling or the pedalling is locked, then the planet carrier will remain stationary and the planet gears will rotate about their axis only. In this case, the power from electric drive is used to propel the vehicle as a result the vehicle works as an electric tractor. This mode is useful when the driver is having fatigue. The limitation is that as there is no human power involved the battery lead time will decrease suitably.

Case 4: When none of the gear is stationary (Hybrid drive)

This is the mode in which the vehicle will perform most of its task and is most efficient in its operation. The power from both the sources, i.e. human pedalling and electric sources is coupled as torque coupling to provide more torque for heavy-load applications. In this mode, sun gear, planet gear and ring gear all are operational. The sun gear (electric power) assists the planet gear (manual drive) which in turn rotates the ring gear. Different speeds can be easily coupled for maximum torque output. This mode is suitable for ploughing, harvesting and other heavy-duty applications.

11.2.2 Power Electronics**Boost Converter Circuit**

Boost converter steps up the DC voltage. The output voltage is always higher than input voltage which depends on the duty cycle of the metal-oxide-semiconductor field-effect transistor (MOSFET) which is decided by the gate pulse.

$$\frac{V_{\text{out}}}{V_{\text{in}}} = \frac{1}{1 - D} \quad (11.10)$$

$$D = \frac{T_{\text{on}}}{T_{\text{on}} + T_{\text{off}}} \quad (11.11)$$

The input voltage of the boost converter is 60 V from the Li-ion battery and the output we want is 415 V which will be fed to the inverter as an input voltage to invert it into AC voltage. In the circuit, when the MOSFET is switched on, the current flows through the inductor, which enables the inductor to store the energy. When the MOSFET is switched off, the diode starts conducting. Now, the energy stored in the inductor acts as a back EMF. Now, there are two EMF source, the input voltage and the inductor. This charges the capacitor and also supplies the load. Now, when the MOSFET is turned on again, the inductor again stores energy and the capacitor supplies the load by its charge. This cycle is gets repeated as the MOSFET is turned on and turned off. The output voltage is measured across the resistance. The graph shows the output voltage across the resistance, which attains the steady state at 415 V [13–17] (Fig. 11.6).

Three-Phase Inverter Circuit

Inverter converts the DC input into AC output. In our vehicle, we are using a 60 V, 50 Ah Li-ion battery which is further coupled to a 415 V three-phase AC induction motor. This necessitates a conversion in the battery input into AC output using a three-phase inverter. The output voltage of the Li-ion battery is 60 V. This voltage is stepped up using a boost converter to 415 V which is further inverted using a three-phase inverter. The IGBT (insulated-gate bipolar transistor) acts as a switch to

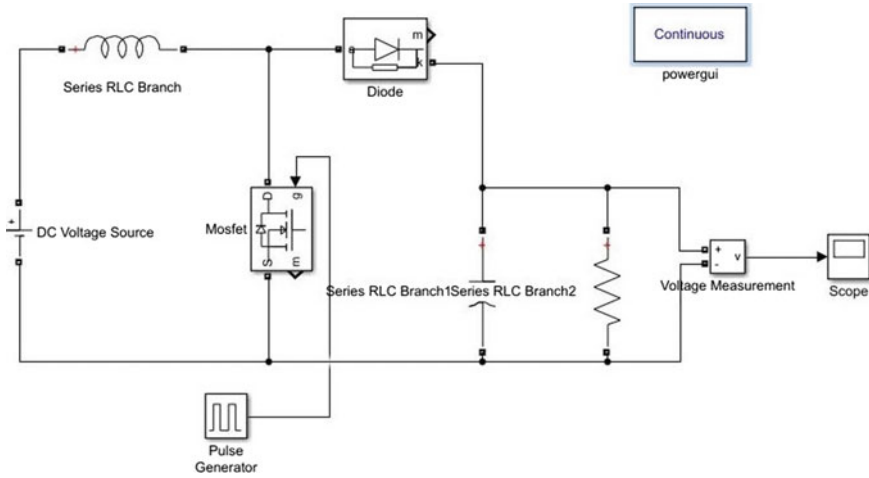


Fig. 11.6 Booster circuit

control the working of the circuit. The control of IGBT depends on the gate pulse, it receives. The gate pulse is provided by the pulse generator. For 180° , the pulse generator operates at a difference of 60° phase delay. The pulse generator operating sequence is $g_1, g_2, g_3, g_4, g_5, g_6$ as shown in the simulation [13, 14].

$$\text{Phase delay} = \frac{\text{Period} * 60 * n}{360},$$

$n = 0, 1, 2, 3, 4, 5$ for $g_1, g_2, g_3, g_4, g_5, g_6$, respectively.

The inverter can operate at anyone of the six modes. At one instant, three IGBTs operate simultaneously, while the other three are switched off. In mode 1, IGBT1, IGBT2 and IGBT6 operate. In mode 2, IGBT2, IGBT3 and IGBT1 operate. In mode 3, IGBT3, IGBT4 and IGBT2 operate. In mode 4, IGBT4, IGBT5 and IGBT3 operate. In mode 5, IGBT5, IGBT6 and IGBT4 operate. In mode 6, IGBT6, IGBT1 and IGBT5 operate. This process continues after completion and the output is obtained. Figure 11.7 shows the output line voltages V_{ab} , V_{bc} and V_{ca} , respectively. These output voltages are fed to the three-phase induction motor as input. In the graph, the AC line voltages are getting varied from $+415$ to -415 V (Figs. 11.8 and 11.9).

11.3 3-D Modelling of the Bio-hybrid Tractor

The 3-D model of the BHT was modelled in Solidworks2016 software, and all the required components were assembled as shown in Fig. 11.10. The BHT was developed with a tubular frame chassis supporting the weight of rider, self-weight of vehicle and the reaction loads. It is a rear-wheel-drive vehicle with the motor resting

on the rear portion of the vehicle. The power-split device has been placed at the axis same as the motor shaft. One of the shafts of the power-split device is connected with motor and other with the sprocket and chain transmission. The transmission ratio of the overall epicyclic gear train was kept 16:1 which is as per our requirement. The transmission ratio for the human-powered transmission is kept 1:1. The battery packs are placed at the front of the vehicle.

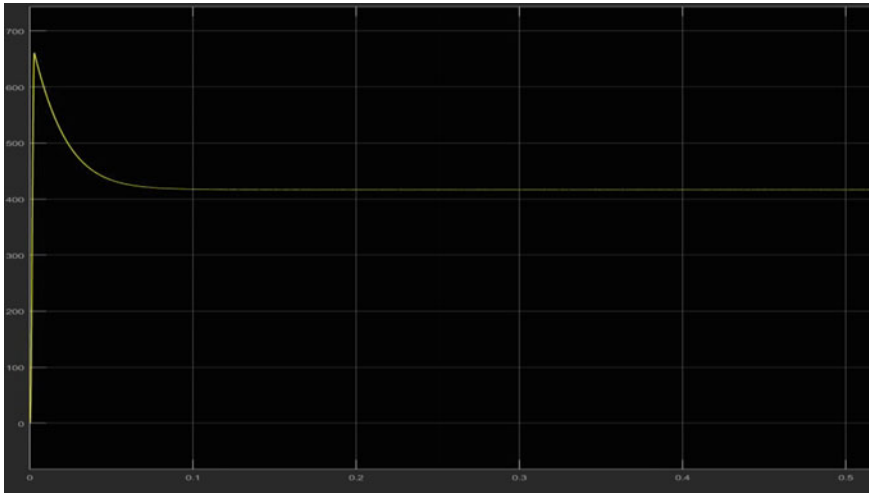


Fig. 11.7 Response of booster circuit

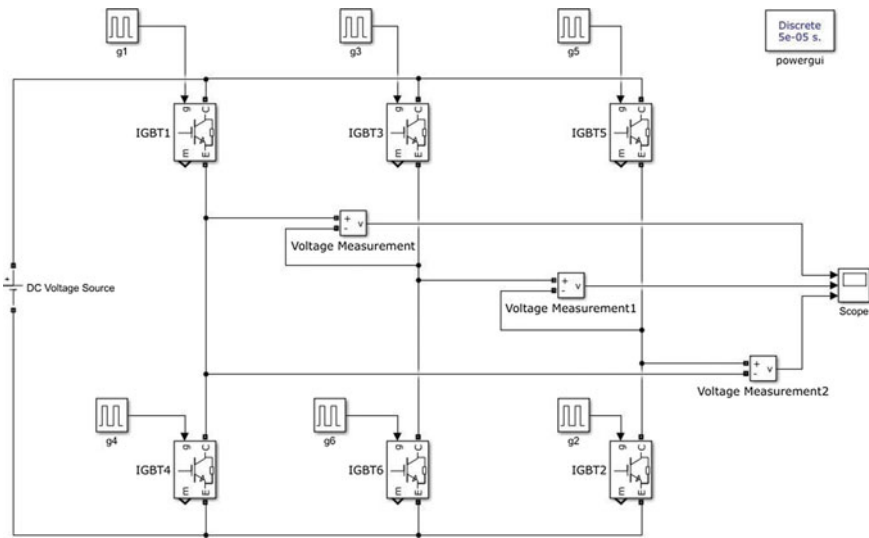


Fig. 11.8 Inverter circuit

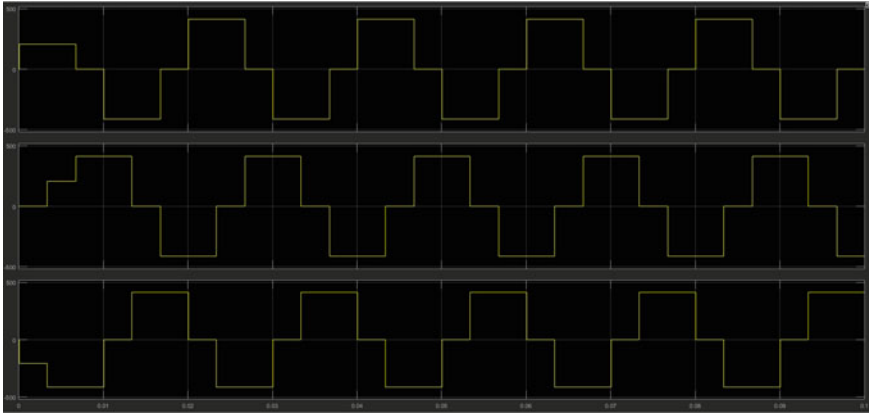


Fig. 11.9 Multi-phase response of inverter circuit for bio-hybrid tractor

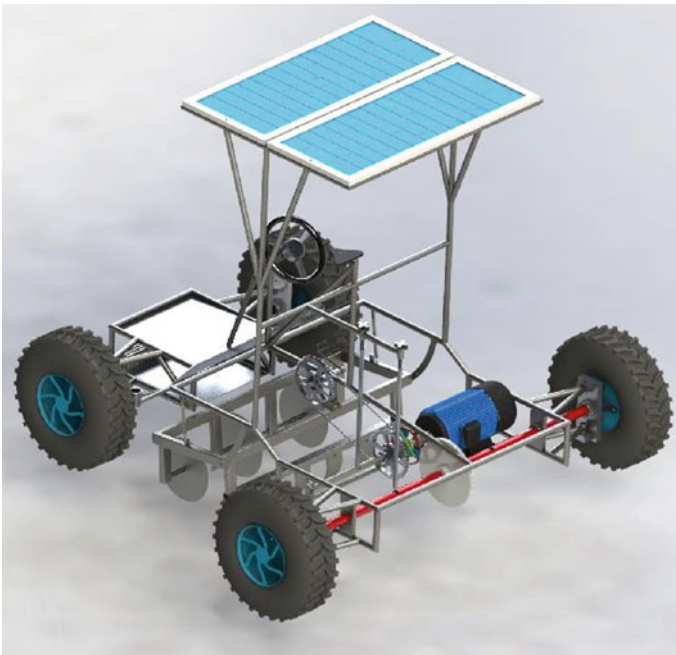


Fig. 11.10 Three-dimensional model of bio-hybrid tractor (BHT)

The steering used is having rack and pinion gear system and attached to the knuckle joint with the help of tie rods. The tyres used are customized so as to decrease the overall weight. The rim is designed with aluminium alloy so as to reduce the overall weight.

It was required to bring centre of gravity (CoG) to the centre so that the plough can be kept at the centre portion of the chassis and the height is changed manually with the help of adjusters provided in chassis. In order to increase the ground clearance, the chassis is made in two parallel planes with the increased height. Solar panels are kept at the centre above the rider seat which can help to prevent the direct exposure to the sun. The solar panel dimensions are kept maximum so as to incorporate maximum cells of solar panels. Two screw threads are provided so as to lock the shafts for different operating conditions. One screw can lock the manual drive shaft, and thus, the vehicle can run only on electric mode. The other screw locks the output shaft, and hence, the pedalling force is used for charging the batteries in this mode.

11.4 Conclusions

Bio-hybrid tractor has been proposed in this work to address the need of increasing demand of sustainable farming as well as to provide an alternate way of farming for poor farmers and low-scale farming.

The bio-hybrid tractor developed is a novel product being the first ever hybrid tractor which combines human effort with electric power. It has the capability to run in manual, assisted and fully electric mode. Also, it can be charged via multiple methods which include solar charging, charging via grid and charging via pedalling.

When the vehicle is running at a velocity of 15 km/h with ploughing, this vehicle requires a total power of 3531 W, out of which 289 W [18, 19] of energy can be provided by the rider's pedalling force. The remaining power will be supplied by an electric motor, which comes about 92%. In this layout, 8% power is provided by human being and remaining is provided by other sources, which include solar PV panels which can charge the batteries in 15 h under non-operating conditions.

The future scope of the project is to use the charged battery packs for lighting homes in remote areas, where electric transmission lines are not viable. Thus, BHT can be considered as prospective product for remote areas and low-scale farming.

References

1. Shafiee, S., Topal, E.: When will fossil fuel reserves be diminished? *Energy Policy* **37**(1), 181–189 (2009). <https://doi.org/10.1016/j.enpol.2008.08.016>
2. Grisso, R.D., et al.: Predicting tractor diesel fuel consumption (2010)
3. Dresselhaus, M.S., Thomas, I.L.: Alternative energy technologies. *Nature* **414**(6861), 332 (2001). <https://doi.org/10.1038/35104599>

4. Veiga, I.A., Zymler, R., Shayani, R., Viana, D., Orrico, M.M.: Sizing of motor and battery pack for an automotive electric vehicle given a specific route. In: 2012 Sixth IEEE/PES Transmission and Distribution: Latin America Conference and Exposition (T&D-LA) (2012). <https://doi.org/10.1109/tdc-la.2012.6522595>
5. Mousazadeh, H., et al.: Optimal power and energy modeling and range evaluation of a solar assist plug-in hybrid electric tractor (SAPHT). *Trans. ASABE* **53**(4), 1025–1035 (2010)
6. ASABE Standards: D497.4: Agricultural Machinery Management Data. ASABE, St. Joseph (2006)
7. Larminie, J., Lowry, J.: *Electric Vehicle Technology Explained*. Wiley (2012)
8. Mousazadeh, H., et al.: Evaluation of alternative battery technologies for a solar assist plug-in hybrid electric tractor. *Transp. Res. Part D: Transp Environ* **15**(8), 507–512 (2010)
9. Carignano, M.G., Cabello, J.M., Junco, S.: Sizing and performance analysis of battery pack in electric vehicles. In: 2014 IEEE Biennial Congress of Argentina (ARGENCON) (2014). <https://doi.org/10.1109/argencon.2014.6868502>
10. Ehsani, M., et al.: *Modern Electric, Hybrid Electric, and Fuel Cell Vehicles*. CRC Press (2018)
11. Chmelicek, P., et al.: Dual rotor magnetically geared power split device for hybrid electric vehicles. In: 2017 IEEE International Electric Machines and Drives Conference (IEMDC). IEEE (2017)
12. Dagci, O.H., Peng, H., Grizzle, J.W.: Hybrid electric powertrain design methodology with planetary gear sets for performance and fuel economy. *IEEE Access* **6**, 9585–9602 (2018)
13. Rashid, M.H.: *Power Electronics Handbook*. Academic Press (2007)
14. Hendawi, E., Bedir, I.: Analysis and simulation of three phase sinusoidal PWM Inverter fed by PV array. *Int. J. Sci. Eng. Res.* **5**(6) (2014). ISSN 2229-5518
15. Bhimra, P.S.: *Power Electronics*. Khanna Publishers, New Delhi
16. Rai, J.N.: Design and analysis of DC-DC boost converter. *Int. J. Adv. Res. Innov.* **4**(3), 499–502 (2016). ISSN 2347-3258
17. Du, H., Lai, X., Liu, C.: Design of a synchronous boost DC–DC converter with constant current mode control in MPP. *Analog Integr. Circ. Sig. Process* **84**(2), 223–235 (2015). <https://doi.org/10.1007/s10470-015-0567-2>
18. TeMorenga, L., Mallard, S., Mann, J.: Dietary sugars and body weight: systematic review and meta-analyses of randomised controlled trials and cohort studies. *BMJ* **346**, e7492 (2013). <https://doi.org/10.1136/bmj.e7492>
19. Atkinson, G., Peacock, O., Gibson, A.S.C., Tucker, R.: Distribution of power output during cycling. *Sports Med. (Auckland, N.Z.)* **37**, 647–667 (2007). <https://doi.org/10.2165/00007256-200737080-00001>

Chapter 12

Study of Lightweight Mortar by Replacing Cement and Aggregates with Admixtures



Pankaj Sharma , Rajat Gupta , Kshethra Pradeep , Hritik S. Kothari 
and A. Sofi 

Abstract The research focuses on the study of admixtures used for producing lightweight mortar by replacing cement and fine aggregates. Mortar is a composition of water, fine aggregate and binding material. The concept of sustainable development and reduction in environmental degradation has been the talk of the hour for numerous years, and its application in the field of civil engineering is inevitable. Since cement production has multiple adverse effects on the environment and also the excessive instream sand mining causes the degradation of rivers, the objective of this research is to replace cement with metakaolin, silica fumes, ground granulated blast furnace slag (GGBS), lime and nano-silica materials. Plenty of aforementioned admixtures are basically waste products. Solid glass beads and cenosphere are used to replace sand entirely. Fifteen mix designs of different composition have been tested and analysed. Variety of tests including ultrasonic pulse velocity test, split tensile strength test and compressive strength test was performed to determine structural characteristics of the concrete mix. The optimum percentage of substitution is as follows: cement (35%), metakaolin (28%), silica fumes (12%), slag (15%), lime (10%) and nano-silica (0%). The selected mortar samples were characterized by the means of destructive and non-destructive tests, and the efficient mortar mix was analysed using scanning electronic microscope (SEM analysis).

Keywords Cement · Metakaolin · Silica fume · Slag · Lime · Nano-silica · Mortar

P. Sharma · R. Gupta · K. Pradeep · H. S. Kothari
School of Civil Engineering, VIT Vellore, Vellore, India

A. Sofi (✉)
Department of Structural and Geotechnical, School of Civil Engineering, VIT Vellore, Vellore,
India
e-mail: asofi@vit.ac.in

12.1 Introduction

Mortar is construction material which consists of binding materials such as cement (ordinary Portland cement or pozzolana Portland cement) and some cementitious materials like silica fumes, GGBS, nano-silica particles, fly ash, metakaolin and fine aggregates being sand, solid glass beads and cenosphere along with water and chemical admixtures.

The admixture is the substance which is used as an ingredient to the batch immediately during mixing to enhance its performance. There are two types of admixtures, namely mineral admixtures and chemical admixtures. During the study, the following admixtures were taken into account:

- Mineral admixture: metakaolin, silica fumes, slag, lime and nano-silica
- Chemical admixture: MasterGlenium SKY 8941.

The capacity of every admixture centres around a particular requirement, and each has been created freely of the others. A few admixtures as of now have science that influences in excess of a particular property of cement and some have merely been mixed in order to ease the addition amid the batching process.

The specific gravity of each mineral admixture and lightweight aggregates is given in Tables 12.1 and 12.2.

In this study, high replacement of cement is achieved through various mineral admixtures which are by-products of different industries; hence, the objective of elevating the sustainability of mortar mix is obtained. Mortar mix consists of lightweight aggregates which result in the very low density of mortar [1]. The advantages of such mortar mix include decreased self-weight of the structure and increased strength.

Table 12.1 Specific gravity of cementitious components

Cementitious	
Component	Specific gravity
Cement (OPC 53)	3.15
Metakaolin	2.6
Silica fumes	2.2
GGBS	2.4
Nano-silica	0.3
Lime	2.3

Table 12.2 Specific gravity of aggregates

Aggregates	
Component	Specific gravity
Cenosphere	0.8
Solid glass sphere	2.3

12.2 Experimental Procedure

Fifteen different mixes were studied during the analysis. Different mixtures had different proportions of cementitious materials and lightweight aggregates according to specific gravity and strength comparison. Superplasticizer is used to maintain constant workability. The main variable in the mix is cement which has to be replaced with different proportions of cementitious materials. The main objective was to obtain a design which is both lightweight and of adequate strength. Due to the high replacement of cement with mineral admixtures and to perform easier calculations, weight batching was adopted over standard volume batching throughout the study.

The ratio of cementitious to lightweight aggregates is adopted as 1:0.7 by weight, in which the proportion of lightweight aggregates varies as per requirement.

Scanning electron microscope analysis, X-ray diffraction and three tests were performed, namely:

- Compressive strength test
- Split tensile strength test
- Ultrasonic pulse velocity test.

For compressive strength (IS 516: 1959) test cubes of dimensions, 50 mm * 50 mm * 50 mm were used. Mortar mix of mentioned water–cement ratio was prepared and filled in the moulds. After filling, the vibratory machine was adopted for compacting the mix into layers, following the surface finish by trowel. The sample is then stored at room temperature (27 ± 2 °C) for 24 h and then kept inside the curing tank. At the interval of 7 and 28 days, samples were removed from the tank, and their testing was then done by the compressive testing machine accordingly.

To perform split tensile strength (IS 5816: 1999), test cylinder moulds of 100 * 200 mm were adopted. After casting and curing of the test specimen of the most optimum mix (in order to reduce the wastage of material) for desired no. of days, the cylinder was horizontally carried in between the compression testing machine with two wooden plates of 5 mm above and below the specimen. Load on the specimen was continuously applied till failure of the cylinder, along with the vertical diameter.

For ultrasonic pulse velocity, test cylinder moulds of 100 * 200 mm are used. After casting and curing of the cylinders are working out for the desired amount of days, cylinders are kept between the two transducers which are connected via pulse generator. The velocity of travel can be calculated by dividing path length from the time taken for its travel.

$$V(\text{m/sec}) = L(\text{metres})/T(\text{sec})$$

The concrete quality according to the range of pulse velocity is mentioned below in Table 12.3.

Table 12.3 Relation between pulse velocity and concrete quality

Pulse velocity (m/s)	Concrete quality
Greater than 4500	Excellent
4000–4500	Very good
3500–4000	Good
3000–3500	Doubtful
2000–3000	Poor
Less than 2000	Very poor

12.3 Materials and Mix Proportion

12.3.1 Cement

Ordinary Portland cement 53 grade (Brand: Ramco Cements) was used in this study confirming to IS: 12269-1987 for control mix [2].

12.3.2 Metakaolin

Metakaolin is a pozzolanic material produced for a definite purpose under carefully controlled circumstances conforming to the requirement of IS-456 [3]. Metakaolin is manufactured by heating kaolin, one of the profusely found natural clay minerals, to the conditions of 650–900 °C [4]. Flexural strength increases when metakaolin is used and reduce the specific gravity of the mix [5]. It also enhances workability and refines the pore structure of the mix.

12.3.3 Silica Fume

Silica fume is a by-product of ferrosilicon industry and formed in electric arc furnaces as a result of the production of elemental silicon or silica alloys [6]. It is a pozzolanic material. When it is added to concrete, it remains unreacted initially. Once the hydration reaction between Portland cement and water starts, it results in two compounds: calcium silicate hydrate (CSH gel) that is responsible for the strength and calcium hydroxide (CH), a derivative also named as free lime that causes leaching and increases pH of concrete.

The chemical reaction occurs between calcium hydroxide and silica fume, which creates additional CSH gel in many of the voids around hydrated cement particles. The additional CSH gel formed during this reaction not only enhanced compressive, tensile and bond strength of concrete but also lead to a much denser matrix, mostly

in stretches that would have remained as small voids subject to possible admission of deleterious materials [7]. Silica fumes also provide early strength to the concrete.

12.3.4 Lime

Lime is an inorganic material which mainly consists of calcium in which carbonates, hydroxides and oxides dominate. In other words, lime is calcium hydroxide or calcium oxide. It is a naturally occurring mineral which formed as an output of coal seam fires and in altered limestone xenoliths in volcanic ejecta. The word lime derives with its primal use as construction mortar and has the sense of fixing or adhering.

Following is the composition of lime: SiO₂ (0.43%), Al₂O₃ (0.07), Fe₂O₃ (0.06), CaO (65.21%), MgO (12.34%), MnO (0.01%), SO₃ (0.08%), LOI (21.76%) and others (0.04%) [8]. *LOI represents loss on ignition*

12.3.5 Granulated Blast Furnace Slag (GGBS)

GGBS is produced by swiftly cooling the molten ash from the blast furnace ash by a drive of water. While this development takes place, the slag gets disintegrated and transformed into amorphous granules (glass), which is the requirement of IS 12089:1987 [9, 10].

It enhances the workability and final strength of concrete. It also increases the durability of concrete [11].

12.3.6 Nano-Silica

Nano-silica is the nanoparticle of silicon dioxide. It has a density ranging between 0.2 and 0.5 g/cc.

It is generally a very active cementitious material. It typically contains ultra-fine vitreous particles which are nearly 1000 times smaller than the normal cement granules. It has recognized to be one of the best mineral admixtures for the cement to enhance durability and strength. Crystallization of nano-sized crystals of quartz or direct synthesis of silica sol leads to the formation of nano-silica [7].

The particles of nano-silica fill voids present between CSH gel structure and hence decrease the permeability which leads to denser and high strength concrete.

It serves as a nucleus to firmly bond with particles of CSH gel. Hence, the use of nano-silica leads to the reduction in leaching due to calcium hydroxide and enhance the durability of concrete or mortar.

12.3.7 Mixture Proportion

Mix proportion of each mix is shown in Table 12.4 [12].

12.3.8 Solid Glass Spheres

Solid glass spheres possess high density ranging between 2.2 and 2.6 g/cc. They also have high crushing strength making them fit for high-stress structures where these microspheres are exposed to very large stress during processing or application. They are used to provide strength to our mix.

The solid glass sphere used in this study has a size of 450 μm . The chemical composition (%) of this is mentioned in Table 12.5 [13].

12.3.9 Cenosphere

The word cenosphere is coined from two Greek words: kenos (hollow) and sphaira (sphere) that describes the major properties of this material [14]. These are spherical particles which have a hollow centre.

Cenosphere is formed in thermal power plants during the burning of coal. They are produced at very high temperature (1500–1750 °C) [14]. They are ceramic particles present in fly ash which is majorly made up of alumina and silica [7]. They have a very low density ranging from 0.7 to 1.0.

12.3.10 Water

Clean potable water has been used for mixing and curing of concrete [4]. Bore water from college campus is confirmed to be good for drinking.

12.3.11 Chemical Admixture (MasterGlenium SKY 8941)

MasterGlenium SKY 8941 is a new generation admixture that is primarily based on modified polymeric ether. The above product was mainly developed for its application in high-performance concrete owing to high durability and performance that it provides [15]. It is free of chloride and low alkali and is also compatible with all types of cement.

Table 12.4 Mix proportions table

Cementitious	1	2	3	4	5	6	7	8	9	10	11	12	13	14	15
Cement (%)	35	35	35	35	35	35	35	35	35	35	35	35	35	35	35
Metakaolin (%)	30	30	30	25	30	30	28	26	30	28	30	30	30	32	28
Silica fumes (%)	10	10	10	15	10	10	15	15	10	10	10	13	15	15	12
GGBS (%)	15	25	15	25	13	13	20	20	13	15	10	10	5	5	15
Lime (%)	10	0	10	0	10	10	0	0	10	10	15	10	13	10	10
Nano-silica (%)	0	0	0	0	2	2	2	4	2	2	0	2	2	3	0
Aggregates															
Cenosphere (%)	60	60	65	60	65	60	60	65	60	60	65	65	65	60	68
Solid glass sphere (%)	40	40	35	40	35	40	40	35	40	40	35	35	35	40	32
Water (ml)	115	115	119	121	123	122	128	130	125	135	135	140	130	130	130
Superplasticizer (ml)	3	3	3	3	7	7	7	7	8	6.5	6.5	7.5	5	6	5

Table 12.5 Chemical composition of solid glass spheres

SiO ₂	<5
Na ₂ O	12–15
K ₂ O	<1.5
CaO	7–12
MgO	<5
Fe ₂ O ₃	<0.5
Al ₂ O ₃	<2.5
SO ₃	<0.5

Benefits and Features

- A remarkable increase in early and ultimate strengths.
- Increased elastic modulus.
- Improved adhesion to reinforcing and stressing steel.
- Improved resistance to carbonation and other.
- Extreme atmospheric conditions.
- Decreases permeability and enhanced durability of concrete.
- Reduction in creep and shrinkage.

12.4 Results and Discussion

In this study, destructive and non-destructive tests were performed on the above-mentioned mixes. Destructive test such as compressive strength and split tensile and non-destructive includes ultrasonic pulse velocity (UPV) test. Scanning electronic microscope (SEM) and X-ray diffraction analysis have been performed on the final selected optimum mix.

12.4.1 Analysis of Variation of Compressive Strength

Compressive strength test is performed at 7 and 28 days [16]. The values of the compressive strength of mortar mixes with different dosage of admixtures are shown in Figs. 12.1 and 12.2.

As we can observe in the graph that mix no. 14 has the highest compressive strength, and mix no. 11 has the lowest 30 and 5 MPa, respectively. It can also be observed that the percentage of metakaolin is highest in the mix no. 14. It also has the highest early strength due to the presence of silica fumes and metakaolin [16, 17]. From mix no. 14, it can be concluded that the optimum replacement of nano-silica particles is 3%. The reason behind the least strength of 11th mix is that it has a high replacement of lime along with no replacement with nano-silica. Inclusion to this, the

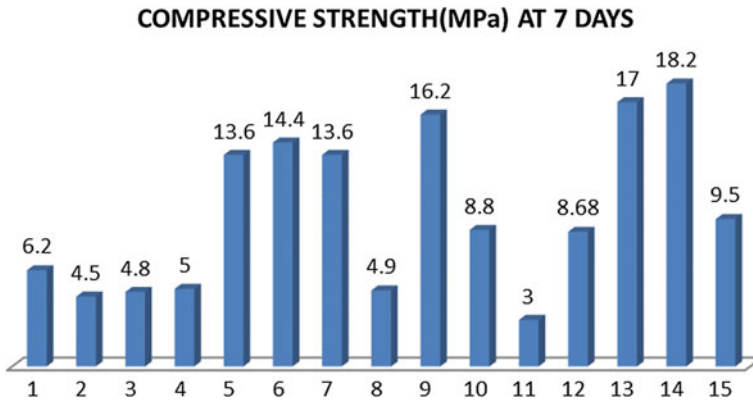


Fig. 12.1 Compressive strength at 7 days

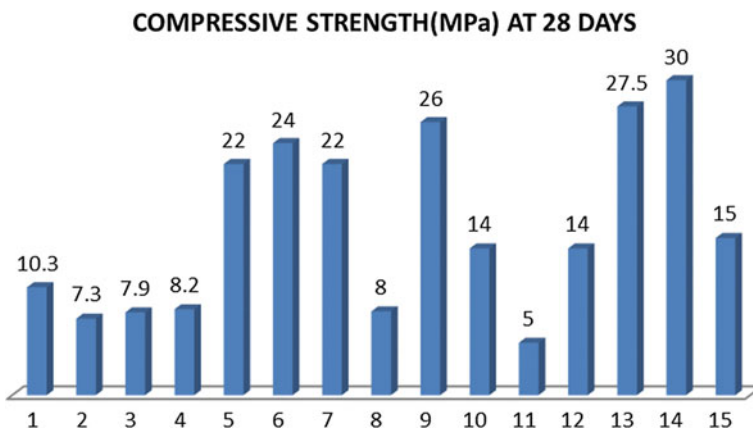


Fig. 12.2 Compressive strength at 28 days

ratio of solid glass sphere is less which results in depletion of compressive strength of mortar.

12.4.2 Analysis of Specific Gravity

The specific gravity of mortar with different dosage of admixtures is shown in Fig. 12.3. The specific gravity of mortar or concrete majorly depends upon the optimum ratio of aggregates. From our study, the mix 15th has the lowest specific gravity which is achieved due to the optimum percentage dosage of aggregates, i.e. cenosphere and solid glass sphere 68 and 32%, respectively. The reason behind reducing the percentage of nano-silica to 0% is that it has a very low particle size which leads

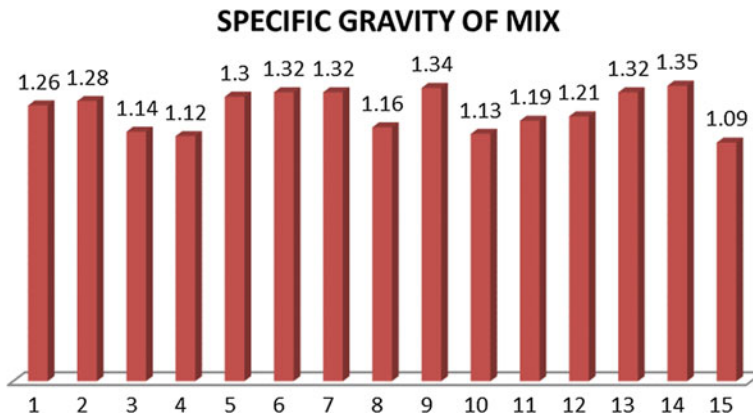


Fig. 12.3 Specific gravity of different mixes

to refinement of pore structure and hence increases the overall density of mortar. To achieve a lower density of mortar, the optimum percentage of silica fumes is obtained 12%.

12.4.3 Analysis by X-ray Diffraction and Scanning Electron Microscope (SEM)

SEM and X-ray diffraction examination have been performed only on the optimum mortar mix. These tests are engaged to analyse the microstructure and quality assurance by providing the elemental composition of the mix and are shown in Fig. 12.4a–c. From the X-ray diffraction, it has been observed the availability of calcium and silicon is more which results in adequate compressive strength even at low specific gravity.

12.4.4 Ultrasonic Pulse Velocity Test (UPV Test)

Ultrasonic pulse velocity test has been performed on every mix to check the homogeneity and uniformity of the mortar.

The values of ultrasonic pulse velocity of different mortar mixes are obtained from the UPV test and shown in Fig. 12.5 [18].

It can be observed that there is no such linearity relationship between ultrasonic pulse velocity and specific gravity since uniformity of mix is depending upon the pore structure of the mortar mix. The uniformity of the matrix mainly depends on

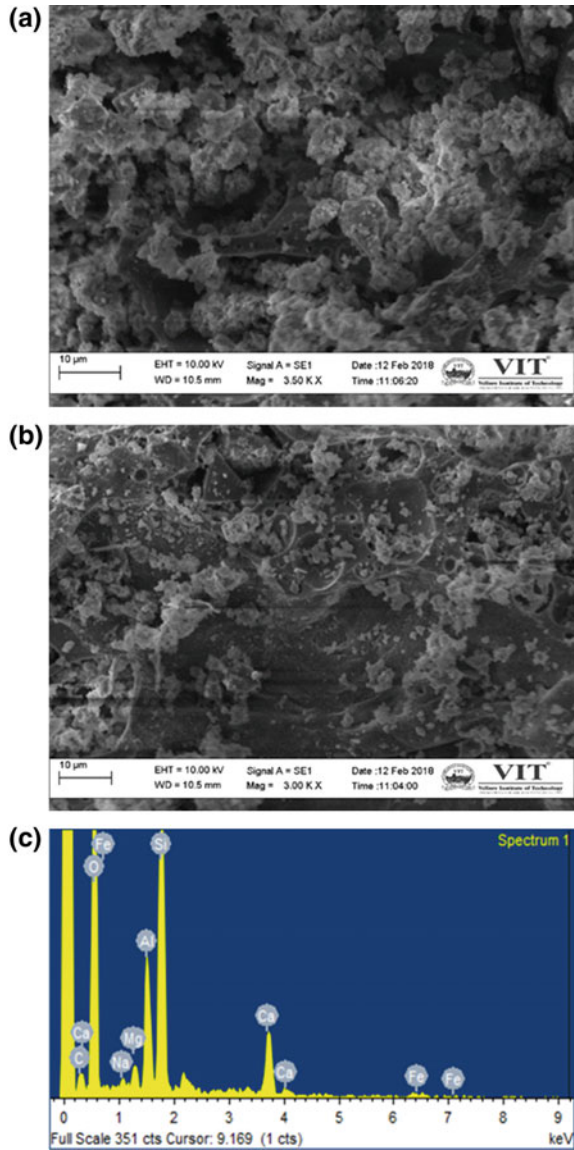
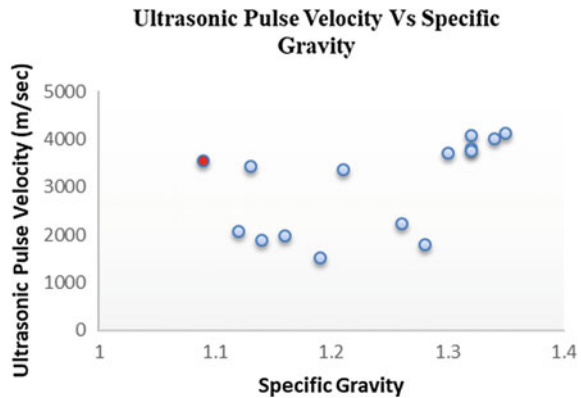


Fig. 12.4 a–c Elemental composition/microstructure of mix

Fig. 12.5 Ultrasonic pulse velocity with respect to specific gravity



the particle distribution with different composition of aggregates and cementitious materials.

It is also observed that the value of ultrasonic pulse velocity of the optimum mix is within permissible value, and hence, mix no. 15 is homogenous.

12.4.5 Relation Between Specific Gravity and Compressive Strength

Generally, concrete or mortar having high specific gravity has high compressive strength also [16]. But from Table 12.6, it can be observed that the relation between both is not always linear.

The values of compressive strength of mix 7th and 13th are different, but they have the same specific gravity 1.32.

It is not required to have high compressive strength for mortar so the aim of this study is to achieve a mortar mix which has adequate compressive strength along with low specific gravity.

12.4.6 Tensile Strength of Optimum Mix

The split tensile test has been performed on the optimum mix only to check the tensile strength of the mortar mix. The value of tensile strength obtained for the optimum mix is 0.95 MPa [19].

Table 12.6 Specific gravity versus compressive strength

Mix no.	1	2	3	4	5	6	7	8	9	10	11	12	13	14	15
Specific gravity	1.26	1.28	1.14	1.12	1.3	1.32	1.32	1.16	1.34	1.13	1.19	1.21	1.32	1.35	1.09
Compressive strength	10.3	7.3	7.9	8.2	22	24	22	8	26	14	5	14	27.5	30	15

12.5 Conclusions

This research was performed to study the effects of lightweight mortar by replacing cement and aggregates with admixtures. The properties investigated were compressive strength, tensile strength, specific gravity and ultrasonic pulse velocity. Specimens have been analysed by X-ray diffraction and scanning electron microscope.

From the above results presented in this paper, the following conclusion is offered:

- Specific gravity and compressive strength of the optimum mix (15th) obtained are 1.09 and 15 MPa, respectively.
- The lowest specific gravity and adequate compressive strength among all the mixes are obtained on adding 68% of cenosphere and 32% of solid glass spheres.
- Compressive strength is not a linear function of specific gravity.
- Increase in percentage of metakaolin results in increased compressive strength.
- Incorporation of nano-silica in the mix leads to an increase in specific gravity as well as compressive strength.
- Better workability is achieved by increasing the percentage of GGBS even at a low dosage of superplasticizer.
- Increase in solid glass spheres results in high compressive strength but also increases the specific gravity of the mix.
- The inclusion of silica fumes and nano-silica provides better cohesiveness to mortar and reduces segregation.

Acknowledgements The authors would like to express our token of gratitude to Dr. Sofi A. and the school of civil engineering (SCE), Vellore Institute of Technology, Vellore, for giving us the golden opportunity to work on this experimental work.

References

1. Shetty, M.S.: Concrete Technology. S. Chand and Company, New Delhi, India (2011)
2. ASTM Designation C 150-00: Standard Specification for Portland cement. Annual Book of ASTM Standards. Designation: C 150-07 (2005)
3. John, N.: Strength Properties of Metakaolin Admixed Concrete, pp. 3–6 (2013). ISSN 2250-3153
4. I.S. Code 456-2000: Code of practice for plain and reinforced concrete. ICS 91.100.30
5. Cai, R., He, Z., Tang, S., Wu, T., Chen, E.: The Early Hydration of Metakaolin Blended Cements by Non-Contact Impedance Measurement, pp. 70–73. <https://doi.org/10.1007/s10973-013-3512-6>
6. Rasol, M.A.: Effect of Silica Fume on Concrete Properties and Advantages for Kurdistan Region, Iraq (2015). ISSN 2229-5518
7. Rai, S., Tiwari, S.: Nano Silica in Cement Hydration, NCNN, pp. 9197–9200 (2017)
8. Suthar, M., Aggarwal, P.: Bearing Ratio and Leachate Analysis of Pond Ash Stabilized with Lime and Lime Sludge, vol. 10, Issue 4, pp. 769–777 (2018). <https://doi.org/10.1016/j.jrmge.2017.12.008>
9. IS 12089: Specification for Granulated Slag for the Manufacture of PORTLAND SLAG CEMENT, pp. 666–943. UDC 66G9 022-492

10. Das, S., Singh, G., Ahmed, A.A., Saha, S., Karmakar, S.: Ground Granulated Blast Furnace Slag (GGBS) based Concrete Exposed to Artificial Marine Environment(AME), pp. 2805–2808 (2018)
11. Suresh, D., Nagaraju, K.: Ground Granulated Blast Slag (GGBS) In Concrete—A Review, pp. 76–78
12. IS 10262:2009: Indian Standards Recommended Guidelines for Concrete Mix Design. ICS 91.100.30
13. Technical Data Sheet (Glass Beads)—Surface Finishing, Peening & Blasting, Masterblast, pp. 1–2
14. Ranjbar, N., Kuenzel, C.: Cenospheres: A Review, pp. 2–5 (2017). <https://doi.org/10.1016/j.fuel.2017.06.059>
15. Material Datasheet of MasterGelium SKY8941 by O-BASF
16. IS 516: Method of Tests for Strength of Concrete. UDC 666.97. 620 17 (1959)
17. Iffat, S.: Relation Between Density and Compressive Strength of Hardened Concrete, vol. 6, Issue no. 4, pp. 182–186 (2015)
18. IS 13311-1: Method of Non-Destructive Testing of Concrete, Part 1: Ultrasonic Pulse Velocity. UDC 666-972-620-179.16
19. ASTM C496: Standard Test Method for Splitting Tensile Strength of Cylindrical Concrete Specimens. Annual Book of ASTM Standards. Designation: C 496/C 496M–04 (2005)

Chapter 13

Design of a Domestic Defluoridizing Unit



Shaheda Parveen, Venkata Nadh Ratnakaram , Sireesha Malladi and K. Kiram Kumar

Abstract While trace amounts of fluorine are essential for life, its excessive intake leads to a disease known as fluorosis. It is a predominant ailment in majority of the countries inclusive of India. It is caused also by drinking fluoride containing water. Retention of fluorine in bones and teeth occurs through $F^--(OH^-)$ exchange on their inorganic component known as hydroxylapatite. Endeavour of the present study is to design a column using activated alumina as an adsorbent for continuous defluoridation of water for domestic purpose. As a part of it, operational defluoridation capacity of alumina was determined by variation of different factors (amount of alumina, time, temperature, added salts). A family of four members was taken as a model. The initial and final fluoride concentrations were taken as 2.0 and 0.7 ppm, respectively. Dimension of the unit (adsorbent bed diameter and height) was determined.

Keywords Design · Domestic defluoridizing unit · Fluorosis

13.1 Introduction

Human beings and animals suffer from fluorosis due to extended acquaintance with fluoride containing water, air or food. India stands in the top listed countries which are challenged with fluorosis problem in view of obligatory consumption of water having high quantities of fluoride (1–48 ppm) [1]. In India, Andhra Pradesh State is one among the many affected belts by endemic fluoride [2]. As per Indian standards,

S. Parveen

Department of Chemistry, Madurai Kamaraj University, Madurai 625021, India

V. N. Ratnakaram (✉)

GITAM University, Bengaluru Campus, Bengaluru 561203, Karnataka, India

e-mail: doctormadh@yahoo.co.in

S. Malladi

Department of Science and Humanities, Division of Chemistry, VFSTR, Vadlamudi 522213, India

K. Kiram Kumar

Department of Chemistry, KBN College, Vijayawada 520001, India

© Springer Nature Singapore Pte Ltd. 2020

B. Subramanian et al. (eds.), *Emerging Technologies for Agriculture and Environment*, Lecture Notes on Multidisciplinary Industrial Engineering, https://doi.org/10.1007/978-981-13-7968-0_13

acceptable limit of fluoride concentration in drinking water is 1.0 mg L^{-1} , whereas its permissible limit is 1.5 mg L^{-1} [3]. Though higher concentrations of fluoride cause fluorosis, its lower concentration is proved to be useful. Fluoride plays a vital role in mineralization of some of the hard tissues [4]. Fluoride is added to community water in some of the countries including USA as a part of health measure in order to inhibit dental decay [5]. Fluoride concentration in mg L^{-1} and associated potential health effects can be given as: <0.5 (dental carries are prevented minimally), $0.5\text{--}1.5$ (favourable to prevent the dental carries), $1.5\text{--}4$ (causes dental fluorosis), $4\text{--}10$ (dental and skeletal fluorosis) and >10 (crippling fluorosis) [6]. Dental fluorosis can be easily recognized by symptom—mottling of teeth [7].

About 300 mg of fluorine per kg is its abundance in earth crust [8]. Fluorspar, cryolite and fluorapatite are some of the fluorine-containing minerals which undergo weathering process leading to its accumulation in soil and hence in water [9]. In some of the areas like Ethiopian Rift Valley, high fluoride concentration in drinking water can be related to volcanic deposits being the natural fluoride sources [10]. High concentrations of fluoride were noticed in thermal waters having basic pH [11]. Different anthropogenic and industrial activities release fluoride into the environment. Some of them are manufacturing units of fertilizers, pesticides, glass, electronics and aluminium [12].

Water supply in rural areas of a maximum number of countries is suffering from poor quality and quantities. Ion exchange, reverse osmosis (RO) and electro-dialysis are the popular methods in developed countries, but they require high capital cost, maintenance and technical backing [13]. Problems in disposal of large volumes of sludge and high operational cost are opposing the adopting the well-known Nalgonda technique. The other defluoridation methods (adsorption, nanofiltration, ion exchange, solar distillation and reverse osmosis) have their own advantages and disadvantages. Hence, adoption of the method must be based on local needs. Compared to other defluoridation methods, adsorption method is more preferable in view of easy operation, lack of sludge formation, low capital cost and easy replacement of exhausted bed [14]. However, the well-known adsorbent—animal charcoal—is facing resistance due to the prevailing social customs. Though a large number of cost-effective biosorbents are reported for defluoridization in the literature, their technical usage in rural areas is not possible in immediate course of time. In spite of availability of a wide variety of adsorbents, AA is the best choice in developing countries. Hence, activated alumina is selected as an adsorbent in the present study.

The rural community in Chebrolu mandal has been distressed by fluorosis (both dental and skeletal) due to consumption of water having more fluoride concentration than the permissible limits. Chebrolu mandal of Guntur District, Andhra Pradesh, was taken as one unit for fluoride estimation in groundwaters. Apart from fluoride estimation, chloride and total hardness were also estimated. Based on this compilation, it is found that in some villages like Gudavarru and Veera Nayakuni Palem, the fluoride concentration is more than the limit 1.5 ppm given by WHO. An effort has been made to design an economically practicable defluoridation unit with continuous flow, which can be used in rural areas.

13.2 Experimental

13.2.1 Selection of Activated Alumina

The literature survey shows that cost of the treated water by activated alumina is less compared to other defluoridizing agents [15]. Compared to adsorption of CaCO_3 (0.03 mg F^- per g), activated alumina is proved to be better adsorbent (0.57 mg F^- per g) [15, 16]. A number of researchers are worked on defluoridation of water using AA since the suggestion of Boruff [17]. Bulusu and Nawlakhe [18] established that its sorption capacity is variable and depends on water quality parameters, ionic environment and regeneration procedures. Simultaneous occurrence of different reactions at AA surface (like ion exchange and hydrolysis) causes a variation in surface electrokinetic properties [19]. It helps to increase the sorption of fluoride ions due to a decline of negative charges at its surface [18]. Hence, activated alumina was selected as an adsorbent for defluoridation of water. Commercially available technical grade activated alumina granules supplied by Sethiya Solvents & Chemicals, Tamil Nadu, were used.

13.2.2 Batch Adsorption Studies

In each system, 300 mL of water (containing 2 ppm of fluoride, 113 ppm of chloride, 420 ppm of total hardness) is taken in a 500-mL polyethylene container and maintained at 31 °C. The solution is stirred at 240 rpm mechanically for definite period after the addition of desired amounts of adsorbent. The suspension is filtered through a sintered crucible (G4). The filtrate is tested for fluoride by SPADNS method, chloride by silver nitrate method and hardness by EDTA method [20]. The final fluoride concentrations were measured by Zr-SPADNS method [21]. The fluoride concentration in the sample after defluoridation is calculated from absorbance value of its coloured solution and standard curve. The same procedure is adopted for all the experiments carried out by varying amount of adsorbent, contact time, temperature and added salts. The percentage removal of fluoride/chloride/total hardness of water is calculated from C_0 (initial concentration in solution) and C_e (final concentration in solution after adsorption).

13.3 Results and Discussion

13.3.1 Batch Mode Defluoridation of Water by Activated Alumina

It is very well-known fact that activated alumina acts as an efficient defluoridizing agent. Therefore, it is thought worthwhile to know the effect of various factors affecting the defluoridation capacity of activated alumina, before designing the column for continuous defluoridation of water using activated alumina as an adsorbent.

It is observed that with an increase in the amount of activated alumina, an increase in the % removal of fluoride is observed (Fig. 13.1a). It can be explained based on the increased active sites availability causing an improvement of active surface area, especially at higher adsorbent doses [22]. Afterwards, equilibrium is attained beyond certain dose. The effect of the agitation time on the removal of fluoride ion is shown in Fig. 13.1b, which clearly indicates that the removal of fluoride is fast during early time but turns out to be slow and almost decays with a further rise in the interaction period beyond 10 min. It hints that the fluoride removal rate is greater in the early phase because of availability of sufficient adsorbent surface area. A decrease in adsorption takes place with further increase in contact interaction period because of a decline in the accessibility to the active sites. Percentage of fluoride ion adsorption increased with an increase in contact time and the observed can be endorsed to the point that higher duration makes acquainted the fluoride ion to make adsorb on adsorbent [23]. The maximum adsorption percentage was recorded at 10 min with all adsorbents, and then onwards, sluggishness was observed. Per cent of defluoridation increased up to 31°C and then decreased (Fig. 13.2b). It shows that chemisorption is activated with an increase in temperature. Further confirmation of governing of chemisorption in the fluoride adsorption on activated alumina is evident as it obeys Langmuir's adsorption isotherm [24].

To study the effect of the existence of anions (like chloride) and cations (like calcium) on the defluoridation capacity of water, sodium chloride and calcium chloride were added. There is no effect of added anions like chloride on the defluoridation of

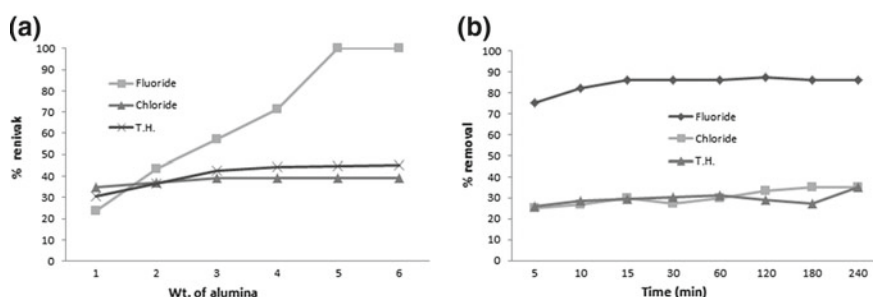


Fig. 13.1 Effect of **a** adsorbent dose and **b** time on % removal of fluoride

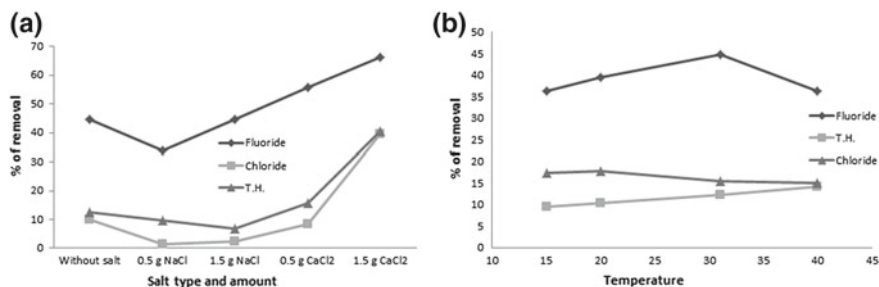


Fig. 13.2 Effect of **a** salt type and amount, and **b** temperature on % removal of fluoride

water as there is no change in the defluoridization capacity with a rise in [chloride ion]. But, the concentration of fluoride decreased progressively with an increase in the concentration of the added calcium chloride (Fig. 13.2a). The observed decrease in fluoride concentration can be attributed to the added calcium ion because there is no effect of chloride ion on defluoridation. Moreover, it is an established fact that the fluoride can be removed as calcium fluoride by the calcium ions. In spite of high affinity towards fluoride by adsorbents containing Al, Zr, Mg and Ca, the presence of some anions (nitrate, sulphate, bicarbonate and phosphate) decreases their affinity [25–27]. Adsorption of chloride and nitrate ions on activated alumina is negligible, whereas sulphate and bicarbonate ions adsorb fairly well. Further, an increase in bicarbonate ions decreases the adsorption of fluoride on activated alumina due to its competitive adsorption [15]. As many other anions are present in the groundwater taken in the present case, the efficiency of fluoride ion adsorption decreases further.

In view of practical conditions, throughout the present study, defluoridation studies were carried out at neutral pH. However, defluoridation capacity of AA was reported as 3, 5.6 and 20 mg g⁻¹ for alkaline, neutral and acidic water, respectively [24]. Davis and Leckie [28] reported that fluoride sorption capacity decreases with an increase in pH due to a decline in the establishment of ligand-like complexes. It is a known fact that defluoridation by adsorption is interfered by hydroxide ions. Defluoridation by activated alumina can be explained by Stern model of double layer. Charge potential on alumina is zero when pH is 9. As hydrogen ion is the potential-determining ion for the surface charge of AA, it is positively charged when [H⁺] is greater (pH < 9). Hence, negatively charged fluoride ion adsorbs on oppositely charged AA. In addition, adsorption process is also governed by “specificity factor” and adsorption order: F⁻ ≫ OH⁻ ≫ HCO₃⁻ ≫ Cl⁻ = SO₄²⁻ [24]. Therefore, defluoridation capacity of AA decreases with an increase in [HCO₃⁻].

13.3.2 Determination of Operational Defluoridation Capacity of Alumina

50 g of activated alumina is added to 1 l of water containing 2 ppm fluoride, 113 ppm chloride and 420 ppm of total hardness and allowed to be at equilibrium for 24 h and then filtered. The amount of removed fluoride is estimated colorimetrically based on the concentration of fluoride in the water before and after adsorption. The process is repeated with the same alumina with the addition of fresh samples of water added at the same amounts fluoride, chloride and total hardness. This process is repeated till there is no defluoridation by the alumina. The total defluoridation capacity is found to be 57 mg fluoride/50 g of alumina. Therefore, operational defluoridation capacity of the alumina is 1.14 mg fluoride/g of alumina. The literature survey shows that adsorption capacities (mg g^{-1}) of AA (OA-25 grade), AA (AD101-F grade), acidic alumina, modified AA and third aluminium hydrate (TAH) are compiled as 1.78, 0.42, 8.4, 0.76 and 25.8, respectively [29]. Probably, there exists a high variance in “degree of activation” in variety of alumina products. Another justification may be a difference in pH in addition to the brand of the product. Most of the previous research works involve the usage of distilled water for fluoride ion solution preparation and high grade alumina with high adsorption capacity. But in the present study, it is based on water having different salts and technical grade alumina. Therefore, the operational capacity—1.14 mg/g—is considered while designing the column for defluoridation.

13.3.3 Design of Continuous Defluoridizing Unit

Compared to other defluoridation methods, packed bed adsorption method is more preferred. Some of its advantages are easier operation, reasonable capital and operational costs, no sludge formation and easy replacement of bed [30]. Batch method faces three main problems, i.e. (1) drying of filter bed and hence shortening of lifetime of filter for intermittent usage, (2) incomplete utilization of adsorbent and (3) limited release of defluoridate water at once. Hence, a continuous defluoridizing unit is designed in the present study. Combined filter contains two filter processes in the same structure to remove fluoride and microbes by using adsorbent and silver nitrate, respectively. However, in view of disadvantages like higher cost, maintenance requirement, low susceptibility to higher turbidity, etc., the concept of combined filters was not considered.

An attempt has been made to design the column using activated alumina as an adsorbent for defluoridation of water continuously for domestic purpose. A family of four members was taken as a model. The initial and final fluoride concentrations are taken as 2.0 and 0.7 ppm, respectively.

Daily personal water demand = $D = 3$ l/consumer/day

Number of users = $N = 4$

Operation period = $OP = 2 \frac{1}{2}$ months = 75 days
 Operational sorption capacity = $C = 1.14$ g/kg
 Bulk density of alumina = $\rho = 1.12$ kg/l
 Raw water fluoride concentration = $F_i = 2.0$ mg/l
 Mean fluoride concentration in treated water = 0.7 mg/l
 Volume ratio supernatant water/medium = $VR_{SW/M} = 0.2$
 Daily water treatment = $Q = D \times N = 12$ l/day
 Overall quantity of treated water in a filter period = $V_T = Q \times OP = 900$ l
 Overall quantity of removed fluoride in a filter period = $F_T = \frac{V_T \times (F_i - F_o)}{1000} = 1.17$ g
 Amount of Al_2O_3 required for renewal = $M = F_T/C = 1.03$ kg
 Volume of Al_2O_3 in filter = $V_M = M/\rho = 0.916$ l $\cong 0.95$ l
 Treated no. of bed volumes during filter period = $BV = \frac{V_T}{V_M} = 982$
 Supernatant water volume capacity = $V_{SW} = VR_{SW/M} \times V_M = 0.183$ l $\cong 0.2$ l
 Total volume of filter = $V_F = V_m + V_{SW} = 0.95 + 0.2 = 1.15$ l.

13.3.4 Corresponding Dimensions

Karthikeyan et al. [24] studied the rate of water flow in a column filled with activated alumina. According to them, variation in column height and particle size causes a substantial alteration in water flow rate. Particle size increase caused a rise in pore volume leading to an enhancement of flow rate. Bed height increase results in an enhancement of offered resistance which leads to a decline in flow rate. In view of these two reasons, selection of bed height and particle size is the important parameter to be considered while designing a defluoridation unit. Important issue to be noted is that minimum contact period is required between adsorbent and fluoride ion to be removed. At the same time, very lower flow rate design will not be accepted by end-users. Taking into consideration the equal weightage of flow rate and defluoridation capacity, it is decided to choose the intermediate size of the particle in the range 140–180 μ m because both factors are optimal in the chosen range. Based on it, fixation of column height was done. Moreover, it is always advisable to select the ratio of column diameter to particle diameter as more than 20 to decrease the channelling chances [31, 32]. Several trails were made with different dimensions, and it is found that the optimum diameter as 7 cm for the decided quantity of alumina.

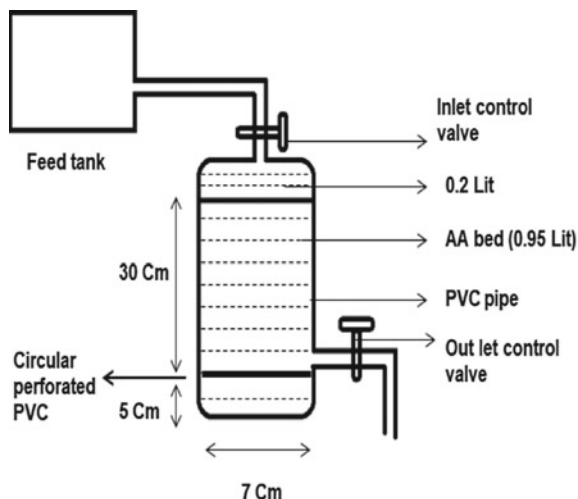
Filter diameter (selected) = $\Phi = 7$ cm

Total height of the filter = $H_F = V_F/[\pi \times (\Phi/2)^2] = 29.897$ cm $\cong 30$ cm.

13.3.5 Defluoridation Studies on the Designed Unit

PVC pipe having an internal diameter of 7 cm was used for this study. The column was connected to a feed tank with inlet control valve. Activated alumina bed was fixed, and proper distribution in it was ensured by packing it between two circular

Fig. 13.3 Design of the proposed house hold defluoridation unit



perforated PVC sheets. Plug pairs encompass these sheets which function as filtering medium to remove any dust/dirt from inlet and support to the bed, respectively (Fig. 13.3). Random packing of adsorbent is ensured by initial filling of the column with deionized water followed by activated alumina, whereas the reverse filling order may result in a decline of adsorbent efficiency due to the development of air gaps which leads to further channelling phenomenon. A closely packed adsorbent bed was ensured by soaking with distilled water and leaving for overnight. It is a known fact that activated alumina on hydration changes from the mineral form boehmite (AlOOH) to gibbsite ($\gamma\text{-Al(OH)}_3$) [33]. Further, it was also established that fluoride better uptake by it happens due to a change in surface morphology, which is done by soaking it for one day [34]. Hence, the above overnight soaking of bed with distilled water also helps to improve defluoridation. Process was carried out at room temperature. Column kept filled with feed water even during resting period. Practical aspects in the usage of AA for defluoridation of water were studied by regulating the flow rate in order to maintain minimum 5 min contact time. Input and output were collected at regular intervals of time in order to analyse the fluoride concentration. The residual amount of fluorine in outlet water was found to be within permissible limits. However, the three key issues involved in realization of any household defluoridation units are (1) motivation, (2) appropriate and cheap technique and (3) technical support including training on efficient regeneration to one of the villagers to continue without any support from external agencies [35]. Similar to defluoridation studies, decontamination units may be designed for the removal of heavy metals using agricultural waste as adsorbents [35–39].

13.3.6 Regeneration of Bed

A fourfold higher regeneration was observed with 0.1 N sodium hydroxide solution compared to 0.1 N hydrochloric acid solution. High negative charges are created on the surface of AA during elution of fluoride using sodium hydroxide. Hence, the already adsorbed F^- experience repulsion from the surface leading to their diffusion into solution [24]. For regeneration, the exhausted AA was shifted into a bag made up of nylon mesh and immersed in alkali solution for overnight with intermittent stirring. A marginal decrease in adsorption capacity was observed even after 25 regeneration cycles.

13.4 Conclusions

Lower values of operational defluoridation capacity of alumina can be explained based on the presence of competitive ions in the water to be treated. A continuous defluoridation unit was designed for domestic purpose using activated alumina as an adsorbent. The residual amount of fluorine in outlet water from the unit was found to be within permissible limits. Sodium hydroxide solution (0.1 N) was found to be the best regenerating agent for the exhausted bed.

References

1. Ramesh, H.S., Kamaraju, M.: Continuous flow defluoridation unit for rural water supply scheme of fluoride prone areas. In: World Environmental and Water Resource Congress 2006: Examining the Confluence of Environmental and Water Concerns, pp. 1–10 (2006)
2. Sahu, P., Kisku, G.C., Singh, P.K., Kumar, V., Kumar, P., Shukla, N.: Multivariate statistical interpretation on seasonal variations of fluoride-contaminated groundwater quality of Lalganj Tehsil, Raebareli District (UP). India. *Environ. Earth Sci* **77**(13), 484 (2018). <https://doi.org/10.1007/s1266>
3. Bureau of Indian Standards: Indian Standard: Drinking Water—Specification. Bureau of Indian Standards, New Delhi (2012)
4. Heikens, A., Sumarti, S., Van Bergen, M., Widianarko, B., Fokkert, L., Van Leeuwen, K., Seinen, W.: The impact of the hyperacid Ijen Crater Lake: risks of excess fluoride to human health. *Sci. Total Environ.* **346**(1–3), 56–69 (2005). <https://doi.org/10.1016/j.scitotenv.2004.12.007>
5. American Dental Association (ADA): Fluoridation Facts. ADA Statement Commemorating the 60th Anniversary of Community Water Fluoridation, 211 East Chicago Avenue Chicago, Illinois 60611-2678 (2005)
6. Dissanayake, C.B.: The fluoride problem in the groundwater of Srilanka—environmental management and health. *Int. J. Environ. Stud* **19**, 195–203 (1991). <https://doi.org/10.1080/00207239108710658>
7. Nie, Y., Hu, C., Kong, C.: Enhanced fluoride adsorption using Al (III) modified calcium hydroxypatite. *J. Hazard. Mater.* **233**, 194–199 (2012). <https://doi.org/10.1016/j.jhazmat.2012.07.020>


8. Tebutt, T.: Relationship Between Natural Water Quality and Health. United Nations Educational, Scientific and Cultural Organization, Paris (1983)
9. Murray, J.J.: Appropriate Use of Fluorides for Human Health. World Health Organization, Geneva (1986)
10. Tekle-Haimanot, R., Melaku, Z., Kloos, H., Reimann, C., Fantaye, W., Zerihun, L., Bjorvatn, K.: The geographic distribution of fluoride in surface and groundwater in Ethiopia with an emphasis on the Rift Valley. *Sci. Total Environ.* **367**(1), 182–190 (2006). <https://doi.org/10.1016/j.scitotenv.2005.11.003>
11. Fawell, J., Bailey, K., Chilton, J., Dahi, E., Magara, Y.: Fluoride in drinking-water. IWA publishing World Health Organization and IWA Publishing, London (2006)
12. Pietrelli, L.: Fluoride wastewater treatment by adsorption onto metallurgical grade alumina. *Anal. Chim.* **95**, 303–312 (2005)
13. Maheshwari, R.C.: Fluoride in drinking water and its removal. *J. Hazard. Mater.* **137**(1), 456–463 (2006). <https://doi.org/10.1016/j.jhazmat.2006.02.024>
14. Mehari, B.B., Mayabi, A.O., Kakoi, B.K.: Development of household defluoridation unit based on crushed burnt clay pot as sorbent medium: a case of Keren Community, Eritrea. *Environ. Nat. Resour. Res.* **4**(3), 67 (2014)
15. Samrat, M.V., Rao, K.K., SenGupta, A.K., Riotte, J., Mudakavi, J.R.: Defluoridation of reject water from a reverse osmosis unit and synthetic water using adsorption. *J. Water Process Eng.* **23**, 327–337 (2018). <https://doi.org/10.1016/j.jwpe.2017.07.015>
16. Babu, C.A., Sujish, D., Murugappa, M.S., Mohanakrishnan, G., Kalyanasundaram, P., Raj, B.: A comprehensive treatment method for defluoridation of drinking water. *Indian J. Chem. Technol.* **18**, 314–318 (2011)
17. Boruff, C.S.: Removal of fluorides from drinking waters. *Ind. Eng. Chem.* **26**(1), 69–71 (1934). <https://doi.org/10.1021/ie50289a016>
18. Bulusu, K.R., Nawlakhe, W.G.: Defluoridation of water with activated alumina: batch operations. *Indian J. Environ. Health* **30**(3), 262–299 (1988)
19. Benjamin, M.M., Leckie, J.O.: Conceptual model for metal-ligand-surface interactions during adsorption. *Environ. Sci. Technol.* **15**(9), 1050–1057 (1981). <https://doi.org/10.1021/es00091a003>
20. American Public Health Association, American Water Works Association.: Standard Methods for the Examination of Water and Wastewater. American public health association (1989).
21. Bellack, E., Schouboe, P.J.: Rapid photometric determination of fluoride in water. Use of sodium 2-(*p*-sulfophenylazo)-1, 8-dihydroxynaphthalene-3, 6-disulfonate-zirconium lake. *Anal. Chem.* **30**(12):2032–2034 (1958). <https://doi.org/10.1021/ac60144a050>
22. Gupta, V.K., Sharma, S.: Removal of cadmium and zinc from aqueous solutions using red mud. *Environ. Sci. Technol.* **36**(16), 3612–3617 (2002). <https://doi.org/10.1021/es020010v>
23. Bhattacharya, A.K., Mandal, S.N., Das, S.K.: Adsorption of Zn (II) from aqueous solution by using different adsorbents. *Chem. Eng. J.* **123**(1–2), 43–51 (2006). <https://doi.org/10.1016/j.cej.2006.06.012>
24. Karthikeyan, G., Meenakshi, S., Apparel, B.V.: Defluoridation properties of activated alumina. In: Dahi, E., Nielsen, J.M. (eds.) 2nd International Workshop on Fluorosis Prevention and Defluoridation of Water, pp. 19–25 (1997)
25. Loganathan, P., Vigneswaran, S., Kandasamy, J., Naidu, R.: Defluoridation of drinking water using adsorption processes. *J. Hazard. Mater.* **248**, 1–9 (2013). <https://doi.org/10.1016/j.jhazmat.2012.12.043>
26. Mondal, P., George, S.: A review on adsorbents used for defluoridation of drinking water. *Rev. Environ. Sci. Biotechnol.* **14**(2), 195–210 (2015). <https://doi.org/10.1007/s11157-014-9356-0>
27. Velazquez-Jimenez, L.H., Vences-Alvarez, E., Flores-Arciniaga, J.L., Flores-Zuniga, H., Rangel-Mendez, J.R.: Water defluoridation with special emphasis on adsorbents-containing metal oxides and/or hydroxides: a review. *Sep. Purif. Technol.* **150**, 292–307 (2015). <https://doi.org/10.1016/j.seppur.2015.07.006>
28. Davis, J.A., Leckie, J.O.: Surface ionization and complexation at the oxide/water interface. 3. Adsorption of anions. *J. Colloid Interface Sci.* **74**(1):32–43 (1980). [https://doi.org/10.1016/0021-9797\(80\)90168-x](https://doi.org/10.1016/0021-9797(80)90168-x)

29. Mulugeta, E., Zewge, F., Chandravanshi, B.S.: Development of a household water defluoridation process using aluminium hydroxide based adsorbent. *Water Environ. Res.* **87**(6), 524–532 (2015). <https://doi.org/10.2175/106143014X13975035525627>
30. Eyobel, M.D.: Removal of fluoride from water using granular aluminium hydroxide: adsorption in a fixed bed column. M.Sc. Thesis, Environmental Science Program, Addis Ababa University, Ethiopia (2006)
31. LeVan, M.D., Vermeulen, T.: Channeling and bed-diameter effects in fixed-bed adsorber performance. *AIChE Symp* **80**(233), 34–43 (1984)
32. Zhao, D., SenGupta, A.K.: Ligand separation with a copper (II)-loaded polymeric ligand exchanger. *Ind. Eng. Chem. Res.* **39**(2), 455–462 (2000). <https://doi.org/10.1021/ie990740k>
33. Dyer, C., Hendra, P.J., Forsling, W., Ranheimer, M.: Surface hydration of aqueous γ -Al₂O₃ studied by Fourier transform Raman and infrared spectroscopy—I. Initial results. *Spectrochim. Acta Part A: Mol. Spectrosc.* **49**(5–6), 691–705 (1993). [https://doi.org/10.1016/0584-8539\(93\)80092-o](https://doi.org/10.1016/0584-8539(93)80092-o)
34. Shreyas, L., Kanwar, L., Rao, K.K.: Chemical engineering and the mitigation of fluorosis. *Indian Chem. Eng.* **55**(1), 38–49 (2013). <https://doi.org/10.1080/00194506.2013.785116>
35. Bregnhøj, H.: Critical sustainability parameters in defluoridation of drinking water. In: Dahi, E., Nielsen, J.M. (eds.) *Proceeding of 2nd International Workshop on Fluorosis and Defluoridation of Water*. International Society of Fluoride Research (1997)
36. Mokkaapati, R.P., Mokkaapati, J.M., Ratnakaram, V.N.: Chemical oxygen demand reduction from coffee processing waste water—a comparative study on usage of biosorbents prepared from agricultural wastes. *Glob. Nest. J.* **17**, 291–300 (2015)
37. Mokkaapati, R.P., Mokkaapati, J.M., Ratnakaram, V.N.: Kinetic, thermodynamic and equilibrium studies on removal of hexavalent chromium from aqueous solutions using agro-waste biomaterials, *Casuarina equisetifolia* L. and *sorghum bicolor*. *Korean J. Chem. Eng.* **33**, 2374–2383 (2016). <https://doi.org/10.1007/s11814-016-0078-6>
38. Mokkaapati, R.P., Mokkaapati, J.M., Ratnakaram, V.N.: Kinetic, isotherm and thermodynamics investigation on adsorption of divalent copper using agro-waste biomaterials, *Musa acuminata*, *Casuarina equisetifolia* L. and *Sorghum bicolor*. *Polish J. Chem. Tech.* **18**(2):68–77 (2016). <https://doi.org/10.1515/pjct-2016-0031>
39. Mokkaapati, R.P., Ratnakaram, V.N., Mokkaapati, J.M.: Utilization of agro-waste for removal of toxic hexavalent chromium: surface interaction and mass transfer studies. *Int. J. Environ. Sci. Technol.* **15**(4), 875–886 (2018). <https://doi.org/10.1007/s13762-017-1443-7>

Chapter 14

Simultaneous Saccharification and Fermentation of Watermelon Waste for Ethanol Production



Venkata Nadh Ratnakaram , C. G. Prakasa Rao and Satya Sree

Abstract As the world oil reserves are draining day by day, new resources of carbon and hydrogen must be investigated to supply our energy and industrial needs. An extensive amount of biomass is accessible in many parts of the world and could be utilized either directly or as crude material for the production of different fuels. The motivation behind the present research is to find an appropriate strain for the fermentation of watermelon waste to get ethanol. Saccharification and fermentation (SSF) of watermelon waste were carried out simultaneously in the presence of *A. niger* and *S. cerevisiae* (toddy origin and baker's yeast). Toddy originated *S. cerevisiae* culture is found to be more active than that of baker's yeast. For the ethanol production, the optimized conditions for different parameters like temperature, time, strain and pH are finalized.

Keywords SSF · Bioethanol production · Biowaste · Water melon · Fruit waste

14.1 Introduction

14.1.1 Watermelon Waste and Its Products

Food demand of growing population is fulfilled by the progression in agricultural production, but the same generates large amounts of waste known as “food chain supply wastes” [1]. Substantial amounts of food wastage happen in developed countries at the stage of consumption, whereas, in under developed countries, huge wastage

V. N. Ratnakaram (✉)
GITAM University, Bengaluru Campus, Bengaluru 561203, Karnataka, India
e-mail: doctormadh@yahoo.co.in

C. G. Prakasa Rao
Department of Biotechnology, SKD University, Anantapur 515003, India

S. Sree
Department of Chemistry, VFSTR, Vadlamudi 522213, India

of food is mainly produced in different stages of food supply chain [2]. Food waste, especially from perishable fruits and vegetables, is produced chiefly due to poor storage conditions and various post-harvest unit operations [3]. The usage of food waste to generate value-added products is in alignment with the contemporary notion—sustainable development that is targeted towards security of food, protection of environment as well as energy efficiency. About 15% of total fruit yield is wasted [4]. So the generated large quantities of food or fruit waste can be used to harvest energy and chemicals [5]. Another advantage is that it is renewable.

Watermelon (*Citrullus vulgaris* Schräd) belongs to *Cucurbitaceae* family and grows in tropical areas. It is cultivated in the south and central regions of India and stands in 26th position of its production [6]. In addition to the consumption of fresh fruit, watermelon is also used in the preparation of different food products like sauces, jellies, salads, juices and marmalades. It is considered as medicinal plant due to the pharmacological activities of compounds present in it [7] and its seeds [8]. Hence, the researchers are concentrating on the extraction of oil from seeds of watermelon [9]. As per the available recent literature, watermelon production in India is about 1.83×10^6 metric tonnes [10]. Its biomass contains three major components, viz. flesh (68% w/w), rind (30%) and seeds (2%) [11]. Watermelon waste is generated from fruit juice stalls, restaurants and food industries. Though a small quantity is used as animal feed, a large quantity of watermelon waste (> 90%) is disposed off causing environmental challenges.

A number of products were reported using watermelon waste. Jam was prepared from watermelon waste [12]. It is a source of nutraceuticals like lycopene, useful antioxidant carotenoid, and is useful for health of prostate [13]. Another available nutraceutical is L-citrulline, a precursor of L-arginine and also helpful in detoxifying the catabolic ammonia [14]. Oil and proteins were extracted from watermelon seeds [6]. Sugar was extracted from its rind [11]. Xylanase and polygalacturonase were produced by solid-state fermentation of watermelon rinds by *Trichoderma* species [15]. Cutin was prepared from watermelon peels by using *Fusarium oxysporum* MTCC 2480 [16], and similarly glucose was synthesized using far IR radiated energy [17]. Its shell was used as an adsorbent for the removal of heavy metals [18] and pesticides [19].

14.1.2 Alternatives to Fossil Fuels and Ethanol from Watermelon Waste

Rates of petroleum products are increasing regularly due to fast diminishing of their reserves. To meet the rising needs of chemical industries and automobiles, worldwide search is motivated for different alternatives [20]. Due to the presence of 35% oxygen in ethanol, it undergoes total combustion reaction with a diminished amount of emissions in contrast to the incomplete oxidation of fossil fuels associated with release of harmful gases. In India, the contribution of domestic crude oil towards

country energy demand is 23% and the balance is met from imports [21]. A considerably reduced emission of greenhouse gases is possible by the usage of fuels blended with ethanol [22]. MNRE, India, is aimed at blending of 5% ethanol to the fuels to meet the demands [23]. Hence, a thrust on the field of fermented ethanol production is observed during recent decades.

Biorefinery concept suggests the usage of entire biomass of a biological product to generate a range of value-added products (like commodities, fuels and chemicals) by processing (physical, thermal, chemical or biological) leading to minimization or nil wastage [24]. Successful implementation of this concept is reported in a number of biological products including microalgae [25], lignocellulose [26] and sugarcane [27]. The concept of biorefinery was also extended to watermelon by converting its different components into value-added products including ethanol. In 1925 itself, Henry Ford described ethanol as “the fuel of the future”. He also indicated that “the fuel of the future is going to come from apples, weeds, sawdust—almost anything. There is fuel in every bit of vegetable matter that can be fermented” [28]. His visionary speculations came into true from the recent research outcomes in this area. In 2017, the total fuel ethanol produced worldwide is 17,500 million gallons and the contribution of India is 280 [29]. Even after the extraction of these nutraceuticals, the remaining watermelon waste consists of sugars (about 10% w/v), and the same can be fermented directly to ethanol. Watermelon juice was fermented to get the vinegar as the final product via ethanol production [30]. Bioethanol was produced by the fermentation of watermelon seeds with *S. cerevisiae* after removal of linoleic acid [31]. *Zymomonas mobilis* and *Saccharomyces cerevisiae* were used, respectively, for SSF of watermelon rind for effective ethanol production compared to the usage of single organism for both steps [32]. Ethanol production was reported as 5.86%. Native microorganisms were used for hydrolysis (*Aspergillus fumigatus* and *Leuconostoc dextranicum*) and fermentation (*Z. mobilis*) of watermelon waste to produce 27.62% higher amounts of ethanol [33].

14.1.3 Objective of the Present Work

Whole watermelon waste is chosen as the raw materials in the present work for the production of ethanol. Fermentation has been carried out by using *S. cerevisiae* of toddy and baker’s yeast origin in order to assess the best performer of these two strains. *Aspergillus niger* is used as a saccharifying agent so that a high concentration of ethanol can be produced. The effect of time, temperature, concentration of *S. cerevisiae*, concentration of *A. niger* and variation of pH were studied in the presence of both the strains.

14.2 Experimental

Analytical grade purity chemicals were used throughout the present research work. *Aspergillus niger* (MTCC 281) and baker's yeast obtained from local market were used.

14.2.1 *S. cerevisiae* (Toddy Origin)

Toddy is produced profusely in India, and its availability is high. So, it is selected as an inexpensive source for the development of an appropriate yeast strain which can be used for ethanol fermentation. The *Saccharomyces yeast* was isolated from toddy using serial dilution technique in our laboratory. Isolated the *S. cerevisiae* strain from toddy using the malt extract medium. On the basis of the morphological and physiological properties, the strain was identified as *S. cerevisiae* [34]. Agar slants were prepared comprising agar-agar (2%), glucose (1%), malt extract (3%), beef extract (0.3%) and peptone (0.5%). The culture was maintained for five days at room temperature and then stored at 4 °C. To prepare the yeast inoculum, colonies of growing phase *S. cerevisiae* were taken from PDA slant which were having an age of one week and transferred to dextrose broth (10.0 ml) and then incubated for 24 h at 25 °C.

14.2.2 *Aspergillus niger*

About 200 g of peeled potato slices were taken and boiled for one hour in 500 ml of distilled water to obtain potato infusion. To this, 200 g of dextrose and 20 g of agar-agar were added and then made up to 1000 ml. Then, *A. niger* spores were dispersed in 100 ml sterile water, and it was added to PDA medium. This was maintained at 37 °C for 48 h in orbital shaking incubator. Hemocytometer and binocular microscope were used to count the spore number, and 9.55×10^7 per ml was the spore load.

14.2.3 *Fermentation Inocula Preparation*

It is prepared by using sucrose (10 g), potassium dihydrogen phosphate (0.5 g), MgSO₄ (0.04 g), NH₄SO₄ (0.2 g) and beef extract (0.2 g). Medium pH was maintained at 4.25 using a solution of 1 N H₂SO₄. Later, it was retained in an autoclave for fifteen minutes at a pressure of fifteen psi. The obtained broth was brought to ambient temperature and then inoculated with *S. cerevisiae* colonies. Then, the culture was grown in orbital shaking incubator at 110 rpm.

14.2.4 Preparation of Fruit Extract

Fruit waste of watermelon was obtained from the local fruit market, Guntur city, India. After washing it a number of times using sterile water, the fruit waste was peeled. Both seeds and placenta from the sliced pulp were removed and afterwards stored at 4 °C inside a deep freezer. A sterile blender was used to convert the fruit waste into slurry. Cheesecloth was used to filter the slurry to obtain the fruit extract. Retained the extract in a sterile container. Measured 200 ml of extract and then sterilized it in conical flasks (250 ml). Then added a carbon supplement to each flask in the form of glucose (2% w/v). Loose plugging is done to the conical flasks using non-absorbent cotton wool as well as aluminium foil. The contents were sterilized for fifteen minutes at pressure of 1.0 kg/cm² to achieve the sterilization and then cooled. Separate inoculation of medium was done using *S. cerevisiae* (1.1×10^5 cells/ml) and *A. niger* (4×10^5 spores/ml). Orbital shaker was shaken at 200 rpm to accomplish aeration. Appropriate temperature was maintained to incubate the inoculated flasks. Digital pH metre was used to measure the medium pH.

14.2.5 Estimation of Alcohol

Distillation column was used to distil the contents and heating was done slowly at 78 °C to collect the distillate. Spectrophotometry was used to determine the ethanol concentration. Fermentation was carried out in triplicates. The concentrations of ethanol were monitored using UV-Vis spectrophotometer, after the separation of the cells by centrifugation and by measuring absorbance at 600 nm after following the standard method of using potassium dichromate solution [35]. A calibration curve was used to determine ethanol concentration.

14.3 Results and Discussion

14.3.1 Fermentation of Watermelon Waste

The effect of temperature as well as time on ethanol production from watermelon waste by using *S. cerevisiae* (toddy origin and baker's yeast) was studied by adding *S. cerevisiae* (1.1×10^5 cells/ml) to a broth of 200 ml containing 40 g watermelon waste. Fermentation experiments were conducted up to 93 h under varying temperature in the range 25–40 °C to investigate the temperature effect on alcohol production from watermelon waste using *S. cerevisiae* strains (toddy origin and baker's yeast). With an increase in time, the percentage of ethanol production also increased till 47 h and then there was no appreciable change in ethanol production. From 25 to 35 °C, the ethanol production increased, but a decrease in the ethanol production

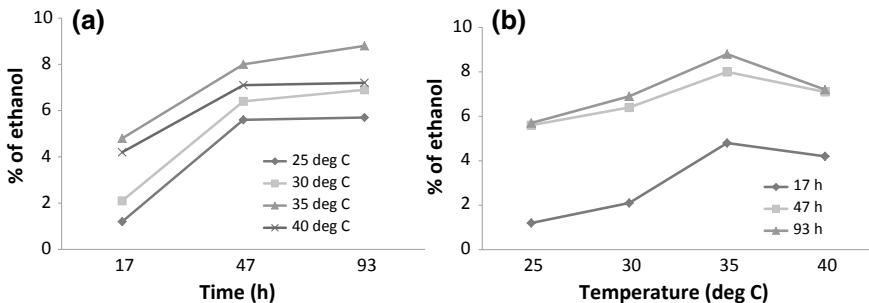


Fig. 14.1 Effect of **a** time and **b** temperature on the ethanol production from watermelon waste by using *S. cerevisiae* (toddy origin)

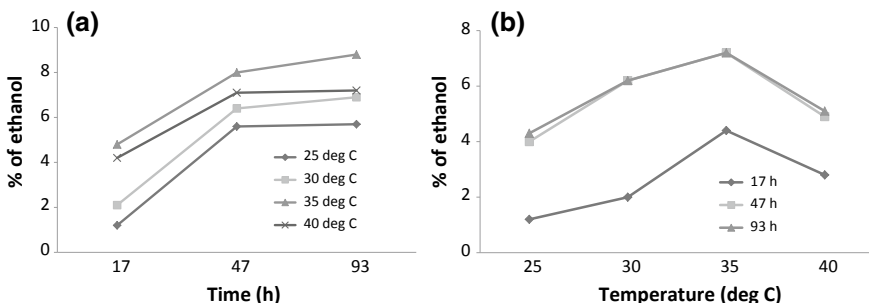


Fig. 14.2 Effect of **a** time and **b** temperature on the production of ethanol from watermelon waste by using *S. cerevisiae* (baker's yeast)

was observed with the increase in temperature to 40 °C. It shows that at 35 °C, the *S. cerevisiae* can sustain well with highest activity on watermelon fermentation. From Figs. 14.1 and 14.2, it is clear that the optimum time and temperature are 47 h and 35 °C for the production of ethanol from watermelon waste using *S. cerevisiae* of both origins (toddy and baker's yeast). The comparison of the effect of *S. cerevisiae* of toddy origin and baker's yeast on ethanol production using waste of watermelon was carried out at 17 h and 93 h fermentation. Both at the shorter (17 h) and longer times (93 h), *S. cerevisiae* (3.3×10^5 cells) of toddy origin is more active than that of baker's yeast (Fig. 14.3).

The effect of the concentration of *S. cerevisiae* (toddy origin and baker's yeast) on ethanol production from the waste of watermelon was carried out at 30 °C. In both instances, with an increase in the concentration of *S. cerevisiae*, the percentage of ethanol produced also increased till 3.3×10^5 cells and then no appreciable effect of concentration is observed (Fig. 14.4). Hence, the optimum concentration of *S. cerevisiae* is 3.3×10^5 cells/200 ml.

pH has a significant influence on alcoholic fermentation in controlling bacterial contamination, yeast growth and by-product formation. Therefore, the maintenance of pH is of paramount importance in fermentation process. In the present study,

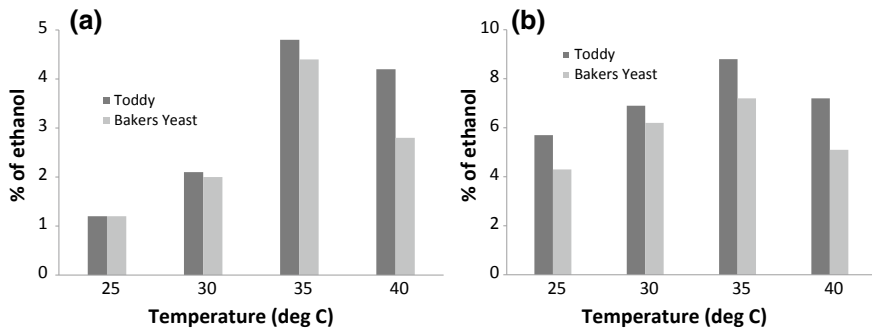


Fig. 14.3 Comparison of effect of **a** *S. cerevisiae* of toddy origin and **b** baker's yeast on the production of ethanol at 17 and 93 h

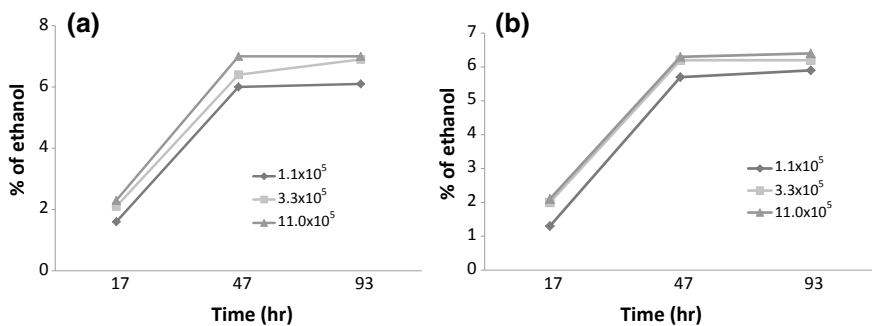


Fig. 14.4 Effect of the concentration of *S. cerevisiae* (**a** toddy origin and **b** baker's yeast) on the ethanol production from watermelon waste

experiments were conducted at diverse pH conditions in the range of 1–10.5 to appraise the efficiency of the *S. cerevisiae* yeast strain. The temperature (30 °C), time period (44 h), amount of fruit waste (40 g/200 ml) and number of cells of *S. cerevisiae* (1.1×10^5) were kept constant throughout the experiments. The optimum pH is nearly neutral (i.e. pH 6.9) for cells of toddy origin, and it is 4.6 for cells of baker's yeast (Fig. 14.5).

14.3.2 Simultaneous Saccharification and Fermentation of Watermelon Waste

In comparison to the traditional SHF (separate hydrolysis followed by fermentation), SSF has many advantages. Energy efficiency is one of them. Another one is poor substrate inhibition as the organism involved in fermentation is engaged in ready consumption of sugars released in hydrolysis process. These advantages were

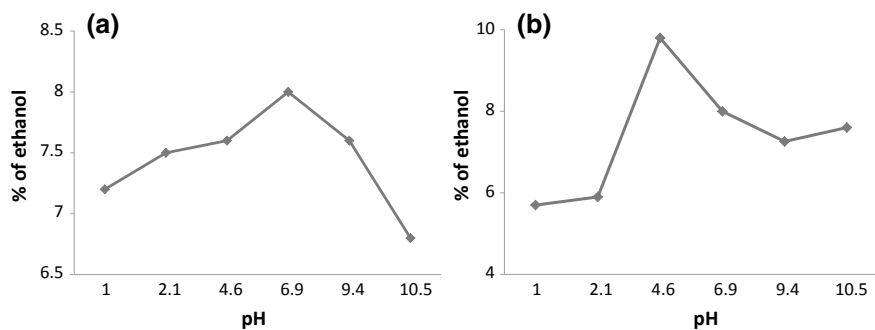


Fig. 14.5 pH effect on ethanol production from watermelon waste by *S. cerevisiae* of **a** toddy origin and **b** baker's yeast

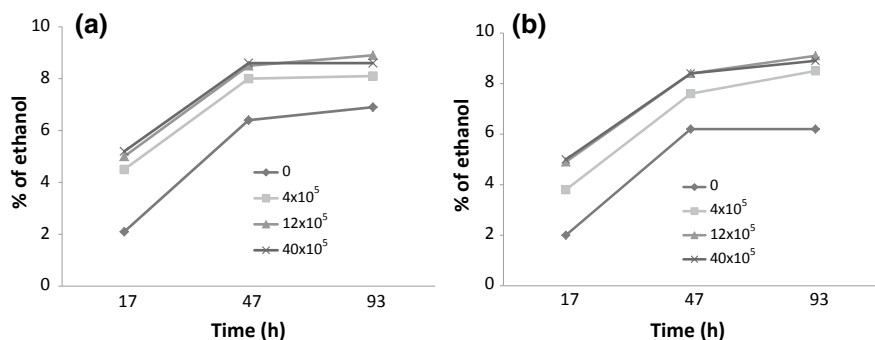


Fig. 14.6 Effect of number of *A. niger* spores on the production of ethanol by *S. cerevisiae* of **a** toddy origin and **b** baker's yeast origin

noticed and reported previously by other researchers for other substrates [36]. In view of the above advantages, simultaneous saccharification and fermentation of watermelon waste were carried out at 30 °C, where *A. niger* and *S. cerevisiae* (toddy origin and baker's yeast, 3.3×10^5 cells) are saccharifying and fermenting organisms, respectively. With the addition of *A. niger*, the percentage of ethanol production increased compared to simple fermentation by *S. cerevisiae*. This improvement could be endorsed mainly to the accelerated hydrolysis of polysaccharides followed by the improved discharge of fermentable sugars [37]. With an increase in the concentration of *A. niger*, the percentage of ethanol production was also increased and the optimum concentration was found to be at 12×10^5 spores/200 ml broth (Fig. 14.6). Improvement in ethanol production in SSF (presence of *A. niger* spores) compared to simple fermentation (zero spores of *A. niger*) process is also visible.

Microorganisms' morphology and growth are determined by various factors, and pH is important among them. It shows their sensitivity towards $[H^+]$ available in the medium. In the present study, the experiments were carried out at diverse pH conditions in the range of 1–10.5 in order to appraise the efficiency of the *S. cerevisiae*

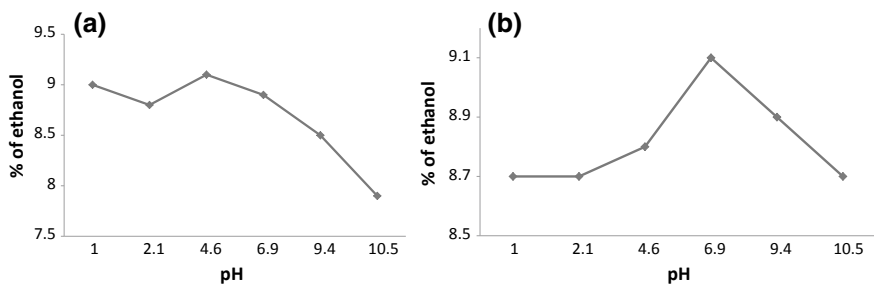


Fig. 14.7 pH effect on ethanol production from watermelon waste by *S. cerevisiae* of **a** toddy and **b** baker's yeast origin in the presence of *A. niger*

yeast strain (toddy and baker's yeast origin) in the presence of *A. niger*. The temperature of 30 °C, time of 44 h and the amount of fruit waste of 40 gm/200 ml were kept constant throughout the experiments. The experimental results for the variation of pH on ethanol production are displayed in Fig. 14.7. The optimum pH is found to be nearly neutral (i.e. pH 6.9) and pH 4.6, respectively, for toddy and baker's yeast origin. The previous studies reveal that slightly acidic and neutral pH conditions are suitable for optimal growth of fungi and bacteria, respectively. Fish et al. [38] reported maximum ethanol yield at pH 5 in the fermentation of watermelon juice. Synthesis, secretion and stability of α -amylase are influenced by pH [39]. Noteworthy α -amylase yields were reported in submerged fermentation by fungi, viz. *A. oryzae*, *ficcium* and *A. niger* in pH range of 5.0–6.0 [40–42]. *S. cerevisiae* and *S. kluyveri* produce maximum amount of α -amylase at pH = 5.0 [43, 44].

Two reasons are assigned to the reported higher yield of ethanol in the present study compared to the values of the literature. For example, 8.35% ethanol production was reported from hydrolysis by 1.5 M acid followed by the fermentation of watermelon peel [45]. Saccharification followed by the fermentation of watermelon rinds by *Trichoderma viride* and *Saccharomyces cerevisiae* produced 3.08 g L⁻¹ ethanol [46].

The first probable reason is the consideration of whole watermelon waste as raw material instead of peel or rind or seeds as in the case of others. Whole watermelon waste as a raw material can be justified as follows. Approximately 20% of its annual yield is left behind in agricultural fields because of blemishes on their surface and misshapes as it is rejected in local fresh fruit market [38]. But most of them are internally healthy. Its juice has sugars, viz. glucose, fructose and sucrose (7–10% w/v in total) which can be directly fermentable to ethanol [38].

The second and third reasons are non-addition and addition of nitrogen source and of glucose (carbon source) to the fermentation medium. It can be substantiated as follows. In general, an adequate amount of nitrogen is required for the maximum growth of yeast and the production of ethanol, but it is not available in some of fermentable sources like molasses. In such cases, watermelon juice also acts as a nitrogen supplement due to the presence of amino acids in free form (15–35 μ mol/ml) [38]. Hence, its juice was used as a feedstock, diluent to dilute the concentrated

fermentable sugars like molasses and nitrogen supplement in the production of ethanol [38]. In addition, the minor effect of nitrogen source addition on ethanol production by the fermentation of watermelon waste was reported by Kim et al. [30]. However, ethanol yield was directly dependent upon the initial sugar level [47]. And also, 12% glucose was used for fortification of juice and 5.3% ethanol was obtained at pH 5.73 [30]. Hence, 2% w/v sugar was added to the fermentation medium in addition to the 7.1–11.3% of sugar in watermelon [48] but not any addition of nitrogen source.

14.4 Conclusion

SSF yields higher % of ethanol compared to simple fermentation. *S. cerevisiae* of toddy origin is more active than that of baker's yeast. Both in presence and absence of *A. niger*, the optimum pH is nearly neutral (i.e. pH 6.9) and pH 4.6, respectively, for *S. cerevisiae* of toddy origin baker's yeast. Three reasons are assigned to the reported higher yield of ethanol in the present study compared to the values of the literature. The first probable reason is the consideration of whole watermelon waste as raw material instead of peel or rind or seeds as in the case of others. The second and third reasons are non-addition and addition of nitrogen source and of glucose (carbon source) to the fermentation medium.

References

1. Matharu, A.S., de Melo, E.M., Houghton, J.A.: Opportunity for high value-added chemicals from food supply chain wastes. *Bioresour. Technol.* **215**, 123–130 (2016). <https://doi.org/10.1016/j.biortech.2016.03.039>
2. Ong, K.L., Kaur, G., Pensupa, N., Uisan, K., Lin, C.S.: Trends in food waste valorization for the production of chemicals, materials and fuels: case study South and Southeast Asia. *Bioresour. Technol.* **248**, 100–112 (2018). <https://doi.org/10.1016/j.biortech.2017.06.076>
3. Jha, S.N., Vishwakarma, R.K., Ahmad, T., Rai, A., Dixit, A.K.: Report on Assessment of Quantitative Harvest and Post-harvest Losses of Major Crops and Commodities in India. All India Coordinated Research Project on Post-Harvest Technology, ICAR-CIPHET (2015)
4. Manneppula, S., Bathal, V.K., Obulam, V.S.: A comparative study on utilisation of citrus and mango peels for lactic acid production and optimisation by *Rhizopus oryzae* in submerged fermentation. *Eur. J. Biotechnol. Biosci.* **3**, 18–26 (2015)
5. Lin, C.S., Pfaltzgraff, L.A., Herrero-Davila, L., Mubofu, E.B., Abderrahim, S., Clark, J.H., Koutinas, A.A., Kopsahelis, N., Stamatelatou, K., Dickson, F., Thankappan, S.: Food waste as a valuable resource for the production of chemicals, materials and fuels. Current situation and global perspective. *Energy Environ Sc.* **6**(2), 426–464 (2013)
6. Fakir, A.D., Waghmare, J.S.: Watermelon waste: a potential source of omega-6 fatty acid and proteins. *Int. J. Chem. Tech. Res.* **10**(6), 384–392 (2017)
7. Simpson, R., Morris, G.A.: The anti-diabetic potential of polysaccharides extracted from members of the cucurbit family: a review. *Bioact. Carbohydr. Dietary Fibre* **3**(2), 106–114 (2014)

8. Rahman, H., Manjula, K., Anoocha, T., Nagaveni, K., Eswaraiiah, C.M., Bardalai, D.: In-vitro antioxidant activity of *Citrullus lanatus* seed extracts. *Asian J. Pharm. Clin. Res.* **6**(3), 152–157 (2013)
9. Colivet, J., Oliveira, A.L., Carvalho, R.A.: Influence of the bed height on the kinetics of watermelon seed oil extraction with pressurized ethanol. *Sep. Purif. Technol.* **169**, 187–195 (2016). <https://doi.org/10.1016/j.seppur.2016.06.020>
10. Directorate of Economics and Statistics: Agricultural Statistics at a Glance 2014, p. 206. Oxford University Press, New Delhi (2014)
11. Kumar, C., Mythily, R., Chandraju, S.: Studies on sugars extracted from water melon (*Citrullus lanatus*) rind, a remedy for related waste and its management. *Int. J. Chem. Anal. Sci.* **3**(8), 1527–1529 (2012)
12. Souad, A.M., Jamal, P., Olorunnisola, K.S.: Effective jam preparations from watermelon waste. *Int. Food Res. J.* **19**(4), 1545–1549 (2012)
13. Fang, Y.Z., Yang, S., Wu, G.: Free radicals, antioxidants, and nutrition. *Nutrition* **18**(10), 872–879 (2002). [https://doi.org/10.1016/S0899-9007\(02\)00916-4](https://doi.org/10.1016/S0899-9007(02)00916-4)
14. Marletta, M.A.: Nitric oxide: biosynthesis and biological significance. *Trends Biochem. Sci.* **14**(12), 488–492 (1989). [https://doi.org/10.1016/0968-0004\(89\)90181-3](https://doi.org/10.1016/0968-0004(89)90181-3)
15. Mohamed, S.A., Al-Malki, A.L., Khan, J.A., Kabli, S.A., Al-Garni, S.M.: Solid state production of polygalacturonase and xylanase by *Trichoderma* species using cantaloupe and watermelon rinds. *J. Microbiol.* **51**(5), 605–611 (2013). <https://doi.org/10.1007/s12275-013-3016-x>
16. Chaudhari, S.A., Singhal, R.S.: Cutin from watermelon peels: a novel inducer for cutinase production and its physicochemical characterization. *Int. J. Biol. Macromol.* **79**, 398–404 (2015). <https://doi.org/10.1016/j.ijbiomac.2015.05.006>
17. Chatterjee, S., Barman, S., Chakraborty, R.: Far infrared radiated energy-proficient rapid one-pot green hydrolysis of waste watermelon peel: optimization and heterogeneous kinetics of glucose synthesis. *RSC Adv.* **6**(78), 74278–74287 (2016). <https://doi.org/10.1039/C6RA13391>
18. Banerjee, K., Ramesh, S.T., Gandhimathi, R., Nidheesh, P.V., Bharathi, K.S.: A novel agricultural waste adsorbent, watermelon shell for the removal of copper from aqueous solutions. *Iran J. Energy Environ.* **3**(2), 143–156 (2012). <https://doi.org/10.5829/idosi.ijee.2012.03.02.0396>
19. Memon, G.Z., Bhangar, M.I., Akhtar, M., Talpur, F.N., Memon, J.R.: Adsorption of methyl parathion pesticide from water using watermelon peels as a low cost adsorbent. *Chem. Eng. J.* **138**(1–3), 616–621 (2008). <https://doi.org/10.1016/j.cej.2007.09.027>
20. Lee, S.J., Shin, J.S., Park, K.W., Hong, Y.P.: Detection of genetic diversity using RAPD-PCR and sugar analysis in watermelon [*Citrullus lanatus* (Thunb.) Mansf.] germplasm. *Theor. Appl. Genet.* **92**(6), 719–725. <https://doi.org/10.1007/bf00226094>
21. Ministry of New and Renewable Energy: Annual report. New Delhi. <http://mnre.gov.in/mission-and-vision-2/publications/annual-report-2/> (2016). Accessed on 15 Mar 2017
22. Wang, M.C., Saricks, D.S.: Effects on Fuel Ethanol Use on Fuel-Cycle Energy and Green House Gas Emissions. Agronne National Laboratory, Agrone, IL (1999)
23. Ministry of New and renewable Energy: National Policy on Biofuels. http://mnre.gov.in/file-manager/UserFiles/biofuel_policy.pdf (2013). Accessed on 15 Mar 2017
24. Kamm, B., Kamm, M.: Principles of biorefineries. *Appl. Microbiol. Biotechnol.* **64**(2), 137–145 (2004). <https://doi.org/10.1007/s00253-003-1537-7>
25. Postma, P.R., Barbosa, M.J., Wijffels, R.H., Eppink, M.H., Olivieri, G.: Microalgal biorefinery for bulk and high-value products. In: *Handbook of Electroporation*, vol 3, pp. 2205–2224. Springer International Publishing (2017)
26. Shinde, S.D., Meng, X., Kumar, R., Ragauskas, A.J.: Recent advances in understanding the pseudo-lignin formation in a lignocellulosic biorefinery. *Green Chem.* **20**(10), 2192–2205 (2018). <https://doi.org/10.1039/C8GC00353J>
27. Oliveira, C.M., Pavao, L.V., Ravagnani, M.A., Cruz, A.J., Costa, C.B.: Process integration of a multiperiod sugarcane biorefinery. *Appl. Energy* **213**, 520–539 (2018). <https://doi.org/10.1016/j.apenergy.2017.11.020>
28. Agarwal, A.K., Agarwal, R.A., Gupta, T., Gurjar, B.R. (eds.): *Biofuels: Technology, Challenges and Prospects*. Springer (2017)

29. Fuel ethanol production worldwide in 2017, by country (in million gallons). <https://www.statista.com/statistics/281606/ethanol-production-in-selected-countries/>
30. Kim, S.L., Kim, W.J., Lee, S.Y., Byun, S.M.: Alcohol fermentation of Korean watermelon juice. *Appl. Biol. Chem.* **27**(3), 139–145 (1984)
31. Song, B.Y.: Inventor method for production of bio-ethanol using watermelon seeds. United States patent US 8,642,300
32. Alex, S., Saira, A., Nair, D.S., Soni, K.B., Sreekantan, L., Rajmohan, K., Reghunath, B.R.: Bioethanol production from watermelon rind by fermentation using *Saccharomyces cerevisiae* and *Zymomonas mobilis*. *Indian J. Biotechnol.* **16**, 663–666 (2017)
33. Darwin, R.O., Alexandra, A., Elena, M., Manjunatha, B., Bryan, R.B., Subbareddy, G.V., Madhela, N.R., Rajeswari, B.: Comparative study of native microorganisms isolated from watermelon (*Citrullus lanatus*) waste and commercial microorganism (*Clostridium thermocellum*) used for bioethanol production. *Afr. J. Biotechnol.* **16**(9), 380–387 (2017). <https://doi.org/10.5897/AJB2016.15643>
34. Barnett, J.A., Payne, R.W., Yarrow, D.: *Yeasts: Characteristics and Identification*. Cambridge University Press (1983)
35. Caputi, A., Ueda, M., Brown, T.: Spectrophotometric determination of ethanol in wine. *Am. J. Enol. Vitic.* **19**(3), 160–165 (1968)
36. Svetlana, N., Ljiljana, M., Marica, R., Dusanka, P., Savic, D.: A microwave-assisted liquefaction as a pretreatment for the bioethanol production by the simultaneous saccharification and fermentation of corn meal. *Chem. Ind. ChemEng. Q.* **14**(4), 231–234 (2008)
37. Kunlan, L., Lixin, X., Jun, L., Jun, P., Guoyoing, C., Zuwei, X.: Salt-assisted acid hydrolysis of starch to D-glucose under microwave irradiation. *Carbohydr. Res.* **331**, 9–12 (2001). [https://doi.org/10.1016/S0008-6215\(00\)00311-6](https://doi.org/10.1016/S0008-6215(00)00311-6)
38. Fish, W.W., Bruton, B.D., Russo, V.M.: Watermelon juice: a promising feedstock supplement, diluent, and nitrogen supplement for ethanol biofuel production. *Biotechnol. Biofuel.* **2**(1), 18 (2009). <https://doi.org/10.1186/1754-6834-2-18>
39. Fogarty, M.W.: Microbial amylases. In: Fogarty, W.M. (ed.) *Microbial Enzymes and Biotechnology*, pp. 1–92. Applied Science Publishers Ltd., London, UK (1983)
40. Hayashida, S., Teramoto, Y.: Production and characteristics of raw-starch-digesting α -amylase from a protease negative *Aspergillus ficuum* mutant. *Appl. Environ. Microbiol.* **52**, 1068–1073 (1986)
41. Carlsen, M., Nielsen, J., Nielsen, J.: Growth and α -amylase production by *Aspergillus oryzae* during continuous cultivations. *J. Biotechnol.* **45**, 81–93 (1996). [https://doi.org/10.1016/0168-1656\(95\)00147-6](https://doi.org/10.1016/0168-1656(95)00147-6)
42. Djekrif-Dakhmouche, S., Gheribi-Aoulmi, Z., Meraihi, Z., Bennamoun, L.: Application of a statistical design to the optimization of culture medium for α -amylase production by *Aspergillus niger* ATCC 16404 grown on orange waste powder. *J. Food Eng.* **73**, 190–197 (2005). <https://doi.org/10.1016/j.jfoodeng.2005.01.021>
43. Moller, K., Sharif, M.Z., Olsson, L.: Production of fungal α -amylase by *Saccharomyces kluyveri* in glucose-limited cultivations. *J. Biotechnol.* **111**, 311–318 (2004). <https://doi.org/10.1016/j.jbiotec.2004.04.013>
44. Knox, A.M., du Preez, J.C., Kilian, S.G.: Starch fermentation characteristics of *Saccharomyces cerevisiae* strains transformed with amylase genes from *Lipomyces kononenkoae* and *Saccharomyces fibuliger*. *Enzym. Microb. Technol.* **34**, 453–460 (2004). <https://doi.org/10.1016/j.enzmictec.2003.12.010>
45. Ezejiofor, T.I., Enenebeaku, U.E., Enenebeaku, C.K., Nwankwo, M.U., Ogbonnaya, C.I.: Comparative study of bioethanol yield from yam, potato, watermelon, and pineapple peels using different concentrations of hydrochloric acid. *World News Nat. Sci.* **16**, 18–32 (2018)
46. Bhandari, S.V., Panchapakesan, A., Shankar, N., Kumar, H.A.: Production of bioethanol from fruit rinds by saccharification and fermentation. *Int. J. Sci. Res. Eng. Technol.* **2**(6), 362–365 (2013)

47. Sandhu, H., Bajaj, K.L., Arneja, J.S.: Cellulolytic saccharification of rice straw and ethanol production. *Indian J. Agric. Biochem.* **10**(1&2), 19–22 (1997)
48. Lee, J.M., Pollard, J.F., Coulman, G.A.: Ethanol fermentation with cell recycling: computer simulation. *Biotechnol. Bioeng.* **22**, 497 (1983). <https://doi.org/10.1002/bit.260250215>

Chapter 15

Autonomous Multifunctional Quadcopter for Real-Time Object Tracking and Seed Bombing in a Dynamic Environment



Pratham Nar, Shashank Sadanand Amin, Sashwata Banerjee, Vaibhav Garg and Arjun Pardasani

Abstract In recent years, a staggering increase in the development and use of unmanned aerial vehicles has been noticed in a comprehensive range of applications. This paper is based on the utilization of autonomous quadcopter in plantation monitoring (Krishna in *Agricultural drones: a peaceful Pursuit*, [1]). Agricultural drones are set to revolutionize the global food generation system. Agricultural drones are already flocking and hovering over farms situated in a few agrarian zones. This quadcopter will autonomously navigate, avoid collisions and collect data using computer vision for post-analysis and drop seeds in specified locations. Using aerial quadcopter for surveying vast agricultural land can reduce human efforts. The quadcopter is designed to detect moving objects and identify rodents using an object recognition method. The motive of the paper is to design a low-cost unmanned autonomous aerial vehicle system which will accurately and efficiently locate potential threats and notify the owners about their location and severity.

Keywords Quadcopter · Computer vision · IoT · OpenCV · Seed bombing

P. Nar (✉) · A. Pardasani

School of Electronics Engineering, Vellore Institute of Technology, Vellore 632014, India
e-mail: narpratham.vijay2015@vitstudent.ac.in

A. Pardasani

e-mail: arjunravi.pardasani2016@vitstudent.ac.in

S. S. Amin

School of Chemical Engineering, Vellore Institute of Technology, Vellore 632014, India
e-mail: shashanksadanand.amin2015@vistudent.ac.in

S. Banerjee

School of Electrical and Electronics Engineering, Vellore Institute of Technology, Vellore 632014, India
e-mail: sashwata.banerjee2016@vitstudent.ac.in

V. Garg

School of Information Technology and Engineering, Vellore Institute of Technology, Vellore 630014, India
e-mail: vaibhav.garg2016@vitstudent.ac.in

© Springer Nature Singapore Pte Ltd. 2020

B. Subramanian et al. (eds.), *Emerging Technologies for Agriculture and Environment*, Lecture Notes on Multidisciplinary Industrial Engineering, https://doi.org/10.1007/978-981-13-7968-0_15

15.1 Introduction

Agriculture plays a crucial role in a country's development. Agriculture provides us with raw food materials to consume. It is also the cornerstone of economic system of a country. It contributes majorly to the national income. It also furnishes people with products of export, thereby helping in economic upswing. Present global population is around 7.6 billion, and it is estimated that it will reach 9 billion by 2050.

With rise in population, demand for food will also increase. To cater the need of the billions of people, there must be a boom in the production of raw materials and food materials. There are several factors which hinder the agricultural production, for example, extreme weather conditions, unavailability of water, excessive use of pesticides, invasive species like pests and diseases. One more major drawback is the decrease of human labour. It is evident that we need revolutionary technological strategies to be applied in the field of agriculture not only to increase its production but also to automate the process of farming and to monitor crops. The segmentation of images also plays an important role in achieving the desired result [2].

Unmanned aerial vehicles or drones are used since the 1990s, it now has a broad field of applications, and recently drones are being widely used in the field of precision agriculture. UAV or drones have become common to farmers, and they are utilizing them for crop monitoring, livestock monitoring and transporting items from one point to another. Using drone has many advantages over manual farming. It helps in getting a better view of the field and can monitor a large area in short span of time. Modern-day drones come with lots of sensors to get more details of the field so that one can know what crops are affected, and how much water and pesticide they need. Nowadays, most advanced systems fuse information gained from various sensors for both localization (position) and navigation purposes [3].

This saves lots of water, and soil contamination is less as usage of pesticide decreases.

To increase the crop yield, crops need proper pesticides and exact amount of water. As data is gathered, the parameter estimates are refined and the trajectory is improved. An illustrative example is given to demonstrate to capability of the method [4]. Drones can carry waters and fertilizers and can spray it on a large scale. This saves a lot of time and money for the farmer. Using infrared sensors in drones, one can know the health of the crop and can act accordingly. Drones can use cameras to survey which part of the field requires more water and can monitor livestock. To accomplish all these tasks, it is needed to develop a system capable of controlling and navigating the UAV in an unknown environment using only On-board sensors, without markers or calibration objects [2].

We worked on a drone system which can be utilized in farming. The drone we developed is an autonomous one and hence does not require any pilot to control it. It can survey large areas and can spray water from the cache attached on it. It can also drop seeds and pesticides, can check soil moisture level and can also detect potential threats to the crop. Thus, it can be used for efficient farming with reduced labour cost and consuming lesser time. The use of multiple collaborative robots is ideally



Fig. 15.1 CAD render of the developed drone

suitable for such tasks. A major thrust within this area is the optimal control and use of robotic resources to reliably and efficiently achieve the goal at hand [5].

15.2 Motivation

Agriculture suffers from a great deal of problems. Excessive use of water and fertilizers may result in damage of crops. It is impossible to constantly monitor large areas of agricultural land and protect them. Moreover, some parts of the field may require lesser water, whereas some parts may require more. We developed a drone keeping all the drawbacks in mind and tried to come up with a viable solution. We developed an autonomous drone which can survey and transfer data wirelessly. Our main objective was to reduce human effort by integrating two major contemporary technologies, namely UAV and Internet of things. The drone which we proposed can monitor crops, spray water as per requirement, plant seeds and detect potential threats [2]. This work presents a systematic review that aims to identify the applicability of computer vision in precision agriculture.

15.3 Design

15.3.1 System Design

The below diagram describes the physical layout of quadcopter (Fig. 15.1).



Fig. 15.2 Sectioned view of the seed dropper CAD model

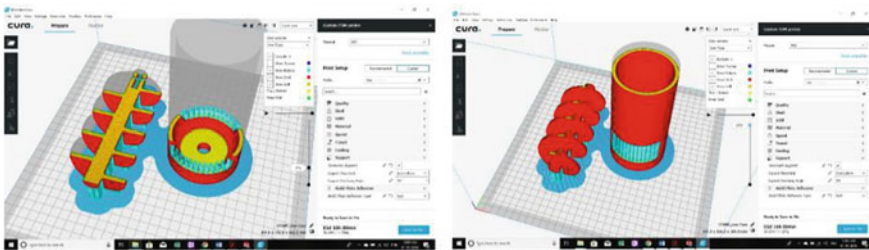


Fig. 15.3 Sliced layer view on the Cura slicer

15.3.2 Seed Bombing Mechanism

Physical Layout:

See Fig. 15.2.

Description of the seed dropping mechanism:

The design of the seed dropper was done on SolidWorks. It consists of an Archimedes screw with a length of 136 mm and a pitch of 30 mm completing 4.5 revolutions. It has a diameter of 65 mm. The pitch was given such that the seeds would not drop when the motor was switched off due to the slope and friction against the surface.

The seed dropper also consists of a case that has two openings at the bottom used for deploying the seeds in both directions.

The design was sliced on a 3D printing slicer called Ultimaker Cura with a tri-hexagon 50% infill and 3 shells printed at a 0.2-mm layer height. The total weight of the parts was 193 g and took 10 h to print. The part was made of ABS.

The dropping mechanism consists of the 3D printed Archimedes screw and case, a 12 V DC motor and balsa plate at the bottom to prevent seeds from getting stuck and facilitating easy deployment (Figs. 15.3 and 15.4).

Fig. 15.4 Three-dimensional printed seed dropper



15.3.3 Hardware

- Drone frame
- 4 × brushless DC motors
- Electronic speed controller
- Flight controller
- Power distribution board
- Receiver module X6B
- Transmitter
- Battery: LIPO
- Soil moisture sensor
- Infrared camera
- Bluetooth module
- Seed bombing mechanism
- Water storage area.

15.3.4 System Architecture

See Fig. 15.5.

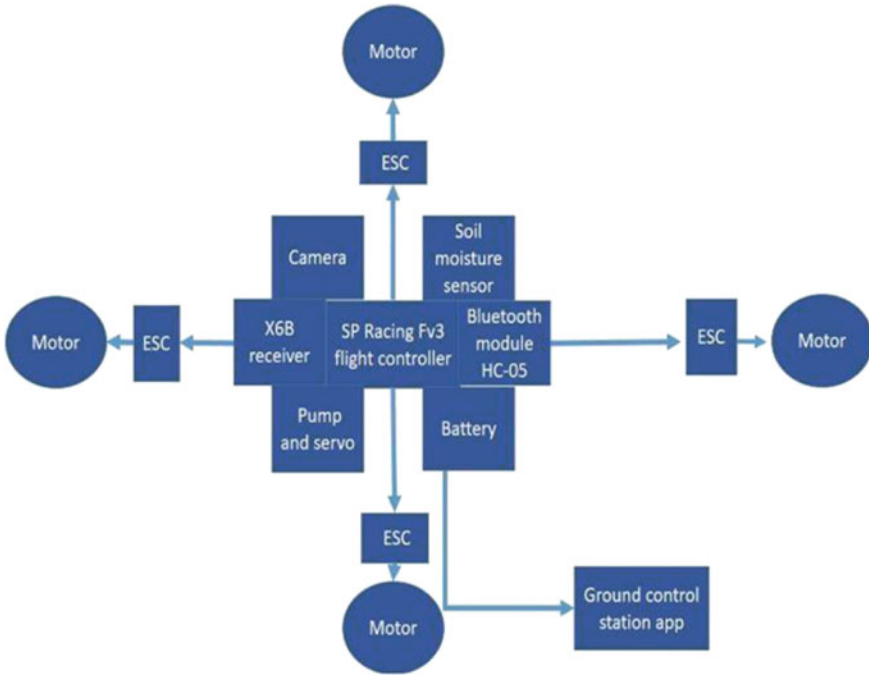


Fig. 15.5 Diagram of the system architecture of quadcopter

15.4 Methodology

The drone we proposed is an autonomous drone and can be controlled remotely by using an application. The drone uses GPS to autonomously move from a point to another which is set by the user. The GPS input is a waypoint co-ordinate input which is fed into the algorithm.

Algorithm

The algorithm is developed to make sure it does not collide with any obstacle on its way and simultaneously scanning the field. After the drone is turned on, it first checks the battery life. If the battery is sufficient, it proceeds with the next step, i.e. checking for its current longitude and altitude. According to the GPS co-ordinates set by the user, it plans its trajectory in such a way to avoid obstacles in its way. After reaching its destined location, it activates its camera. The mission planner component generates routes for individual [6]. It can also land down to check the soil moisture if asked by the user. The drone has the capability to drop seeds, spray water and pesticides and check for rodents in the farm. It can detect objects using a camera and process the images in real time to identify a potential threat to the crop which can be a rodent. This can be done by capturing the image first and then tracking objects in it. Then, the tracked object is identified by image classification technique. This entire process is done in a dynamic environment. Improvements are needed regarding flight length, camera vibration image acquisition and provision of the possibility of autonomous take-off and landing [7].

Software

We developed a mobile application which displays the telemetry sensor data acquired from the Bluetooth module positioned on the drone (Figs. 15.6 and 15.7).

The on-board Bluetooth module (HC-05) transmits the telemetry data to the Bluetooth connected node on a cellular device. This developed application is used to view the data.

The console software is used to change the configuration of the drone. Alongside telemetry data, the software also shows the yaw, pitch and roll of the drone (Fig. 15.8). The algorithm has been optimized for embedded CPUs commonly employed in light-weight robotic platforms [8].

15.5 Results

The following table describes the yaw, pitch and roll setting on the quadcopter and gives a real-time plot of it (Figs. 15.9, 15.10 and 15.11).

The algorithm is implemented to recognize particular symbols and send the current location of the drone to the mobile application. The process of dropping the seeds is controlled by means of a feedback from the wireless sensor network deployed at the seed container using the servo attached. The sample video is of a flying micro-drone in a room. The algorithm was able to accurately detect the multiple symbols in the two-minute video, regardless of the picture quality (Figs. 15.12, 15.13 and 15.14). Image preprocessing plays a central role that significantly impacts to the results of any classifiers [9].

Fig. 15.6 Diagram of the developed algorithm for autonomous drone navigation

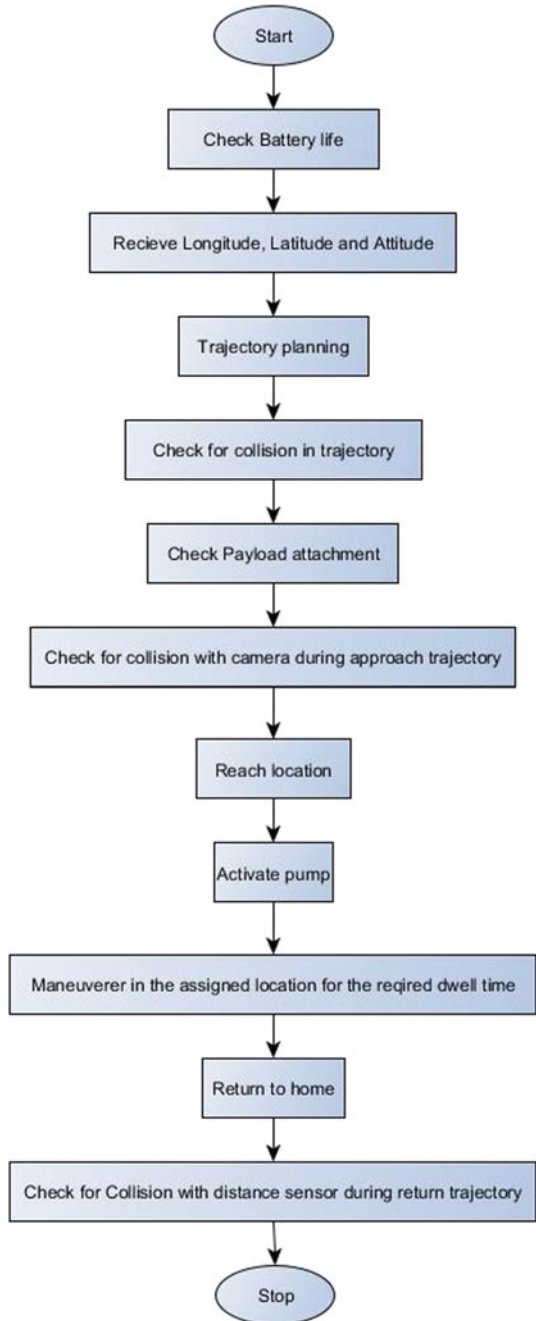


Fig. 15.7 Application

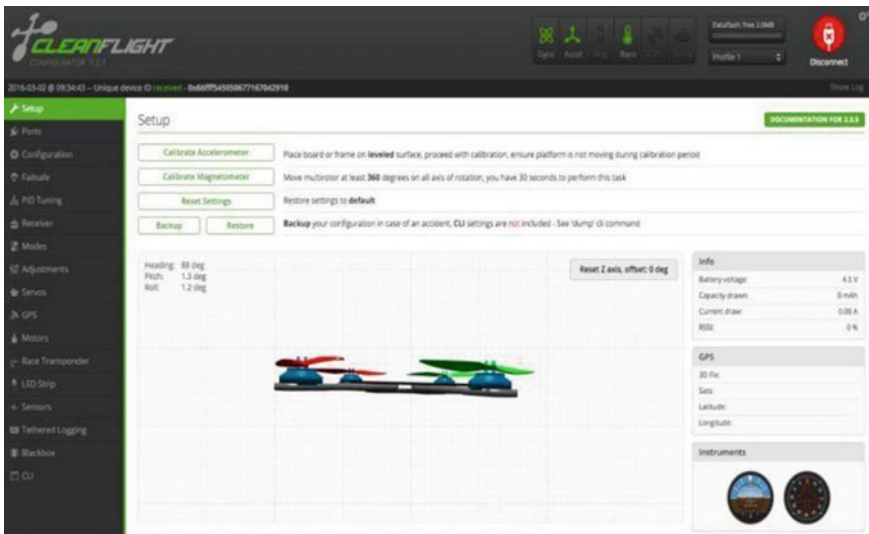
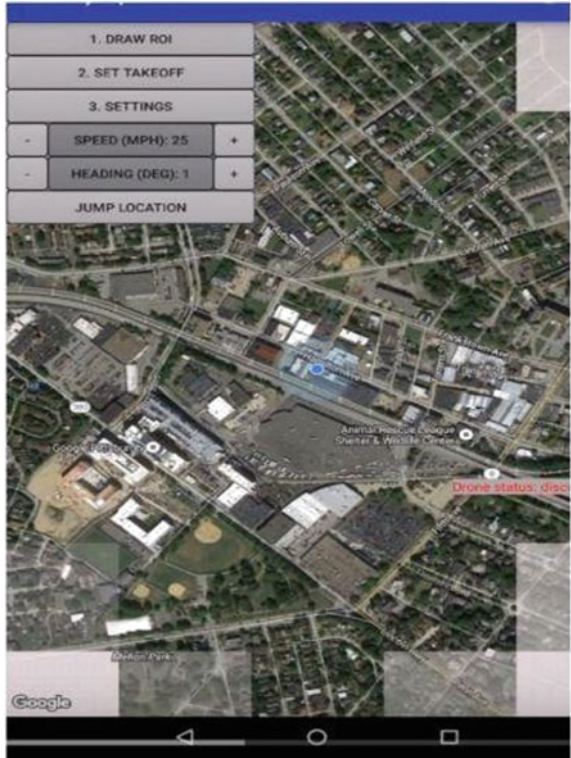


Fig. 15.8 Console software

	Proportional	Integral	Derivative	RC Rate	Super Rate	Max Vel [deg/s]
Basic/Acro						
ROLL	44	40	20	1.00	0.70	667
PITCH	58	50	22		0.70	667
YAW	70	45			1.00	0.70

Fig. 15.9 Yaw, pitch and roll settings for the drone

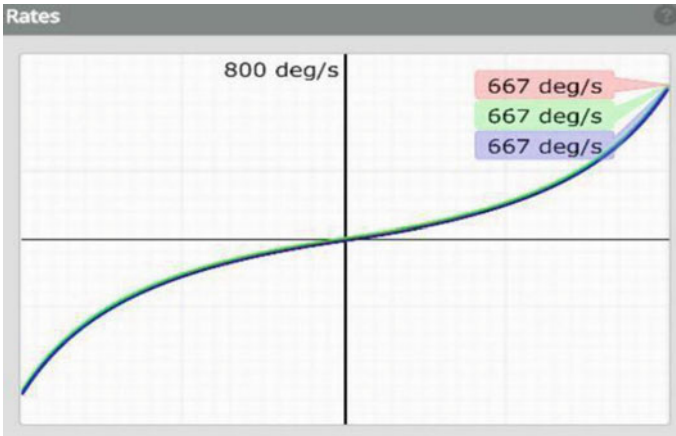


Fig. 15.10 Yaw, pitch and roll versus time graph



Fig. 15.11 Testing of the seed bombing mechanism

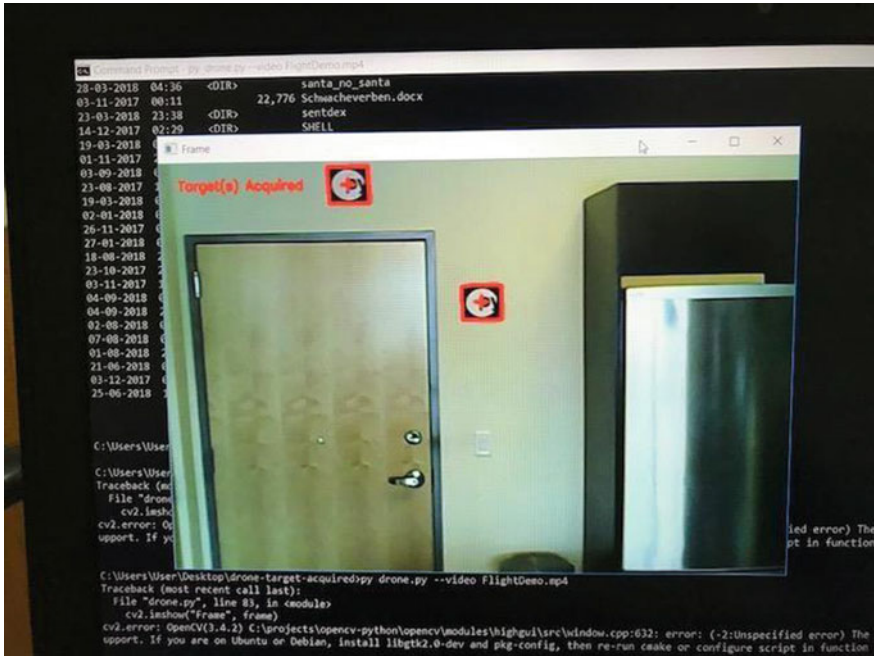


Fig. 15.12 Implementation of the object tracking algorithm



Fig. 15.13 Side view of the assembled quadcopter



Fig. 15.14 Top view of the assembled quadcopter

We manufactured the U-shaped landing gear from section cut-outs of large diameter PVC pipes. These circular cut-outs were cut in half and then moulded into shape using boiling water. Zip ties were used to attach the landing gear to the quadcopter.

This type of landing gear is used to give sufficient ground clearance for the seed dropper and other equipment attached to the bottom of the drone.

15.6 Conclusion

Farming requires a lot of manual labour in areas such as the distribution of seeds on the field, countering pests and monitoring the water requirement of every crop. The soil moisture and quality are some of the reasons that force us to shift towards the modern ways of farming. The “autonomous multifunctional quadcopter” embedded with the technologies like object detection and algorithms to spread seeds while avoiding a collision. The drone also has the ability to detect rodents using image processing. It also has the ability to check the soil and provide a practical solution to these problems. Assisted natural regeneration (ANR) will play a vital role in assisting the United Nations target, to restore degraded forest land to 350 million hectares, by 2030. In fact, they provide a low-cost solution for imagery collection, and the small size and manoeuvrability makes UAVs a viable and low-cost option [10].

References

1. Krishna, K.R.: Agricultural Drones: A Peaceful Pursuit
2. Patricio, D.I., Rieder, R.: Computer vision and artificial intelligence in precision agriculture for grain crops: a systematic review. *Comput. Electron. Agric.* **153**, 69–81 (2018)
3. Grocholsky, B., Keller, J., Kumar, V., Pappas, G.: Cooperative air and ground surveillance. *IEEE Robot. Autom. Mag.* **13**(3), 16–25 (2006)
4. Vasudevan, A., Ajitkumar, D., Bhuvanewari, N.S.: Precision farming using unmanned aerial and ground vehicles. In: *Proceedings of IEEE International Conference on Technological Innovations in ICT For Agriculture and Rural Development*, pp. 146–150 (2016)
5. Yahyanejad, S., Wischounig-Strucl, D., Quaritsch, M., Rinner, B.: Incremental mosaicking of images from autonomous small-scale UAVs. In: *Seventh IEEE International Conference on Advanced Video and Signal Based Surveillance (AVSS) 2010*, pp. 329–336 (2010)
6. Tricaud, C., Chen, Y.Q.: Smart remote sensing of environmental systems using unmanned air vehicles. In: *8th World Congress on Intelligent Control and Automation (WCICA) 2010*, pp. 1800–1805 (2010)
7. Tripicchio, P., Unetti, M., Giordani, N., Avizzano, C.A., Satler, M.: A lightweight slam algorithm for indoor autonomous navigation. In: *Australasian Conference on Robotics and Automation ACRA 2014*
8. Tripicchio, P., Satler, M., Avizzano, C., Bergamasco, M.: Autonomous navigation of mobile robots: from basic sensing to problem solving, pp. 1–6 (2014)
9. Bacco, M., Chessa, S., Di Benedetto, M., Fabbri, D., Girolami, M., Gotta, A., Moroni, D., Pascali, M.A., Pellegrini, V.: UAVs and UAV swarms for civilian applications: communications and image processing in the SCIADRO project. In: *International Conference on Wireless and Satellite Systems*, pp. 115–124 (2017)
10. Primicerio, J., Di Gennaro, S.F., Fiorillo, E., Genesio, L., et al.: A flexible unmanned aerial vehicle for precision agriculture. *Precision Agric.* **13**(4), 517–523 (2012)
11. Tri, N.C., Duong, H.N., Van Hoai, T., Van Hoa, T., Nguyen, V.H., Toan, N.T., Snasel, V.: A novel approach based on deep learning techniques and UAVs to yield assessment of paddy fields. In: *9th International Conference on Knowledge and Systems Engineering (KSE) 2017*, pp. 257–262 (2017)

Chapter 16

Designing of a Bulk Dishwasher for Water Conservation in Mega Kitchens



Adheesh Shah , Vinayak A. Modi  and M. Boopathi

Abstract Water shortage can be tackled by conserving water to the maximum extend. Efficient usage of water is therefore important in all applications. Dishwashing in mega kitchens results in water wastage as well as time-consuming. The aim of this project is to design a continuous flow bulk dishwasher employing image processing to identify the intensity of strain and control the quantity of water. It is executed by fixing water jets controlled by a controller which sprays programmed quantity of water on the plates on the conveyer belt and suitable angles of jet resulting in effective cleaning, and efficient usage of water as well as reducing human effort, in minimum lead time. If implemented, it will serve as a useful product for all mega kitchens serving large number of people.

Keywords Dishwasher · Bulk dishwasher · Mega kitchens · Continuous flow · Sustainable energy

16.1 Introduction

Water consumption for dishwashing in mega kitchens like buffets and parties is huge owing to the fact that most of them are hand-washed dishes. Hand washing involves more of an individual's time while the conventional dishwasher takes more time as a whole to wash dishes.

A. Shah · V. A. Modi · M. Boopathi (✉)

School of Mechanical Engineering, Vellore Institute of Technology, Vellore 632014, Tamilnadu, India

e-mail: boopathim@vit.ac.in

A. Shah

e-mail: adheesh.shah021@gmail.com

V. A. Modi

e-mail: vinayaka.modi2015@vit.ac.in

© Springer Nature Singapore Pte Ltd. 2020

B. Subramanian et al. (eds.), *Emerging Technologies for Agriculture and Environment*, Lecture Notes on Multidisciplinary Industrial Engineering, https://doi.org/10.1007/978-981-13-7968-0_16

Using heated water for sterilization [1–3] adds an additional hazard for the person. Hand washing plays an important role in small batches but becomes increasingly inefficient with the increment in batch size.

Mega kitchens have huge number of dishes to be washed in a minimum lead time which is a problem that cannot be addressed with hand washing.

Jenny et al. [4] compared the hand washing and dishwashing machines on basis of life cycle analysis and found that hand washing and dishwashing are similar along the dimensions of energy use and greenhouse gas (GHG) emissions but differ in the terms of intensity. It was also found out that hand washing uses more water than dishwashing the same dishes.

Therefore, a mechanism to continuously clean the dishes is proposed, thereby introducing the concept of continuous washing mechanism by the use of belt conveyer to reduce the lead time for washing.

Current designs in dishwasher [5–8] is a box type in which different chambers are provided for keeping dishes which are kept for prolonged duration for washing [9]. Although, these designs are suitable for home or low-scale applications. The required time for washing large number of dishes makes these dishwashers infeasible for mega kitchens.

Reusability of water is the main criterion selected here during the design. Adjustable nozzles and multiple detergent dispensers allowing effective circulation [10] of water are provided for human feedback. It will adjust and improve the quality of cleaning during various loading conditions.

A mechanism for usage of hot water is also proposed for the dual purpose of cleaning and sterilization [11–13]. The hot water used is heated through solar water heater, thereby reducing the conventional energy consumption and carbon footprint.

Energy consumptions for conventional dishwasher in comparison with hand washing was only 9000 J more [4], and the GHG emissions were low for dishwasher in comparison with dishwasher. Hence, dishwasher, specifically designed for bulk dishwashing, can result in significant water savings as well as can be green solution resulting in lesser GHG emissions at almost equivalent energy consumptions.

Different types of dishwashers both market ready and proposed [14] were also studied, and their energy and water requirements have been taken into consideration for the calculation purposes [15, 16].

16.2 Principle of Operation

Bulk dishwasher incorporates conveyer system rather than box type to decrease the lead time of operation. Bulk dishwasher consists of two washing chambers instead of one chamber partitioned into two compartments as in conventional chambers. The input hot water for dishwashing is preferred to be solar water heated so as to have minimum environmental impact.

Flow process is shown in Fig. 16.1. The unclean dishes enter into Chamber 1 and pass on to Chamber 2. Chamber 1 has a set of nozzles which sprinkle pressurized

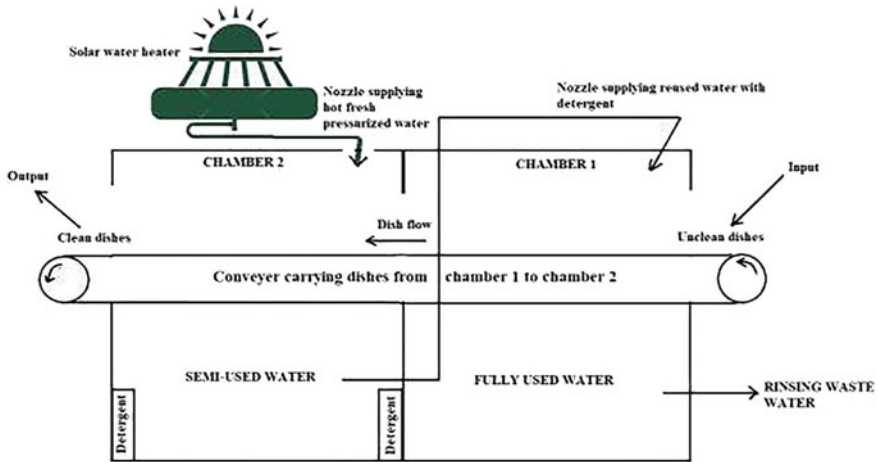


Fig. 16.1 Flow process of the bulk dishwasher

detergent water onto the dishes. This detergent water is supplied via a pump at the base of Chamber 2 which contains semi-used water which is obtained via post-washing of dishes. The used water from Chamber 1 flows down from the conveyer to the fully used water tank which is rinsed periodically.

Chamber 2 is for removal of all sorts of debris and detergent from the plates. Chamber 2 contains a set of nozzles which is fed by hot water from solar water heater or heat exchanger (as available). This water is fresh and is used for final cleaning and sterilization of the dishes. This water after cleaning flows into Chamber 1 tank and is called as semi-used water as it can be used for further cleaning.

Water in Chamber 2 is mixed with detergent available at the base. This is accomplished by using a semi-permeable membrane or a sieve to optimize the usage of detergent in the dishwasher. This semi-used water is fed into Chamber 1 for applying detergent. As the water collected in Chamber 2 is still hot than the normal water. This increases the total thermal efficiency of the dishwasher.

As water is being reused till maximum saturation, this decreases the water consumption and hence has lesser impact on environment.

Dish movement is continuous; hence, the dishes can be washed in minimum lead time without compromising cleaning quality.

16.3 Modelling of Bulk Dishwasher

The hydraulic circuit of the bulk dishwasher is shown in Fig. 16.2. There are two pumps and four nozzles and hose pipes provided for flexible motion of the nozzles. The reused water pump pumps the water from Chamber 2 base which contains semi-

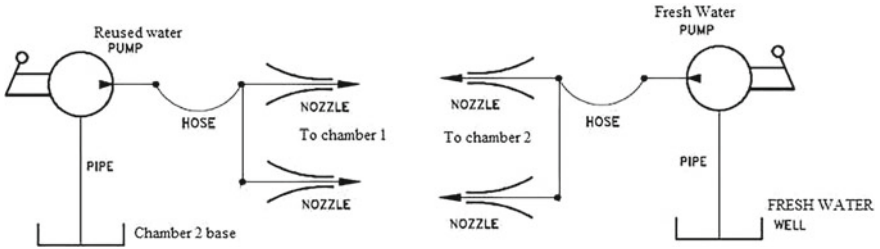


Fig. 16.2 Hydraulic circuit diagram

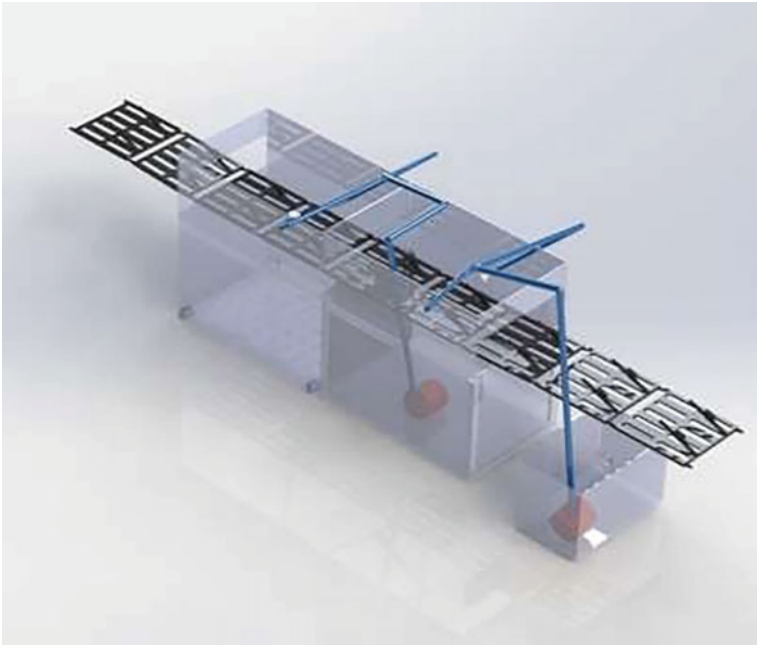


Fig. 16.3 Three-dimensional model of bulk dishwasher

used water (filled with detergent). This water is pumped to Chamber 1 where it is used for applying detergent and for pre-cleaning of dishes. The freshwater pump is used for pumping water from solar water heater source for final cleaning of the dishes via pumping the water to nozzles present in Chamber 2 (Fig. 16.3).

Initially, the dishes are placed on the moving conveyer belt marked with specific dish holders and major soiled plates are sponged off. Conveyer along with the dishes enters into the first chamber where water mixed with the detergent is sprayed on the plates with the help of two nozzles (one nozzle and one shower).

The pressurized detergent-mixed water serves the dual purpose of removing the lightly soiled stains and emulsifying the strongly soiled parts. The nozzles are kept adjustable so as to facilitate its orientation as per the need.

Two-nozzle arrangement is preferred over one nozzle because the shower arrangement shall cover more area of the plate and emulsifying majority of stains. The nozzle part shall deliver the water with high kinetic energy, thereby removing light stains and some freshly emulsified stains in the initial stage itself, thereby reducing the load in second stage.

After passing through the first chamber, the plates are moved to the second chamber. Here, the preheated water (through a solar heater arrangement) is drawn through a pump and sprayed on the plates with the help of two-nozzle arrangement (one nozzle and one shower), thereby removing the leftover stains. Using heated water (70–80 °C) in the process also sterilizes the plates, thereby eliminating the need for any post-processing operation other than drying.

The chief highlight of this method is water reusability as the water used in Chamber 2 (freshwater) for rinsing the plates is collected in the tank below and is concentrated with the detergent by using the immersed detergent containers equipped with semi-permeable membranes allowing the slow but steady mixing of detergent with water.

The concentrated water is then pumped to nozzles in first chamber with the help of a submersible pump of the required rating, thereby reusing the water and reducing the water consumption by a factor of 2.

Pumping the water from second chamber also ensures higher water temperature (>50 °C), thereby increasing the emulsifying capacity of concentrated detergent mixed water and also increasing de-soiling capacity of water at the given kinetic energy (Table 16.1).

16.4 Life Cycle Assessment (LCA) Study [17]

16.4.1 Goal and Scope

The goal of this study is to determine whether or not a bulk dishwashing machine is more efficient than hand washing for both energy and water consumption.

The analysis aims to see which method has a larger environmental impact as measured by carbon dioxide (CO₂). The scope of this life cycle assessment (LCA) is limited to the phase when the dishwasher is being used. The stages of manufacturing and disposal are not considered for this LCA study.

Table 16.1 Bulk dishwasher specifications

Parameter	Specifications
Conveyer speed	5 inch/s
Time to transverse (1 dish)	50 inch/5 inch per second = 10 s
Time in freshwater chamber	10/2 = 5 s
Nozzle output (for 1 unit)	0.15278 L/s
Total output (2 nozzles)	0.305 L/s
Total freshwater used (per dish)	0.305 l/s * 5 s = 1.5 L
Power used by one pump	18 W
Total power used by 2 pumps	36 W
Weight of conveyer	0.3 * 25 = 7.5 kg
Weight of standard SS plates	0.25 * 10 = 2.5 kg
Total load on conveyer motor	10 kg
Conveyer motor type	BLDC
Conveyer motor power	1 KW
Continuous motor torque	3 Nm
Motor peak torque	14 Nm
Motor operating voltage	48 V

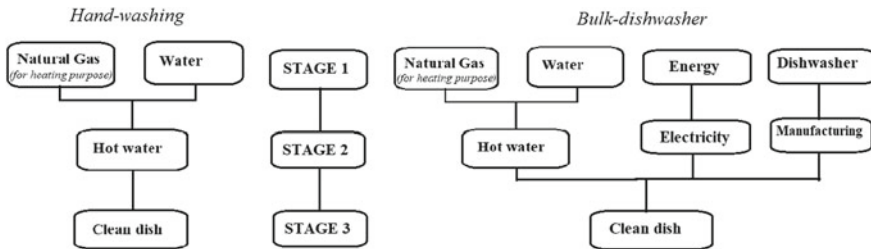


Fig. 16.4 Different stages of dishwashing

16.4.2 Function Unit of Analysis, Impact Categories, and System Boundary

Function units taken for analysis are the maximum dishes and cutlery which can be washed in dishwasher.

The impact categories that will be examined are CO₂ emissions, total water use and total energy use.

The system boundary includes stage 1 and stage 2 of washing. Soaps and sinks are excluded as inputs. (Natural Gas if applicable) (Fig. 16.4).

Table 16.2 Hand washing energy consumption data

Hand washing inputs (per dish)			
		Units	Base values
Phase1	Water	Water used (L)	1.18 (L)
Phase2	Water supply	Energy (J) to distribute water	8520
	Heated water	Natural gas (J) to heat water	99,161

16.4.3 Methodology

Water and energy consumption analysis of hand washing is referred from [4] and compared with theoretically calculated for the proposed bulk dishwasher. The formula used for energy calculation is Eq. 16.1:

$$Q = m \cdot c \cdot \Delta T \quad (16.1)$$

where Q is the heat consumed in the dishwashing process, m is the mass of water and c is the specific heat of water and Δ is the temperature loss/gain of water.

16.4.4 Lifecycle Inventory Analysis

Manual Hand Washing: The general trend in hand washing is to wash dishes with running water rather than using pool of water. The water used for dishwashing is heated from 15 to 35 °C in colder regions. Heating above 50 °C results in scaling which is undesirable [18]. As majorly, dishwashers are used in developed countries, unlike India. Hence, hand washing data from the US households is referred to [4]. Here, the underlying assumption is that water is not heated or heated via sustainable sources like solar water heater. Hence, energy consumption for both hand washing and bulk dishwasher is ignored as shown in Table 16.2.

The total energy consumed was 107.6 kJ for dishwashing dishes by hand washing. This will be compared by commercial and proposed bulk dishwasher.

Commercial dishwasher: This data was considered for older dishwashers with lesser efficiency because dishwashers have a lifetime of 15 years [19]. Dishwashers have become efficient over time [20], hence older dishwasher study reflects a more reasonable study.

Consumption study of commercial dishwashers [4] was done with various assumptions like the water heater was set to 50 °C as shown in Table 16.3.

The dishwashers use 9000 J more energy than hand washing owing to the fact of requirement of electricity for dishwasher operation.

Table 16.3 Commercial dishwasher consumption data

Commercial dishwasher inputs (per dish)			
Phase 1	Water used	Litres used	18.9 (L)
Phase 2	Heated water	Energy to heat water	2,767,716 (J)
	Water supply	Energy for distribution	1,340,000 (J)
	Manufacturing	Manufacturing energy	110.4 (J)

Table 16.4 Proposed Bulk dishwasher consumption data

Bulk dishwasher inputs (per dish)			
Phase 1	Water used	Litres used	1.5 (L)
Phase 2	Heated water	Energy to heat water	220,000 (J)
	Water supply	Energy for distribution	1,137,240 (J)
	Manufacturing	Manufacturing energy	Not available

Bulk dishwasher: Bulk dishwasher inputs were theoretically calculated as shown in Table 16.4. Water consumption per dish was calculated as 1.5 L (Table 16.1). Energy to heat water was calculated as 220,000 J which is considerably lower than commercial dishwashers. Water supply energy was found to be 15% less than the existing commercial dishwashers. Manufacturing energy consumption data is unavailable as the proposed dishwasher is currently in design phase.

Comparative analysis of LIA: The comparative analysis was done for energy consumption for heating water and supplying water for hand washing, commercial dishwasher and bulk dishwasher (Fig. 16.5). Heated water for both hand washing and bulk dishwasher is less due to the fact that bulk dishwasher derives its heated water from external sources like solar water heater. Water supply energy is comparatively lower for hand washing as compared to dishwashers. It was observed that bulk dishwasher used significant lesser water supply energy than commercial dishwashers.

In Table 16.5, Comparison of time consumption for dishwashing was done for hand washing, Commercial dishwasher and bulk dishwasher. The bulk dishwasher will use considerably less time to wash the dishes than hand washing and commercial dishwashers. The time taken by bulk dishwasher is 10 s which is 12 times faster than hand washing.

Fig. 16.5 Comparison of energy consumption of LIA

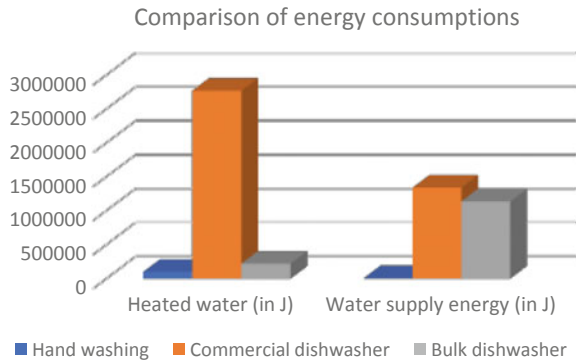


Table 16.5 Comparison of time consumption under various considerations (Hand washer Vs Dish washer Vs Bulk dish washer)

Water (L)	Per dish	Per loading (10)	Per day	Time per dish (s)
HW	1.18	11.8	94.4	120
DW	1.83	18.3	146.4	60
BDW	1.52	15.2	121.6	10

16.5 Conclusion

The idea for development of bulk dishwasher was pitched to us by ISKCON Trust due to the issue of overuse of water and time wastage in dishwashing during large religious feasts. The problem was solved by designing a belt-conveyer-based dishwasher which uses water twice, firstly for rinsing and secondly by collecting and concentrating the semi-used water with detergent and then using it again for initial rinsing of other plate and then finally discarding it, thereby reducing the water usage by a factor of 2.

The energy required for transporting the water has been reduced by approximately 15%. The water heating element in the dishwasher had been eliminated as it uses completely solar heated water, thereby considerably reducing the electrical energy usage.

References

1. David, D.E., et al.: How energy efficient are modern dishwashers? Florida Solar Energy Center
2. Fuss, N., Bornkessel, S., Mattern, T., Stamminger, R.: Are Resource Savings in Manual Dishwashing Possible? Household and Appliance Technology. University of Bonn, Bonn, Germany (2011)
3. Parpal, M.: Dishwashers: Wash Up and Save a Buck. Food Service Warehouse. Web. 9 Oct 2013

4. Jenny, B., et al.: Life Cycle Analysis: Comparison of Hand-Washing and Dishwasher Machines. UCLA Institute of the environment and sustainability
5. Jung, Y.T., Park, S.J., Oh, H.G.: Dishwasher. U.S. Patent Application No. 29/266,054
6. Kim, J.H.: Dishwasher. U.S. Patent Application No. 29/357,773
7. Ott, T., Vetter, R.: Dishwasher. U.S. Patent Application No. 29/182,518
8. Kaczmarek, W.: Dishwasher. U.S. Patent Application No. 29/182,951
9. Mercer, R. L.: Dishwasher system. U.S. Patent Application No. US0562603
10. Schmid, R.A.: Detergent supply control for automatic dishwasher. U.S. Patent Application No. US05963795
11. Dhale, A.D., et al.: Design and development of semi-automatic dishwasher. *Int. J. Eng. Res. and Gen. Sci.* 3(3), May–June (2015), ISSN 2091-2730
12. Persson, T.: Dishwasher and washing machine heated by a hot water circulation loop
13. Venkatesh, R.B., Sivaramkumar, V.: Design and fabrication of automatic dishwasher machine. *Int. J. SSRG* 26–31 (2017)
14. Tsouknidas, P., Zhang, X.: Dishwasher Improvement at ASKO. Chalmers University of Technology
15. Landwier, W.G.: Dishwasher Condenser System. Maytag Co, assignee. Patent US 3704170 A. 28 Nov 1972. 21 Nov 2013
16. Rakita, M.: Comparison of Consumption Between Dishmaster Faucet and Automatic Dishwasher Machines, 24 Nov 2009
17. ISO, ISO14040: 14040: Environmental Management–Life Cycle Assessment Principles and Framework. British Standards Institution, London (2006)
18. Public Health Association of Australia: Policy-at-a-Glance—Hot Tap Water Temperature and Scalds Policy. Public Health Association: Australia. N.p., September 2012. Web. 6 June 2013
19. Otto, R., Ruminy, A., Mrotzek, H.: ApplianceMagazine.com. Assessment of the Environmental Impact of Household Appliances—Engineering—Energy Consumption, BSH Bosch und Siemens Hausgeräte GmbH
20. Hoak, D., Parker, D., Hermelink, A.: How energy efficient are modern dishwashers. In: Proceedings of ACEEE 2008 Summer Study on Energy Efficiency in Buildings, American Council for an Energy Efficient Economy, Washington, DC, Publication number: FSEC-CR-1772-08, August 2008

Chapter 17

Modelling Water Resources in the Ancient Indus Valley City of Dholavira and Lessons Learnt



Satyajit Ghosh , M. Umashankar  and Sayan Chowdhury 

Abstract Dholavira was a part of the Indus Valley Civilisation known for its efficient town planning and water conservation. Dating back to 2600 BC, when cast iron and steel pipes were sporadic and rather scarce, unskilled builders within the city cut trapezoidal channels for water to flow into the city. These channels were excavated from natural earth with low Hazen–Williams constant (0.01) avoiding major and minor losses. Modern materials like cast iron when used cause excessive frictional losses inside the pipes, resulting into loss of hydraulic gradient. The most crucial fact that this paper establishes is a new calculation of the city’s natural hydraulic gradient which is estimated to be about 12–20 m. This is sufficient for an efficient distribution of water from reservoirs to the inner dwellings of the city. The reservoirs with a height of 22–24 m could supply a unit demand of 11–16 MLD and store 2–3 MLD. The hydraulic gradient obtained from a Bentley WaterGEMS simulation was around 24 m which was close to the natural hydraulic gradient. The Scenario energy cost for Dholavira was also calculated using an energy pricing model which was then compared to modern-day water management systems. When superimposed on the 2600-BC-old distribution channel, it gave a savings of about 7.02 million USD annually in terms of energy efficiency.

Keywords Dholavira · Flow lines · Distribution network · Savings

S. Ghosh (✉) · M. Umashankar · S. Chowdhury
Vellore Institute of Technology, Vellore, Tamil Nadu, India
e-mail: satyajitg@vit.ac.in

M. Umashankar
e-mail: mumashankar@vit.ac.in

S. Chowdhury
e-mail: sayan96.dps@gmail.com

S. Ghosh
School of Earth and Environment, University of Leeds, Leeds, UK

© Springer Nature Singapore Pte Ltd. 2020
B. Subramanian et al. (eds.), *Emerging Technologies for Agriculture
and Environment*, Lecture Notes on Multidisciplinary Industrial Engineering,
https://doi.org/10.1007/978-981-13-7968-0_17

17.1 Introduction

17.1.1 Historical Prelude

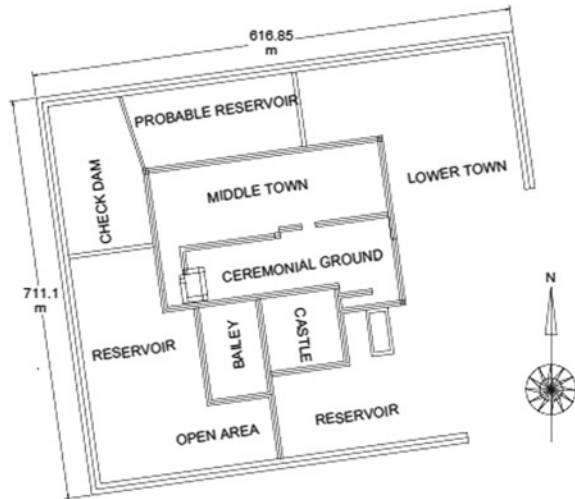
Dholavira (230 53' 10" N; 700 13' E) in Western India is etched in the annals of history. It has its own story to narrate. Dholavira is the biggest of the two most noteworthy excavations of the Indus Valley Civilisation [1]. Encompassed by Lothal and the Rann of Kachh, this archaeological site was exhumed out and is presently in Khadirpet, Bachau Taluka of Kutch district, modern-day Gujarat, Western India. Its name began from a name of a town found 1 km south of it. The 120-acres quadrangular city lay between two occasional streams—Mansar in north and Manhar in the south [2]. These two streams are the fundamental wellspring of water supply to the natural reservoirs of the city. The site was occupied from 2650 BCE until the point when it was relinquished. It was re-possessed from 1450 BCE. During 1967–1968, the site was discovered by Joshi, Deputy General of Archaeological Survey of India [3]. An aggregate of seven noteworthy social stages reported the progressive ascent and fall of the urban arrangement of the Harappan human advancement in its premises (Fig. 17.1).

Dholavira comprises interlinked check dams with eastern and western supplies ceaselessly encouraged by the surges of the Mansar and the Manhar [4]. The city was separated based on class structure into a citadel, a middle town and the lower town (Fig. 17.2). The Manor and a Bailey were a piece of the stronghold alongside a graveyard. The whole lower town and two-tenths of the middle town incorporated intense projections and breaks. The city divisions were accommodated based on the



Fig. 17.1 Artist's impression of Dholavira. Source <https://www.sindhulogy.org/sindh-at-a-glance/>

Fig. 17.2 Two-dimensional line plot of Dholavira showing internal divisions within the city. *Source* Authors, made with Autodesk AutoCAD Software



living segments and the city likewise incorporated a main road which kept running from the east to the west [5]. The excavations show the presence of check dams, drains, channels, reservoirs and bunds—essential arrangements to divert outflows from the Manhar into an eastern reservoir along the Harappan site. What was truly remarkable was that the Harappans had the technology to lessen flood flow turbidity along the Manhar. This was possible through a process that involved the diversion of the silty water through a chain of interconnected reservoirs allowing the sediments to settle and make the water potable when it occupied the eastern reservoir [6].

The citizens of Dholavira were efficient and innovative people who strove to conserve water employing rainwater harvesting in a parched landscape athirst for potable water. Extant amounts of rain (554.3 mm/year) prevailed even then. They engineered an intricate system with massive rock-cut reservoirs along the eastern and southern edges. One is able to discern its large stone drains that directed the collected storm water to the western and northern flanks in the lower city. This was separated by bunds effecting reservoirs connected in tandem. The city's imposing well is a very early example of a rock-cut well [7].

17.2 Population Density, Water Demand and Flow Lines

Reassessing previous estimates of population density from Mohenjo-daro and Harappan settlements, it was found that both Dholavira and Lothal, along with eight other Mohenjo–Harappan settlements, accounted for a total population of 33,000–41,000 each yielding a rough density of 76 people per acre with an estimated area of 458.28 acre [8].

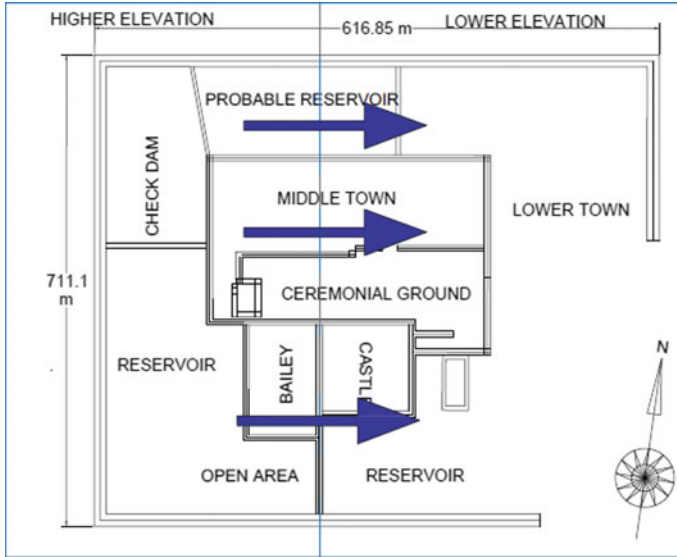


Fig. 17.3 Hydraulic flow line patterns superimposed on 2D plot of Dholavira town made with Autodesk AutoCAD software

The population count was different for different divisions of the town, with the most populated division in the lower town where people were considered poor. In the middle town, the population comprised mainly of the warrior class and the priests, whilst the elite, comprising ministers and bureaucrats, occupied the citadel. It was evident that the lower town had less access to water from the reservoirs directly as shown in Fig. 17.1. The lower town citizens were made to work for the upper classes. Thus, the per capita demand of the lower town was much higher than that of the middle town and the citadel.

The modern-day per capita demand for water is placed around 135 L/Day accounting for cooking, washing, bathing, drinking, fire demand, sanitation and cleaning works [7]. However, the water demand per capita was supposed to be much lower than present-day values owing to a lower population. Considering the count of population, they had facilities with extensive storage of water for subsequent use in Matkas, Tankas and clay pots. Whilst the demand was around 120 L/Capita/Day for the citadel, for that of the middle town it was estimated to be 130 L/Capita/Day. From Fig. 17.2, it is quite evident that an extremely efficient water distribution system was required so that even the lower town got a minimal water supply. From common knowledge of water resources and hydraulics, one knows that the hydraulic gradient line (HGL) runs from a higher elevation towards a lower elevation [9], i.e. water from the reservoir should first flow towards the middle and then finally to the lower town (Fig. 17.3).

17.3 Design and Simulation of an Extensive Water Distribution Network Using WaterCAD

The entire water distribution network of Dholavira was designed and analysed in WaterCAD. The software used was WaterGems Water-CAD, provided by Bentley Systems. Google Earth Pro was integrated with WaterGEMS for dimensional and geographical accuracy.

17.3.1 Prerequisites for Design

The most important consideration for the design was the elevation of each and every node and junction. The respective elevations were obtained from Google Earth Pro using a polygon extraction method. Around 12 points were marked along the periphery of Dholavira, and it was connected using lines to form a polygon. The polygon was saved as a KMZ file. The file was auto-converted to a DEM terrain data extraction file format, and the elevation of each node was imported into an Excel sheet [10]. The elevation data for the reservoirs and tanks were sourced from the Archaeological Survey of India reports [11].

17.3.2 The Water Distribution Network

A two-dimensional AutoCAD plot in the form of DWG or JPEG was imported as the background image for WaterGEMS. The image was prescaled according to a Google Earth scaling system. Network elements like junctions, reservoirs and tanks, were assigned according to the prescaled background plans for Dholavira. Then pipelines were drawn connecting all other elements forming a rectangular open grid network (Fig. 17.4). A water distribution network provided values for the elevation, water demand, pipe length, pipe diameters, roughness of the pipe and the Hazen–Williams constant.

17.3.3 The Junction Input Data

Each and every junction as shown in Fig. 17.4 has a unique dynamic elevation profile. These elevation data were taken from the elevation profile obtained by image processing as shown in Google Earth. The junction elevation data decide the flow direction of the water, the hydraulic gradient profile and the discharge at various nodes. The elevation of each junction was given as input to the WaterCAD software (Table 17.1).

17.3.4 The Pipe Input Data

Pipes are the main component in a water distribution network. It interlinks the nodes and junctions with each other. Thus, one needs to provide various physical properties comprising the length of pipes, the diameter of pipes and Hazen–Williams constant for the pipes (Table 17.2). These, in turn, determine the coefficient of minor losses. Whilst major losses are mainly frictional generated inside the pipe and dependent on its material composition, the minor losses arise from sudden expansion and contraction along bends, elbows and other fittings. The Hazen–Williams constant is used in the Hazen–Williams equation given below in Eq. (17.1). It is an empirical equation relating the flow of water inside a pipe with its physical attributes of the pipe and depends on the pressure drop caused due to friction [12].

The general form of Hazen–Williams equation is:

$$V = KCR^{0.63}S^{0.54} \quad (17.1)$$

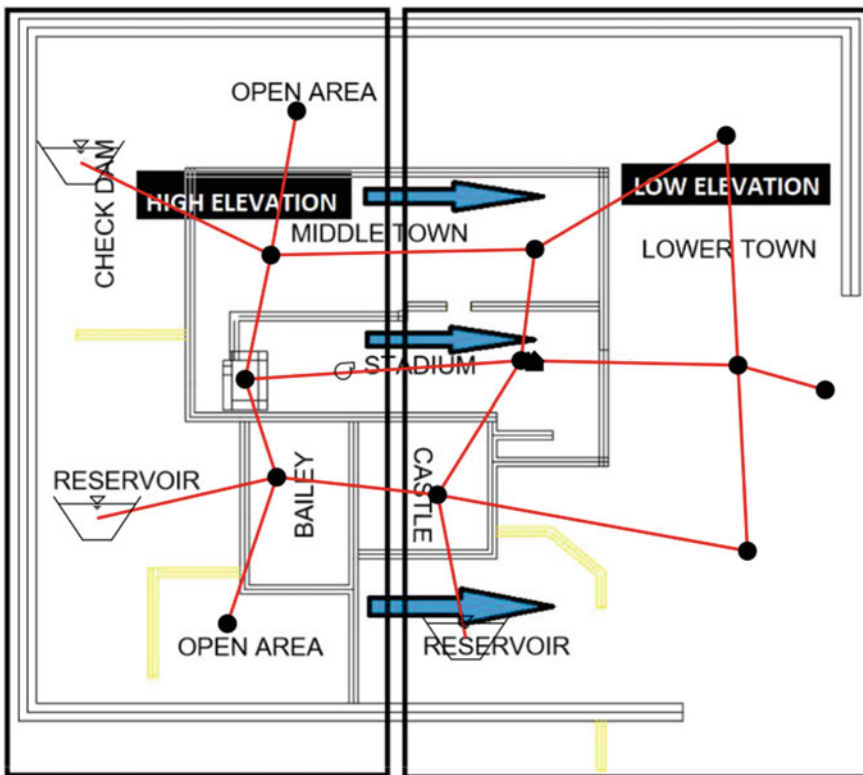


Fig. 17.4 Water distribution network showing junctions, pipes, reservoirs. *Source* Authors, made with Bentley WaterGEMS

where V is velocity, K is a conversion factor for the unit system ($K = 0.8449$ in SI units), C is the roughness coefficient, R is the hydraulic radius, and S is the slope of the energy line (hf/L , i.e. head loss per unit length of pipe) [13].

17.3.5 The Reservoir Elevation Data

Reservoirs are largely natural or artificial lakes used to collect, store and supply water as and when required. Thus, reservoir elevation data are very important input to the water distribution simulator (Table 17.3). It helps in finding out the capacity of reservoirs and the hydraulic gradient pattern along with the flow velocity.

Table 17.1 Elevation of junctions considering mean sea level as datum

Label	Level ID	Elevation (m) + MSL
J-1	116	21.25
J-2	139	20.6
J-3	123	22.6
J-4	121	22.2
J-5	137	20.1
J-6	117	17.6
J-7	122	18.6
J-8	120	16.9
J-9	118	10.26
J-10	143	12.26
J-11	119	11.2
J-12	141	11.1

Table 17.2 Properties of different pipe lines

Pipe	Length (m)	Diameter (m)	Material	Hazen–Williams constant	Minor loss coefficient
P-51	208	0.2	Natural stream clean	130	0.5
P-52	260	0.2	Brick in mortar	130	0
P-53	219	0.2	Brick in mortar	100	0
P-57	159	0.2	Brick in sewer	100	0
P-58	101	0.2	Brick in mortar	100	0
P-59	125	0.2	Brick in mortar	100	0

17.3.6 The Unit Demand Based on Population Census

Unit demand is the measure of the amount of water demanded by the general public for daily use. This includes drinking potable water, water for washing, bathing, cooking and other necessities. This is also known as the per capita demand. The unit demand was different for different regions of Dholavira due to the dynamic population distribution amongst the lower town, the middle town and the citadel (Table 17.4). It is expressed as L/day/Capita.

17.3.7 The Flow Patterns

The flow pattern is an important property since it affects the hydraulic gradient pattern by creating time-dependent and demand-dependent flows (Table 17.5). For instance, we show in Fig. 17.5 that during peak hours of the early morning, the water demand is high because of mundane activities like showering, washing and overall cleaning.

The network was then validated for errors. Since no errors were found, the network was simulated for the final water flow analysis. The results obtained are given in Table 17.6.

Table 17.3 Elevation of reservoirs considering mean sea level as datum

Label	Level ID	Elevation (m) + MSL
R-9	113	24
R-10	114	24
R-12	171	22

Table 17.4 Per capita unit demands for various subdivisions

Label	Demand type	Demand per capita (L/day)
Middle town	Population	130.00
Lower town	Population	145.00
Citadel	Population	120.00

Table 17.5 Continuous-type flow pattern for lower town starting at 05:00 am

S. No.	Time from start (h)	Multiplier
1	2.000	1.000
2	3.000	2.000
3	4.000	3.000
4	5.000	4.000
5	6.000	2.000
6	7.000	3.000

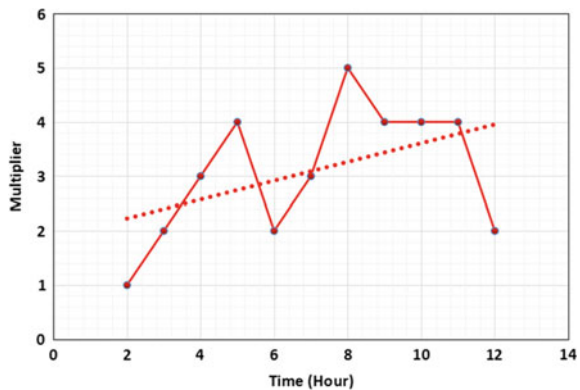
Table 17.6 Water flow simulation analysis results in million litres daily (MLD)

Time (h)	Relative flow change	Flow supplied (MLD)	Flow demanded (MLD)	Flow stored (MLD)
0.00	0.00	11	11	0
0.00–24.00	0.0003894	11	9	2

17.3.8 Hydraulic Gradient and Pressure Obtained at Various Junctions

The hydraulic gradient also known as Darcy’s slope is a vector gradient of the hydraulic head between two or more points. The hydraulic gradient at each and every junction, when linked together, forms a gradient line known as HGL. This HGL determines the direction of flow and the discharge of water in a network [14]. The hydraulic gradient at every junction was thus obtained at an average elevation of 20 m (Table 17.7). The pressure at every junction was also calculated by the simulator, and it is observed that a negligible amount of negative pressure was generated at junction J-3. Such minute negative pressures can be ignored. The hydraulic gradient patterns at different junctions and the head loss for different pipes obtained using extended period simulation are shown in Figs. 17.6 and 17.7. A time-dependent extended period simulation analysis generated colour contours of the hydraulic gradient-driven flows throughout the distribution network. It is well evident from these contours that the discharge at the middle town was higher than the discharge at the lower town as shown in Fig. 17.8.

Fig. 17.5 Hourly continuous flow-type hydraulic pattern of lower town incorporated with time multipliers



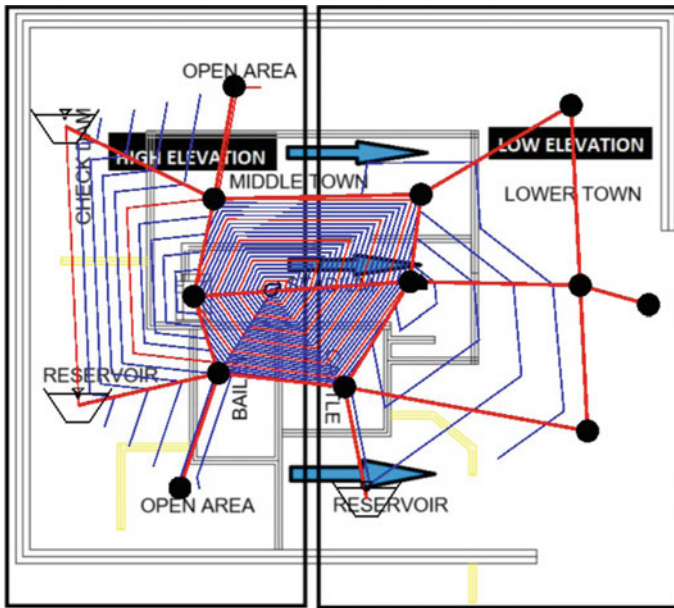


Fig. 17.8 Colour contour showing hydraulic gradient pattern around the divisions of the city made with Bentley WaterGEMS

Table 17.7 Hydraulic gradient and pressure at the junctions

Label	Level ID	Elevation (m)	Demand (MLD)	Hydraulic gradient (m)	Pressure (Psi)
J-1	116	21.25	1	21.91	1
J-2	139	20.6	1	20.78	5
J-3	123	22.6	2	19.65	13
J-4	121	22.2	1	19.93	12
J-5	137	20.1	0	21.46	6
J-6	117	17.6	0	22.21	0
J-7	122	18.6	0	20.92	3
J-8	120	16.9	1	21.84	-1
J-9	118	10.26	0	22.21	3
J-10	143	12.26	0	21.91	2
J-11	119	11.2	1	19.55	12
J-12	141	11.1	3	19.62	10

17.3.9 Contexting Dholavira with Modern-Day Distribution Networks

The objective of this paper is to compare the modern-day water distribution system (with the inclusion of pumps) with the ancient network present in Dholavira during 2600 BC. The modern-day distribution network was superimposed on Dholavira's map keeping the geographical properties constant. Centrifugal pumps were added to the network wherever pressure drops were observed for a meaningful comparison. Natural flow channels were replaced with cast-iron pipelines. Cast-iron pipes have surface roughness values in between 0.25 and 1.00 [15], and the Hazen–Williams coefficient varies between 130 and 145, thus resulting in more frictional losses and significant amount of head losses as shown in Fig. 17.7 [16].

17.4 A Scenario Energy Pricing and Energy Management Discourse

For a meaningful rationale, the following approach was adopted. The cost of energy required for supplying water to the lower town, the middle town and the citadel, clearly depended on the geographical extent and on the resultant hydraulic gradients. This information was sourced from Table 17.7. Most importantly, it must be borne in mind that in Dholavira, there were no pumps operated, water flowed into the town from the reservoirs due to the natural hydraulic gradients present.

This is in sharp contrast to the present-day situation—The use of pumps to address the sudden pressure drops in between the flow lines, along low hydraulic gradient flows proved to be costly. This extra cost in terms of energy lost due to pumping operations is factored in the energy calculations for the present-day estimates.

Cost of pumping water can be calculated as:

$$C = \frac{0.746Qhc}{3960\mu_p\mu_m} \quad (17.2)$$

where C is cost per hour (USD), Q is the volume flow (US gpm), h is the head (ft), c is the cost rate per kWh (USD/kWh), μ_p is the pump efficiency (0–1), and μ_m is the motor efficiency (0–1) [17].

A scenario energy pricing analysis was done using Darwin designer and calibrator which takes into consideration Eq. (17.2) for processing the back-end calculation [18]. Energy pricing was kept at a constant rate of \$5/kWh of energy generated and \$10/kWh during peak energy demand for a billing period of 720 h [19]. The energy calculation gave an estimated amount of 410.7239 kWh/MG of energy used in the overall distribution network which amounted to a price of \$15.54 per day (Table 17.8). The total carbon emission was estimated to be 983.32 lb/day.

Table 17.8 Energy pricing model

S. No.	Description	Value (with units)
1	Tariff type	Constant
2	Energy price	5.00 \$/kWh
3	Peak demand charge	10.0 \$/kW
4	Billing period	720.00 h
5	Daily cost	15.54 \$
6	Usage cost	0.00 \$
7	Overall energy used	410.724 kWh/MG
8	Overall unit energy cost	0.000 \$/MG
9	Total carbon emission	983.32 lb/day

Table 17.9 Expense of energy in the operation of modern-day water supplies in Gujarat, India

S. No.	Energy expense	Value
1	\$ (Million)	5.7
2	Percentage	74
3	\$ Thousand/MLD	21.43

17.4.1 Energy Cost of Water Distribution Network in Present Day

During the present day, natural channels have been replaced by cast-iron pipelines, excessive numbers of pumps and other hydraulic machines in a water distribution network. This results in a large carbon footprint [20]. An average value of energy expenses on water supply in India was obtained from data provided by Excreta Matters, 2012, for the year 2004–2005 expressed as \$ Thousand/MLD as shown in Table 17.9 [21], where MLD stands for million litres daily. The value obtained from the table was multiplied by the amount of water used in MLD which gave an approximate cost of the total energy usage.

17.4.2 Energy Pricing Comparison Between Dholavira in 2600 BC with Integrated Pumping Mechanisms and Modern-Day Distribution Networks

The cost incurred in running the water supply can be given as:

$$\text{Total Cost} = (\text{Total MLD Supplied} - \text{Total MLD Stored}) * \text{Cost Per MLD} \quad (17.3)$$

From Table 17.9, considering present-day water supply in Gujarat:

$$\text{Energy Cost/MLD} = \$21430/\text{MLD} \tag{17.4}$$

$$\text{Total Cost} = \$7.02 \text{ million} \tag{17.5}$$

From Table 17.10, considering standard operations during 2600 BC augmented with pumping system:

$$\text{Energy Cost/MLD} = \$15.54/\text{MLD} \tag{17.6}$$

$$\text{Total Cost} = \$5097.12 \tag{17.7}$$

From Eqs. (17.5) and (17.7), the annual energy savings, in terms of cost incurred, is estimated to be 7.02 million USD.

17.5 Conclusions

First, we summarise the main conclusions from a precipitation model.

Dholavira receives an average annual rainfall of 543.3 mm per year which is 50–60% less than of average rainfall In India. Though it receives less amount of rainfall, water conservation strategy such as rainwater harvesting and storm drain has been effectively implemented. The construction of check dams and stone drains to store storm water in reservoirs conserves every drop of water. Despite of harsh environment and low rainfall the city had a sufficient quantity of water to meet the needs of the people. Hence, it becomes role model for the present urban system to effectively conserve rainwater to meet the demands of the society.

Now we draw the main conclusions obtained from the energy pricing model.

Dating back to 2600 BC, when there were no such concepts of water distribution networks and water resource managements, residents of Dholavira showed extraordinary skill and dexterity through intuitive applications of fluid mechanics. They used their knowledge of fluid flow along natural gradients. There were neither pipelines nor pumping systems involved in the distribution system, whereas the present-day water distribution network has junctions, pipelines and pumping stations involved in it. From even a cursory knowledge of fluid dynamics, we know that pipes have a

Table 17.10 Expense of energy in the operation of 2600-BC-old water distribution network integrated with pumping systems

S. No.	Description	Value
1	Energy cost per MLD (\$)	15.54
2	Total MLD supplied	334
3	Total MLD stored	6

significant amount of roughness coefficient which results in major and minor losses including head loss due to friction, loss due to bends and fittings, etc. These losses, in turn, reduce the amount of flow at the discharge end. This reduces the efficiency of the distribution system, and energy is lost in between the process as heat due to friction and non-elastic collision. In this paper, we generated an energy pricing model by superimposing modern-day water distribution system on the natural water distribution system of Dholavira. This involved a full discourse on the regeneration of the original water distribution system operational in ancient Dholavira and a detailed calculation of first the hydraulic gradient, followed by a pricing analysis. Upon, redoing the procedure under present-day conditions under identical conditions, interesting differences were observed particularly with the installation of pumps at strategic positions.

References

1. Ghosh, S., Goenka, A., Deo, M., Mandal, D.: Vernacular architecture as an idiom for promoting cultural continuity in South Asia with a special reference to Buddhist monasteries. *AI & Soc.*, 1–16 (2017)
2. Subramanian, T.: The rise and fall of a Harappan city. *Frontline* **27**, 12 (2010)
3. Joshi, J.P.: Harappan architecture and civil engineering. Rupa Publications (2008)
4. Bisht, R.S.: A new model of the Harappan town planning as revealed at Dholavira in Kutch: a surface study of its plan and architecture. *Hist. Archaeol.*, 397–408 (1989)
5. Kenoyer, J.M., Heuston, K.B.: The ancient South Asian world. Oxford University Press, USA (2005)
6. Hlavinek, P.: New/old ways for storm water: learning from the history. In: IWHA 2007 Conference CD (2007)
7. IGNOU.: Interpretation and explanation of archaeological record. MAN-002 Archaeological Anthropology (2011)
8. Lahiri, N.: South Asian demographic archaeology and Harappan population estimates: a brief reassessment. *The Indian Economic & Social History Review* **35**(1), 1–22 (1998)
9. Mays, L.W.: Water resources engineering. Wiley (2010)
10. Tavani, S., Granado, P., Corradetti, A., Girundo, M., Iannace, A., Arbués, P., et al.: Building a virtual outcrop, extracting geological information from it, and sharing the results in Google Earth via OpenPlot and Photoscan: an example from the Khaviz Anticline (Iran). *Comput. Geosci.* **63**, 44–53 (2014)
11. Bisht, R.: Dholavira excavations: 1990–94. Facets of Indian civilization: recent perspectives essays in honour of Prof. BB Lal Aryan Books International, New Delhi, pp. 107–120 (1997)
12. Brater, E.F., King, H.W., Lindell, J.E., Wei, C.: Handbook of hydraulics for the solution of hydraulic engineering problems, vol. 7. McGraw-Hill, New York (1976)
13. Christensen, B.A.: Discussion of “flow velocities in pipelines” by Richard D. Pomeroy (August, 1983). *J. Hydraul. Eng.* **110**(10), 1510–1512 (1984)
14. Chanson, H.: Hydraulics of open channel flow. Elsevier (2004)
15. Nikuradse, J.: Laws of flow in rough pipes. National Advisory Committee for Aeronautics Washington (1950)
16. Dini, M., Tabesh, M.: A new method for simultaneous calibration of demand pattern and Hazen-Williams coefficients in water distribution systems. *Water Resour. Manage.* **28**(7), 2021–2034 (2014)
17. Brion, L.M., Mays, L.W.: Methodology for optimal operation of pumping stations in water distribution systems. *J. Hydraul. Eng.* **117**(11), 1551–1569 (1991)

18. Shamir, U.Y., Howard, C.D.: Water distribution systems analysis. *J. Hydraulics Div.* **94**(1), 219–234 (1968)
19. Wu, Z.Y., Arniella, E.F., Gianella, E.: Darwin calibrator—improving project productivity and model quality for large water systems. *J. Am. Water Works Assoc.* **96**(10), 27–34 (2004)
20. Ramos, H.M., Vieira, F., Covas, D.I.: Energy efficiency in a water supply system: energy consumption and CO₂ emission. *Water Sci. Eng.* **3**(3), 331–340 (2010)
21. Kumar, M.D., Singh, O.: Market instruments for demand management in the face of scarcity and overuse of water in Gujarat, Western India. *Water Policy* **3**(5), 387–403 (2001)

Chapter 18

Smart Printed Paperboard for Green Infrastructure



T. K. S. LakshmiPriya and N. Alagusundari

Abstract The living infrastructure, consisting of both the natural and man-made infrastructure constituting the green infrastructure, is undergoing serious imbalances, thereby affecting the ecological balance. Drastic ecological balance is a threat to the human existence on earth. Presently, awareness of this threat and the need to save the earth are being felt at large. Initiatives around the globe are underway to protect the earth from all disciplines and communities across nations. Green buildings and green roof with temperature control measures play a key role in green infrastructure. However, the use of thermocol is a widely prevalent, irreplaceable lining for air-conditioned halls. Thermocol is manufactured from polystyrene, a petroleum-based plastic, and its incineration emits toxic gases causing damage to the environment. Our work presented in this paper deals with an alternative eco-friendly solution to this issue. Our work deals with a paperboard-based material as an alternative to thermocol, and the use of printed electronic components embedded within these boards acts as temperature control mechanisms in a green building. As a proof of concept, a prototype printed circuit has been prepared and embedded in a one-inch multi-ply recycled paperboard.

Keywords Paperboard walls · Smart infrastructure · Printed electronics

18.1 Introduction

Green infrastructure refers to the range of practices that restores some of the natural processes required for a sustainable, healthy environment, and also contributing to a better social and economic society. Green infrastructure, also known as ‘low-carbon

T. K. S. LakshmiPriya (✉) · N. Alagusundari
Department of Printing Technology, School of Engineering, Avinashilingam Institute for Home Science and Higher Education for Women, Coimbatore, India
e-mail: tkslp.dr@gmail.com

N. Alagusundari
e-mail: alagusundari124@gmail.com

© Springer Nature Singapore Pte Ltd. 2020
B. Subramanian et al. (eds.), *Emerging Technologies for Agriculture and Environment*, Lecture Notes on Multidisciplinary Industrial Engineering, https://doi.org/10.1007/978-981-13-7968-0_18

infrastructure,' is a major solution to restore the imbalance in nature caused by modernization and man-made infrastructure.

Green infrastructure can be understood as a process of protecting and enhancing nature and natural process. The green infrastructure is a strategically planned network of nature and semi-natural areas. These practices include rain gardens, vegetable swales, green roof, and porous pavements. Green infrastructure and green roof will absorb less amount of heat and will have cooling effects which can be controlled by sensors.

Green infrastructure is also considered as the basic building blocks of smart cities which facilitate good urban planning methods with the help of either digital technology and/or reengineered old concepts. Green infrastructures have anthropocentric functionalities. One of the functions is to maintain the temperature of buildings at moderate levels using approaches environment friendly or in a low-carbon mode. Such a facility is supposed to contribute to three benefits: (i) a better human health, (ii) reduction in costs for maintaining the temperature, and (iii) provide a sustainable environment.

In this paper, one such approach is presented. Green infrastructure is made a reality in this work, by employing a recycled paperboard as the interior walls and ceiling of a temperature-controlled enclosure. This infrastructure has inherent thermal insulation properties, and hence, the duty cycle of temperature control mechanisms such as air-conditioners will lead to lower carbon footprint. Secondly, an Internet of things (IoT) approach is adopted to monitor and control the temperature. This IoT system is built using the printed electronics technology, thereby becoming an integral part of the paperboard infrastructure.

The rest of the paper is organized as follows. Section 18.2 reviews the literature for the concepts adopted in this work. In Sect. 18.3, the novel idea of integrating printed electronics technology with recycled paperboards to prepare green infrastructure is described. The work in progress is elaborated in Sect. 18.4, and the paper concludes in Sect. 18.5.

18.2 Literature Survey

This section gives a short insight into the applications of paperboards and printed electronics, specifically in the building construction sector.

18.2.1 *Recycled Paperboards as Interiors for Buildings*

For over a decade, paperboard tubes have been in use in structural and construction engineering [1]. Some of the earlier works by one of the authors deal with the preparation of handmade paperboards with water hyacinth fibers as ingredients. It

has been found that such boards have thermal insulation property apart from being eco-friendly. These boards are potential candidates for green infrastructure.

Multiple plys of water hyacinth-based recycled paperboards were formed into a one-inch thick slab to test the feasibility of its usage as construction material. Alternately, due to thermal insulation property, these boards can be used as liners for inner walls and ceiling of enclosures that are air-conditioned.

From the eco-friendly perspective, the authors note that the use of water hyacinth in paperboards is a reduction-by-elimination approach to do away with water hyacinth which is a menace to corporations and municipality who are responsible for the maintenance of water bodies [2–4].

18.2.2 Printed Green Infrastructure

The last decade has witnessed the success of innovative application areas for printed electronics, and green infrastructure is one of them. Some of the research works, relevant to the contribution of this paper, are presented here.

Fernandes et al. have developed an algorithm to control the luminance level of split-pane electrochromic windows [5] that operate like Venetian blinds, so as to achieve better lighting energy saving. Such windows not only provide the inmates of the rooms with an unobstructed view of the outside but also saves 30–40% of lighting energy, thereby contributing to a greener infrastructure.

Building integrated photovoltaics (BIPV) refers to photovoltaic materials (solar cells) that are mounted on building materials used in roofing or wall systems. These servers dual purpose: building coverage and a source for electric power generation. This energy harvesting approach requires not additional cooling system as it becomes an integral part of the concrete in the walls. In his work, Jelle reviews the development and application of BIPV [6].

Hancke and Silva discuss the role of sensors that help in monitoring and controlling operations in smart cities [7]. The authors emphasize the significance of sensors in this domain with numerous applications and also discuss the challenges.

The increasing use of electronics into building infrastructure has attracted the printed electronics researchers to explore the use of printed components for building infrastructure. The National Research Council of Canada has identified printed electronics as a key enabling platform technology for smart infrastructure and cities of the future. Building integrated organic photovoltaic cells (BIOPVs) have been integrated in concrete façade elements, which form the building blocks for constructing green buildings [8].

Thus, it is evident that the growing need for green infrastructure and smart cities calls for the use of sensor-based infrastructure, which is now moving toward thin films and printed sensors. In this paper, we present a case where recycled paper boards can house printed electronic components for control operations in a smart building for energy-saving purposes.

18.3 Proposed Smart Printed Paperboard

Over the years, the use of air-conditioners for maintaining lower indoor temperatures has increased significantly. The hydro-fluoro-carbon (HFC) in air-conditioners is a greenhouse gas (GHG) and contributes to global warming. The carbon footprint of air-conditioners ranges from 300 kg CO₂ per year to over many thousands, depending on the capacity and application [9].

Recently, conscious efforts are being taken to minimize the use of GHGs. The proposed work in this paper is one such effort. This work has two contributions—(i) the use of multi-ply paperboard-based lining material as a replacement for thermocol for thermal insulation in buildings and (ii) the use of printed electronic circuits embedded in these linings, to regulate the air-conditioners. This is illustrated in Fig. 18.1.

Thermocol is manufactured from polystyrene, a petroleum-based plastic, and its incineration emits toxic gases. Paperboards, on the other hand, are eco-friendly. The carbon footprint of paperboard production (for 1000 kg of books) is about 1093 kg CO₂ [10]. Some of the earlier works of the author indicate that paperboards have thermal insulation property and hence are potential substitutes for thermocol for lining air-conditioned enclosures [2]. Hence, the use of multi-ply paperboard-based slabs can become an eco-friendly element for green infrastructure.

Secondly, the use of thin film technology and printed electronics, in making these paperboard-based slabs into walls smart, will further enhance the functionalities and capabilities of green infrastructure.

The primary advantage of the proposed system is that the carbon footprint is significant only during the manufacturing process and neither during usage nor during disposal.

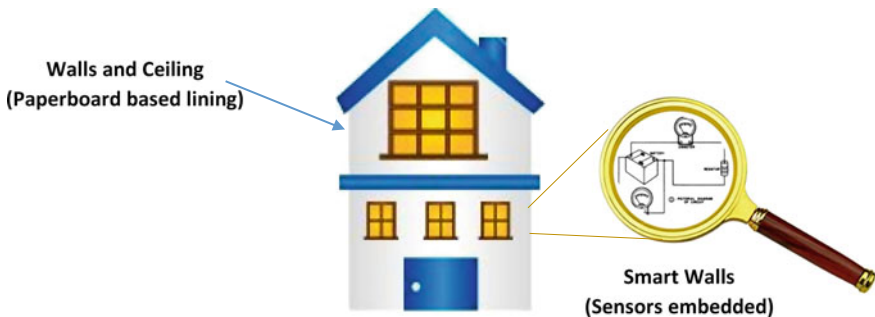


Fig. 18.1 Environment of operation

18.3.1 Methodology

The stages involved in the setting-up of a smart printed paperboard-based green infrastructure are shown in Fig. 18.2.

The production cycle begins with obtaining the specifications of the enclosure that needs temperature control, i.e., the room to be fitted with air-conditioner. The size of the enclosure, preferred temperature, tolerances on temperature variation, air-conditioner type, and carbon footprint, etc., are some of the essential parameters.

Using the data collected above, the specification of the temperature regulator mechanism is determined, i.e., the thickness of the paperboard lining, number of layers in the lining, ingredients of the paperboard.

The subsequent stages are concerned with the manufacture of the proposed lining for walls and ceilings, namely (i) preparation of the paperboard layer, (ii) preparation of a smart layer, and (iii) preparation of a multi-layer (or multi-ply) lining. The final stage is the testing product for correct operation and quality.

18.3.2 Manufacture of Paperboard Layer

Paperboard is prepared from waste paper and other ingredients such as cotton waste, water hyacinth fibers, sisal fibers, or kitchen waste. The manufacturing process flow is depicted in Fig. 18.3.

Paper waste is shredded or split and soaked for about 5 h or more depending on the coating and GSM of paper. If agriculture waste or kitchen waste are used, they also soaked along with paper. The mixture is then put in a beater for pulping during which additives are added to enhance mechanical and printable properties of the paper. This pulp is then sieved and hard pressed for the formation of paper base. The paper base is dried on a flat surface and then calendered for a glossy surface. The

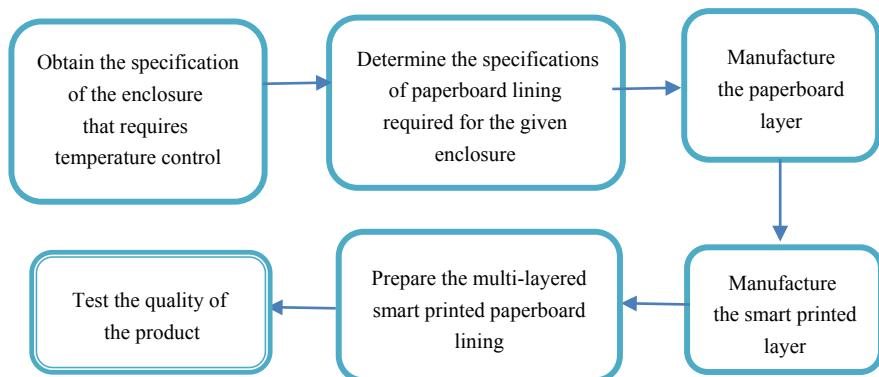


Fig. 18.2 Production cycle of smart printed paperboard

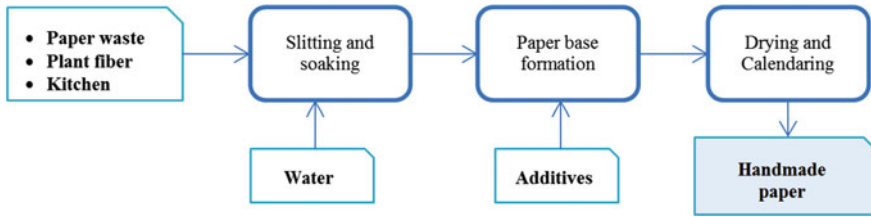


Fig. 18.3 Paperboard manufacturing process

paperboard thickness can be varied as per the requirement, by controlling the pulp quality while sieving the pulp to form the paper base.

18.3.3 Manufacturing the Smart Printed Layer

The process of manufacturing the smart printed layer is illustrated in Fig. 18.4.

- The process begins with gathering the requirements for the manufacture of the smart printed layer. The dimensions of the enclosure, its temperature requirements, normal operating temperature range, unacceptable temperature range, and temperature control requirements are some of the parameters that contribute to the design of the smart control circuit.
- The specifications collected in the previous stage are used to design the temperature control circuit. Care is taken to keep the power consumption at the minimum. The ratings of the circuit elements are finalized, and the circuit is drawn to suit the needs

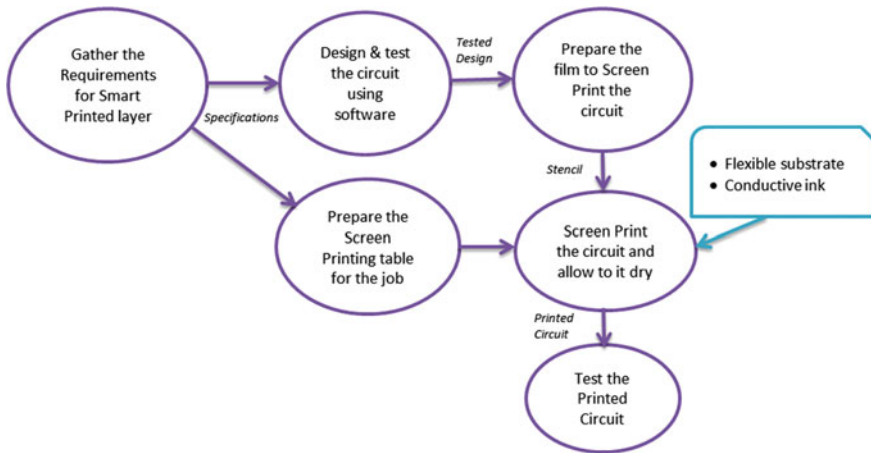


Fig. 18.4 Process of preparing the smart printed layer

of screen printing process. The thickness of the conducting lines and crossing overs is the key factors. The simulated circuit is tested.

- The vector image of the circuit design is generated and used for preparing the film, which is the image carrier for screen printing.
- Meanwhile, the table for the screen printing process is prepared with the required substrate and ink.
- The circuit is screen printed on the CT5 film substrate using conductive ink. Care is taken to maintain high resolution and consistency in the print, to ensure uniform conductivity. The print is allowed to dry and heated if required. The circuit elements are connected to the conductive lines, and the external power supply is connected.
- The screen printed circuit is tested for accurate functioning.

18.4 Work in Progress

As a proof of concept, a prototype printed circuit has been prepared and embedded in a one-inch multi-ply recycled paperboard. The details of these are presented below.

18.4.1 Multi-ply Paperboard

Paperboards were prepared using the waste papers and used record sheets of the students in our campus. The recycling was done in the recycling unit attached to the Department of Printing Technology. Many layers of paperboards are made and its been glued into a single board-ply. These are illustrated in Fig. 18.5.



Fig. 18.5 a Slitting and soaking. b Paper base formation. c Paperboards

18.4.2 Smart Printed Layer

The circuit for the smart printed layer consists of a thermal sensor for data acquisition and LEDs for status display. The design was carried out on Proteus 8.0 which is an electrical suite for circuit design and simulation. The smart layer is a SMT-type flexible circuit, and hence, provisions were provided in the PCB layout for placing the components. The evaluations and testing of the circuit were made on the simulator.

The tested circuit was redrawn on a CorelDRAW, vector graphic software, to fit into $1\frac{3}{4}'' \times 3''$ layout. The circuit was printed on a chromo film and exposed in a UV unit, and the screen stencil was ready.

The circuit was screen printed on the CT-5 film using conductive ink and allowed to dry at 60°C for 2 h. The circuit thus printed was tested for conductivity, wherein the conductivity between various segments of the circuit was tested using a multi-meter. It is essential to have uniform conductivity throughout the circuit for the proper functioning of the circuit.

The next stage was the placement of components—namely, the temperature sensor (LM35), LED (SMD), resistors (1–10 $\text{K}\Omega$), transistor (BC847)—following which an external power supply (5 V) is crimped to the printed circuit.

The completed circuit was tested for proper functioning and performance. These steps are depicted in Fig. 18.6a–f.

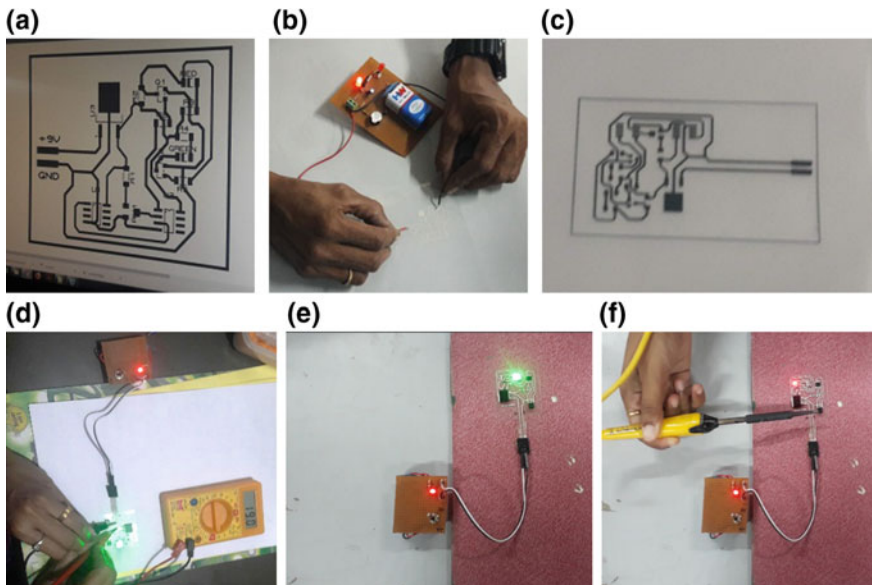


Fig. 18.6 a Design on Proteus. b Preliminary testing. c Printed circuit. d Conductivity test. e Normal temperature: green LED glows. f Temperature rises above threshold: red LED glows

Table 18.1 Measured average width of the conductive line

Point of measurement	Width (mm)
Outer vertical line (left)	0.43
Outer horizontal line (top)	0.40
Inner vertical line (near sensor)	0.41
Inner horizontal line (near red LED)	0.43
Inner horizontal line (near LM258)	0.41
Average width	0.416

Table 18.2 Measured characteristics of the prototype

Description	Value
Size of printed circuit	40 mm × 70 mm
Average width of the conductive line	0.416 mm
Standard deviation in width	0.012 mm
Voltage drop	10 mV

18.5 Result and Discussion

The circuit designed and printed was first checked for correctness which is done by checking the compliance of the dimensions with the expected specifications, the width of the printed lines, the placement of the components and by carrying out the conductivity. The readings are tabulated in Table 18.1.

The average width of the circuit is 0.416 mm with a standard deviation of 0.012 mm which is acceptable for a prototype done on a low-cost basis.

The characteristics of the circuit are given in Table 18.2. These values are sufficient for a working prototype to serve as a proof of concept. However, the circuit has to be tested for stretchability of the substrate, performance of the circuit with varying deviation width, failure conditions, etc.

18.6 Conclusion

Paperboards have significantly low carbon footprint as compared to thermocol. Hence in this work, paperboards have been prepared to serve the purpose of linings for air-conditioned rooms. Secondly, for moving toward green infrastructure, these linings have been embedded with a smart layer, namely the smart printed layer which comprises printed circuit for monitoring the temperature of the enclosure. Thus, this paper presents a new avenue for incorporating components in a green infrastructure.

References

1. Bank, L., Gerhardt, T.: Paperboard tubes in structural and construction engineering. In: Harries, K.A., Sharma, B. (eds.) *Nonconventional and Vernacular Construction Materials—Characterisation, Properties and Applications*, Chapter: 16, 1st edn, pp. 453–480. Woodhead Publishing Series in Civil and Structural Engineering: Number 58 (2016). <https://doi.org/10.1016/b978-0-08-100038-0.00016-0>
2. Keerthana, S., Sanjanababu, Ambika, S., LakshmiPriya, T.K.S.: Hand-made paper production utilizing water-hyacinth—application as thermal insulating material. In: *International Conference on 21st Century Printing*, Guru Jambheshwar University of Science and Technology, Hisar, Feb 2015. *Printing Conference Proceedings* ISBN 978-8-19071-455-6
3. Ambika, S., LakshmiPriya, T.K.S.: Protecting the aquatic environment by consuming water-hyacinth in the manufacture of packaging material. In: *5th International Printing Technologies Symposium*, Istanbul University, Turkey, Nov 2016, pp. 425–435. Available at <http://iprints.istanbul.edu.tr/?p=7549>. ISBN 798-605-07-0613-0
4. Ambika, S., LakshmiPriya, T.K.S.: Manufacturing handmade paperboard products—a ToT towards Gandhian villages. In: Geetha, K.T., Vimala, V. (eds.) *5th International Conference on Development Policy—Transfer of Technology for Sustainable Growth and Development: Lessons and Experiences*, 21, 22nd August 2014, (Avinashilingam University in collaboration with The Institute of Finance Management Dar es Salaam, Tanzania). *Conference Proceedings* ISBN-978-81-8371-7076
5. Fernandes, L.L., Lee, E., Ward, G.: Lighting energy savings potential of split-pane electrochromic windows controlled for daylighting with visual comfort. *J. Energy Build.* **61**, 8–20 (2013). <https://doi.org/10.1016/j.enbuild.2012.10.057>
6. Jelle, B.: Building integrated photovoltaics: a concise description of the current state of the art and possible research pathways. *Energies* **9**, 1–30 (2016). <https://doi.org/10.3390/en9010021>
7. Hancke, G.P., Silva, B.: The role of advanced sensing in smart cities. *Sensors* **13**(1), 393–425 (2012)
8. Article on BIOPV in Printed Electronics World: <https://www.printedelectronicsworld.com>
9. Kumar, R., Aggarwal, R.K., Gupta, D., Sharma, J. D.: Carbon emission from air conditioning. *Am. J. Eng. Res. (AJER)* **2**(4), 72–74. e-ISSN: 2320-0847, p-ISSN: 2320-0936. Available: [https://ajer.org/papers/v2\(4\)/I0247274.pdf](https://ajer.org/papers/v2(4)/I0247274.pdf)
10. A weekly blog on science, news and ideas related to climate change “The climate in Emergency “ wordpress.com, Article “Carbon footprint of a hardback book”. Available: <https://climateinemergency.wordpress.com/2016/04/12/the-carbon-footprint-of-a-book/>

Chapter 19

WSN-Based System for Forest Fire Detection and Mitigation



Kotish Grover , Ditsha Kahali , Shreya Verma 
and Balaji Subramanian 

Abstract The risks, consequences and severity of wildland fires are well-known. Hence, the demand for timely, high-quality fire information in the least amount of time possible and the subsequent intimation to concerned authorities would help in scaling down the loss of life and property. This paper discusses a WSN system which collects data using multiple sensors to monitor temperature, humidity, smoke and oxygen levels in several spots in a forest environment. The forest would be divided into square-shaped clusters for monitoring, each containing a sensor system. The localisation of the node would be done using satellite communication to reduce coverage holes and ensure maximum range with the least latency. This node would communicate data to a monitoring station with its location and send alerts according to the sensed thresholds breached based on the novel logic algorithm. This paper describes the overall structure of the sensing system, detection and prediction algorithms, topology of the WSN, localisation techniques and an insight into a suggested drone-based mitigation system to localise the fire.

Keywords Wildfire · WSN · Forest fire detection · WSN in forests · Localisation techniques · Forest fire mitigation

K. Grover (✉) · D. Kahali · S. Verma · B. Subramanian
VIT, Vellore, India
e-mail: kotish97@gmail.com

D. Kahali
e-mail: ditsha.kahali@gmail.com

S. Verma
e-mail: shreyav1@gmail.com

B. Subramanian
e-mail: sbalaji@vit.ac.in

19.1 Introduction

Wildfires are natural or man-made occurrences, where combustible floral areas are harmed due to fire. According to the area affected, they might be categorised into brush fire, bush fire, desert fire, forest fire, grass fire, hill fire, peat fire, vegetation fire and veld fire. At present, ground patrolling, watching tower, aerial prevention, long-distance video detection and satellite monitoring are used to prevent as a traditional forest fire.

India is not unknown to the losses of life and property caused due to forest fires. In 2016, Indian state of Uttarakhand suffered heavy casualties due to an estimated 3,500 ha (8,600 acres) of forest area burnt. The fire also had environmental consequences with the average temperature of northern India facing an increment of 0.2 °C. In the past 16 years, India has an increase of 46% in forest fires which in total is a 125% increment from 15,937 in 2003 to 35,888 in 2017. In 2017, Madhya Pradesh saw the majority of the forest fires followed by Odisha and Chhattisgarh [1]. Another incident in the Indian state of Tamil Nadu occurred where 20 young trekkers lost their lives due to a forest fire in Theni forest cover. The consequence of this was that some of the Indian states had to ban trekking in the forest areas for an indefinite period.

Hence, the need of the hour is to find systems which can detect forest fires with precision in an energy efficient and self-sustaining manner. One of the most effective ways to approach this problem is using wireless sensor networks (WSN). It generally comprised of spatially disseminated sensors to monitor physical and natural conditions, for example, temperature, smoke, flame, humidity and location data to control room.

Many models such as US Rothermel model, Australia's McArthur model, national forest fire spread model of Canada and China's Zheng Wang model have been proposed since R. Forts put forward the mathematical model of the spread of forest fire. However, the implementation of a mathematical model had limitations, especially those based on an assumption, once out of the event, there will be an error.

Forest fires anywhere in the world are primarily detected by NASA's Moderate Resolution Imaging Spectroradiometer (MODIS) and Visible Infrared Imaging Radiometer Suite (VIIRS) satellites. These are highly specialised satellites which detect fire and relay information to various responsible departments all over the world.

A few years ago, the time lapse between spotting the fire and the news reaching the responsible departments was five to six hours, but this has been reduced to about two hours recently.

In this paper, we address this pressing issue and propose an effective WSN method to resolve it which gives us accuracy and speed to react to stop the fire from spreading and harming human life and property. We propose a self-sustaining sensing mechanism with a novel algorithm and give accurate positioning of the fire within a few seconds of the fire starting using Global Positioning System-based localisation.

Table 19.1 List of components and their application in the system

Components	Specification	Remarks
Microcontroller	Node MCU	Microcontroller with ESP8266 microprocessor
Smoke sensor	MQ-2	Used for smoke and combustible gas detection
Temperature and humidity sensor	DHT11	Used for measuring temperature (°C) and humidity (RH)
Flame sensor	RKI3100	This sensor is a short-range sensor which senses light between 760 and 1100 nm wavelength
Oxygen sensor	Grove gas sensor (O ₂)	(Optional)
GPS module	GY-NEO6MV3	For localisation
Arduino Nano	For GPS module	Aids localisation and communication
SAT-202	Communication module	For satellite communication
Voltage regulator	LM 7805	Voltage regulation
Power supply	2.5 W 9 V Polycrystalline solar panel solar cell	For power supply of self-sustained system

19.2 Structure of the System

The structure of the system consists of two parts: a sensing system and a communication system. The sensing system, placed in the forest, acts as the nodes of the WSN and consists of the following components (Table 19.1).

The circuit diagram for each node, consisting of the above components, is given in Fig. 19.1.

The communication system is covered in Sect. 19.5.

19.3 Algorithm

As the system retrieves the data from the sensors, in every cycle it computes the conditions for temperature, humidity and flame as given by the flow chart in Fig. 19.2.

1. Indicators corresponding to each sensing parameter (e.g. temperature, smoke, etc.) get activated if its threshold is crossed.
 - Temperature indicator is switched on if temperature >50 °C.
 - Humidity indicator is switched on if humidity <40%. This prescribed value changes from place to place depending upon its geographical location, winds

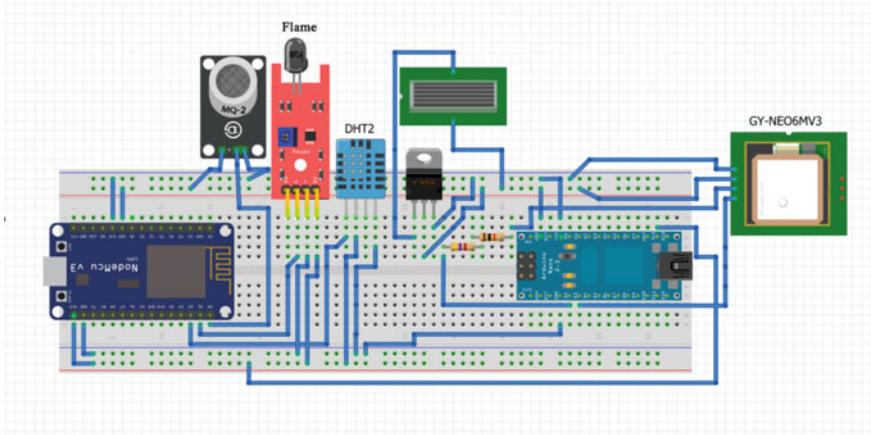


Fig. 19.1 Circuit diagram of every node

blowing and the season. This data will be different for different settings and has to be adjusted accordingly when installing the system up. For the sake of example, we have used the example of a somewhat dry area, with only seasonal rainfall, and set the threshold to be 40% relative humidity (RH).

- Smoke indicator is switched on if smoke detected.
 - Flame indicator is switched on if flame is detected.
2. If the flame detector goes high, the fire alert is sent irrespective of any other sensor reading as the presence of flame at the height of tree branches is extremely dangerous and a clear indication of a wildfire.
 3. If smoke is detected, as is the case in most scenarios as forest fires mostly light on the grass levels and the smoke is the first element which rises up, the temperature is tested.
 - a. If the temperature is high ($>50\text{ }^{\circ}\text{C}$), there is a clear indication of a wildfire, and alert is sent.
 - b. If the temperature is low, chances are that there is a campfire whose smoke is reaching the sensors. However, if the temperature steadily rises to more than $50\text{ }^{\circ}\text{C}$, the fire alert is sent.
 - c. If humidity is between 40 and 50% RH, a slow spreading fire detection message is sent, and if the humidity is less than 40%, a fast-spreading fire alert is sent, as fire spreads easily when the air is dry.
 4. If smoke is not detected, but the temperature is high, and humidity is low, the chances of occurrence of fire are high and the corresponding alert is sent to the department.
 5. If smoke is not detected, but the temperature is high, and humidity is high, the chances of occurrence of fire is low, and hence, the system is stable.

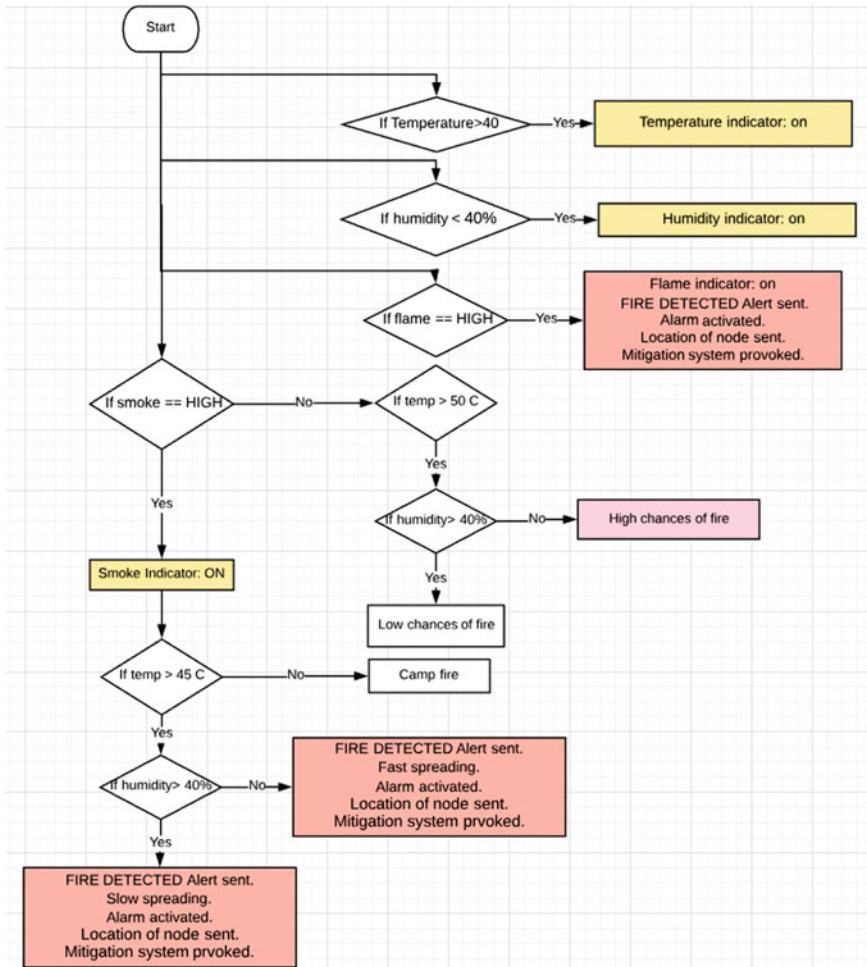


Fig. 19.2 Algorithm flow chart

6. If a temperature surge is noticed for a very brief period when humidity is high. Chances are that there was a lightning strike. Fire alert sent immediately. If it is followed by smoke, fire alert sent again.

19.4 Localisation

Once a fire has been detected, it is paramount to know its location for mitigation. In a sensor network, localisation can be best described as ‘recognising the node’s location’. For any wireless sensor network, an important factor is the accuracy of

its localisation mechanism. The absolute position of sensor and between sensor estimation, for example, distance and bearing measurement, is used by network localisation algorithms to evaluate the location of sensor at first obscure data.

Localisation mechanisms can be categorised as anchor based or anchor free, GPS based or GPS free, stationary or mobile sensor nodes and range based or range free [2]. Localisation algorithm for wireless sensor networks depends on different measurement technique. Network architecture, number of nodes, signalling bandwidth and shape of the area are one of the few factors to be weighted while we design a localisation algorithm [2].

Range-based localisation uses techniques based on distance estimation and angle estimation. Received signal strength indication (RSSI), angle of arrival (AOA), time difference of arrival (TDOA) and time of arrival (TOA) are the techniques used for range-based localisation [3]. Range-free localisation uses regular radio modules and is only dependent on the received messages content. The techniques under range-free localisation are DV hop, multi-hop, centroid, gradient [4]. GPS-based localisation is categorised under absolute localisation. Sensors with known location are known as anchors, and the Global Positioning System is used to locate their position [4, 5].

From the comparison in Table 19.2, we can infer that GPS-based localisation is the most accurate technique. Accuracy is of absolute importance to our fire detection system. The Global Positioning System is a network of 24 satellites circling the earth at elevation of 20,000 km. At any point of time, four GPS satellites are visible. The information is transmitted about their position and current time at normal interim of time. GPS receiver intercepts these signals and figures the separation of each satellite in view of the time taken by the message to arrive. The distance from four or more satellite is calculated by the receiver to confirm the location of the node. GPS does not require transmission of data by the user, rather it operates independently of any telephonic or internet reception. Global coordinate system is used by the anchors to determine the position of the network. High-quality GPS receivers based on Standard Positioning System (SPS) can attain accuracies of 3 m; hence, we use Global Positioning System-based localisation mechanism to detect the position of nodes [4, 6]. Although, the technique used to compute locations and the measurement conditions in its surroundings affect the localisation accuracy of any GPS system [7].

Table 19.2 Comparison of various localisation mechanisms [2]

Technique	Cost	Accuracy	Energy efficiency
GPS	High	High	Less
TDOA	Low	High	High
RSSI	Low	Medium	High
TOA	High	Medium	Less
GPS free	Low	Medium	Medium
AOA	High	Low	Medium
DV hop	Low	Medium	High

19.5 Communication

For communication, we use a satellite communication model based on the Honeywell communication system. The steps of communication are illustrated in Fig. 19.3.

Honeywell provides a global IsatM2 M data service using its system of five Inmarsat geostationary satellites. Honeywell Global Tracking uses the attached SAT-202 which is a monitoring and tracking satellite terminal.

Discrete channels are used to transmit information to and fro from terminals, and which channels to use for receiving or transmitting is set when the terminal powers up for the first time. Each terminal has a unique Inmarsat Serial Number (ISN) to identify it for message delivery purposes. A unique address code (AdC) is provided by the service provider and is mapped to the ISN at the application. A unique identifier known as the service identifier is pre-programmed in the SAT-202 as it plays a vital role in sending of receiving data. Each satellite sends a ‘bulletin board’ on a pre-established frequency.

Output Form:

Using Inmarsat-M2 M network we send a double burst message containing two long bursts. The first burst contains the sensor values, which is sent one by one in the following manner:

- SR 1 00XX Smoke Level
- SR 2 00XX Temperature
- SR 3 10XX Humidity
- SR 4 00XX Flame
- MB D9//Transmit Data Message.

Where the ‘XX’ would be the 2-byte hexadecimal values from sensor 1 to 4.

The two long bursts are a custom sensor report and a standard GPS report [5].

The Message Handling System by Honeywell stores the messages sent through the satellites, by the SAT-202 terminals. Application service providers (ASP) must connect with the handling system to procure the values for monitoring [5].

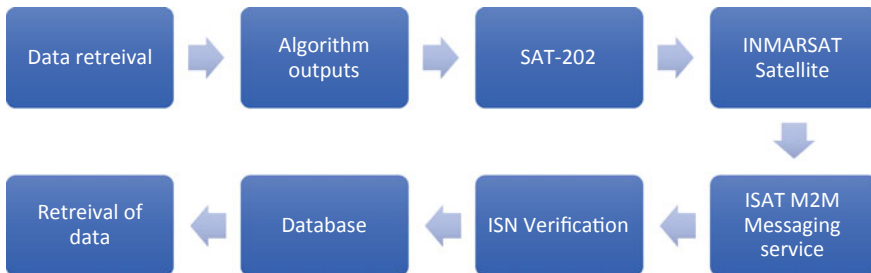


Fig. 19.3 Flow chart of the communication mechanism

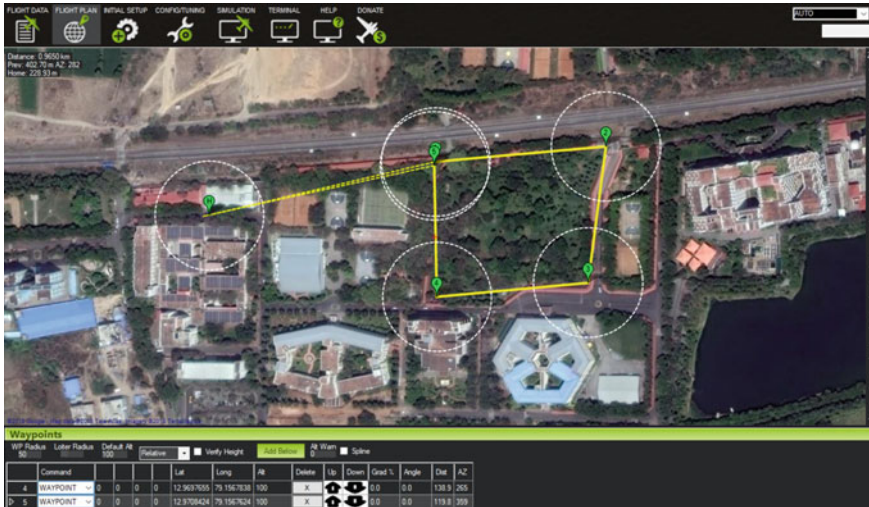


Fig. 19.4 Flight plan for localisation mechanism

19.6 Mitigation

Once the information about the initiation of fire is provided to the base station, the next step is to mitigate the fire and localise it as soon as possible. As it is difficult for the fire department to provide support, we use a multi-rotor drone for the mitigation purpose which can fly autonomously to the cluster which is under distress (Figs. 19.4 and 19.5).

As the coordinate of the given fire will be known, we use those coordinates as a feed for our drone to plot a flight path.

The drone, after reaching the cluster location, would spray a class A extinguisher around the fire to localise it, and once localisation is done, we can proceed towards extinguishing the fire.

19.7 Results and Discussions

The system discussed in this paper is an improvement on the existing NASA’s MODIS system which is the current technology in use. The limitation of this system is that as the resolution of these satellites is nearly $375\text{ m} \times 375\text{ m}$, fire can only be detected when it reaches the resolution of half a pixel, i.e. which is roughly 7 ha. Added to this is the latency of transmission. This would imply that there is a huge latency in the detection of fire. This latency is needed to be removed, and a more efficient system is paramount. If the forest fire can be detected in seconds within its start, valuable time can be saved, and proper measures can be taken.

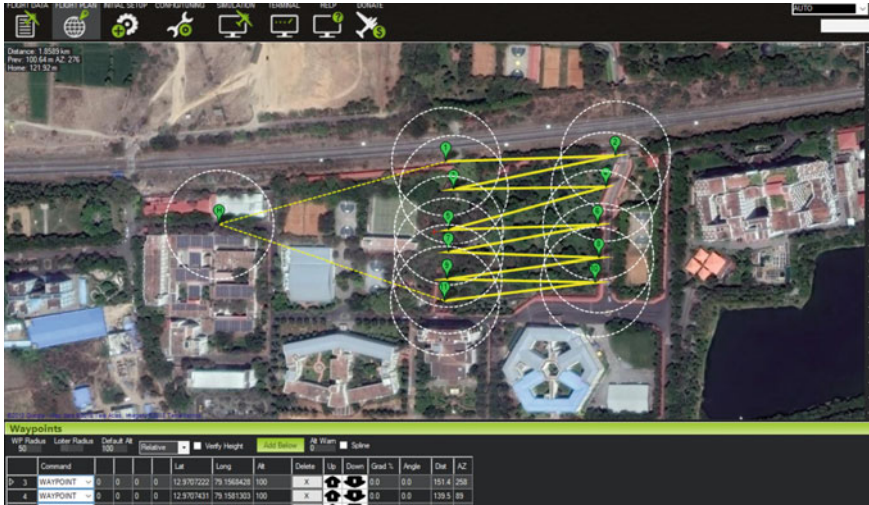


Fig. 19.5 Flight plan for extinguishing the fire mechanism

The improvement introduced in this system is that instead of detecting fire from a distant satellite, we instead detect fire from within the forest and depend on satellites only for communication. The sensors mentioned above were further calibrated in experimental conditions and tested for accuracy.

In the experiment, we tested the temperature, humidity, smoke and flame sensors. A fire was ignited on a wooden block at 20 s mark, and time taken by sensors to detect the fire was checked. The fire was extinguished at 50 s mark.

As shown in Fig. 19.6, the smoke sensor detected the fire in the very first 2 s of ignition, while the flame sensor took some time to detect the fire. When the fire was extinguished, the flame sensor immediately reacted while the smoke sensor retained its value for the next 9 s.

Figure 19.7 describes the reaction of the temperature sensor post-ignition. The temperature increased gradually at first and at 26 s mark it crossed the danger point. When the fire was extinguished at 50 s mark, it was seen that the temperature around the system gradually decreased and came below the danger point 16 s after the fire was extinguished.

Figure 19.8 describes the reaction of the humidity sensor post-ignition. The humidity around the system decreased sharply at the 23 s mark and crossed the danger point at 26 s mark. When the fire was extinguished at 50 s mark, it was seen that the relative humidity was recovered at the 90 s mark.

The timeline of the above experiment is given in Table 19.3.

It is inferred from the table that all the four sensors are active from 26 s mark to 55 s mark, and the designed system can transmit the status of mentioned sensors to the control room.

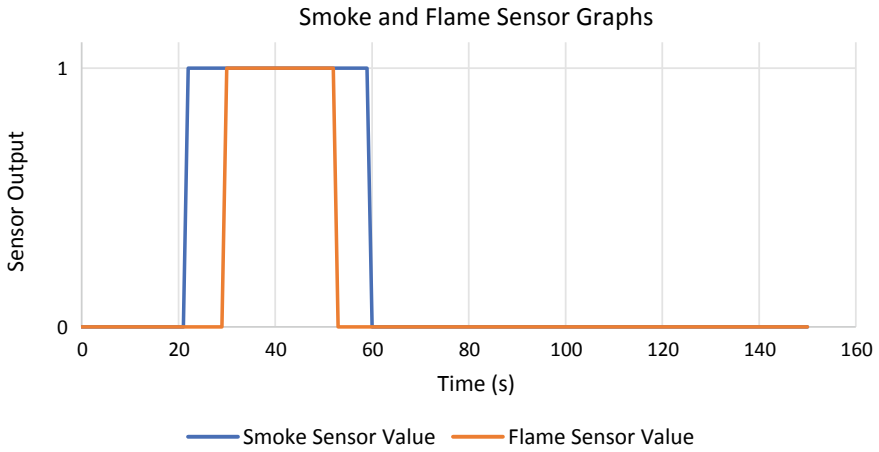


Fig. 19.6 Graph of reaction of smoke and flame sensor when introduced to fire

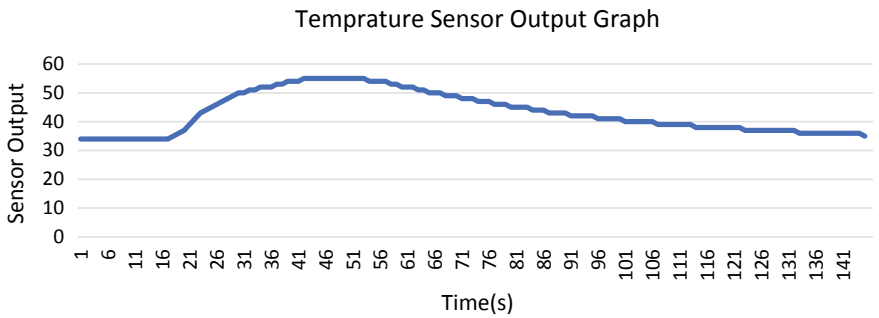


Fig. 19.7 Graph of reaction of temperature sensor when introduced to fire

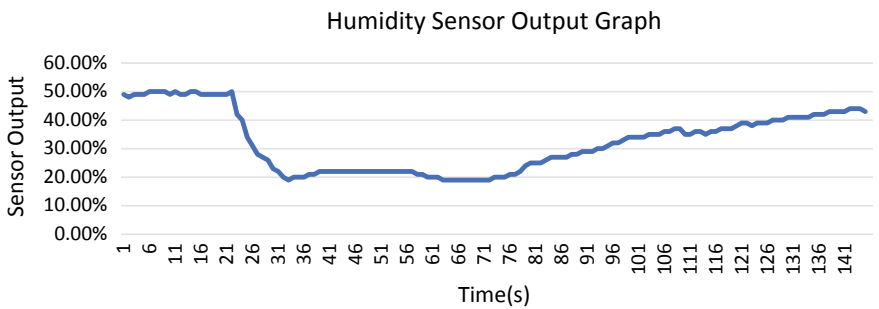


Fig. 19.8 Graph of humidity sensor when introduced to fire

Table 19.3 Timeline of system outputs received by the authorities

Time (s)	Status of sensors
1–19	Normal
19–26	Smoke indicator on
26–55	Temperature indicator on; humidity indicator on; smoke indicator on. FIRE DETECTED. Location sent. Fire alarm: ON; and provoke mitigation system.
55–91	Temperature indicator on; humidity indicator on
97–121	Humidity indicator on
127–145	Normal

The above results clearly demonstrate that the proposed system detected the fire in a faster manner than the existing system.

19.8 Conclusion

In this paper, an idea for forest fire detection has been proposed which is much quicker and efficient at early detection and warning of wildfires than the currently used methods. The implementation and working details were also included. The task was divided into five sections, namely the WSN sensor node architecture, the detection algorithm, localisation of each node, communication of sensor and position data and drone mitigation system. In this method, the fire is detected within seconds of lighting, as discussed and shown in Sect. 19.6, and the information is communicated to the authorities for timely fire extinguishing using the mitigation system proposed before it spreads and goes out of control. This system has innumerable social impacts as forest fires result in a number of deaths year-round and loss of property and also ecological impacts as forest fires result in mass green cover destruction and release of harmful greenhouse gasses and smoke particles which heavily contribute to air pollution and global warming.

References

1. Indian State of forest Report (ISFR) (2017)
2. Alrajeh, N.A., Bashir, M., Shams, B.: Localization techniques in wireless sensor networks. <https://doi.org/10.1155/2013/304628> (2013)
3. Boudhir, A.A., Mohamed, B., Mohamed, B.A.: New technique of wireless sensor networks localization based on energy consumption. *Int. J. Comput. Appl.* **9**(12), 0975–8887 (2010)
4. Paul, A.K., Sato, T.: Localization in wireless sensor networks: a survey on algorithms, measurement techniques, applications and challenges. *J. Sens. Actuator Netw.* **6**(4), 24 (2017)
5. Cheng, B., Du, R., Yang, B., Yu, W., Chen, C., Guan, X.: An accurate GPS-based localization. In: *Wireless Sensor Networks: A GM-WLS Method*; 2011 40th International Conference on Parallel Processing Workshops. <https://doi.org/10.1109/icppw.2011.32> (2011)

6. Singh, S.P., Sharma, S.C.: Range free localization techniques in wireless sensor networks: a review. *Procedia Comput. Sci.* **57**, 7–16. <https://doi.org/10.1016/j.procs.2015.07.357> (2015)
7. Singh, Y., Saha, S., Chugh, C., Gupta, C.: Distributed event detection in wireless sensor networks for forest fires. Department of Computer Science and Engineering, Jaypee University of Information and Technology
8. Shahzada, F.: Satellite monitoring of wireless sensor networks (WSNs). In: *The 5th International Symposium on Application of Ad hoc and Sensor Networks (AASENT'13)*, KFUPM, Dhahran
9. Zhang, J., Li, W., Yin, Z., Liu S., Guo, X.: Forest fire detection system based on wireless sensor network. School of Technology, Beijing Forestry University, Beijing

Chapter 20

Analysis of Grid Parameter Variation with Renewable Energy Sources on Variable Frequency Drive DC Capacitor Reliability



P. Ramesh, R. Govarathanan, K. Palanisamy and S. Paramasivam

Abstract This paper investigates the influence of the grid-connected renewable energy sources and their effect on the utilities having diode front-end rectifiers. The grid interface in the renewable energy converters generally has PWM Inverters with LCL filters. These LCL filters are tuned for different resonance frequencies based on their switching frequency and system parameters. With multiples of renewable energy source converters connected in parallel, the grid parameters and harmonic interaction change differently based on the individual LCL filter design and operating conditions. This condition becomes worse if inverters connected in the same PCC are significantly increased. The utility rectifiers are designed for a specific range of grid specification according to various international standards. Effect of grid parameter variation such as voltage and current harmonic injection due to these inverters in a specific grid configuration and application from earlier studies is referenced. Grid model is generated from earlier studies and simulation was carried out for a specific diode front-end model of VFD. Reliability variation in front-end rectifier utilities such as variable frequency drives with a special emphasis on DC filter capacitor and DC link inductor is also discussed.

Keywords PWM inverters · LCL filters · Variable frequency drives · PCC · DC filter capacitor · DC link inductor

P. Ramesh · R. Govarathanan · S. Paramasivam
Power Electronics—R&D, Danfoss Drives, Chennai, India
e-mail: ramesh@danfoss.com

K. Palanisamy (✉)
Department of Energy and Power Electronics, Vellore Institute of Technology, Vellore, India
e-mail: kpalanisamy@vit.ac.in

© Springer Nature Singapore Pte Ltd. 2020
B. Subramanian et al. (eds.), *Emerging Technologies for Agriculture and Environment*, Lecture Notes on Multidisciplinary Industrial Engineering,
https://doi.org/10.1007/978-981-13-7968-0_20

20.1 Introduction

Renewable energy sources in utilities have grown significantly across the globe due to various government subsidies [1]. Photovoltaics (PV) are widely used on rooftops and also on commercial buildings. These distributed power inverters (DP) are connected together in the same distributed power network. Obviously, single-phase and three-phase PV inverters are widely used in such low-voltage grid. Due to different inverter topologies and control techniques inherent in these DP inverters, there is harmonic interaction [2] between these inverters with the distributed network in addition to power quality problems. Harmonic interaction results in the generation of current harmonics, background voltage distortion, and resonance effect between inverters and the network. These PV distributed power inverters have LCL filters in their front-end design. LCL design and its values vary between inverters resulting in resonance effect with the connected network. The grid is polluted considerably with current and voltage harmonics due to the above effects. Front end devices of Variable frequency drives (VFD) reliability is greatly affected when connected in such grid configuration. There are no much researches addressing VFD lifetime reduction due to pollution offered by such PV connected grid. Simulated model was developed using a typical PV grid application [1] and its effect on reliability and lifetime reduction of DC filter capacitor in VFD is calculated through simulation results.

20.2 Power Quality Concerns

New developments in power quality standards indicate that harmonic interaction and resonance effects of distributed power inverters grid are in increasing trend. Although PV Inverters meet international standards such as IEC 61000-3-2 under the specified conditions, the limits are getting deviated when they are connected at the point of common coupling (PCC) of such grid conditions. Analysis and practical measurements of power quality problems in such PV grid paves way for the study on connected inverters and distributed network layout. Single-phase PV Inverters are common for household in smaller power ranges up to 5 KW. To meet IEC 61000-3-2 standards, these inverters use PWM controllers to generate sinusoidal output currents. Generally switching frequency is in the order of 20–500 kHz, with MOSFETs and IGBTs as switching elements.

Inverter topologies used commonly in such PV inverters [1] are as below:

- (i) Single-stage PWM DC-AC converter topology (H-bridge or push–pull) directly coupled to the grid via LF isolation transformer and filter.
- (ii) Multistage pulse width modulation (PWM) dc-ac converter front-end topology includes HF isolation transformer, rectifier, and line-frequency unfolding bridge coupled to the network.

DP inverters commonly have controllers with multiple control loops performing tasks such as MPPT, DC-AC power conversion, reactive power compensation, and

harmonic cancellation. AC output current of such inverters is mainly through inner control references and feedback synchronized with supply voltage. Background distortion of supply voltage pollutes output current waveshape. To achieve sinusoidal output current at output of inverter, its impedance as a function of frequency should be higher to avoid harmonic current injection into the network. Internal controller with active or passive filtering techniques fulfils the same. As inverter operates at high-switching frequency, filtering and damping are adequately taken care during inverter design. PQ issues can be addressed with current reference source being generated internally, output impedance made higher with respect to line-frequency harmonics and low output capacitance as an output filter.

Resonance is a common phenomenon wherein large number of DP inverters connected to low-voltage network. Based on the configuration of network and location of harmonic generating sources, series and parallel resonance occurrences are obvious. Parallel resonance situation arises due to harmonic distortion current generated by PV inverter corresponds with parallel resonance frequency on the network voltage at PCC resulting in high-voltage distortion. Series resonance situation arises due to harmonics present in network background distortion corresponds with series resonance frequency resulting in high resonance current flowing in the network. Increased voltage and current distortions are the adverse effects of DP inverters connected in same distribution network. Series and parallel resonances can be calculated at frequency f_r by Eq. (20.1) as below

$$f_r = \frac{1}{2\pi\sqrt{LC}} \quad (20.1)$$

where L and C are equivalent reactance and capacitance of equivalent series or parallel network.

20.3 Modelling and Simulation of DP Photovoltaic Network Grid

Harmonic interaction between DP inverters and distributed network is analysed in detail by considering a real-time residential network which comprises of PV arrays roof-mounted operating under different topologies and control concepts. Network modelling and technical study are referenced from earlier studies [1] in Fig. 20.1. Various inverter type models have been validated using the experimental set-up. MATLAB model has been developed for various inverters connected to individual points. From the simulation results in Fig. 20.2a, b captured with the back ground distortion of 3% V_{THD} (reduced by 2% in order to keep the voltage within the regulation limits), the V_{THD} was increased up to 6.71%. This increased voltage distortions and double zero crossings reduce the quality of the voltage waveform. The distortion is mainly due to the series resonance initiated by the background supply harmonics and network components. The large magnitude of voltage harmonics was

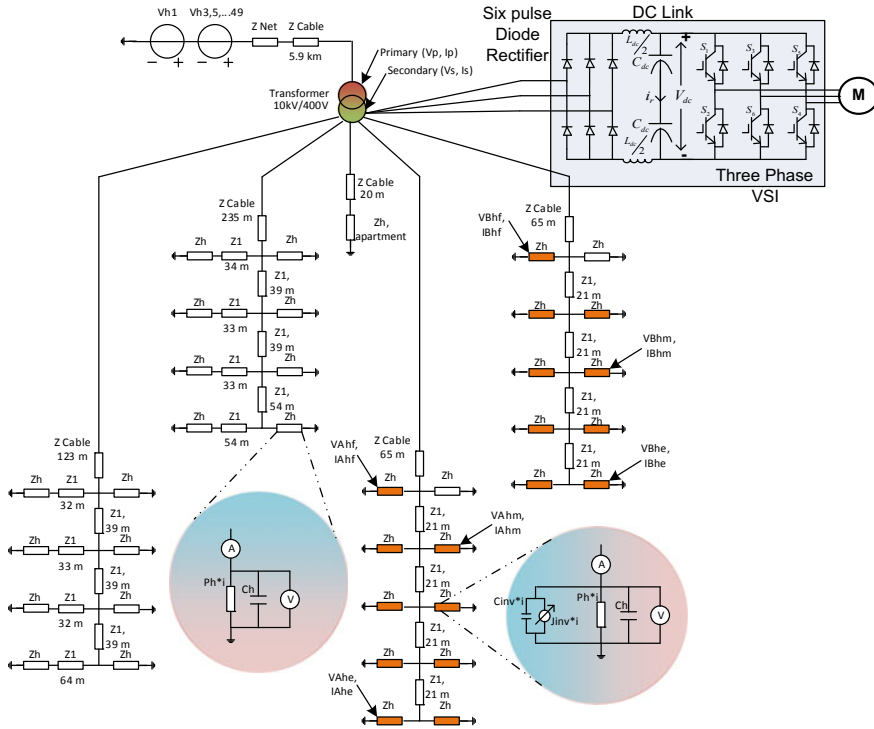


Fig. 20.1 Model of low-voltage distributed power inverters network with photovoltaic renewables (Source [1])

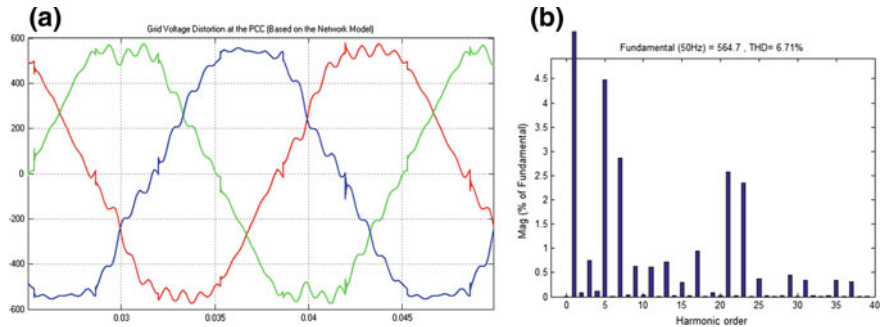


Fig. 20.2 **a** Voltage waveform at PCC on simulated grid and **b** harmonic distortion at PCC on the simulated grid

seen around twenty-first and twenty-third orders. The most increased harmonics are around twenty-first harmonics due to the parallel resonance circuit which is clearly dominated.

20.4 Review of Utility Interface on VFD Reliability

Six pulse diode bridge of a Variable Frequency Drive is connected to the PV grid as shown in Fig. 20.1. A VFD Model of 315 kW, 400 V, 580 A, and 50 Hz is considered for the simulation studies. The Effective DC filter capacitor and inductor are 14,000 uF and 62 uH respectively. DC capacitor filters both harmonic components of DC link current and the high-frequency ripple current due to inverter switching in VFD. DC link inductor supports the ripple current reduction in the capacitor. AC line impedance connected additionally at input of VFD depends on short-circuit capability of the utility grid. For simulation studies, grid is considered with a short-circuit ratio (R_{scc}) at 120 without distortion. But the short-circuit current varies due to the DP inverter interaction in the PV grid. Reliability and lifetime of the front-end rectifier diode, DC filter capacitor, and DC link inductor in VFD are significantly affected due to the dynamic grid impedance variation. The core losses of DC Link Inductor significantly increase due to high-frequency harmonic voltages present in voltage waveform as shown in Fig. 20.10. Various parameters, relationship factors and equations involved in DC capacitor lifetime are discussed below.

20.4.1 Capacitor Lifetime

Capacitor Heating Effect due to ESR

Lifetime of the DC filter electrolytic capacitors in VFD mainly depends on mains voltage, ripple current of the capacitor, ripple current frequency, temperature and air flow. The insulation stress is increased if the ripple voltage is increased. If the operating temperature is close to capacitor rated temperature value, extra leakage current that results from operation under highest voltage rating can cause electrochemical degradation which reduces the capacitor lifetime. Reducing the applied DC voltage will extend the capacitor lifetime, even at elevated operating temperatures. If the surrounding temperature, ripple current, air velocity, and the operating frequency change, the capacitor lifetime will also change. The lifetime is the function of these factors [3, 4].

The capacitor ripple current will contain different harmonic frequency components. The magnitude and the frequency of each harmonic content in the grid side will vary the capacitor current drastically. ESR is equivalent series resistance of the capacitor and is the loss-producing element in the capacitor. The power loss in the capacitor is the multiplication of the square of different frequency ripple currents and the ESR. ESR is the function of the operating frequency and decreases with the increase of frequency. If the ESR changes with the frequency, the losses will also change. To quantify these factors and to calculate the losses P_d , the following formulae in Eq. (20.2) is used. I_n is rms current at frequency f_n through capacitor weighted with respect to ripple current multiplier M_{fn}

Table 20.1 Ripple current multiplication factor as a function of frequency

Frequency (Hz)	Multiplication factor (M_f)
50	0.4
120	0.5
400	1.09
700	1.113
1000	1.123
3000	1.146
4000	1.15
5000	1.153
7000	1.16
10,000	1.17

$$P_d = \text{ESR}_{120} \sum_{n=1}^{\infty} \frac{I_n^2}{M_{f_n}^2} \quad (20.2)$$

Capacitor manufacturers used to specify the ESR at 120 Hz. The power loss will be calculated for different frequencies with the multiplication factors (M_f) as shown in Eq. (20.3). M_f is the multiplying factor [5] where it gives the ratio of ripple currents I_f and I_{120} .

$$M_f = \frac{I_f}{I_{120}} = \sqrt{\frac{\text{ESR}_{120}}{\text{ESR}_f}} \quad (20.3)$$

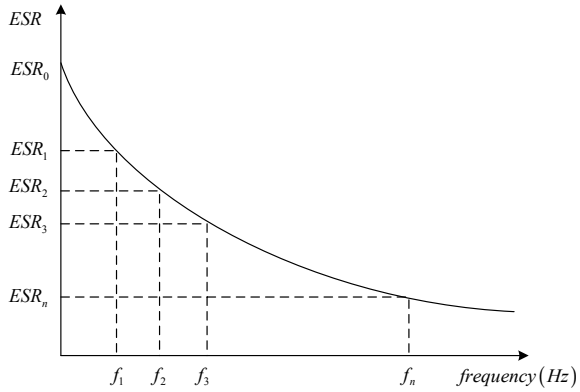
These multiplication factors will account the ESR variation effect into the power loss calculation. These multiplication factors will also be provided by capacitor manufacturer. Table 20.1 shows the data provided by the capacitor manufacturer for the capacitor used in the evaluation and its ESR behaviour with respect to frequency is as in Fig. 20.3.

Calculating the Hot Spot Temperature

The capacitor hot spot temperature is calculated using the information provided by the capacitor manufacturer for the particular capacitor type. The hot spot temperature is the key factor for determining the lifetime of the capacitor. The value of the total rms ripple current can be determined from the harmonic spectrum. The capacitor hot spot temperature (T_h) is calculated as in Eq. (20.4) with the known value of power loss (P_d) and thermal resistance (R_{th}) with the surrounding temperature information (T_A) of the capacitor [3, 4].

$$T_h = T_A + P_d \cdot R_{th} \quad (20.4)$$

Fig. 20.3 ESR as a function of frequency



Capacitor Lifetime Calculation

The predicted lifetime is calculated using the relationship between the calculated hot spot temperature and manufacturer recommended co-efficients. The lifetime is calculated as below in Eq. (20.5).

$$L_{op} = A \cdot 2^{\frac{85-T_h}{c}} \tag{20.5}$$

where *A* and *C* are the lifetime coefficients given by the manufacturer. With the available hot spot information (*T_h*), lifetime (*L_{op}*) is calculated [3–5].

20.5 Modelling and Simulation of VFD

Simulink® model was developed for simulation study with 315 kW, 400 V, 580 A, and 50 Hz VFD connected to both PV grid and non-polluted or pure grid. Rectifier input voltage on distorted and non-distorted grid is as in Fig. 20.4a, b. Harmonics in the range of twenty-first to twenty-third order have significantly increased because of the PV grid as shown in Fig. 20.5a. Lower-order harmonics are also increased even though the fundamental is less in such conditions.

Rectifier input current on distorted and non-distorted grid is shown in Fig. 20.6a, b.

Capacitor ripple current is heavily distorted because of the line voltage distortion in Fig. 20.7a. The reflected DC capacitor current is shown in Fig. 20.7a, b.

The ripple current has higher order components present in Fig. 20.8a. This, in turn, varies the ripple current magnitudes and results in more heating. ESR value changes due to these effects resulting in the capacitor lifetime reduction [6]. 300 Hz current component value of the capacitor is less because of grid impedance changes due to the PV grid model in Fig. 20.8a.

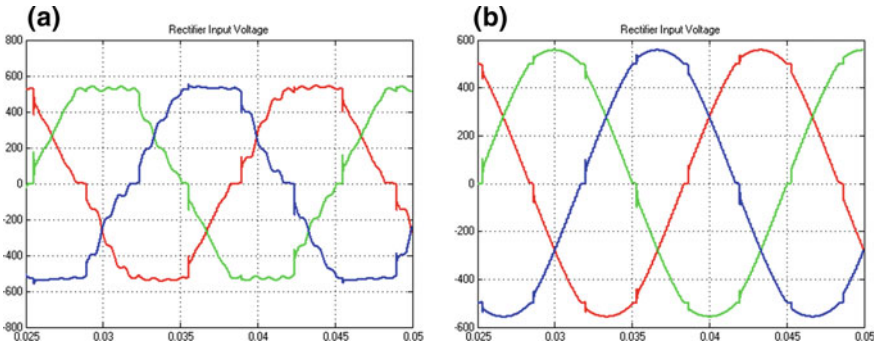


Fig. 20.4 a Rectifier input voltage on distorted grid and b rectifier input voltage on non-distorted grid

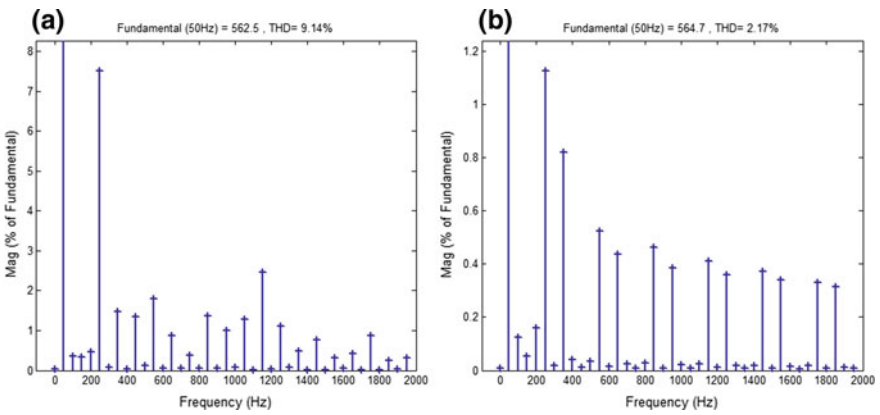


Fig. 20.5 a Rectifier input V_{THD} on distorted grid and b rectifier input V_{THD} on non-distorted grid

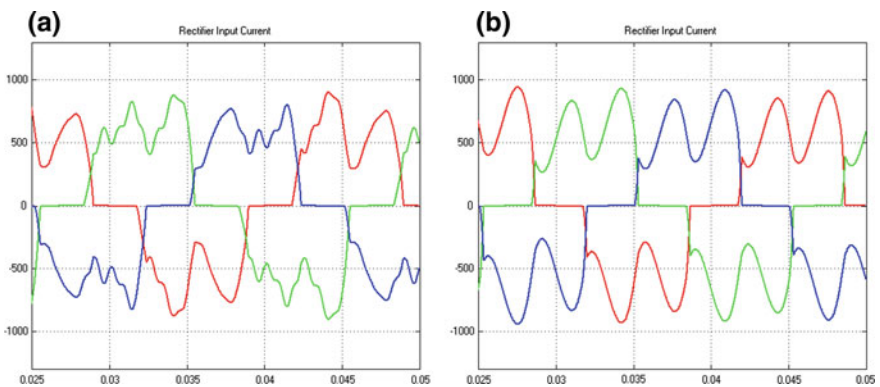


Fig. 20.6 a Rectifier input current on distorted grid and b rectifier input current on non-distorted grid

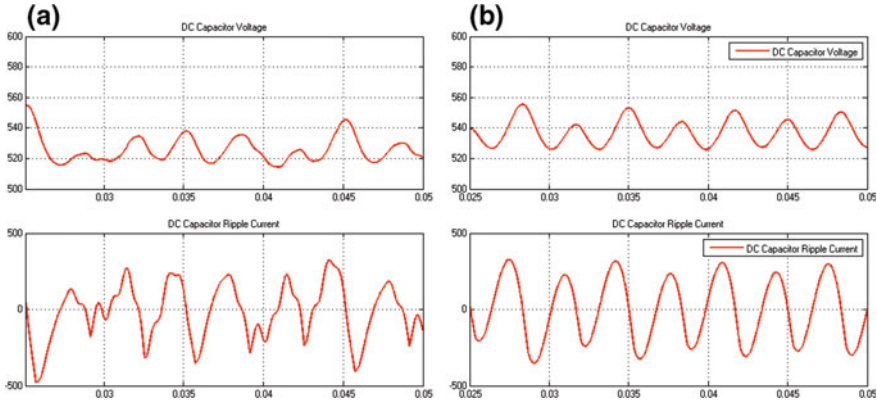


Fig. 20.7 DC capacitor voltage and ripple current in a distorted grid and b non-distorted grid

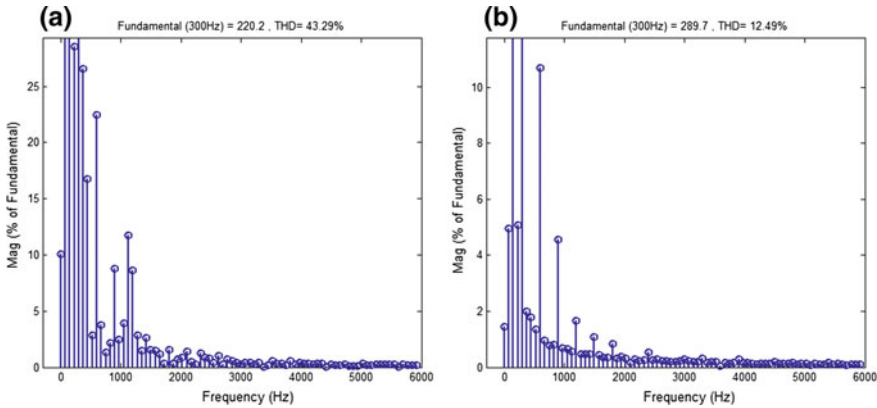


Fig. 20.8 a FFT of capacitor ripple current with distorted grid and b FFT of capacitor ripple current with non-distorted grid

DC voltage across inductor on distorted and non-distorted grid is shown in Fig. 20.9a, b. In addition, V_{THD} of inductor voltage waveform on distorted and non-distorted grid is shown in Fig. 20.10a, b, respectively.

Due to the presence of the high-distorted current voltages in the grid, the DC link inductor will experience faster flux reversals. Majority of the magnetic flux density of the DC inductor consists of the DC components and the AC ripple components in the multiples of the fundamental frequency component. The relevant Eq. (20.6) governs the stated conditions.

$$B_{pk} = B_{dc} + B_{h=300Hz} + B_{h=600Hz} + B_{h=900Hz} + B_{h=1200Hz} + \dots \quad (20.6)$$

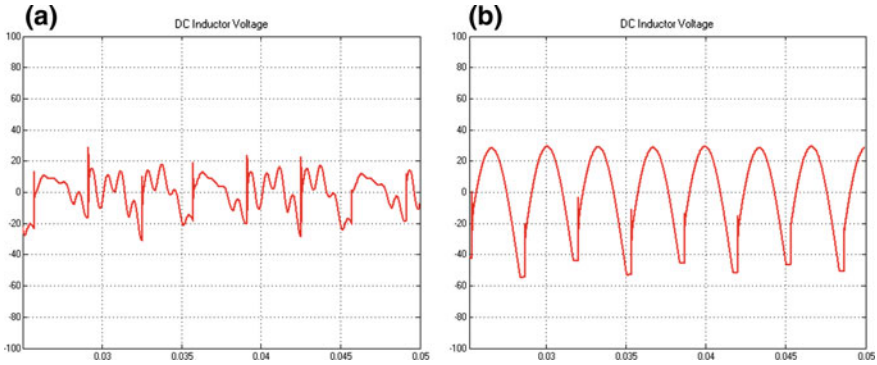


Fig. 20.9 DC inductor voltage in **a** distorted grid and **b** non-distorted grid

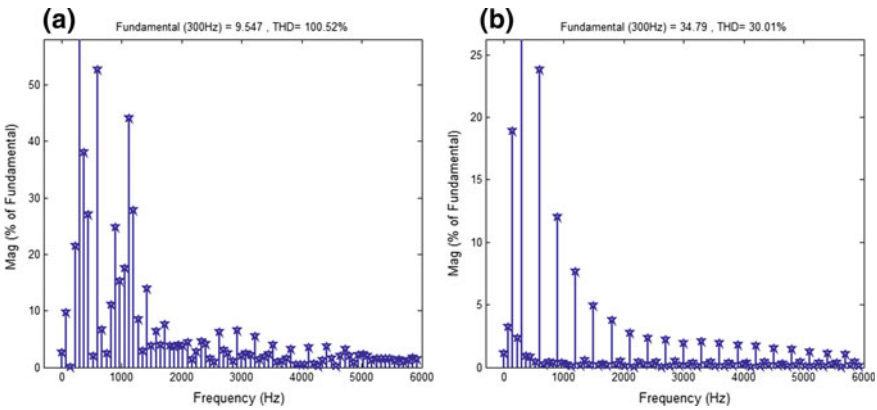


Fig. 20.10 V_{THD} of inductor voltage waveform **a** distorted grid and **b** non-distorted grid

The change in B_{pk} considerably varies the core loss [7]. As the ratio of the fundamental component and the harmonic components are less in case of the DP grid, the core loss will increase considerably.

20.6 Estimation of DC Capacitor Lifetime

The above simulation results show that the capacitor ripple current harmonics are very high in the low-frequency ranges. It was also noticed that the harmonics in the higher order is substantial. There were two cases considered for calculating the Lifetime of the capacitor (with PV or distorted grid and non-distorted or pure grid). While calculating the lifetime based on the calculation principle shown, it is noticed that the capacitor losses are considerably high with the distortion. This is mainly because of the variation in the harmonic levels and the weight factors (M_f).

Table 20.2 Capacitor lifetime (a) pure or non-distorted grid and (b) distorted or PV grid

Grid	R_{th}	T_A	P_d	T_h	A	C	Factor	L_{op} (h)
(a) Pure grid	0.4	40	41.42	56.57	6000	12	2.37	30,996.62
(b) PV grid	0.4	40	45.94	58.37	6000	12	2.22	27,922.87

Because of the increase in losses, the lifetime is significantly reduced on the capacitors as in Table 20.2. Generally, the DC capacitors are considered as the weakest elements with respect to the lifetime characteristics in the VFD. Because of this, the life time of the VFD is also reduced considerably.

20.7 Conclusion

Detailed analysis and simulation in this paper shows VFD capacitors lifetime estimation is greatly influenced due to PV connected grid configuration. The reference grid as shown in Fig. 20.1 is considered for analysis and simulation. The PV grid model was generated and the interface with VFD was simulated to analyse the performance. From the analysis, it is observed that the DC link parameters are considerably distorted. This distortion affects the voltage and current stress on DC link inductor and DC filter capacitor. A specific reference operating condition was considered for simulation studies. The capacitor ripple current variation is analysed from the simulation and the lifetime is estimated. From the results, it is seen that the lifetime is getting reduced considerably. Changes in the DC link inductor voltage and its effect are also addressed.

References

1. Enslin, J.H., Heskes, P.J.: Harmonic interaction between a large number of distributed power inverters and the distribution network. *IEEE Trans. Power Electronic.* **19**(6), 1586–1593 (2004)
2. Soltani, H., Davari, P., Kumar, D., Zare, F., Blaabjerg, F.: Effects of DC-link filter on harmonic and interharmonic generation in three-phase adjustable speed drive systems. In: *Energy Conversion Congress and Exposition (ECCE) IEEE*, pp. 675–681 (2017)
3. Rendusara, D., Cengelci, E., Enjeti, P., Lee, D.C.: An evaluation of the DC-link capacitor heating in adjustable speed drive systems with different utility interface options. In: *Applied Power Electronics Conference and Exposition, APEC'99. Fourteenth Annual*, vol. 2, pp. 781–787 (1999)
4. Lee, K., Jahns, T.M., Lipo, T.A., Venkataramanan, G., Berkopec, W.E.: Impact of input voltage sag and unbalance on DC-link inductor and capacitor stress in adjustable-speed drives. *IEEE Trans. Ind. Appl.* **44**(6), 1825–1833 (2008)
5. Parler, S.G.: Deriving life multipliers for electrolytic capacitors. *IEEE Power Electron. Soc. Newslett.* **16**(1), 11–12 (2004)

6. Kolar, J., Wolbank, T., Schrod, M.: Analytical calculation of the RMS current stress on the DC link capacitor of voltage DC link PWM converter systems. In: Proceeding of ICEMD, pp. 81–89
7. Arnold Magnetic Application Notes [Online]. Available <http://www.arnoldmagnetics.com/>